Representing vertical variation of radiation in cities: a model evaluation and comparison

PhD in Atmosphere, Oceans, and Climate

Department of Meteorology

School of Mathematical, Physical, and Computational Sciences

Megan Alice Stretton

September 2022

Abstract

Radiation exchanges in cities are impacted by their heterogenous structure, driving changes in within-canopy heat fluxes and temperatures, and increasing vulnerability to extreme weather events. However, high computational costs and a lack of knowledge on city structure constrain the representation of cities for numerical weather prediction often to single-layer models with simplified urban form. This thesis assesses the abilities and benefits of a multi-layer urban radiative transfer model "SPARTACUS-Urban" against a complex building-resolving model "DART", and a single-layer infinite street canyon approach to urban radiation.

The SPARTACUS-Urban shortwave and longwave radiation evaluations demonstrate good agreement with DART. Agreement is best for random cuboid geometries that fulfil the SPARTACUS assumptions that buildings are randomly distributed in the horizontal plane, with normalised bias errors in bulk albedo < 6%, and within-canopy facet absorptions < 15%. Shortwave performance in real-world domains is improved with a modification to building edge length to account for large open spaces, leading to better prediction of radiation penetrating to ground level. The infinite street canyon approach predicts top-of-canopy fluxes well, but SPARTACUS-Urban model performance is better due to the ability to represent realistic descriptions of within-canopy roof and wall variation.

To apply SPARTACUS-Urban, vertical urban form data are needed. Statistical relations are developed using data from six cities to obtain profiles from surface building fraction, mean building height, and the effective building diameter. Reducing the needed inputs has little effect on the bulk albedo, but produces considerably larger within-canyon absorption errors, particularly if total wall area is not used. Potentially, the statistical relations can be used globally.

SPARTACUS-Urban coupled to the SUEWS urban energy balance model, is used to investigate impacts of real-world geometry. The results are similar for older top-of-canopy net all-wave radiation approaches, but the new system enables simulation of spatially variable surface temperatures.

Declaration

I confirm that this is my own work and the use of material from other sources has been properly and fully acknowledged. This work contains three publications, and a science chapter that will be prepared for publication. The papers presented are:

Chapter 3: Stretton, M. A., W. Morrison, R. J. Hogan, C. S. B., Grimmond, 2022: Evaluation of the SPARTACUS-Urban Radiation Model for Vertically Resolved Shortwave Radiation in Urban Areas. *Boundary Layer Meteorology* **184**, 301–331 https://doi.org/10.1007/s10546-022-00706-9

Stretton performed all SPARTCUS-Urban simulations, data analysis, and wrote the initial manuscript (Hogan assisting with section 3.5). Morrison developed the 3D model and performed the DART simulations. Hogan is the main author of the Fortran SPARTACUS-Surface code. Hogan developed the early modifications to SPARTACUS-Urban. Morrison produced the initial Figure 3.11. Stretton, Morrison, Hogan, and Grimmond designed the manuscript structure, and all co-authors read and provided feedback on the manuscript. Two anonymous reviewers provided comments on one earlier version of the manuscript. Hogan and Grimmond formulated the initial idea. Grimmond applied for and obtained the funding to support all except for Hogan.

Chapter 4: Stretton, M. A., W. Morrison, R. J. Hogan, C. S. B. Grimmond, 2022: Evaluation of vertically resolved longwave radiation in SPARTACUS-Urban and the sensitivity to urban surface temperatures. *Submitted to Geoscientific Model Development.* Available on EGUsphere: https://doi.org/10.5194/egusphere-2022-1002.

Stretton performed all SPARTACUS-Urban simulations, data analysis, and wrote the initial manuscript. Morrison developed the 3D model, and performed the DART simulations with input from Stretton. Hogan is the main author of the Fortran SPARTACUS-Surface code, which was modified by Stretton. Stretton, Morrison, Hogan, and Grimmond designed the manuscript structure, and all co-authors read and provided feedback on the manuscript. Hogan and Grimmond formulated the initial idea. Grimmond applied for and obtained the funding to support all (including the observations) except for Hogan.

Chapter 5: Stretton, M. A., R. J. Hogan, C. S. B. Grimmond, W. Morrison, 2022: Characterising the vertical structure of buildings in cities for use in atmospheric models. *Accepted by Urban Climate.* DOI: https://doi.org/10.1016/j.uclim.2023.101560

Stretton performed all modelling, all data analysis, and wrote the initial manuscript. Stretton and Hogan developed the parameterisation method. Stretton, Hogan, and Grimmond designed the manuscript structure, and all co-authors read and provided feedback on the manuscript. Hogan and Grimmond formulated the initial idea. Grimmond applied for and obtained the funding to support all (including earlier Kent obtained data) except for Hogan.

The final research chapter is:

Chapter 6: Vertical variability of urban morphology: implications for modelling surface fluxes and temperatures.

Stretton performed all simulations, data analysis, and wrote the chapter. Ting Sun, Lewis Blunn, and Ruidong Li coupled SPARTACUS-Surface to SUEWS, and developed the new multi-layer heat storage scheme, tested by Stretton. Morrison collected and processed the thermal camera observations. Denise Hertwig provided the materials data. Hogan is the main author of the Fortran SPARTACUS-Surface code. Grimmond is the original developer of SUEWS. Grimmond and Hogan provided feedback on the manuscript. Hogan and Grimmond formulated the initial idea. Grimmond applied for and obtained the funding to support all (including the observations) except for Hogan, Sun, and Li.

Megan Alice Stretton

Whether the weather be hot,

Or whether the weather be cold,

Whatever the weather,

We’ll weather the weather,

Whether we like it or not.

- Anon

Acknowledgements

Firstly, I would like to thank my supervisors Sue Grimmond and Robin Hogan, for the opportunity to conduct this research. You have both been a huge support throughout the past four years, and I am sad that the pandemic has resulted in most of our interactions being virtual. Sue; I have valued your always-thorough feedback and guidance, and your availability no matter the time of day. The progression of this PhD has been benefitted greatly from your knowledge of urban meteorology, and as a female scientist it has been particularly inspiring to have a mentor who is the first woman ever to win the RMetS Symons Gold Medal. Robin; your technical advice and patience have been invaluable! Without you I am sure I would still be stuck on that first day trying to use MATLAB. A special thank you goes to William Morrison, for the work with DART simulations, but also for some enjoyable discussions. Will, your advice has always been greatly appreciated.

I would also like to thank Ting Sun, for the many hours spent chasing bugs in the SUEWS model, and also Lewis Bunn, for their combined work in the coupling with SPARTACUS-Surface. I would like to thank my monitoring committee: Tristan Quaife, Geoff Wadge, and Peter Clark. Although our meetings were not often one of my favorites, I am grateful for your insightful comments and encouragement.

Thank you to all of those who have been part of the Micromet research group over the past four years, including but not limited to: Denise Hertwig, Natalie Theeuwes, Mat Lipson, Elliot Warren, Kit Benjamin, Xiaoxiong Xie, Yiqing Liu, and Martina Frid. Your comments in the weekly meetings were always helpful, and I have enjoyed watching your work evolve. I will also begrudgingly admit I enjoyed the times spent maintaining the instruments up various tall buildings in London. A special thanks goes to Beth Saunders, for always being willing to discuss my scientific ideas and problems, and for all of the computing help at the start of my PhD.

I would like to thank everyone in 2U08 for all the fun times and support, but not for the paper airplanes. Additional thanks go to Hannah Bloomfield, Caroline Wainwright, and Natalie Harvey for your motivational pep-talks at lunchtimes and coffee breaks.

I can remember very clearly taking a maths test when my family moved back to the UK from Australia, and I couldn’t remember how to do any of the questions. Since then, I have had many teachers with a passion for science and maths, who have truly believed in their students, and helped me to retain my curiosity for the world around me. In particular, I owe my mathematical ability to my secondary school maths teacher, Theresa Devine, for her enthusiasm and kindness in the classroom that made me want to learn. I also thank my A-level physics teacher, David Boyce, whose rebellious lessons were always captivating. Without both of these teachers, I know I would never have written this thesis.

Finally, I would like to thank my closest family and friends. Alex Doyle, Kieran Pope, and Simon Lee – I am so glad I got to share this meteorological journey with you from the very start. Thank you to Alec Vessey for all your support, particularly since the pandemic, whether it be through doing the mountains of washing up, as a running buddy when times became stressful, or through making the many cups of tea and coffee needed to write this thesis. The biggest thank you of all goes to my parents and little sister, who have always been my team no matter what. I am more grateful than you can imagine for your support.

Contents

List of Figures

Main text:

Chapter appendices:

List of Tables

Main text:

Chapter appendices:

Notation

a_{Roof}	Roof absorption
a_{Wall}	Wall absorption
a_{Ground}	Ground absorption
$a_{Wall+Roof}$	Combined roof and wall absorption
a	Coefficient for building fraction parameterisation
b	Coefficient for building fraction parameterisation
C	‘Concavity parameter’
D	Effective building diameter
$\overline{H}$	Area weighted mean building height
H_{max}	Maximum height of buildings
H	Building height
$\overline{H}/W$	Height-to-width ratio
i	Layer index
L	Normalised building edge length
$L(z = 0)$	Normalised building edge length (surface)
$\hat{L}$	Effective building edge length
LW^*	Longwave net flux
$\mathrm{LW}_{\uparrow}$	Upwelling longwave
$\mathrm{LW}_{\downarrow}$	Downwelling longwave
$\mathrm{LW}_{\mathrm{Out}}$	Outgoing longwave flux from a surface
$\mathrm{LW}_{\mathrm{In}}$	Incoming longwave flux into a surface
n	Number
N	Number of streams (SPARTACUS-Surface)
P	Building perimeter length
p	Coefficient for effective building edge length parameterisation
q	Coefficient for effective building edge length parameterisation
Q^*	Net all-wave radiation
Q_F	Anthropogenic heat flux
Q_H	Sensible heat flux
Q_E	Latent heat flux
ΔQ_S	Net storage heat flux
R	Canyon-plus-roof distance
r	Coefficient for effective building edge length parameterisation
$\mathrm{SW}_{\mathrm{Diffuse}}$	Diffuse shortwave flux
$\mathrm{SW}_{\mathrm{Direct}}$	Direct shortwave flux
SW^*	Shortwave net flux
$\mathrm{SW}_{\uparrow}$	Upwelling shortwave
$\mathrm{SW}_{\downarrow}$	Downwelling shortwave
T	Surface temperature

T_{Air}	Air temperature
T_{Roof}	Roof temperature
T_{Wall}	Wall temperature
T_{Ground}	Ground temperature
V	Normalised building volume
W_S	Width of a building shadow
W	Canyon width
Δx	Horizontal resolution
X	‘e-folding’ distance
z	Height
α	Albedo
α_{Bulk}	Bulk top-of-canopy albedo
α_{Wall}	Wall albedo (also Roof, Ground)
β	Bowen ratio
ε	Emissivity
ε_{Bulk}	Bulk emissivity
θ_0	Solar zenith angle
λ_f	Frontal area index
λ_i	Plan area fraction of impervious surfaces
λ_p	Plan area fraction of buildings
$\lambda_p(z = 0)$	Plan area fraction of buildings (surface)
λ_w	Normalised wall area
λ_v	Plan area fraction of vegetation
ψ_{Sky}	Sky view factor
E	Energy loss
Ω	Azimuth angle

List of Acronyms

1D	One-dimensional
2D	Two-dimensional
3D	Three-dimensional
ABL	Atmospheric Boundary Layer
a.g.l	Above ground level
AnOHM	Analytical Object Hysteresis Method
BCT	Barbican Cromwell Tower
BE	Bias Error
BEERS	Building Energy Envelope Radiation Scheme
BEP	Building Effect Parameterisation
BOA	Bottom of Atmosphere
CBD	Central Business District
CFD	Computational Fluid Dynamics
CL-UHI	Canopy-Layer Urban Heat Island
COSMO	Comprehensive Outdoor Scale Model
DART	Discrete Anisotropic Radiative Transfer
DEM	Digital Elevation Model (v – vector, r – raster)
DNS	Direct Numerical Simulation
DOY	Day of Year
DSM	Digital Surface Model (v – vector, r – raster)
E-W	East-West
ECMWF	European Centre for Medium Range Weather Forecasts
ERA5	ECMWF Reanalysis 5th Generation
ESTM	Elemental Surface Temperature Method
F	Form
GHSL	Global Human Settlement Layer
GUF	Global Urban Footprint
IFS	Integrated Forecasting System
IMU	Islington Michael Cliff House Upper
ISL	Inertial Sub-Layer
LES	Large Eddy Simulation
LCZ	Local Climate Zones
LOD	Level of Detail
LULC	Land-use land-cover
LiDAR	Light Detection and Ranging
LW	Longwave
MAE	Mean Absolute Error (n – normalised)
mEHC	Multi-layer explicit heat conduction scheme
MBE	Mean Bias Error (n – normalised)
MORUSES	Met. Office-Reading Urban Surface Exchange Scheme

MOST	Monin-Obukhov Similarity Theory
N-S	North-South
NARP	Net All-Wave Radiation Parameterisation
NWP	Numerical Weather Prediction
NYC	New York City
ODE	Ordinary Differential Equation
OHM	Objective Hysteresis Method
ORM	Object Resolving Model
P	Parameterisation
PET	Physiological Equivalent Temperature
RANS	Reynolds Averaged Navier Stokes
SEB	Surface Energy Balance
SGS	Sub-grid-scale
SOLWEIG	Solar Longwave Irradiance Geometry model
SPARTACUS	Speedy Algorithm for Radiative Transfer through Cloud Sides
SS	SPARTACUS-Surface
SU	SPARTACUS-Urban
SUEWS	Surface Energy and Water balance Scheme
SUEWS-SS	SUEWS coupled to SPARTACUS-Surface
SW	Shortwave
TEB	Town Energy Balance
TUF	Temperature of Urban Facets
UCL	Urban Canopy Layer
UHI	Urban Heat Island
UK	United Kingdom
UKV	UK Variable resolution model
UTC	Coordinated Universal Time
UTCI	Urban Thermal Climate Index
UZE	Urban Zones for Energy partitioning
WCT	Wycliffe Court Tower
WUDAPT	World Urban Database and Access Portal Tools

Chapter 1 Research Overview

1.1 Motivation for research

The interactions between the Sun’s energy and the Earth’s surface drive the weather and climate experienced on Earth (Sellers 1969). The proportion of energy stored and released as heat is driven by surface properties, including morphology, materials, and sun-surface geometry. Land-use changes driven by human activities, e.g., agriculture and urban development, lead to the replacement of natural surfaces – in the case of urbanization by impervious surfaces, modifying the existing natural energy exchanges. In urban areas, the spatial variation of the heterogenous surface structure, and the spatial and temporal variation in human activities, play large roles in these changes in the surface energy balance (Kawai and Kanda 2010).

The exact influence of a given city on the surface energy balance (SEB) depends on factors such as geographical location, economics, city layout, and human behavior, as these lead to differences in materials, morphology, and anthropogenic emissions (Piringer et al. 2002; Oke et al. 2017). Impervious building materials often have high heat capacities (e.g., concrete or tarmac roads and pavements, Asaeda et al. (1996)), or reflect and transmit radiation (e.g., glass skyscrapers). Additionally, the geometry of densely packed buildings in city centres exacerbates heat retention, altering the exposure to the cold sky, and increasing the reflection between buildings (Ward and Grimmond 2017). With less vegetation, evaporation is reduced (Oke 1987) but some cities in arid regions may irrigate exotic vegetation, enhancing evaporation relative to the surroundings (Wang et al. 2015; Broadbent et al. 2018). The most frequently studied contrast between urban and rural areas, is air temperature, known as the canopy layer urban heat island (CL-UHI) effect at 1-2 m above ground level (Oke 1982a; Zhang et al. 2012; Wu et al. 2014; Guo et al. 2016; Dou and Miao 2017; Gaitani et al. 2017). This is a net result of differences in surface energy balance exchanges between the two areas.

The proportion of the world’s population living in cities is predicted to rise to > 60% of current (2018) global numbers by 2030 (United Nations 2018) (Figure 1.1a), although this varies based on the country of interest (Figure 1.1b). Urban surface properties, increased population, and existing UHI effects will lead to increased vulnerability and exposure to extreme weather events (e.g., heatwaves, Grimmond (2007); Ellena et al. (2020); Chen et al. (2022)), linked to the decreased evapotranspiration and warmer nocturnal air temperatures. Furthermore, heatwaves can magnify the UHI effect, as more heat is stored by the urban surface, increasing temperatures further (Mccarthy et al. 2010; Li et al. 2015a). These impacts will vary with location, socio-economic situation, and morphology (Bathiany et al. 2018).

Such extreme heat events, which are predicted to increase in intensity, duration, and frequency over most land areas in the 21st century (Meehl and Tebaldi 2004; IPCC 2014a), are already linked to updating of operational heatwave definitions for several counties (Met Office 2022). A +1.5 °C climate is expected to more than double health-related heat integrated exposure in 26 countries (Sun et al. 2019), with US cities expected to experience up to a 4.5% increase in mortality risk per 1 °F (~ 1.8 °C) heatwave increase, depending on location (Brooke Anderson and Bell 2011). Increased heat stress has economic as well as health implications (Pascal et al. 2006).

With more potentially more frequent, and severe hazardous weather, it is crucial that city-based services, including transport, energy, water, and building planning and management are supported with appropriate information to mitigate future effects on the public and infrastructure. To improve resilience in cities, stakeholders should be provided with relevant and well-translated urban climate information, to assist in decision making and to help services adapt to future climate variability. This needs to be dynamic and evolve as cities and technology adapt into the future (Barlow et al. 2017). Such information could include urban meteorological and air-quality observations, combined hazard early warning systems, and high-resolution forecast information (Baklanov et al. 2018; Masson et al. 2020a), alongside socio-economic and agricultural data, and relevant risk and vulnerability maps.

To achieve this, researchers must firstly understand the radiation-bioclimatic interactions as human health, thermal comfort, and radiation fluxes, are influenced by building morphology shading and reflection (Lin et al. 2010; Lindberg et al. 2011; Thorsson et al. 2011; Yang and Li 2015; Konarska et al. 2016a; Fischereit 2021), as well as the presence (or lack) of green spaces and street vegetation (Grimmond et al. 1996; Lindberg et al. 2011; Chen et al. 2014; Konarska et al. 2016b; Segura et al. 2022). Both observation- and model-based research have contributed to our current understanding of the feedbacks between cities and local temperatures, downstream weather, and human health.

Data provided for city-based climate services should be accessible (i.e., easy to process with common formatting), but often are not – with complex formats or non-consistent coverage or level of detail across cities (and globally) (Lindberg et al. 2018; Masson et al. 2020b). Ideally, forecasts provided to stakeholders and services would be high resolution across all cities in order to provide detailed information about risk and vulnerability. However, computational costs limit modelling of the complex energy exchanges in urban areas. The coarse resolution of both current operational numerical weather prediction (NWP) models and global data on city structure, prevent a full description of the urban canopy in these models.

An additional limitation of current operational NWP models is that urban areas are often represented simply without the real-world urban heterogeneity. NWP schemes commonly either have no urban scheme (e.g., ECMWF’s IFS, Boussetta et al. (2021)) or take an urban canyon approach to represent urban morphology (e.g., UKV MORUSES, Porson et al. (2010); Hertwig et al. (2020)). As NWP models advance to higher resolutions, more intra-city variability (including parks, tall buildings, and deep canyons) need to be resolved (Lean et al. 2019), for more accurate weather predictions across cities.

In this thesis, urban radiative transfer modelling is addressed using three complexity levels: (1) single-layer infinite street canyon, (2) multi-layer urban canopy, and (3) an explicit 3-D object-resolving model (ORM). The latter are the slowest, and more complex than simpler radiative transfer schemes, but inappropriate for NWP. Therefore, in this thesis the question addressed is whether a multi-layer model could ‘bridge the gap’ between the simpler single-layer and 3-D ORM approaches. If so, the multi-layer radiative transfer model, when coupled with multi-layer urban energy balance schemes, should improve the calculation of vertical variation within the urban canopy of both facet radiative fluxes and surface temperatures. These in turn should improve weather forecasts in urban areas, and the assessment of both the thermal climate, and heat stress experienced by urban populations.

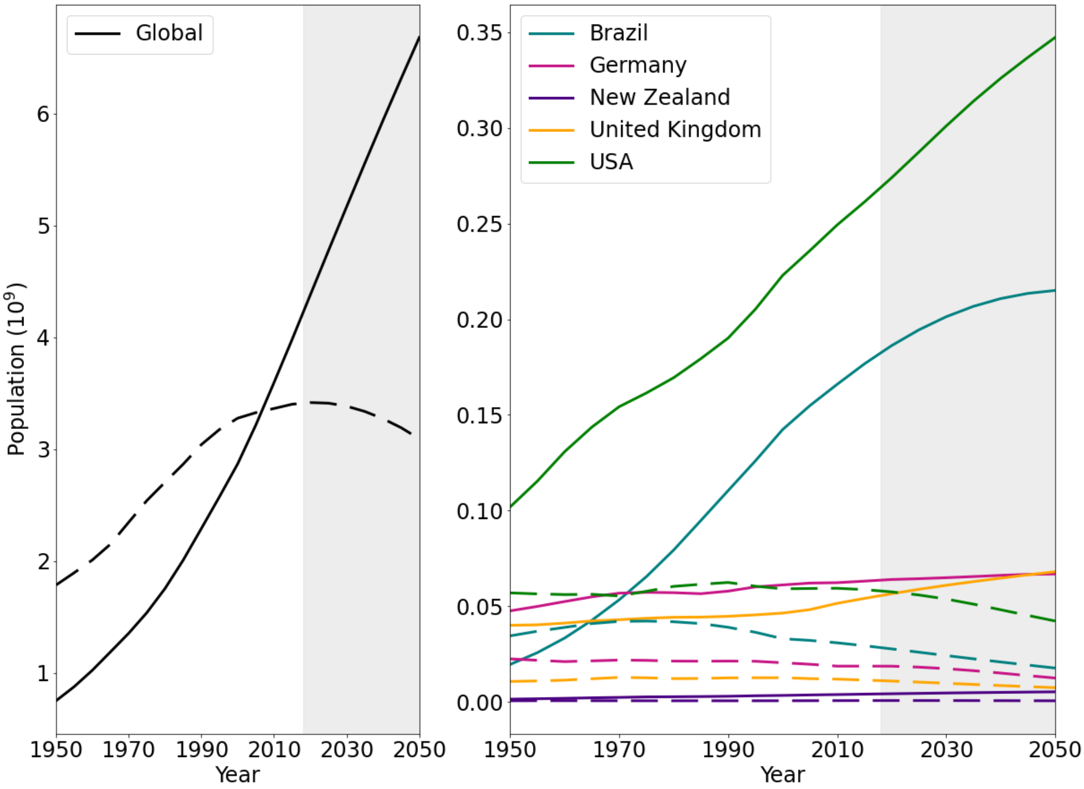

Figure 1.1: Changes in urban (solid) and rural (dashed) population (a) globally and (b) in cities worldwide. Shaded areas denote projected population changes. Data obtained from United Nations (2019).

1.2 Thesis objectives and structure

This thesis focusses on assessing and using the multi-layer radiative transfer model, SPARTACUS-Surface (Hogan 2019a). Here, only radiation exchanges in non-vegetated urban areas are considered, so the model is referred to as ‘SPARTACUS-Urban’. The specific objectives of this thesis are:

1. To evaluate both the performance of SPARTACUS-Urban using the 3D ORM “DART” for shortwave and longwave fluxes, and the benefits of using multi-layer models with a comparison to a commonly used single-layer infinite street canyon approach.
2. To propose and evaluate how the vertical structure of buildings across and between cities can be characterised using simple parameterisations.
3. To examine the impact of using the SPARTACUS approach to urban radiation within an urban canopy model to simulate energy balance fluxes and within-canopy surface temperatures.

To address these objectives, this thesis has four major science chapters after a background chapter on urban morphology and radiation modelling (Chapter 2). SPARTACUS-Urban's performance is evaluated for shortwave (Chapter 3, Stretton et al. (2022)) and longwave (Chapter 4) radiation for varying urban geometry against the ORM model and relative to a current NWP 1-D approach. The urban form parameters used by SPARTACUS-Urban are explored using data from six cities (Chapter 5). The Surface Energy and Water Balance Scheme (SUEWS, Järvi et al. (2011); Ward et al. (2016); Omidvar et al. (2022)) with SPARTACUS-Surface is used to explore the impact of resolving the vertical variation of urban morphology on fluxes and surface temperatures (Chapter 6).

Chapter 2 Scientific Background

It is currently too computationally expensive for numerical weather prediction (NWP) models to realistically represent the heterogeneity of urban environments across all scales. Consequently, weather forecasts in the most populated or densely built areas could be inaccurate. In addition to modelling challenges, there are further uncertainties in the parameters required for urban modelling, such as those related to human activities, urban morphology, and indoor environments (Chen et al. 2011). These can vary greatly across a city, further impacting NWP model accuracy.

Radiative fluxes are often the largest urban energy source, influencing meteorological conditions within and above the urban canopy layer (UCL). This the lowest layer of the atmospheric boundary layer (ABL), where human activities are greatest, and extends to the height of the tallest urban elements e.g., tall buildings or vegetation (Oke 1982a). Therefore, there is a need to seek out, and evaluate, more detailed but computationally efficient modelling approaches for urban environments. This thesis focuses on evaluating one of these new approaches for radiation modelling.

This chapter describes the impact that urban heterogeneity has on radiation and energy balances (2.1, 2.2), and common methods used to model urban radiation (2.4). The models used in this work are detailed in Section 2.4. Finally, the parameters required by models to describe urban material and morphological characteristics, and methods/datasets to provide these are discussed (2.5). The equations in section 2.1 and 2.2 can be found in relevant textbooks, for radiation (e.g., Petty (2004)) or urban meteorology (e.g., Oke et al. (2017)), and so are not referenced in the text.

2.1 The radiation balance

Electromagnetic radiation received by the Earth from the Sun distributes energy at a rate across a given horizontal area, giving a flux (W m^{-2}) (Petty 2004). This can be split by its wavelength; with radiation at a wide range of wavelengths described as broadband radiation, in contrast to single-wavelength monochromatic radiation. The largest portion of electromagnetic radiation received by the Earth-atmosphere system is shortwave radiation (SW), with wavelengths between 0.1 and 4 μm, i.e., in the near-infrared, ultraviolet, and visible bands (Niemela et al. 2001). Both the Earth’s surface and the atmosphere emit longwave (LW), or thermal infrared, radiation at wavelengths 4 – 100 μm (Trenberth et al. 2009).

2.1.1 Shortwave radiation (SW)

Downwelling shortwave radiation at the surface, $SW_{\downarrow}$, can be split into the direct (SW_{Direct}) beam from the sun and a diffuse radiation ($SW_{Diffuse}$) from scattering (Iqbal 1983):

$$SW_{\downarrow} = SW_{Direct} + SW_{Diffuse} \,. \tag{2.1}$$

$SW_{\downarrow}$ varies with latitude, longitude, day of year (DOY) and time of day (i.e., solar zenith angle). Sky conditions (cloud, air quality) can also modifying sky transmissivity, and the amount of diffuse radiation (Kanda et al. 2005b). The upwelling shortwave flux ($SW_{\uparrow}$) is determined by the surface albedo, α (Fortuniak 2008):

$$\alpha = {}^{SW_{\uparrow}}/_{SW_{\downarrow}} \,. \tag{2.2}$$

The α controls the amount of SW radiation absorbed or reflected from a surface, driving both surface temperature (T) and air temperature (T_{Air}) changes. Therefore, it is a crucial parameter to model correctly.

Building and vegetation densities, shapes, and materials differ within and between cities (Table 2.1), e.g., central business districts (CBD) often have high building density and heights (Lindberg and Grimmond 2011b). The distribution of these elements is typically defined using the plan area ratio of their areal coverage to total the horizontal grid-cell area (e.g., plan area fraction of buildings, λ_p; impervious surfaces, λ_i; and vegetation, λ_v). Variations of these surface covers, along with the area-weighted mean building heights ($\overline{H}$), lead to variations in SW radiative exchanges across a city.

The scale of corrugated urban surfaces is large cf. rural areas, with a larger total surface area per grid area for radiative exchange with the same $SW_{\downarrow}$. If areas of cities have high surface building plan area, $\lambda_p(z = 0)$, and large building heights, they often also have short building-building distances, and a reduced sky view factor, ψ_{Sky} (the fraction of the visible sky (Lindberg and Grimmond 2010; Dirksen et al. 2019)). These building-building distances are often expressed through the ratio of $\overline{H}$ to street width, W, $\overline{H}/W$. These features increase the reflection of radiation between individual surfaces, leading to more radiative trapping compared to bare-soil fields, and increased absorption by the urban surface (Aida and Gotoh 1982; Harman et al. 2004; Jin et al. 2005; Dou et al. 2019).

The albedo at the canopy top, across the whole grid-box of interest, is described as the bulk albedo, α_{Bulk}. If the urban facets (walls, roof, ground, Figure 2.1) are assumed a consistent α, an unrealistic assumption with real-world materials, the α_{Bulk} decreases as the area covered by buildings increases, or the building height increases (Sailor and Fan 2002). This is due to the role of multiple-scattering within the urban canopy, as the SW radiation is reflected back toward the urban surface due to the low ψ_{Sky}.

Because of the nature of urban structure, diffuse reflections are common, although most energy is exchanged in the first reflection (Salim et al. 2022). Perfectly diffuse reflectors are described as Lambertian, where radiation is reflected equally in all directions (Petty 2004). However, real urban reflections are non-Lambertian. These variations in reflections, particularly when SW_{Direct} is high, make determining radiometer source areas challenging, impacting the ability to accurately measure the α_{Bulk} (Kotthaus and Grimmond 2014a).

Measured urban α_{Bulk} are ~ 0.05 smaller than those of rural environments (Oke 1988), but they are challenging to measure due to the anisotropy of the urban surface (Offerle et al. 2003; Voogt 2008; Kotthaus and Grimmond 2014a; Adderley et al. 2015). Pyranometers need to be situated high enough that their field of view does not just cover roof facets, as this can lead to differences in albedo even between close observation sites, e.g., the two-site London comparison in Kotthaus and Grimmond (2014b) where measured $\alpha_{Bulk} = 0.11$ and 0.14. Measurements must be representative of a given neighbourhood (Figure 2.1), if to be used for NWP applications, which ideally would include equal sampling of wall and street orientations within the area of interest, due to their material albedo and shadowing differences (Offerle et al. 2003; Soux et al. 2004).

With strategic sensor placement, combining sub-facet materials into one value, facet material α are easier to measure than α_{Bulk}. The albedo of individual building facets varies within and between cities (Table 2.1), note differences across even European cities, e.g., Basel and Marseille), due to building materials surface aging. From observational campaigns, values for different facets are: 0.2-0.25 for walls (α_{Wall}), 0.08-0.25 for roofs (α_{Roof}), and 0.08-0.25 for ground (α_{Ground}) surfaces (Grimmond and Oke 1995; Feigenwinter et al. 1999; Grimmond et al. 2004; Lemonsu et al. 2004; Offerle et al.

2005b; Balogun et al. 2009; Bergeron and Strachan 2012) (Table 2.1). Detailed categorisation of urban materials have been undertaken under controlled conditions. These include Kotthaus et al. (2014) reported material albedos of 0.05 – 0.68, leading to differences between facets due to common building materials, which vary spatially – such as brick walls in suburban areas or glass walls in the CBD, e.g., bricks 0.2 – 0.4, or glass 0.05 – 0.5 (Oke 1987).

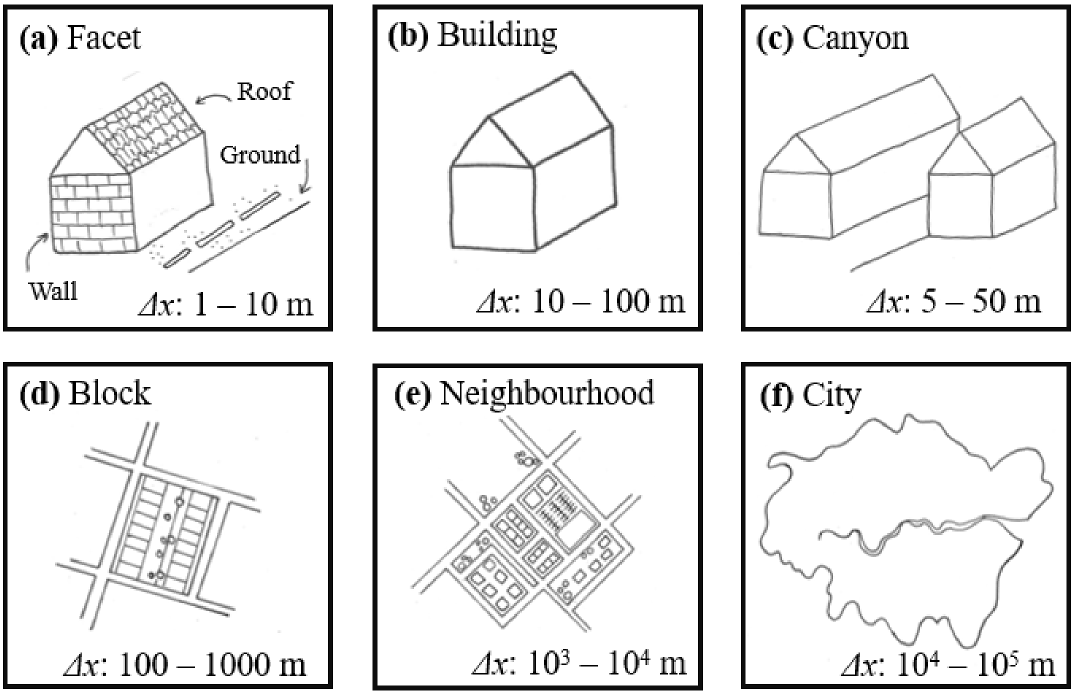

Figure 2.1: Elements of an urban area increasing in horizontal scales. Horizontal length scales (Δx) from Oke et al. (2017)

Table 2.1: Plan area fractions of buildings (λp), vegetation (λv), and impervious surfaces (λi), mean building height ($\overline{H}$), and albedo (α: αRoof, αGround, αWall, and αBulk), for observational campaigns in Oke et al. (2017)

City	Area Type	$\overline{H}$ (m)	λ_p	λ_v	λ_i	α_{Roof}	α_{Ground}	α_{Wall}	α_{Bulk}	References
Arcadia, CA	Suburban	5.2								Grimmond and Oke (1999b)
Basel	Urban	24								Feigenwinter et al. (1999); Christen and Vogt (2004)
	Urban	14,6	0.54		0.3	0.10				
	Urban	12.5	0.37		0.32	0.11				
	Urban	18.8				0.32				
	Suburban	7.5	0.28		0.28	0.13				
Beijing	Residential	20-50	0.65							Song and Wang (2012)
Chicago, IL	Suburban	6.7	0.33	0.34	0.22					Grimmond and Oke (1995, 1999b)
	Suburban	5.9								
Christchurch	Residential	6.1	0.22							Spronken-Smith and Oke (1999); Spronken-Smith (2002)

Essen	Urban Suburban	17 15	0.55 0.48	0.15 0.28	0.15 0.28					Weber and Kordowski (2010)
Florence		25								Matese et al. (2009)
Greenwood, MO	Suburban	6.9	0.295	0.08			0.25			Balogun et al. (2009)
Helsinki	Residential Urban Urban Urban	20 21.7 24.1 20	0.43 0.57 0.55 0.14	 0.46						Vesala et al. (2008); Nordbo et al. (2012)
Kugahara	Residential	7.3	0.326	0.21						Moriwaki and KANDA (2004)
Lodz	Urban Urban Urban Industrial Suburban	17 16 10.2 8.5 7.7	0.35 0.29 0.35 0.17 0.10						 0.10 0.14 0.14	Offerle et al. (2006b); Fortuniak et al. (2013)
London	Urban	21	0.4	0.05						Kotthaus and Grimmond (2014b)
Los Angeles, CA	Residential	5.2	0.22	0.32	0.18					Grimmond and Oke (1995)
Marseille	Urban Urban	15.6 15.6	0.86 0.60	0.15 0.14		0.22 0.22	0.08 0.08	0.20 0.20	0.17	Lemonsu et al. (2004); Grimmond et al. (2004)
Melbourne	Urban Urban Suburban	8.8 6.4 7.2	0.46 0.45 0.39	0.23 0.23 0.29					0.19 0.15 0.17	Coutts et al. (2007)
Mexico City	Urban Urban	12 18.4	 0.54	 0.01	 0.44					Grimmond and Oke (1999b); Velasco et al. (2005)
Miami, FL	Residential Suburban	6.9 8.0	0.33 0.35	0.42 0.34	0.20 0.29					Grimmond and Oke (1999b); Newton et al. (2007)
Montreal	- Residential Suburban	9.5 7.9 6.4	0.84 0.27 0.12	 0.26 0.20	0.16	0.08	0.16	0.25		Lemonsu et al. (2009); Bergeron and Strachan (2011)
Oberhausen	Urban Suburban	14 6.2	0.82 0.42	0.18 0.58					0.11 0.18	Goldbach and Kuttler (2013)
Ouagadougou	Urban Residential	10 3	0.40 0.30	< 0.10 0.10		0.25 0.25	0.08 0.25	0.20 0.25		Offerle et al. (2005b)
Sacramento, CA	Residential	4.8	0.36	0.34	0.12					Grimmond and Oke (1995)
Salt Lake City, UT	Residential	4.4	0.17	0.49						Ramamurthy and Pardyjak (2011)
San Gabriel, CA	Suburban	4.7	0.29	0.37	0.31					Grimmond and Oke (1999b)
Sapporo	Residential	7.0	0.25							Oikawa and Meng (1995)
Toulouse	Urban	20								Masson et al. (2008)
Tuscon, AZ	Suburban	5.2	0.23	0.18	0.42					Grimmond and Oke (1995)
Vancouver	Industrial Urban Suburban	5.8 34.3 4.7	 0.31	 0.44	0.23					Grimmond and Oke (1999b)

2.1.2 Longwave radiation (LW)

A given object emits radiation as a function of its surface temperature (T). For a blackbody (i.e., a perfect absorber and emitter), the intensity (B) of radiation for a given wavelength (λ) and T in W m^{-2} μm^{-1} sr^{-1}, is defined by Plank's law (Petty 2004), for example:

$$B(\lambda, T) = \frac{2hc^2}{\lambda^5}\left(e^{\frac{hc}{\lambda k_B T}} - 1\right)^{-1}, \tag{2.3}$$

Where Planck's constant, h = 6.62 x 10^{-34} m^2 kg s^{-1}, the speed of light, c = 3 x 10^8 m s^{-1}, and the Boltzmann constant, k_B = 1.38 x 10^{-23} m^2 kg s^{-2} K^{-1}. Integrating the Planck function (Eq. 2.3) over all wavelengths gives Stefan Boltzmann's law, which states that the maximum broadband radiation (or power, P) emitted from a surface is proportional to the fourth power of its temperature, e.g.,

$$P = \sigma\varepsilon T^4, \tag{2.4}$$

where σ = 5.67 x 10^{-8} W m^{-2} K^{-1} (Petty 2004). The emissivity (ε) is the ratio of the emission by a given surface, and the emission if it were a blackbody. Most urban surfaces have an emissivity in the range 0.89 – 0.97 (Kotthaus et al. 2014), although for some metals this is much lower.

Generally, urban surface temperatures are largest in the daytime. Urban morphology, in particular ψ_{Sky} influences the temperatures, with building shadowing leading to variations in SW$_\downarrow$, that vary with solar zenith angle (Harman and Belcher 2006; Antoniou et al. 2019). This can lead to microscale variations in surface temperature across individual facets (Figure 2.1a) (Lindberg and Grimmond 2011b; Morrison et al. 2018, 2021).

One example of how morphology influences the surface temperatures and LW emission is in wide streets or large open spaces e.g., industrial areas, airports, or car parks. In these locations, where impervious cover dominates and there is a large ψ_{Sky}, large SW absorption increases temperatures (Sakakibara 1996; Oke et al. 2017). This contrasts with densely built areas where SW absorption by roads and walls is reduced (Ryu et al. 2011; Oke et al. 2017). But, these closed areas also experience reduced LW loss, and as such warm temperatures remain into the night (Voogt and Oke 1991; Kondo et al. 2005; Ryu et al. 2011). These temperatures then influence the LW fluxes, through the LW emission in Eq. 2.3 (Krayenhoff and Voogt 2016; Morrison et al. 2018; Hogan 2019a). Within the canopy, particularly with taller buildings, warmer T and high ε can lead to increased LW$_{\downarrow}$ onto lower surfaces, e.g., from walls to lower roofs (Oke and Fuggle 1972; Suckling 1981).

Contrasts in T_{Air} and T between the cities and their rural surroundings are described by the urban heat island effect (UHI), which can be defined at different scales. For example, T_{Air} differences are defined as the canopy layer UHI (CL-UHI). The CL-UHI is one of the most widely studied influence of urban areas on the atmosphere (Terjung and Louie 1973; Oke 1982a; Wu et al. 2014; Guo et al. 2016; Gaitani et al. 2017). These larger air temperatures within urban areas lead to increased pedestrian thermal discomfort (Lindberg et al. 2011; Li et al. 2020). This can be measured by a range of parameters such as physiological equivalent temperature (PET, Matzarakis et al. (1999); Lin et al. (2010); Fröhlich et al. (2019)), universal thermal climate index (UTCI, Błazejczyk et al. (2013); Takane et al. (2020)), and mean radiant temperature (T_{mrt}).

The T_{mrt} is defined as the temperature of a uniform enclosure in which the radiant transfer from the human body equals the radiant heat transfer in the actual non-uniform enclosure (Ashrae 2001). The urban geometry, including $\overline{H}/W$ and canyon orientation (Herrmann and Matzarakis 2012), influences the incoming SW and LW fluxes, therefore impact the T_{mrt}. In open areas, near sunlit walls, the T_{mrt} is greatest, particularly in summer, with more hours where T_{mrt} exceeds heat stress thresholds in north-south (N-S) oriented canyons (Lindberg et al. 2014; Lau et al. 2016; Lindberg et al. 2016a). Daytime T_{mrt} is lowest in denser areas due to shading from buildings and trees (Lindberg and Grimmond 2011a), which mitigates large swings in thermal comfort indices (Thorsson et al. 2011).

2.2 The urban surface energy balance

2.2.1 Surface energy balance (SEB) components

The layer of the atmosphere affected by the surface on timescales of up to an hour is the atmospheric boundary layer (ABL) (Stull 1988). The structure of the ABL is modified by urban environments, as their complex morphology changes both the surface energy balance (SEB) (Harman and Belcher 2006; Coutts et al. 2007a; Newton et al. 2007; Middel et al. 2012; Ward et al. 2016; Ward and Grimmond 2017), and the atmospheric flow (Kent et al. 2019; Hertwig et al. 2019). The urban SEB combines radiation, convection, and conduction, and assuming no net horizontal advection within a given area, e.g., NWP grid-box, is given by:

$$Q^* + Q_F = Q_H + Q_E + \Delta Q_S. \tag{2.5}$$

The primary source term is the net-all-wave radiation (Q^*), with an additional urban source of energy, the anthropogenic heat flux (Q_F) (which is absent in the rural SEB). Heat in the urban system is dissipated by the turbulent sensible heat flux (Q_H), turbulent latent heat flux (Q_E), and net heat storage change (ΔQ_S).

The net all-wave radiation, Q^*, is the sum of the SW and LW radiation budget for any surface (Section 2.1):

$$\mathrm{Q}^* = SW^* + LW^* = \mathrm{SW}_{\downarrow} - \mathrm{SW}_{\uparrow} + \mathrm{LW}_{\downarrow} - \mathrm{LW}_{\uparrow}., \tag{2.6}$$

where SW* and LW* are the net SW and LW fluxes, determined from the upwelling and downwelling fluxes (i.e., $\mathrm{LW}_{\uparrow}$ and $\mathrm{LW}_{\downarrow}$). In the daytime, Q^* generally follows the pattern of the SW radiation and is therefore positive. At night-time, as the $\mathrm{SW}_{\uparrow}$ is zero, Q^* is equal to the LW*, and is negative. Some studies suggest that Q^* changes w.r.t morphology, with the averaged Q^* decreasing as buildings become taller and more densely packed, e.g., increased $\overline{H}/W$ in central cities (Mills 1993; Harman et al. 2004), as this alters the α_{Bulk} through radiative trapping (Frey et al. 2007). However, some observational studies have also found that there is little influence of urban fraction on Q^* (Christen and Vogt 2004, Dou et al. 2018), with the decreased $\mathrm{SW}_{\uparrow}$ (increased α) offset by increased $\mathrm{LW}_{\uparrow}$.

The Q_F is predominantly driven by heat released from buildings (e.g., heating and air conditioning systems, and industry), transport and metabolism (Sailor 2011; Bergeron and Strachan 2012; Capel-Timms et al. 2020). The magnitude of Q_F varies both spatially and temporally (Lindberg et al. 2013), and is influenced by climate, land use, socio-economic (e.g., commercial activity, areas with significant use of central heating or air conditioning (Offerle et al. 2005a)), and time of day and year. In high-latitude climates and densely built urban areas, Q_F can become the main energy source (i.e., $Q_F > Q^*$). In these cases, Q_F supplies a constant turbulent heat flux to the atmosphere, and as such is important in winter or at night-time (Kimura and Takahashi 1991; Hamilton et al. 2009; Miao et al. 2012; Nie et al. 2014; Hertwig et al. 2020). This night-time heat source is exacerbated by the large available wall areas in cities, and building materials with high heat capacities, alongside the low ψ_{Sky} at ground level (Kusaka and Kimura 2004a). As such, high temperatures can be linked to absorption and retention of Q_F, as well as radiation (Resler et al. 2017).

When considering the temperature differences between urban areas and their surroundings, ΔQ_S is important (Grimmond et al. 1991; Taha 1999). The magnitude of ΔQ_S is dependent on the thermal mass (Lindberg et al. 2020), and as large building heights and high building cover increase the building volume and surface area, this leads to high ΔQ_S (Sailor and Fan 2002; Coutts et al. 2007a; Loridan and Grimmond 2012a; Loridan et al. 2013). Additionally, commonly used urban materials with low α and high heat capacities lead to an increase of ΔQ_S (Rosenfeld et al. 1995; Taha 1997), amplifying these effects of large wall areas in areas with high $\overline{H}$ (Bohnenstengel et al. 2011; Lindberg et al. 2020; Sugawara et al. 2001). Urban ΔQ_S is highest in the daytime, up to 2-6 times rural values (Chrysoulakis et al. 2018). This is balanced by ΔQ_S becoming a heat source (negative) at night when T is higher than T_{Air} (Grimmond and Oke 1999a; Christen and Vogt 2004; Offerle et al. 2005a). At night-time ΔQ_S is more negative in areas where the urban fraction is higher (Rotach et al. 2005). The spatially variable nature of the urban surface means that for ΔQ_S, it is not sufficient to just characterise the building form using building cover and $\overline{H}$. More detailed data and/or modelling approaches are needed.

The availability of water for evaporation in urban areas drives the magnitudes of the turbulent heat fluxes, Q_E and Q_H. The Bowen ratio ($\beta = Q_H / Q_E$) is often used to indicate whether water is limiting in a given environment, therefore determining whether energy is available to warm the air. The Bowen ratio varies significantly across and between cities (Grimmond and Oke 1995, 2002), with vegetation (e.g., in suburban and residential areas (Lee and Park 2008; Redon et al. 2017)), irrigation (Grimmond and Oke 1995), and maritime climates (Grimmond and Oke 2002). These factors can influence the partitioning of Q_H and Q_E, although this is not always the case in areas with sites surrounded by large water bodies, which may increase ΔQ_S (Newton et al. 2007). Generally, β tends towards higher values due to an increase in impervious surfaces in cities (cf. rural areas), and in these areas (with a lower Q_E), higher T are observed (Wang et al. 2015).

Like ΔQ_S, Q_H magnitudes are impacted by morphology (Oleson et al. 2008c), and can be up to double rural Q_H in the daytime (e.g., in European cities, Christen and Vogt (2004)). Q_H is influenced by materials with high thermal inertia, and so urban Q_H peaks later in the day than in rural areas. Additionally, the reduced urban α_{Bulk} increases Q_H (Porson et al. 2010b). As such urban, fraction is a key driver of Q_H diurnal variability (Cleugh and Oke 1986; Bohnenstengel et al. 2011; Middel et al. 2012). High ΔQ_S are released as Q_H, and so a key feature of the urban SEB are a positive Q_H after sunset, compared with negative Q_H in rural areas (Kusaka and Kimura 2004b). Some studies suggest that this feature remains into the night, particularly for denser areas (Lemonsu and Masson 2002; Grimmond et al. 2004; Hamdi and Masson 2008).

2.2.2 Surface energy balance at different scales

Although there are common features of the diurnal urban SEB, the variation in morphology, materials, and populations across a city drive changes in SEB parameters depending on the spatial scale considered (Britter and Hanna 2003).

The smallest scales examined in this thesis are building facets (Figure 1.1a). Roofs have a high ψ_{Sky}, particularly when building height variation within a given area is low. This influences the radiative balance, increasing the receipt of SW radiation, and the highest daytime facet Q^* (Harman and Belcher 2006). The increased SW absorption drives high observed roof temperatures (T_{Roof}), and large LW losses at night (Kusaka et al. 2001a; Voogt and Oke 1991). Higher daytime ΔQ_S in roof facets is then released as night-time Q_H. In open areas, ground facets behave similarly to roofs, with large LW losses at night. However when $\overline{H}/W$ increases, SW interception by the ground decreases, and there is increased SW and LW trapping (Oleson et al. 2008c). The fraction of radiation emitted by the walls that reaches the sky is reduced compared to roofs, leading to lower wall temperatures (T_{Wall}), and a lower Q^*. Further complexities in facet SEB come from smaller-scale sub-facets (including wall orientation, sloped roofs, alcoves, and balconies).

Combinations of buildings, and therefore facets, with different orientations and materials, form streets. Typical ‘canyon’ like streets, e.g., inner city housing, are commonly used to simplify the urban modelling problem. Although, studies like Hogan (2019b) have shown that this ‘urban-canyon’ is a poor characterisation of urban areas, particularly for radiation modelling at building-building distances of up to 200 m, due to the presence of urban irregularities including parks and intersections in real cities. Assumptions made within this can influence the SEB. For example, in east-west (E-W) orientated streets, the ground is the warmest facet during the daytime, as the sun moves from E-W across the sky (Sakakibara 1996), leading to ground temperatures (T_{Ground}) having the highest magnitude of the three facet temperatures. North-south (N-S) oriented canyons have two peaks in T_{Wall}, and hence two peaks in Q_H (Martilli et al. 2002). The SEB also varies across neighbourhoods (Figure 1.1e) due to variations in building height, vegetation, or land-use.

The complex SEB of urban areas depending on the morphology, materials, and location support the need for improved urban representation in models, and the separate treatment of building facets, in preparation for NWP application. This is important as within-canyon fluxes impact pedestrians (at street-level) (Steeneveld et al. 2011), whereas top-of-canyon fluxes (i.e., from roofs and tall buildings) have a large impact on the interactions between the UCL and the rest of the ABL.

2.2.3 Modifying the surface energy balance by altering urban characteristics

Knowing how certain changes will modify the surface energy balance is key for urban planners, as this can allow them to avoid poor design choices, or to manipulate built characteristics and improve the urban climate. Suggested methods to reduce high urban temperatures, and mitigate the CL-UHI include modifying surface material properties (i.e., reflectivity), and increasing water and vegetation within urban spaces to modify the partitioning between Q_E and Q_H (Ward and Grimmond 2017). Employing these solutions will increase the thermal comfort of the public, and can also increase resilience against other hazards, e.g., natural drainage from vegetated areas improving against urban flooding.

One solution to improve both indoor and outdoor urban temperatures, is to apply high reflectivity materials to urban surfaces. This decreases their SW absorption, reducing surface temperatures and Q_H (Santamouris 2013; Costanzo et al. 2016; Broadbent et al. 2020). This would influence indoor temperatures by reducing heat flow into buildings (Pomerantz et al. 1999). The benefits of this method can be limited depending on the urban geometry (Salvati et al. 2022), so tools should be made accessible to building developers to test how this would be applicable to specific projects.

Urban planners and building developers can make additional modifications to the building and street design to influence urban temperatures and fluxes. One approach could be to add canopies across wide streets, which would decrease SW$\downarrow$ at street-level (Emmanuel and Johansson 2006). This would then reduce ground temperatures, improving thermal comfort experienced by pedestrians.

Popular urban planning strategies to mitigate urban climate effects include implementing increased green urban infrastructure, e.g., street-trees and vegetation cover (Coutts et al. 2016a; Lindberg et al. 2016b; Aminipouri et al. 2019). Areas of large vegetation e.g., parks, are shown to modify the SEB through evapotranspiration and cool surrounding areas (Grimmond et al. 1996). Increasing tree cover can increase shadowing of roofs and walls, decreasing SW$\downarrow$ and T_{Ground} and T_{Wall} (Tan et al. 2013; Krayenhoff et al. 2014; Thorsson et al. 2017), but also impact wind flow and pollutants (Lindberg and Grimmond 2011a). However, the impact of street trees can depend on canyon geometry, the fraction of tree cover, tree species, and water availability (Coutts et al. 2016b; Krayenhoff et al. 2020).

These vegetation effects are seen in a variety of climates, including arid (Shashua-Bar et al. 2011), subtropical (Lin and Lin 2010), and high-latitude (Konarska et al. 2014) cities. Increasing green spaces assist in mitigating heatwaves through the role they plays in reduction of air temperatures and turbulent flux partitioning (Lindberg and Grimmond 2011a,b), whilst also whilst also improving public health, and building local communities (Demuzere et al. 2014).

Including thermal comfort indices (e.g., T_{mrt}) within climate scenarios, and within urban modelling tools (for research and decision makers) would enable users to test the impact of multiple climate variables on human health (Thorsson et al. 2011). Additionally, it would allow users to determine the suitability of climate mitigation measures, such as those above, on individual risks and cities using relevant building and material data and local vulnerability maps.

2.3 Modelling urban areas

With realistic representation of surface characteristics between model-grid cells, comes better predictions of the top-of-canopy fluxes that drive the large-scale atmosphere. Therefore, it is increasingly essential to develop sub-grid-scale (SGS) parameterisations that incorporate this heterogeneity. To aid with this, observations (including in hardware models), and numerical studies for both radiation and airflow are being investigated and developed.

Hardware models are reduced scale city-like structures, often arrays of aligned cubes e.g., the 1/5th COSMO project scale model (Kawai and Kanda 2010), used for surface temperature or airflow studies (Pearlmutter et al. 2005; Yang and Li 2015; Gough et al. 2018, 2019; Guo et al. 2020), and validation of neighbourhood-scale radiation models (Aida and Gotoh 1982; Voogt and Oke 1991; Kanda et al. 2005b; Kondo et al. 2005; Morrison et al. 2018). Hardware models, including wind-tunnel models, have additionally been used in studies of canopy flow and pollutant dispersion (e.g., Davidson et al. 1996; Macdonald et al. 1998; Fuka et al. 2018). These can capture real-world building form, and have been developed for parts of Nantes (Kastner-Klein and Rotach 2004), London (Hertwig et al. 2019), and Beijing (Hertwig et al. 2021; Lim et al. 2022).

High resolution computer models that resolve interactions between individual built and vegetated elements (object resolving models, ORM's), are available to simulate both the radiative and turbulent interactions within urban canopies. They require large amounts of forcing information, both morphological and meteorological, and have high computational requirements. For modelling radiation, common approaches in ORM's are to use a ray-tracing or Monte-Carlo approach (Aida and Gotoh 1982; Kobayashi et al. 1994; Montavez et al. 2000; Kondo et al. 2001; Sailor and Fan 2002). Some ORM's consider interactions between both buildings and vegetation, e.g., DART (Discrete Anisotropic Radiative Transfer, Gastellu-Etchegorry (2008); Gastellu-Etchegorry et al. (2015)) or TUF-3D (Temperatures of Urban Facets 3D, Krayenhoff and Voogt (2007)). These models have applications for thermal comfort and shadowing studies, e.g., SOLWEIG (Solar Longwave Irradsiance Geometry model, Lindberg et al. (2008); Lindberg and Grimmond (2011a)), and RayMan (Thorsson et al. 2007; Matzarakis et al. 2010), and for studies of energy consumption or anthropogenic heat fluxes, commonly known as building energy simulations (e.g., Yaghoobian and Kleissl (2012); Burdet et al. (2014); Liu et al. (2022a); Xie et al. (2022)).

There are multiple approaches to ORM's for urban airflow and dispersion, described as computational fluid dynamics (CFD) models (Toparlar et al. 2017). The most computationally expensive CFD approach is DNS (direct numerical simulation), as all turbulence scales are resolved (e.g., Coceal et al. 2007; Branford et al. 2011; Castro et al. 2017), where the urban form has to be simplified due to computational cost (i.e., not real-world building descriptions). More applicable approaches include LES (large eddy simulation) – where larger scale eddies are explicitly resolved and smaller eddies are parameterised (e.g., Deardorff 1970; Nazarian et al. 2020), and less computationally demanding RANS (Reynolds Averaged Navier Stokes) approaches (e.g., Assimakopoulos et al. 2003; Gowardhan et al. 2011; Salim et al. 2011). These often simplify the real-world geometry as street-canyons (e.g., Cai et al. 2008), or cuboid arrays with realistic urban properties (e.g., orientation and height variation) (Sützl et al. 2020; Blunn et al. 2022). However, their low computational cost (particularly RANS) allows the real-world building information to be used to describe objects blocking the flow (Xie and Castro 2009). Further, they can be used to examine the influence of within-canopy vegetation on airflow (Krayenhoff et al. 2015).

Other standalone ORM approaches are used for modelling the SEB, thermal comfort, and local temperatures. These are particularly used for urban planning. Some combine ORM approaches resolving both airflow and radiative fluxes, e.g., TUF-3D (Krayenhoff and Voogt 2007; Resler et al. 2017), or ENVI-met (Bruse and Fleer 1998; Ali-Toudert and Mayer 2006; Jamei et al. 2017), and SOLENE-microclimat (Miguet and Groleau 2007; Morille et al. 2015).

Urban schemes for NWP must be simpler than the above models, due to their computational constraints and the need for a large, global, dataset on urban input urban parameters. Early, simple, approaches to urban parameterisations include empirical models, that simulate energy balance fluxes using statistical approaches based on observations (Grimmond et al. 1991; Offerle et al. 2003; Loridan et al. 2011). They also include adapted vegetation and soil models (or 'bulk') approaches, where to mimic urban areas, the surface roughness is increased and a low urban α_{Bulk}, prescribed. The latter also assume all urban surfaces have the same temperature. But, to increase the accuracy of forecasts in cities, a higher accuracy of representation of urban processes and heterogeneity is required.

A common method used in radiation and energy balance modelling is to simulate the built fraction independent of the vegetated area, as an urban canyon (Nunez and Oke 1977). In this approach, the canopy is described as two buildings of equal height that are assumed to be infinitely long with constant separation (canyon width, *W*), described by the *H/W*. These can determine the interaction between four facets (roof, ground, and two walls) (Harman et al. 2004), or two-facets (canyon, roof) (Porson et al. 2009), due to the differences in SEB between the roofs and canyon (Section 2.2.2). However, they often calculate the radiation or energy exchanges as an average over a given facet, and with outputs at roof-level (Verseghy and Munro 1989; Kobayashi et al. 1994; Masson 2000; Kusaka et al. 2001b). Within-canyon reflections for both SW and LW radiation area are also considered to reduce computation time e.g., for SW: none (Noilhan 1981), one (Kusaka et al. 2001b), or infinite reflections (Harman et al. 2004; Fortuniak 2008), with one reflection found to be sufficient to capture LW trapping (Harman et al. 2004).

The orientation of the canyon in this approach has implications for radiative interactions (e.g., section 2.2.2), with some models simulating prescribed canyon orientations, e.g. E-W or N-S canyon (Kusaka et al. 2001b; Oleson et al. 2008a). For NWP speed, canyons are often assumed to be randomly oriented, by averaging across all possible street angles, mimicking those seen in European cities (Porson et al. 2010a). Moreover, assumptions are made on wall shadowing. Some schemes prescribing sunlit and shaded surfaces based upon solar zenith angle and canyon orientation Oleson et al. (2008) and Ryu et al. (2011). Other schemes do not make the distinction and treat all walls the same (Masson 2000; Kusaka et al. 2001b; Lee and Park 2008). This will influence the surface temperatures, and therefore the upward fluxes from the surface.

Few single-layer schemes treat within-canyon vegetation, in the form of both surface-level and street trees e.g., Lee and Park (2008); Young et al. (2015). Most models however incorporate vegetation through a tile scheme (Grimmond et al. 2010). The latter approach can have implications for urban temperature and the SEB, as the two elements do not explicitly shade or radiatively interact with each other.

However, due to their ability to represent more realistic urban features, such as within-canyon vegetation and building height variations (Yang and Li 2015), some progress in multi-layer modelling has been made, and radiative and turbulent exchanges are being more realistically modelled. Examples of these models for both radiation only and the SEB include the Town Energy Balance model (TEB, Hamdi and Masson (2008)), TUF-2D (Krayenhoff et al. 2014), the Seoul National University Urban Canopy Model (Ryu and Baik 2012; Ryu et al. 2013), NJUC-UM-M (Kondo et al. 2005; Kanda et al. 2005a,b), and SPARTACUS-Urban (Hogan 2019a). Where most models still assume a canyon-like geometry, Hogan (2019a) takes a new approach assumes the horizontal probability distribution of wall-to-wall separation distances fit an exponential distribution (Hogan 2019b), allowing for simpler treatment of vertical radiation exchanges (as the Beer-Lambert law applies to rays penetrating the canopy). A further benefit of this approach is that more realistic horizontal (cf. infinite-street) and vertical geometry can be captured by just using profiles of building and wall area.

Iterations of multi-layer models build more realism into the simulated SEB. For example, iterations of BEP incorporate building height variations into the infinite canyon framework using two adjacent canyons, such that taller buildings can shade lower roofs (Schubert et al. 2012), improving the roof radiation balance. One focus of model development is to better represent within-canyon vegetation, to allow interactions between urban elements, e.g., shadowing, and offline investigations of influence on surface temperatures and UHI mitigation. Recent developments in TEB include ground-level vegetation (Lemonsu et al. 2012), and vegetation extending vertically (Redon et al. 2017; Krayenhoff et al. 2020).

2.4 Radiative transfer models used in this thesis

2.4.1 Object resolving model (ORM): Discrete Anisotropic Radiative Transfer (DART) model

The explicit ORM for radiative transfer, DART (Discrete Anisotropic Radiative Transfer, Gastellu-Etchegorry 2008; Gastellu-Etchegorry et al. 2017) was developed to model radiative interactions within vegetation canopies (Schneider et al. 2014; Dissegna et al. 2019). It has been evaluated against observations and other vegetation models (Widlowski et al. 2007; Sobrino et al. 2011; Widlowski et al. 2015). It now can model radiative transfer in urban areas (e.g., Chrysoulakis et al. 2018; Landier et al. 2018; Morrison et al. 2020). Although unevaluated in urban areas, it has been used for urban surface temperature studies (Zheng et al 2020, Dandan and Wang 2021), for correcting thermal camera observations (Yin et al. 2017), and for urban T_{mrt} studies (Dissegna et al. 2021).

DART scenes (i.e., combinations of geometry/obstacles, emissivity, temperature), have grid-like voxels and sub-voxels (Figure 2.2) which can contain obstacles to radiation.

Vegetation elements can be represented as either planar ‘triangles’, as individual leaves on trees, or as ‘turbid media’, which is a given volume filled with randomly distributed infinitely small facets. To represent roofs and walls, DART uses triangles of a given area, orientation and optical properties. Turbid media are simply characterised of an angular distribution and area volume density. Additionally, DART can include a within-canopy atmosphere, and variations in topography (Wang et al. 2020). Radiative fluxes in DART are calculated iteratively, with radiation tracked along discrete angles with each sub-voxel and voxel, allowing surfaces within individual voxels to interact.

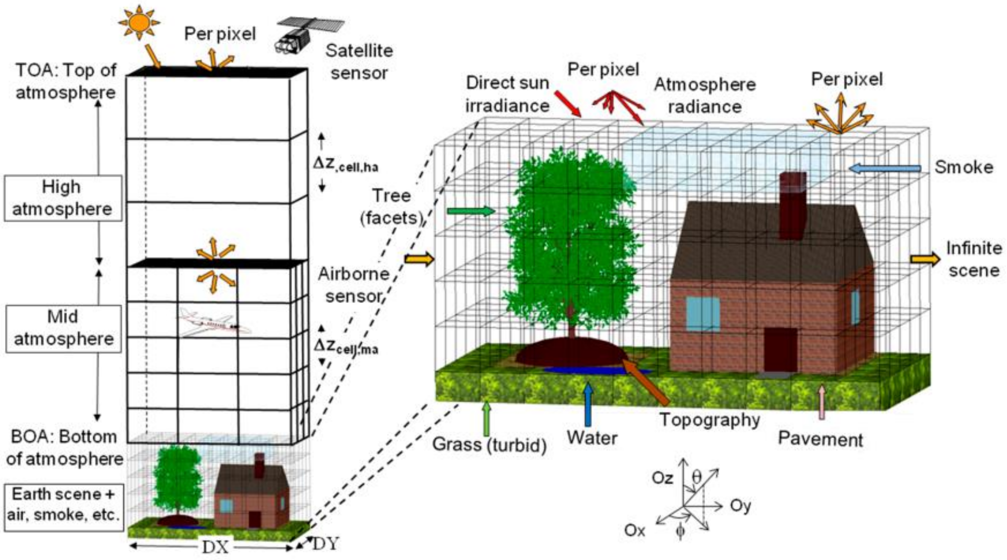

Figure 2.2: Visualisation of the structure of DART scenes, comprised of voxels that include scene elements made of planar facets and turbid mediums. DART can be used to simulate realistic buildings, vegetation, and ground surfaces. Source: Gastellu-Etchegorry et al. (2015)

2.4.2 Multi-layer radiative transfer model: SPARTACUS-Surface

The multi-layer radiation model, SPARTACUS-Surface (Hogan 2021), is evaluated in this thesis for areas with buildings. The SPARTACUS (Speedy Algorithm for Radiative Transfer through Cloud Sides) approach, initially developed for radiative interactions in cloud fields (Hogan et al. 2016), and vegetation (Hogan et al. 2018), is utilised. Within SPARTACUS-Vegetation, both within tree-crown heterogeneity crowns, and realistic tree separation (e.g., crown shyness (Van Der Zee et al. 2021)) are included. SPARTACUS-Surface incorporates the vegetation capabilities of Hogan et al. (2016), alongside the newer building areas model (Hogan 2019a). Hence, with both vegetation and building canopies can be modelled allowing urban areas with street trees to be modelled.

SPARTACUS-Surface scenes (or NWP model grid-cells) are split into horizontal 'regions' of clear-air, vegetation, and buildings (Figure 3). Both the clear-air and vegetation regions are permeable to radiation. To capture vertical variations, the scenes can also be split into vertical layers of building and vegetation cover with differing optical properties (e.g., albedo). SPARTACUS-Surface can represent atmospheric scattering and absorption and can be coupled to the free atmosphere (Hogan 2019b).

SPARTACUS is based on a 1D discrete ordinate scheme (Stamnes et al. 1988), which is commonly used for atmospheric radiative transfer in weather and climate modelling. In this approach, when implemented into an atmospheric radiative transfer scheme, coupled ordinary differential equations (ODEs) are solved for 2 streams of radiation, i.e., a single stream of diffuse radiation per hemisphere (one upwelling and one downwelling stream), plus one stream for the direct solar beam. For the radiative transfer calculations, the direct beam at any height within the canopy is split into one component per permeable region included in that layer (i.e., clear-air, vegetation). Previous SPARTACUS implementations use this 2-stream approach, but SPARTACUS-Urban (and SPARTACUS-Surface) generalise to $2N$ streams ($N = 1$ in the traditional approach), due to it leading to better representation of the net outward longwave flux in urban areas (Hogan 2019a).

The SPARTACUS approach is underpinned by the assumption that horizontal distances between obstacles in the canopy follow an exponential distribution (Hogan 2019). This assumption allows for a 1D scheme to predict a radiation stream for each prescribed solar zenith angle attenuated by buildings according to the Beer-Lambert law (as in a turbid atmosphere). This allows the model to represent realistic geometry and complex within-canyon vegetation. Assuming the obstacle separation has an exponential distribution, implies building walls face equally in all directions.

For a given scene, the SPARTACUS approach simulates vertically resolved lateral exchanges between the clear-air and obstacles to radiation (e.g., cloud sides, trees, buildings), with the lateral exchange proportional to the area of the interfaces (e.g., length of walls) between two regions. From this, the width of a shadow cast by a building in

SPARTACUS-Surface is equal to the building edge length divided by π (when averaged across all azimuthal orientation). This is true for convex shapes, e.g., cubes (any shape where corners point outwards). As building canopies are assumed randomly distributed in the SPARTACUS scheme, there are no explicit individual buildings, and shadow location is not explicitly controlled. Shadows randomly overlap with any roofs or ground that they are cast on, which means low roofs are randomly shadowed by taller buildings above, with no accounting for how close those lower buildings may be.

SPARTACUS model outputs include vertically resolved facet level absorptions (including the absorption by direct radiation only), as well as clear-air upwelling and downwelling fluxes within the canopy. Additional outputs are the sunlit fraction per layer of roofs at each layer top, walls, and the one-sided leaf area, and the sunlit area of the ground. These are calculated consistent with the assumptions above for random horizontal building placement. As this thesis uses the building modelling capabilities (but not the vegetation capabilities) of SPARTACUS-Surface, the algorithm is referred to as 'SPARTACUS-Urban'.

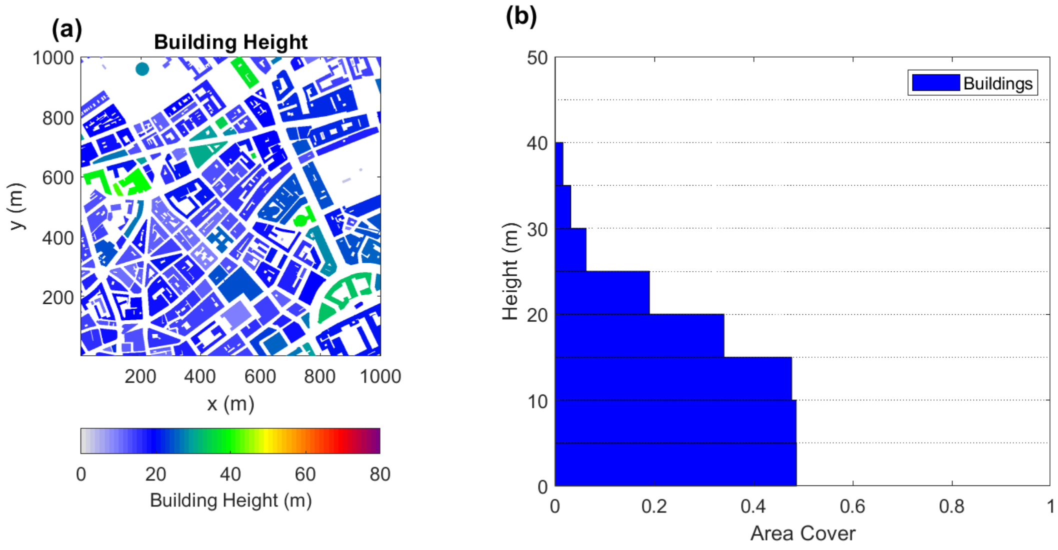

Figure 2.3: An urban 1 km x 1 km grid-box (London, UK) using EMU (2018) building footprint data, with the urban scene divided into vertical layers and horizontal 'regions'

2.4.3 Single-layer street-canyon approach: Harman et al. (2004)

The single-layer Harman et al. (2004) model uses the solution for diffuse radiative exchange in a canyon, originally developed by Sparrow and Cess (1978) and applied by Verseghy and Munro (1989). This work uses the Harman et al. (2004) implementation within the SPARTACUS-Surface software package. This method parameterises the urban form using the infinite street-canyon approach, with a fixed $\overline{H}$/W, averaging across all canyon orientations. The radiative fluxes are assumed to be uniform across each of the urban facets, by considering the interaction at the centre point of each.

This approach to radiation has been used within an NWP scheme, in Porson et al. (2010), in the MORUSES scheme. Additionally, it has been used in comparison to Hogan's (2019a) SPARTACUS-Urban, with a modified configuration so that both models assume buildings of equal height, but with exponential urban geometry (Hogan 2019b). This work showed agreement between SPARTACUS-Urban (N = 4) against the matrix-inversion Harman et al. (2004) method, supporting the use of the SPARTACUS approach for urban canopies.

2.5 Describing the variability of urban morphology

As NWP computational and data constraints require SGS processes to be parameterised, only a few morphology and material parameters are used to characterise area for simulating the surface fluxes in each grid-box (Masson 2006; Jackson et al. 2010). Such parameters are required at the scale of the model grid-box.

Key morphological parameters required for urban modelling include the plan areal rations of cover-types (e.g., λ_p, λ_i, λ_v), used by standalone SEB models or urban schemes for NWP. The vertical area of walls is expressed as a ratio of the grid-box area (λ_w), and as the frontal area index (λ_f). The latter only accounts for the area encountered in a given wind direction (Sützl et al. 2020). If buildings are assumed to be randomly distributed, λ_w and λ_f are related by π (Hogan and Shonk 2013). The λ_f and λ_p are related using the $\overline{H}$ (e.g., by Zhu et al. 2019; Masson et al. 2020) and W (Porson et al. 2010b):

$$\frac{W}{R} = \left(1 - \lambda_p\right), \tag{2.7}$$

$$\frac{\overline{H}}{W} = \frac{\pi}{2}\frac{\lambda_f}{\left(1 - \lambda_p\right)}, \tag{2.8}$$

where R is the width of the combined roof and floor (i.e., canopy) in an urban canyon, and the $\overline{H}$ /W represents the verticality of the grid-box. Some multi-layer models utilise the building probability distributions, which can be given as a vertical profile of building fraction, $\lambda_p(z)$, with height, z (Martilli et al. 2002; Schubert et al. 2012; Krayenhoff et al.

2020). For example, this is required by SPARTACUS-Urban (Hogan 2019), alongside the vertically distributed normalised building edge length, L (m^{-1}) (i.e., $L(z)$).

A range of data is available that can provide such parameters, although not globally, and methodologies are often inconsistent between datasets (Frantz et al. 2021). Building footprints with attached height information can be obtained from local authorities, in the form of digital elevation and surface models (DEM, DSM). These are developed from stereography or LiDAR (Gamba and Houshmand 2002; Xu et al. 2017), for the individual city, or part of a city, at high resolution (< 1 m) (Holland et al. 2008; Lindberg et al. 2011; Lindberg and Grimmond 2011a; Goodwin et al. 2009; Gage and Cooper 2017), but rarely include data on the verticality of cities. Citizen science projects, including Open Street Maps, aided by larger organisations, e.g., Microsoft (Heris et al. 2020), can benefit the collection of data across wider areas. Satellite products can also be used to determine building heights (Rao 1972; Champeaux et al. 2005), but few satellite missions have coverage and resolution to provide building information for large areas (Frantz et al. 2021).

To overcome the urban heterogeneity and data requirement problems, approaches have been developed to categorise and characterise the urban form. One approach is land-use and land-cover (LULC) maps, which use hierarchical classes of common land-cover/use properties, often derived from satellite data. Some datasets are available globally, with limited (or singular) urban classifications e.g., MODIS land cover (500 m resolution, Friedl et al. (2010)), or the Global Urban Footprint dataset (12 m resolution, Esch et al. (2017)). A further example of a global dataset is the Global Human Settlement Layer (GHSL, Pesaresi et al. (2016)) which combines satellite data and DSMs. Other datasets are available for smaller regions, including the CORINE land cover for Europe (EEA 2021), or the Urban Atlas dataset providing 17 urban classes for 700 urban areas worldwide (Prastacos et al. 2017; Masson et al. 2020a).

Other classifications of urban areas include the development of form classifications, including UZE's (Urban Zones for Energy partitioning, Loridan and Grimmond (2012); Loridan et al. (2013) and LCZ's (Local Climate Zones, Stewart and Oke (2012)). The LCZ framework considers seven rural (A-G) and ten urban (1-10) categories (

Table 2.2), based on surface cover fractions, and the height and spacing of roughness elements, and is widely used within urban climate studies (e.g., Brousse et al. 2016; Kotharkar and Bagade 2018). Attempts to incorporate LCZs into LULC mapping techniques include Ecoclimap (Masson et al. 2003), combining LCZs and CORINE to develop a global urban dataset, and WUDAPT (Ching et al. 2019), with a global LCZ map recently available (Demuzere et al. 2022a).

Some high-resolution morphology data is becoming available on the country or continent scale (e.g., Lipson et al. 2022), but whilst this level of data is unavailable globally, parameterisations of the urban form could be useful to fill the knowledge gap. One parameterisation, using the urban fraction of the grid-box, developed by Bohnenstengel et al. (2011) derives key parameters used to describe the urban canyon: λ_p, λ_f, and $\overline{H}$. This is used operationally in the UKV (Hertwig et al. 2020). Such relations may have limitations, e.g., are developed for a single city (or few), for a single resolution. This can lead to constraints, such as values cities cannot exceed, but do in reality (Figure 2.4). Further parameterisations have been derived for maximum building height using idealised cities, for airflow in urban areas (Sützl et al. 2021).

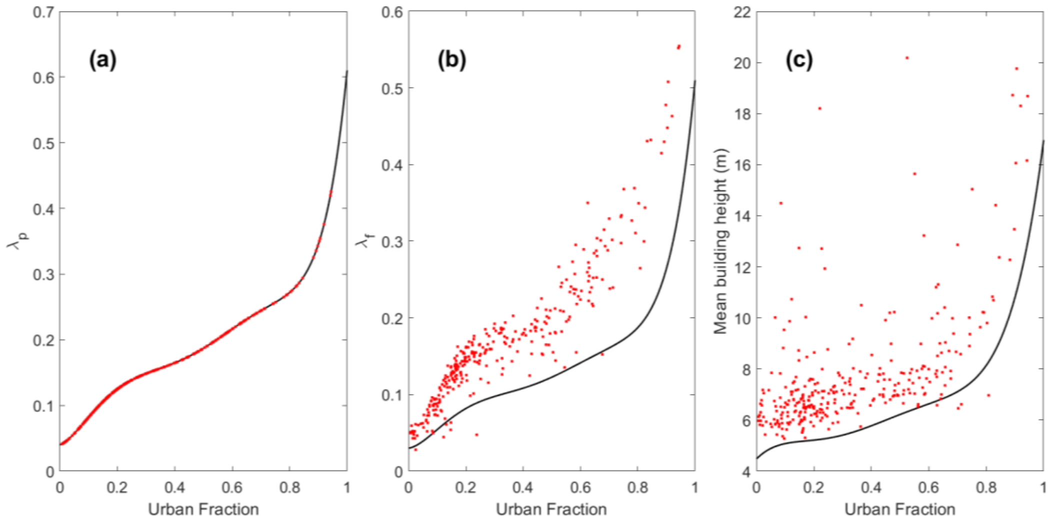

Figure 2.4: Relations between the urban fraction and common urban parameters developed by Bohnenstengel et al. (2011) used within MORUSES (black) and data from real-world 2 × 2 km grids across London (EMU Analytics 2018) for: (a) building fraction (λ_p), (b) frontal area index (λ_i), and (c) mean building height. Relations from Hertwig et al. (in prep) and differ slightly to those in Bohnenstengel et al. (2011).

Table 2.2: Local climate zone (LCZ) categories, recreated from Demuzere et al. (2020). Zone boundaries of the plan area fractions of buildings (λ_p) and impervious surfaces (λ_i), mean building height ($\overline{H}$), and sky view factor (ψ_{Sky})

LCZ	Description	λ_p	λ_i	$\overline{H}$ (m)	ψ_{Sky}
1	Compact high-rise	0.4-0.6	0.4-0.6	>25	0.2-0.4
2	Compact midrise	0.4-0.7	0.3-0.5	10-25	0.3 -0.6
3	Compact low-rise	0.4-0.7	0.2-0.5	3-10	0.2-0.6
4	Open Highrise	0.2-0.4	0.3-0.4	>25	0.5 -0.7
5	Open midrise	0.2-0.4	0.3-0.5	10-25	0.5-0.8
6	Open low-rise	0.2-0.4	0.2-0.5	3-10	0.6-0.9
7	Lightweight low-rise	0.6-0.9	<0.2	2-4	0.2-0.5
8	Large low-rise	0.3-0.5	0.4-0.5	3-10	>0.7
9	Sparsely built	0.1-0.2	<0.2	3-10	>0.8
10	Heavy industry	0.2-0.3	0.2-0.4	5-15	0.6-0.9
A	Dense trees	<0.1	<0.1	3-10	<0.4
B	Scattered trees	<0.1	<0.1	3-15	0.5-0.8
C	Bush/Scrub	<0.1	<0.1	< 2	0.7-0.9
D	Low plants	<0.1	<0.1	<1	>0.9
E	Bare rock/paved	<0.1	<0.1	< 0.25	>0.9
F	Bare soil/sand	<0.1	<0.1	< 0.25	>0.9
G	Water	<0.1	<0.1	-	>0.9

Chapter 3 Evaluation of the SPARTACUS Urban Radiation Model for Vertically Resolved Shortwave Radiation in Urban Areas[1]

Abstract

The heterogenous structure of urban environments impacts interactions with radiation, and the intensity of urban–atmosphere exchanges. Numerical weather prediction (NWP) often characterizes the urban structure with an infinite street canyon, which does not capture the three-dimensional urban morphology realistically. Here, the SPARTACUS (Speedy Algorithm for Radiative Transfer through Cloud Sides) approach to urban radiation (SPARTACUS-Urban), a multi-layer radiative transfer model designed to capture three-dimensional urban geometry for NWP, is evaluated with respect to the explicit Discrete Anisotropic Radiative Transfer (DART) model. Vertical profiles of shortwave fluxes and absorptions are evaluated across domains spanning regular arrays of cubes, to real cities (London and Indianapolis). The SPARTACUS-Urban model agrees well with the DART model (normalized bias and mean absolute errors < 5.5%) when its building distribution assumptions are fulfilled (i.e., buildings randomly distributed in the horizontal). For realistic geometry, including real-world building distributions and pitched roofs, SPARTACUS-Urban underestimates the effective albedo (< 6%) and ground absorption (< 16%), and overestimates wall-plus-roof absorption (< 15%), with errors increasing with solar zenith angle. Replacing the single-exponential fit of the distribution of building separations with a two-exponential function improves flux predictions for real-world geometry by up to half. Overall, SPARTACUS-Urban predicts shortwave fluxes accurately for a range of geometries (cf. DART). Comparison with the commonly used single-layer infinite street canyon approach finds SPARTACUS-Urban has better performance for randomly distributed and real-world geometries. This suggests using SPARTACUS-Urban would benefit weather and climate models with multi-layer urban energy balance models, as it allows more realistic urban form and vertically resolved absorption rates, without large increases in computational cost or data inputs.

---

[1] Stretton, M. A., W. Morrison, R. J. Hogan, C. S. B., Grimmond, 2022: Evaluation of the SPARTACUS-Urban Radiation Model for Vertically Resolved Shortwave Radiation in Urban Areas. *Boundary Layer Meteorology* **184**, 301–331 https://doi.org/10.1007/s10546-022-00706-9

3.1 Introduction

Given their high concentrations of both people and infrastructure, cities are places of high vulnerability to variations in weather, climate, and air quality (Baklanov et al. 2018). Currently, limited-area numerical weather prediction (NWP) models have spatial resolutions such that cities span multiple model grid boxes (e.g., Hagelin et al. (2017)). In addition, global NWP models generally have poor representation of urban structure and energy exchanges, for example the European Centre for Medium-Range Weather Forecasts IFS (Integrated Forecasting System) model with 9–18 km resolution, with no urban model (Hogan et al. 2017). As NWP spatial resolution increases, smaller-scale processes will need to be resolved. Alongside this, global population and urban land cover are expected to increase, bringing about a need for greater understanding of energy exchanges between the surface and the atmosphere (Loridan and Grimmond 2012b).

Cities have complex three-dimensional structures, with varying building heights, densities, materials, arrangements, shapes, and surroundings. This impacts the radiative exchanges and heat storage within the urban surface (Grimmond et al. 2010a; Yang and Li 2015; Ao et al. 2016), e.g., altering the effective shortwave albedo due to multiple reflections in the street canyon (Aida and Gotoh 1982). Given that shortwave radiation is the most important contribution to the surface energy balance, it is vital to understand how it is absorbed within urban areas (Fortuniak 2008).

Models have been developed to account for the three-dimensional nature of urban surfaces. A common approach is to simplify the urban form as a canyon of infinite length between buildings that are of equal height with a fixed height-to-width (*H/W*) ratio (Nunez and Oke 1977). This urban-canyon approach is fast enough for NWP, and has been applied to urban radiation specifically (e.g., Aida 1982; Arnfield 1982a, 1988; Harman et al. 2004) and other energy balance fluxes (e.g., Masson 2000; Kusaka et al. 2001a; Lee and Park 2008). This approach subdivides the canyon into three facets: walls, roof, and ground. Advancements of this approach include models subdividing facets further into sunlit and shaded, with varying canyon orientation (e.g., Oleson et al. 2008a,b), accounting for different building heights (Martilli et al. 2002), and the interactions between neighbouring canyons (Schubert et al. 2012). Some models have added vegetation, both at ground level and in the vertical plane (e.g., street trees) (Lemonsu et al. 2012; Krayenhoff et al. 2014; Redon et al. 2017).

These improvements in the vertical structure of urban form have led to improvements in the prediction of shortwave fluxes onto roofs (Schubert et al. 2012). Despite this, many models still make the unrealistic assumption of an infinitely long urban canyon. This leads to models neglecting key features of the urban form, such as intersections, building height variations, courtyards, and clusters of buildings. Ignoring these features impacts building shadowing, radiation trapping between buildings, and increased penetration of shortwave radiation to the surface in open areas such as parking areas, hence impacting the overall energy balance.

Building-resolving models, with details of each individual building and facet, are suitable for microscale research applications but not NWP, given their high data and computational demands (e.g., Krayenhoff and Voogt 2007; Krayenhoff et al. 2015; Resler et al. 2017). These models simulate radiative interactions between individual buildings, requiring detailed three-dimensional (3D) geometry and material data, which are hard to obtain for large areas (Ghandehari et al. 2018; Masson et al. 2020a). Gastellu-Etchegorry et al. (2012) suggested a key application for complex building-resolving models is both to calibrate and evaluate simpler radiative transfer models (e.g., suitable for NWP). However, very few urban radiative transfer models have been evaluated against these models. One exception is the evaluation of shortwave radiation in the Town Energy Balance (TEB) model against the SOLENE explicit radiative transfer model, considering vertical vegetation (Redon et al. 2017), although an infinite street canyon is used in both the TEB and SOLENE models. Other urban radiative transfer models suitable for NWP could (or should) be calibrated and/or evaluated using explicit 3D models.

Here, we evaluate the shortwave performance of the SPARTACUS (Speedy Algorithm for Radiative Transfer through Cloud Sides) radiative transfer model for urban areas, SPARTACUS-Urban (Hogan 2019a), with respect to the more detailed explicit 3D Discrete Anisotropic Radiative Transfer (DART) model (Gastellu-Etchegorry 2008). The SPARTACUS-Urban model resolves the vertical structure of the urban canopy and exploits the recent finding that wall-to-wall separation distances in an urban area fit an exponential distribution well (Hogan 2019b). It can account for atmospheric absorption, emission, and scattering in the urban environment, rather than assuming a vacuum, as is done by most urban radiation models (e.g., Masson 2000; Harman et al. 2004), while being fast enough for use in NWP. Although it can represent vertical profiles of vegetation, this capability is not evaluated here. We examine SPARTACUS-Urban's ability to predict the vertical profile of the clear-air downwelling and upwelling fluxes, and the absorption into walls and roofs, across a range of urban forms: from simple cuboid 'buildings' to highly realistic.

The methods include a description of the SPARTACUS-Urban (Section 3.2) and DART (Section 3.3) models, and of the evaluation techniques (Section 3.4). After an investigation of the underpinning assumptions that SPARTACUS-Urban makes about the urban form (Section 3.5), the results of the evaluation are presented (Section 3.6). Finally, a comparison of SPARTACUS-Urban with DART is made with respect to the Harman et al. (2004) method for radiation within an urban street canyon (Section 3.7).

3.2 Description of the SPARTACUS-Urban Model

The SPARTACUS-Urban model (Hogan 2019a) uses an approach that originates from the SPARTACUS model for simulating 3D radiative transfer in complex cloud fields (Hogan and Shonk 2013; Hogan et al. 2016) and SPARTACUS-Vegetation for 3D interaction of radiation in forest-type vegetation (Hogan et al. 2018). These algorithms share a common mathematical approach for treating radiative transfer in the presence of objects that are randomly distributed in the horizontal. The SPARTACUS-Surface open-source software package (Hogan 2021) combines the capabilities of SPARTACUS-Urban and SPARTACUS-Vegetation, but since vegetation is not considered here we refer to the algorithm as SPARTACUS-Urban.

The SPARTACUS-Urban model is underpinned by the one-dimensional discrete ordinate method (Stamnes et al. 1988), which assumes that diffuse radiation travels in $2N$ streams of different elevations, with N streams per hemisphere. As N increases, the radiation field is described more accurately, but with increased computational cost. Here 16 streams ($N = 8$) are used. The SPARTACUS-Urban model splits a scene (defined here as any combination of building geometry, solar zenith angle, and albedo) vertically by height, z, into n horizontal layers above an assumed flat ground level. Each layer is split horizontally into 'regions' of clear sky, vegetation, or buildings. As with other urban models, SPARTACUS-Urban computes the interaction of radiation with three urban facets (wall, roof, ground) and optionally vegetation.

Through the process of this work, we have found that two modifications to SPARTACUS-Urban are needed. Section 3.2.1 describes how to treat the more common occurrence of large open spaces such as parking areas and parks than predicted by the exponential model of urban geometry used by SPARTACUS-Urban. Section 3.2.2 describes a correction to account for fine structure in the building perimeters.

3.2.1 Modification to Treat Non-Exponential Building Separations

To characterize urban geometry, SPARTACUS-Urban takes building plan area fraction (λ_p) and the normalized building perimeter length (L) as a function of z for the city area of interest (hereafter "domain"). Thus, $L(z)$ is the total building perimeter normalized by the horizontal area of the domain (units: m^{-1}). The SPARTACUS-Urban model discretizes the vertical profile into n layers where layer i has thickness Δz_i and normalized perimeter length L_i. Following this, the normalized wall area (λ_W) is

$$\lambda_W = \sum_i^n L_i \Delta z_i \ = \ \pi \lambda_f, \tag{3.1}$$

which is proportional to the frontal area index (λ_f) or projected wall area for a particular azimuthal direction (Raupach and Shaw 1982; Grimmond and Oke 1999b; Sützl et al. 2020). The SPARTACUS-Urban model assumes that walls face in all azimuthal directions with equal probability.

Based on analysis of the geometry in real cities (Hogan 2019b), SPARTACUS-Urban assumes that the probability distribution of wall-to-wall horizontal separation distances, $p_{ww}(x)$, and the distribution of ground-to-wall separations, $p_{gw}(x)$, each follow an exponential distribution:

$$p_{ww}(x) = p_{gw}(x) = \frac{1}{X} exp\left(-\frac{x}{X}\right), \tag{3.2}$$

where x is the horizontal wall-to-wall distance in any azimuthal direction, and X is the mean wall-to-wall distance, or 'e-folding' distance (Hogan 2019). This exponential distribution allows the direct and diffuse streams of radiation to be attenuated according to the Beer–Lambert law (Hogan 2019a).

The assumption that buildings are randomly distributed horizontally has two other important consequences. First, the horizontal distribution of radiation between buildings (or vegetation, if included) need not be explicitly simulated; rather the horizontal-mean radiation field in each direction is computed as a function of height alone. Second, at a given height, the rate of interception of radiation by buildings is proportional the total building perimeter. However, in real cities Eq. 3.2 tends to underpredict the frequency of large building separations such as parks, parking-areas, and plazas (e.g., Figure 6, Hogan

(2019b)). Hence, the penetration of direct shortwave radiation to street level tends to be underpredicted when the sun is low in the sky, leading to an overprediction in absorption of shortwave radiation by walls. To address this, we replace Eq. 3.2 with the sum of two exponentials, with a weighting between them (G_{ww}):

$$p_{ww}(x) = \frac{G_{ww}}{X_1} \exp\left(-\frac{x}{X_1}\right) + \frac{1 - G_{ww}}{X_2} \exp\left(-\frac{x}{X_2}\right). \tag{3.3}$$

Where X_1 and X_2 are the e-folding distance of each exponential. The weighting function (Eq. 3.3) better predicts the frequency of large building separations by up to three times that of Eq. 3.2, in theory improving the prediction of radiative fluxes. Applying Eq. 1 of Hogan (2019b) leads to an equation for $p_{gw}(x)$ with both the same form as Eq. 3.3 and the same X_1 and X_2 values, but a different weighting coefficient G_{gw}:

$$G_{gw} = \frac{G_{ww} X_1}{G_{ww} X_1 + (1 - G_{ww}) X_2} \, . \tag{3.4}$$

To use the two-exponential model within SPARTACUS-Urban, we modify $L(z)$ so that it varies with θ_0, where θ_k is the zenith angle of a stream k, where $k = 0$ indicates the solar zenith angle, defining an effective normalized perimeter length, $\hat{L}$, given by

$$\hat{L} = \frac{\pi\left(1 - \lambda_p\right)}{\hat{X}} \, . \tag{3.5}$$

This is identical to Eq. 8 of Hogan (2019b) except for the use of an effective e-folding building separation ($\hat{X}$) in place of the e-folding building separation used to characterize the horizontal distribution of urban geometry. To derive an analytical relation between $\hat{L}$ and the two-exponential fit coefficients (G_{gw}, X_1 and X_2), we assume that if all buildings had the same height, H, the fraction of direct solar radiation penetrating to street level (F_{0g}) can be predicted exactly using Eq. 3 of Hogan (2019b):

$$F_{0g} = \int_{x_0}^{\infty} p_{gw}(x)\,dx, \tag{3.6}$$

where $x_0 = H \tan \theta_0$. As buildings are typically not all the same height, we use the mean building height ($\overline{H}$). Substituting our Eq. 3.3 (but for p_{gw}) in Eq. 3.6 gives

$$F_{0g} = G_{gw} \exp\left(-\frac{x_0}{X_1}\right) + \left(1 - G_{gw}\right) \exp\left(-\frac{x_0}{X_2}\right). \tag{3.7}$$

However, as SPARTACUS-Urban follows an exponential building distribution (Eq. 3.2) we apply Eq. 3.6, leading to

$$F_{0g} = \exp\left(-\frac{x_0}{\hat{X}}\right) \, . \tag{3.8}$$

This is equal to Eq. 20 of Hogan (2019b), but using the effective e-folding building separation, $\hat{X}$. Combining this with Eq. 3.5 gives

$$\hat{L}(z = 0) = -\frac{\pi\left(1 - \lambda_p(z = 0)\right)\ln\left(F_{0g}\right)}{x_0}, \tag{3.9}$$

where $\hat{L}(z = 0)$ is $\hat{L}$ at the surface. This can be applied to any city with building footprint data, but probability distributions can only be computed using the Hogan (2019b) method near the surface for building densities, $\lambda_p > 0.01$. Using $\hat{L}(z = 0)$ we scale $L(z)$ at each height using the building cover fraction at that height:

$$\hat{L}(z) = L(z)\left(\frac{\hat{L}(z = 0)\,\lambda_p(z)}{L(z = 0)\,\lambda_p(z = 0)} + \frac{\lambda_p(z = 0) - \lambda_p(z)}{\lambda_p(z = 0)}\right). \tag{3.10}$$

This leads to the scaling factor to $L(z)$ (Eq. 3.10) having a greater impact near the surface where λ_p is larger, and a reduced impact as buildings thin out towards the top of any urban canopy, where $\hat{L}$ tends toward L. The appropriateness of the single- and two-exponential methods in describing urban environments is discussed in Section 3.5 and their use in calculating fluxes is assessed in Section 3.6.

3.2.2 Modification to Treat Building Concavity

From SPARTACUS-Urban's use of L to describe the rate of interception of radiation by building walls, it follows that the width of the shadow cast by any building (W_S), averaged over all azimuthal illumination directions, is assumed to be equal to P/π where P is the building's perimeter length. This is true for convex shapes such as cylinders and cuboids, but not for many real-world buildings, which have fine structure in their perimeters, and so the shadows cast in SPARTACUS-Urban tend to be wider than reality. We therefore define the "concavity parameter" C as the ratio of the true perimeter length to the perimeter length of the equivalent convex hull, which for an individual building is given by

$$C = \frac{P}{\pi W_S}\,. \tag{3.11}$$

Values of C are found to be 1 or greater, and to vary with height (Figure 3.A.1, Appendix 3.AThe effective concavity parameter of all the buildings at a particular height can be calculated by replacing the numerator and denominator of Eq. 3.11 each by the average over all buildings. In this work, the median of C at all heights above $\overline{H}$ for each domain is used as a scaling factor to $L(z)$ at all heights (i.e., $L(z)/C$).

3.3 Description of the Discrete Anisotropic Radiative Transfer Model

The three-dimensional DART model (Gastellu-Etchegorry et al. 2015; Landier et al. 2018) simulates radiation propagation for heterogenous scenes that can include vegetation, buildings, a within-canopy atmosphere, and variations in ground height (i.e., topography). The latter can be imported using 3D vector models. The DART model has been evaluated using observations and other 3D radiative transfer models for vegetation (Sobrino et al. 2011; Widlowski et al. 2015), and has been applied in urban areas (e.g., Landier et al. 2018; Chrysoulakis et al. 2018; Morrison et al. 2020a).

Radiative fluxes are calculated iteratively, with radiation tracked and emitted along a number of discrete directions within angular cones (Gastellu-Etchegorry et al. 2015) using a 3D array of voxels to facilitate radiation tracking. Radiation interacts with the scene elements in each voxel. Per-voxel scattered, absorbed, emitted, upwelling and downwelling radiative fluxes are updated after each iteration, with upwelling and downwelling fluxes for each voxel stored in the top face of each voxel. Here, we use DART's ability to calculate the radiative budget to assess the SPARTACUS-Urban emission and absorption of shortwave radiation.

3.4 Evaluation Methods

3.4.1 Model domains

Four types of urban form (F) (Table 3.1) are used in the evaluation, from simplest to most complex:

1) Regular array of cubes that repeat on a regular grid (F_{REG1} and F_{REG2}, Table 3.1). Cubes are often used to approximate urban processes (e.g., Aida 1982; Kondo et al. 2005; Kanda et al. 2005; Kanda 2007; Morrison et al. 2018) as they create a regular grid street pattern that occurs in many cities in the U.S. and China (Figueiredo and Amorim 2007; Han et al. 2020).
2) Random cuboids (F_{RAND}) where building centroids are randomly located within a domain with random building heights, widths, and orientations. Twelve domains are used, but four are focussed on, with building fraction at the surface ($\lambda_p(z = 0)$) and $\overline{H}$ values spanning those found in areas of real cities (F_{RAND1}–F_{RAND4}, Table 3.1) based on prior studies (Loridan and Grimmond 2012b). This form type tests situations where the SPARTACUS-Urban building layout assumptions are met. These might be more typical of European cities, where street orientation is more random.

3) Low level-of-detail (LOD) real-world geometry using building footprint data, with one height per building creating flat roofs and walls that do not taper, and flat ground (Figure 3.1a, d). Building footprints used are for part of central London ($F_{Lon,L}$, Table 3.1).
4) High LOD real-world geometry where heights can vary across a building (Figure 3.1b, e). Parts of two cities are analyzed: a dense European megacity London ($F_{Lon,H}$) — and an open low-density U.S. grid-city — Indianapolis ($F_{Ind,H}$).

The three real-world domains (i.e., 3 and 4) are 2000 × 2000 m^2, to sample a wide range of streets with different widths, orientation, intersections, parking areas, plazas, and parks.

The DART model uses vector 3D building models to describe the urban form. For the low LOD, a raster digital surface model (DSM) and digital elevation model (DEM) are used to determine the building roof and ground level from the "Virtual London" building footprint dataset (Evans et al. 2006), using the 25th percentile of the DEM height, and the 75th percentile of the DSM height. Each building is assigned one height value from these building footprints. The 3D building models in the high LOD domains are created using the Morrison et al. (2020) method from Google Earth imagery (Google Inc. 2019) and building footprints (Evans et al. 2006; Heris et al. 2020).

For SPARTACUS-Urban, profiles of λ_p and L are calculated from rasterized (1 m resolution) building heights derived from the 3D building models. As SPARTACUS-Urban assumes no topographic variation within an individual NWP grid cell (i.e., flat), the DART 3D array of voxels is re-gridded to give heights relative to local ground level for high LOD scenes (Morrison and Benjamin 2021). To balance computational time and simulation resolution, the DART voxel resolution used is 1 m vertically and 15 m horizontally for both the real-world and F_{RAND} scenes. For F_{REG}, a vertical resolution of 0.5 m is used. In all scenes, SPARTACUS-Urban uses the same vertical resolution as DART.

As the real-world 3D building models are found to not conserve energy in DART, primarily because of periodic boundary conditions, the energy loss (always < 2%) needs to be redistributed. The rationale and method are explained in Appendix 3.B.

Fluxes from the DART model for F_{REG} (Table 3.1) scenes are offset by the voxel vertical resolution, as DART provides the fluxes at the 'top face' of each voxel and all roofs are at 5 m, so at the top of a voxel. As SPARTACUS-Urban outputs wall absorption profiles between height intervals, DART wall absorption for F_{REG} scenes is offset by 0.25 m. All data used and code are archived at https://zenodo.org/10.5281/zenodo.5145851.

Table 3.1: Different urban forms (F, code subscripts) that are simulated with different: horizontal raster resolution (Δx), vertical height intervals (Δz), domain sizes, building fraction at the ground ($\lambda_p(z = 0)$), normalized building perimeter length at the ground ($L(z = 0)$), and mean building height ($\overline{H}$)

Type	Form (F) code	Δx (m)	Δz (m)	Domain size (m^2)	$\lambda_p(z = 0)$	$L(z = 0)$ (m^{-1})	$\overline{H}$ (m)	Derived from
Regular cubes	F_{REG1}	0.5	0.5	20 × 20	0.0625	0.050	5.0	-
	F_{REG2}			10 × 10	0.250	0.20	5.0	
Random cuboids	F_{RAND1}	1	1	2000 × 2000	0.050	0.0080	7.0	Span range of urban values in Loridan and Grimmond (2012)
	F_{RAND2}				0.050	0.0081	25.0	
	F_{RAND3}				0.50	0.057	7.0	
	F_{RAND4}				0.50	0.057	25.0	
London low LOD	$F_{Lon, L}$	1	1	2000 × 2000	0.4407	0.055	25.5	Building raster and footprints Google Inc. (2019), Evans et al. (2006)
London high LOD	$F_{Lon, H}$	1	1	2000 × 2000	0.5095	0.075	19.6	As London low LOD
Indianapolis high LOD	$F_{Ind, H}$	1	1	2000 × 2000	0.3461	0.037	17.9	Building raster from Google Inc. (2019) imagery and Heris et al. (2020) building footprints

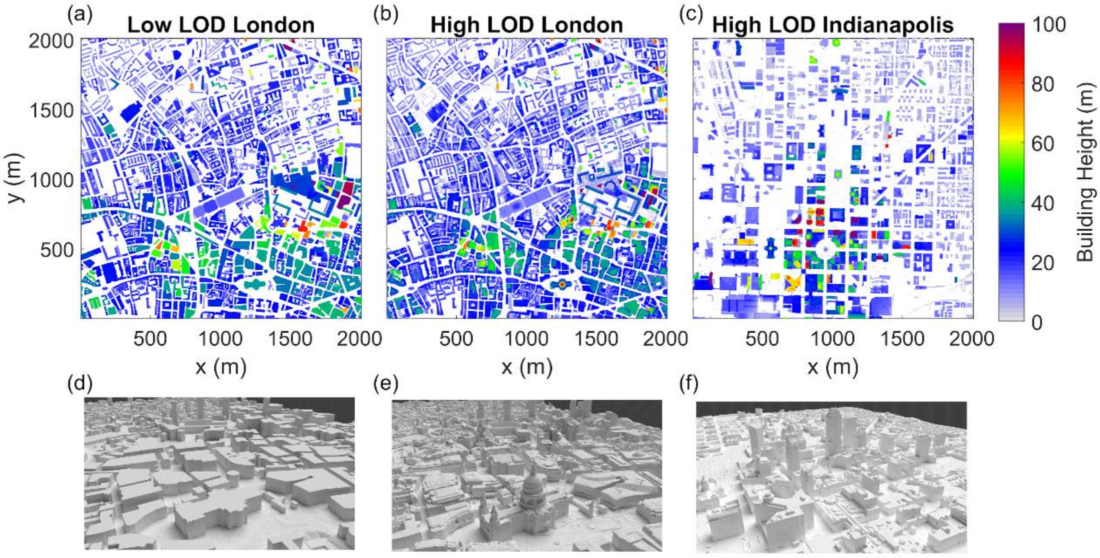

Figure 3.1: Real-world domains in parts of (a, b, d–e) London, and (c, f) Indianapolis; for the following LOD: (a, d) low, and (b, c, e, f) high; with building height for (a–c)

SPARTACUS-Urban – rasterized building footprints, (d–f) DART- 3D building model. Data sources are given in Table 3.1.

3.4.2 Sun angles and albedos

Both the DART and SPARTACUS-Urban models require solar zenith angle, θ_0, to be provided for a simulation. For computational simplicity we use three: directly overhead (0°, although unrealistic when out of the tropics), 45°, and low-sun conditions (75°). Incoming radiation at the top of the canopy is assumed to be directly from the sun; diffuse incoming radiation is set to zero. Similarly, a material albedo (α) is needed. We use two values: low (0.1) as observed in dense urban areas (e.g., 0.11, Kotthaus and Grimmond 2014) and high (0.5) as typical of 'cool' materials (e.g., Santamouris 2014; Santamouris et al. 2018; Jandaghian and Akbari 2018).

As SPARTACUS-Urban assumes that the azimuthal orientation of buildings is random, solar azimuth angle (Ω) is not specified by the model, whereas for DART the value of Ω is specified. Thus, DART has varying shadow patterns with Ω used. The DART simulations use four values for the simpler F_{RAND} and F_{REG} cases, and eight (at 45° intervals) for the real-world cases. The final DART fluxes for comparison use the mean across all Ω intervals.

3.4.3 Evaluation statistics

To quantify SPARTACUS-Urban performance, we compare SPARTACUS-Urban and DART profiles of: mean shortwave upwelling ($SW_{\uparrow}$) and downwelling clear ($SW_{\downarrow}$) air fluxes, and mean wall (a_{Wall}) and roof shortwave absorption (a_{Roof}). The fluxes have units of watts per square metre (W m^{-2}) of the entire horizontal scene (rather than per square metre of the clear-air region excluding buildings), while the absorptions have units of W m^{-3}, since we divide the absorption in a layer by the layer thickness to obtain a resolution-independent quantity. Thus, the vertical integral of a_{Wall} and a_{Roof} provide the total wall and roof absorptions (again per unit area of the entire horizontal scene). Unlike the vertical walls assumed by SPARTACUS-Urban for all domains, for the high LOD geometry in DART there is no simple way to distinguish or define roofs and walls. Hence, we combine the wall and roof absorption ($a_{Wall+Roof}$) for the evaluation of the high LOD scenes. All fluxes and absorptions are normalized by the bottom of atmosphere (BOA) shortwave flux ($SW_{\downarrow,BOA}$). This is defined as the incoming shortwave flux across a horizontal plane above the tallest roughness elements in a scene (Gastellu-Etchegorry et al. 2015; Wang et al. 2020).

Profiles of a_{Wall} and a_{Roof} are compared using the normalized mean-absolute error (*nMAE*) and normalized mean-bias error (nMBE) expressed as a percentage of the mean DART absorption:

$$nMAE = \frac{\frac{1}{n}\sum|a_{SU} - a_{\mathrm{DART}}|}{\frac{1}{n}\sum a_{\mathrm{DART}}} 100\%, \tag{3.12}$$

$$nMBE = \frac{\frac{1}{n}\sum(a_{SU} - a_{\mathrm{DART}})}{\frac{1}{n}\sum a_{\mathrm{DART}}} 100\%, \tag{3.13}$$

where a_{SU} and a_{DART} are the flux at each height from SPARTACUS-Urban or DART, respectively. The metrics nMAE and nMBE are calculated at scene resolution (e.g., 1 m) vertically from 1 m to the maximum height in DART (H_{max}). The $\mathrm{SW}_{\uparrow}$ flux profiles are evaluated using the normalized bias error at a specified height (nBE), expressed as a percentage of the DART flux:

$$nBE = \frac{SW_{SU} - SW_{\mathrm{DART}}}{SW_{\mathrm{DART}}} 100\%. \tag{14}$$

The scene albedo is evaluated using $\mathrm{SW}_{\uparrow}$ at the top of the canopy (H_{max} in DART). We also use the metric *nBE* to evaluate the total ground absorption (a_{Ground}).

3.5 Test of the SPARTACUS-Urban Geometry Assumptions

We examine the underpinning SPARTACUS-Urban assumption – that urban buildings are randomly distributed, or equivalently their horizontal separations follow an exponential distribution (Eq. 3.2) – by analyzing probability distributions from real cities and domains containing randomly placed cuboids (Table 3.1).

For the high density $\mathrm{F_{RAND3}}$ domain, the 'true' probability density of wall-to-wall (p_{ww}) and ground-to-wall (p_{gw}) separations (Figure 3.2) are calculated following Hogan (2019b) with 1 × 1 m^2 resolution building rasters, analyzed in four azimuthal directions 45° apart. Both the p_{ww} and p_{gw} distributions fit a single-exponential well (Figure 3.2b, c) for separations up to 200 m, indicating $\mathrm{F_{RAND3}}$ satisfies SPARTACUS-Urban's assumption of randomly distributed buildings. This behaviour is seen for all $\mathrm{F_{RAND}}$ domains. Here we use Eq. 3.2, where X is obtained from Eq. 3.5 with the surface value of L (denoted $L(z = 0)$).

Figure 3.3 and 3.4 present similar analyses for London and Indianapolis respectively, although here eight azimuthal directions are used to determine p_{gw} and p_{ww}, but offset by

22.5° to not align with major streets orientations (e.g., north–south or east–west in Indianapolis, Figure 3.1c). Comparison of the calculated probability distribution to both the single- and two-exponential fits for central London indicates that the latter is a better fit for $F_{Lon,L}$ (Figure 3.3) and $F_{Lon,H}$ (Figure 3.C.1). For $F_{Lon,L}$, the single-exponential fit diverges from the p_{ww} distribution at approximately 200 m and from the p_{gw} distribution at approximately 100 m (Figure 3.3b,c), whereas for $F_{Ind,H}$ (Figure 3.4) the single-exponential fits diverge at slightly greater distances (these numbers increasing to around 300 and 200 m, respectively). By contrast, the two-exponential (Eq. 3.3) predicts the larger building-separations much better than the single-exponential in both cities.

For $F_{Lon,L}$ the effective normalized building perimeter length, $\hat{L}(z = 0)$, decreases when $\theta_0 > 30°$ (black line Figure 3.3c). This is computed using Eq. 3.5 with the true ground-to-wall probability distribution (i.e., Figure 3.3b), the mean building height ($\overline{H}$ = 25.5 m), and F_{0g} (Eq. 3.6). This shows that more direct solar radiation reaches the surface when the sun is low in the sky (i.e., less chance of wall interception) compared to purely randomly distributed buildings. Using the actual normalized perimeter of 0.055 m^{-1} (blue, Figure 3.3c), equivalent to the single-exponential assumption, would be expected to lead to an overpredicted interception of direct solar radiation by walls for larger θ_0. The $\hat{L}$ obtained from Eq. 3.9 with two-exponential agrees well with $\hat{L}$ obtained using the true probability (Figure 3.3c), and the same behaviour is seen for Indianapolis (Figure 3.4c) ($\overline{H}$ = 17.9 m). Thus, we expect that the two-exponential fit should improve SPARTACUS-Urban simulations for real-world cities. This is tested in Section 3.6.3.

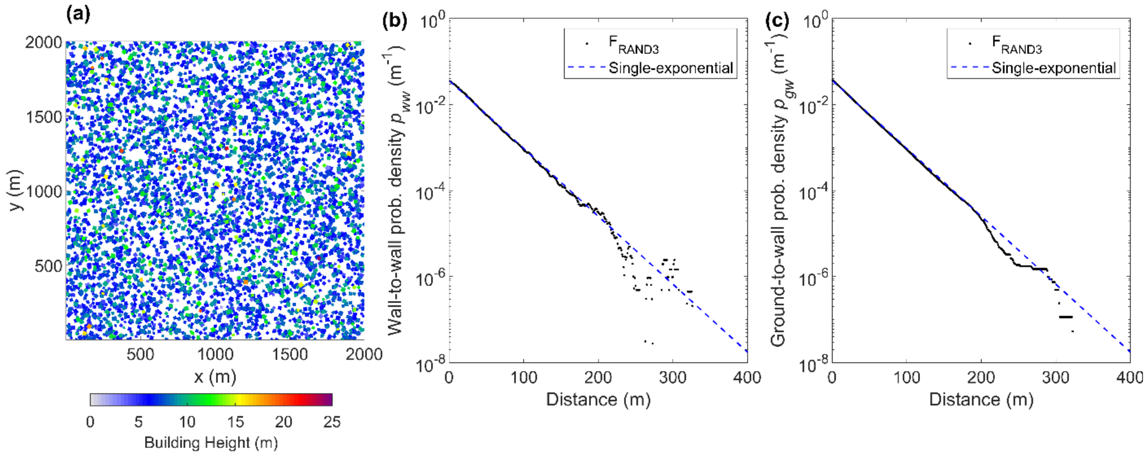

Figure 3.2: Randomly placed cuboid buildings (F_{RAND3}, Table 3.1) within a 2 × 2 km^2 domain with a plan area fraction at the surface, ($\lambda_{p,}(z = 0)$) of 0.5 and a mean height ($\overline{H}$) of 7 m: (a) Plan view, randomly placed cuboid buildings and probability density with a single-exponential (Eq. 3.2) fits to the (b) wall-to-wall and (c) ground-to-wall probability distributions

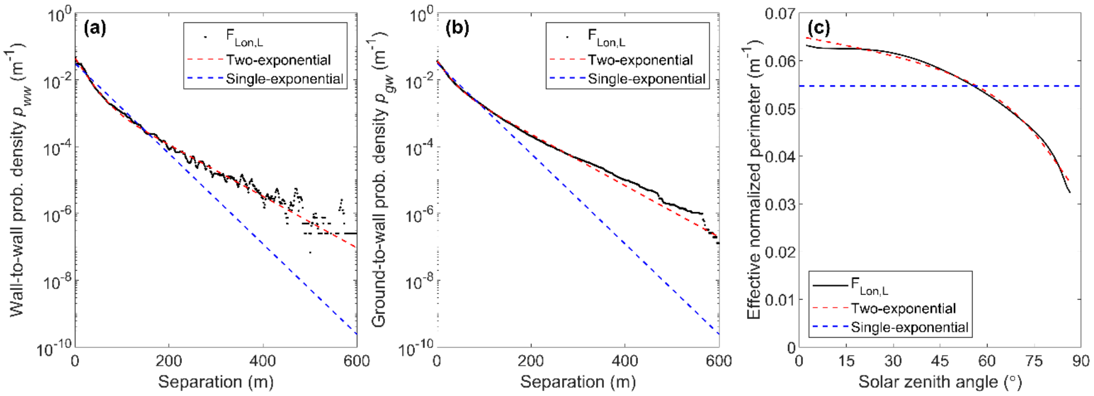

Figure 3.3: For a 2 × 2 km^2 area of central London at low LOD ($F_{Lon,L}$): (a) wall-to-wall and (b) ground-to-wall probability distribution, with single- (Eq. 3.2, blue) and two-exponential fit (Eq. 3.3 where X_1 = 21.6 m, X_2 = 57.4 m and G_{gw} = 0.534, red), and (c) corresponding effective normalized perimeter length at the surface as a function of solar zenith angle, $\hat{L}(z = 0, \theta_0)$, as predicted by Eq. 3.9 when applied to the actual data (black) and fitted (red) ground-to-wall probability distributions, and the true perimeter length at the surface (blue)

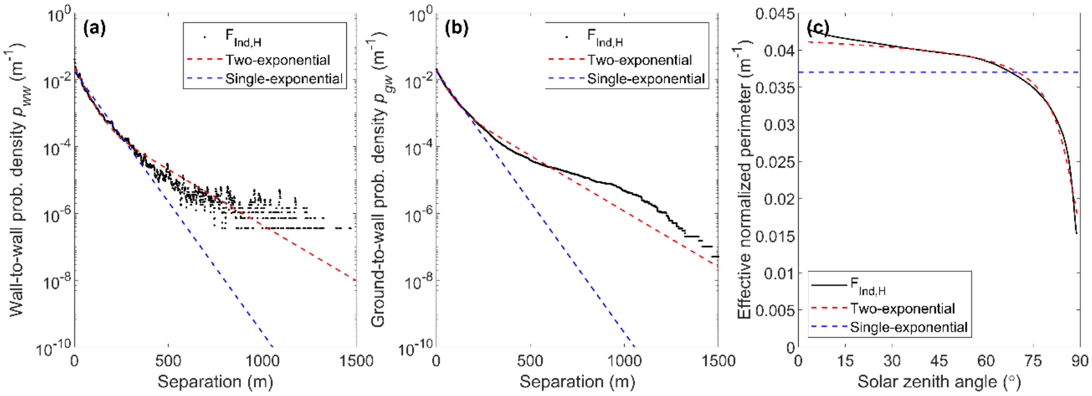

Figure 3.4: For a 2 × 2 km^2 area of Indianapolis at high LOD ($F_{Ind,H}$)): (a) wall-to-wall and (b) ground-to-wall probability distribution, with single- (Eq. 3.2, blue) and two-exponential fit (Eq. 3.3 where X_1 = 21.6 m, X_2 = 57.4 m and G_{gw} = 0.534, red), and (c) corresponding effective normalized perimeter length at the surface as a function of solar zenith angle, $\hat{L}(z = 0, \theta_0)$, as predicted by Eq. 3.9 when applied to the actual data (black) and fitted (red) ground-to-wall probability distributions, and the true perimeter length at the surface (blue)

3.6 Evaluation of SPARTACUS-Urban Shortwave Fluxes

3.6.1 Regular Cubes

Comparison of shortwave radiative flux profiles simulated with DART and SPARTACUS-Urban (single-exponential, Eq. 3.2) in a low-density regular array of cubes (F_{REG1}) shows that $SW_{\downarrow}$ decreases closer to the surface when the zenith angle θ_0 = 75° (Figure 3.5) because more radiation is intercepted by buildings. Hence, less shortwave radiation penetrates to ground level. For all θ_0 values, the roof absorption, a_{Roof}, remains constant, with nMAE = 0 (i.e., machine precision). As the buildings are all the same height, a_{Roof} can be computed exactly from the building fraction and albedo. Maximum values of a_{Wall} increase with θ_0 (Figure 3.5c, g, k), with a_{Wall} increasing with height due to building shadowing at the surface (as θ_0 increases). Azimuth angle (Ω) variations change shadow patterns and alter the wall area exposed to shortwave radiation. Hence, the a_{Wall} vertical profiles differ between DART and SPARTACUS-Urban. The DART model's fluxes are averaged across four Ω values (Section 3.4.2). The SPARTACUS-Urban model's a_{Wall} profiles are within the DART range arising from Ω (Figure 3.5c, g, k shading) when θ_0 = 0° and 45°, but not when θ_0 = 75° and α = 0.1 near the surface (approximately 1 m). Errors in a_{Wall} are lowest when θ_0 = 45° (nMAE between 9.9–17%, nMBE between -7.5 and 1.8%). For the scene albedo the nBE are < 1.2%, with values highest if the sun is overhead (θ_0 = 0°). When α = 0.1, nBE in $SW_{\uparrow}$ and $SW_{\downarrow}$ increase, but are still < 2% (Table 3.C.1). These results are better than expected, given the grid arrangement of the buildings do not have an exponential distribution of building separations (i.e., as SPARTACUS-Urban assumes, Section 3.2.1).

The larger plan area index of F_{REG2} (Table 3.1) causes $SW_{\downarrow}$ to decrease more as height decreases (for high θ_0) (Figure 3.6a, e, i). The form F_{REG2} also increases mutual building shadowing, reducing the shortwave radiation penetrating to the surface. With less shortwave radiation escaping, the scene albedo decreases with increasing θ_0. The metric nBE is larger (up to 10%, Table 3.2b) cf. F_{REG1}. Maximum values of a_{Wall} increase as θ_0 increases (Figure 3.6c, g, k). However, a_{Wall} decreases more rapidly as height decreases than in F_{REG1}, due to the increased shadowing from the buildings/cubes. nMAE is larger (cf. F_{REG1}) for a_{Wall} (up to 35%, Figure 3.5b). The peak in a_{Roof} remains at 5 m, as all buildings are of equal height. The SPARTACUS-Urban model generally overpredicts the $SW_{\uparrow}$ and $SW_{\downarrow}$ profiles, and underestimates a_{Wall} at the top of the canopy (Figure 3.6) in F_{REG2}. Similarly to F_{REG1}, when $\alpha = 0.1$ nMAE in a_{Wall} can be up to 35% when $\theta_0 > 45°$ (Table 3.C.1).

Table 3.2: Evaluation of SPARTACUS-Urban (relative to DART) for F_{REG} scenes (Table 3.1) (a) F_{REG1} and (b) F_{REG2}, for three solar zenith angles (θ_0: 0, 45, 75°) and one albedo (α: 0.5). Upwelling and downwelling clear air shortwave flux profiles ($SW_{\uparrow}$ and $SW_{\downarrow}$) assessed with the normalized bias error (nBE, Eq. 3.14) and wall and roof absorption (a_{Wall}, a_{Roof}) profiles assessed with the normalized mean absolute error (nMAE, Eq. 3.12) and the normalized mean-bias error (nMBE, Eq. 3.13)

θ_0 (°)	Scene Albedo (z = 5.5 m)		a_{Ground}		a_{Wall}	
	DART	*nBE* (%)	DART	*nBE* (%)	*nMAE* (%)	*nMBE* (%)
(a) F_{REG1}						
0	0.461	1.2	0.476	-0.25	17	-7.5
45	0.456	0.36	0.446	0.13	9.9	1.8
75	0.434	0.57	0.372	2.2	16	-3.8
(b) F_{REG2}						
0	0.373	10	0.392	-1.2	29	-22
45	0.356	9.4	0.264	14	31	-22
75	0.346	3.1	0.142	18	26	-8.3

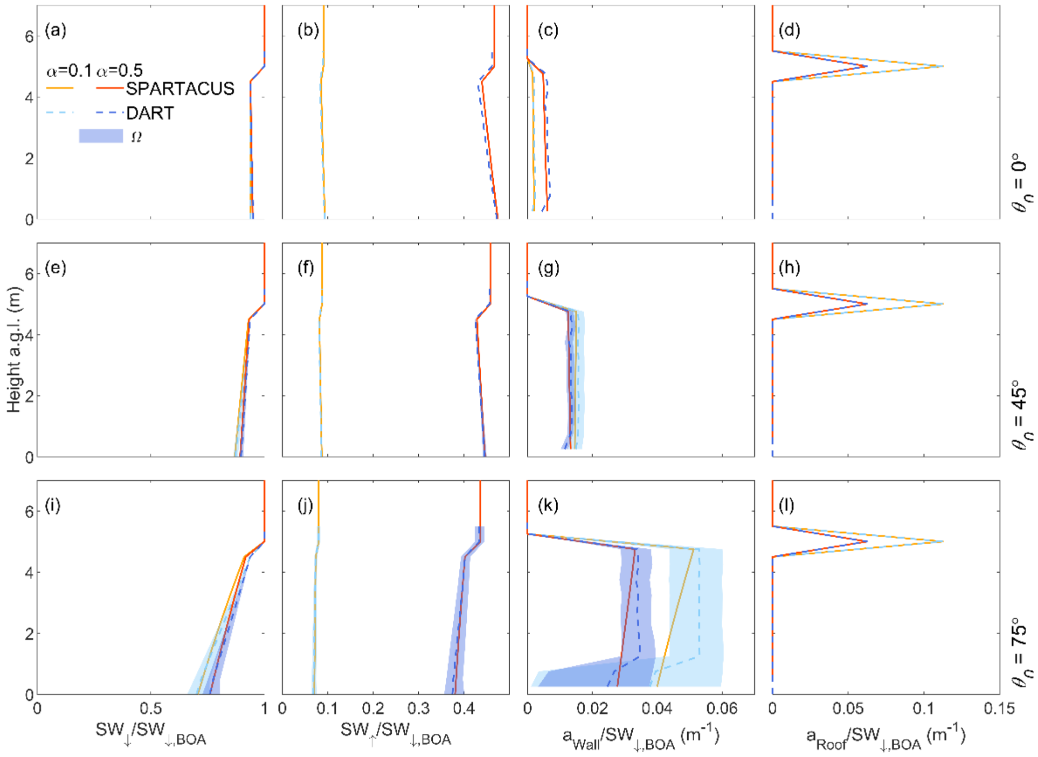

Figure 3.5: Fluxes for a regular repeated array of 5 × 5 × 5 m^3 cubes (F_{REG1}, Table 3.1) normalized by the BOA flux ($SW_{\downarrow,BOA}$) with height, simulated with SPARTACUS-Urban (orange) and DART (blue), for two albedos (α: 0.1, 0.5) and three solar zenith angles (θ_0: 0°, 45°, 75°): (a, e, i) downwelling clear air flux ($SW_{\downarrow}$), (b, f, j) upwelling clear air flux ($SW_{\uparrow}$), (c, g, k) wall absorption (a_{Wall}), (d, h, l) roof absorption (a_{Roof}) with solar azimuth angle (Ω) dependence in DART (shading)

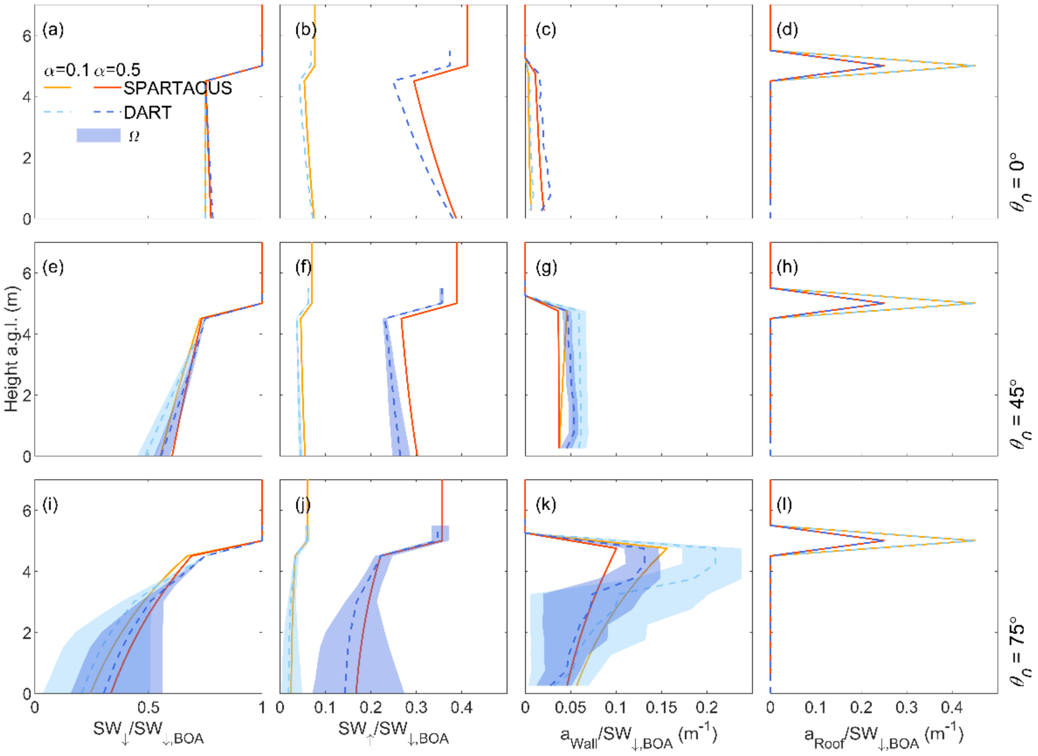

Figure 3.6: Fluxes for a regular repeated array of 5 × 5 × 5 m^3 cubes (F$_{\text{REG2}}$, Table 3.1) normalized by the BOA flux (SW$_{\downarrow,\text{BOA}}$) with height, simulated with SPARTACUS-Urban (orange) and DART (blue), for two albedos (α: 0.1, 0.5) and three solar zenith angles (θ_0: 0°, 45°, 75°): (a, e, i) downwelling clear air flux (SW$_\downarrow$), (b, f, j) upwelling clear air flux (SW$_\uparrow$), (c, g, k) wall absorption (a_{Wall}), (d, h, l) roof absorption (a_{Roof}) with solar azimuth angle (Ω) dependence in DART (shading)

3.6.2 Random Cubes

Four F$_{\text{RAND}}$ domains (F$_{\text{RAND1}}$ to F$_{\text{RAND4}}$) are intended to test SPARTACUS-Urban performance across the $\lambda_p(z = 0)$ and $\overline{H}$ extreme combinations, with more results for eight other F$_{\text{RAND}}$ domains given in Table 3.C.2. All F$_{\text{RAND}}$ simulations use the single-exponential model (Eq. 3.2), as it fits the building distribution data well (Figure 3.2). Figure 3.7 shows the agreement between DART and SPARTACUS-Urban for each θ_0 and α for profiles of a_{Wall}, a_{Roof}, and SW$_\downarrow$ for F$_{\text{RAND3}}$. Overall, for F$_{\text{RAND1}}$–F$_{\text{RAND4}}$, the nBE and nMAE are less than 6% for all quantities (Table 3.3), as SPARTACUS-Urban's urban form assumptions (Section 3.5) are fulfilled. The SPARTACUS-Urban model agrees better with DART when $\lambda_p(z = 0)$ and $\overline{H}$ are small, as buildings are further apart so there is less within-canyon scattering and building shadowing. The largest differences between DART and SPARTACUS-Urban are seen for a_{Wall} between 1 and 5 m for θ_0 = 45°, 75°. The SPARTACUS-Urban model underestimates SW$_\uparrow$ for θ_0 = 0° and 45°. In F$_{\text{RAND1-2}}$, when $\lambda_p(z = 0) = 0.05$, magnitudes of $nBE < 0.7\%$ compared to $nBE = 3.4$–5.0% when $\lambda_p(z = 0) = 0.5$ (FRAND3-4). When $\lambda_p(z = 0) = 0.05$, nMAE < 1%, except for a_{Wall} in FRAND1, where nMAE = 2.1%. Although performance becomes poorer as $\lambda_{p,0}$ increases, FRAND3-4 errors do not exceed 5.5% when $\theta_0 = 75°$ and $\alpha = 0.5$. The differences in nBE and nMAE magnitudes are larger with an increase in $\lambda_p(z = 0)$ (FRAND1–FRAND3), compared with an increase in $\overline{H}$ (FRAND1–FRAND2). This is also seen in the additional scenes in Table 3.C.2.

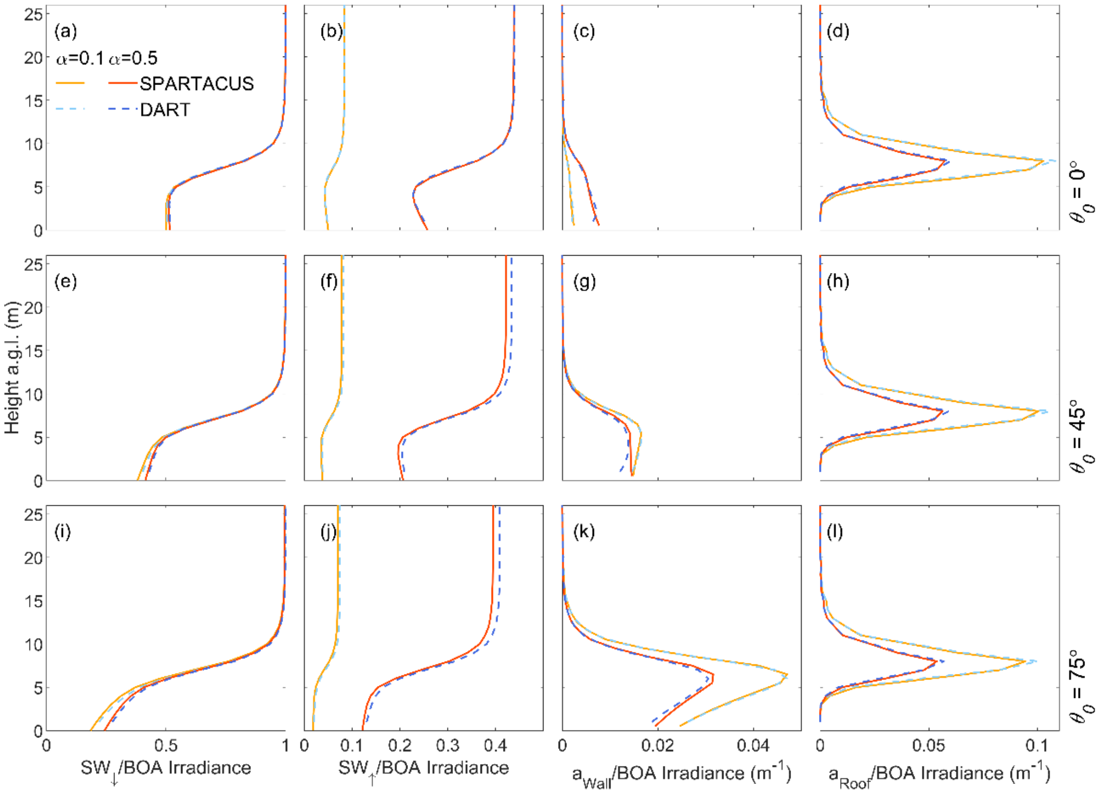

Figure 3.7: Fluxes for a 2 × 2 km^2 domain containing randomly placed cuboid buildings (FRAND3, Table 3.1), with a plan area fraction at the surface, ($\lambda_{p,}(z = 0)$) of 0.5 and a mean height ($\overline{H}$) of 7 m, normalized by the BOA flux ($SW_{\downarrow,BOA}$) with height, simulated with SPARTACUS-Urban (orange) and DART (blue), for two albedos (α: 0.1, 0.5) and three solar zenith angles (θ_0: 0°, 45°, 75°): (a, e, i) downwelling clear air flux ($SW_{\downarrow}$), (b, f, j) upwelling clear air flux ($SW_{\uparrow}$), (c, g, k) wall absorption (a_{Wall}), (d, h, l) roof absorption (a_{Roof}) with solar azimuth angle (Ω) dependence in DART (shading)

Table 3.3: Evaluation of SPARTACUS-Urban (relative to DART) for F_{RAND} scenes (Table 3.1) for $\theta_0 = 75°$ and one albedo (α: 0.5). Upwelling and downwelling clear air shortwave flux profiles ($SW_{\uparrow}$ and $SW_{\downarrow}$) assessed with the normalized bias error (nBE, Eq. 3.14) and wall and roof absorption (a_{Wall}, a_{Roof}) profiles assessed with the normalized mean absolute error (nMAE, Eq. 3.12) and the normalized mean-bias error (nMBE, Eq. 3.13) with H_{max} the maximum building height in DART

F_{RAND}	H_{max} (m)	Scene Albedo ($SW_{\uparrow}$, $z = H_{max}$)		a_{Ground}		a_{Wall}		a_{Roof}	
		DART	*nBE* (%)	DART	nBE (%)	nMAE (%)	nMBE (%)	nMAE (%)	nMBE (%)
1	17	0.483	-0.65	0.451	-0.51	2.1	1.8	1.0	0.68
2	75	0.443	-0.71	0.394	-0.55	2.5	2.3	3.5	0.59
3	26	0.409	-3.4	0.126	-3.4	4.3	4.3	5.1	-0.11
4	81	0.333	-4.7	0.0358	-5.0	5.5	4.7	5.5	-0.61

3.6.3 Real-World Geometry

For the real-world urban form in SPARTACUS-Urban, both the single- (Eq. 3.2) and two-exponential (Eq. 3.3) fits are used, allowing assessment of the impact of the building layout assumptions on shortwave radiative fluxes. Although errors are discussed here, the range of C values in real-world cities (Appendix 3.A) means that the SPARTACUS-Urban flux calculations could be adjusted based on the exact value of C used.

Building height distribution profiles have spikier patterns for $F_{Lon,L}$ than $F_{Lon,H}$ (blue and orange, Figure 3.C.2c), with the largest differences between 25 and 50 m. These spikes occur because individual buildings in the $F_{Lon,L}$ domain each have only one height, and are aggregated per 1 m interval. Despite this, the vertical profiles of a_{Roof} in SPARTACUS-Urban and DART are still close (Figure 3.8d, h, l).

The SPARTACUS-Urban model has good agreement to DART for $F_{Lon,L}$ vertical flux profiles (Figure 3.8), although the agreement is generally poorer with increasing θ_0. The SPARTACUS-Urban model always underestimates $SW_{\uparrow}$, with a nBE within 7% of DART (Table 3.4a). In the SPARTACUS-Urban model, a_{Ground} is overestimated but with nBE < 6%. The SPARTACUS-Urban model is generally in better agreement to the DART model for both $SW_{\uparrow}$ and a_{Ground} when using the two-exponential method. This is most evident as θ_0 increases. Neither nMAE nor nMBE exceed 7.3% for a_{Wall}. Generally, the SPARTACUS-Urban model underestimates a_{Roof}, with nMAE < 12 %, and nMBE up to -4.3% (increases to 13% and -6.3% for the single-exponential method). When $\alpha = 0.1$ for the two-exponential, the maximum nBE for $SW_{\uparrow}$ increases (10%, Table 3.C.3) but *nBE* for a_{Ground}, and nMAE for a_{Roof} are similar (cf. $\alpha = 0.5$).

The vertical absorption profiles (a_{Wall}, a_{Roof}, $a_{Wall+Roof}$) for the London scenes are well captured by SPARTACUS-Urban (Figure 3.8, Figure 3.9). The $a_{Wall+Roof}$ maxima between DART and SPARTACUS-Urban (Figure 3.9f, i) disagree mainly because of the need to adjust for intra-scene local topography heights in DART, in contrast to SPARTACUS-Urban where the ground is assumed to be flat. The SPARTACUS-Urban model fluxes for $F_{\mathrm{Lon,H}}$ are within 12% of DART, except for a_{Ground} when θ_0 = 45° and 75° (*nBE* = -22%, -27%, Table 3.4b). Both scene albedo and transmission to the surface (Table 3.4b) are underestimated at all θ_0. SPARTACUS-Urban overestimates the $a_{Wall+Roof}$ profiles (Figure 3.9c, f, i) leading to less shortwave radiation at ground level (with reduced $SW_{\downarrow}$ with decreasing height as θ_0 increases). This leads to less shortwave reflected to the top of the canopy, reducing the scene albedo. The largest differences between the single- and two-exponential results occurs when θ_0 = 75° (Table 3.4b). Simulations for $F_{\mathrm{Lon,H}}$ using $\alpha = 0.1$ (cf. 0.5) have higher nBE magnitudes for both $SW_{\uparrow}$ (3.0–5.7%), and a_{Ground} (7.5–36%, Table 3.C.3). Error metrics (nBE, nMAE, nMBE) are notably larger when using the single-exponential.

Both $F_{\mathrm{Ind,H}}$ $SW_{\uparrow}$ and a_{Ground} (hence $SW_{\downarrow}$) are generally underestimated, with nBE increasing with θ_0 (0.32 to -3.7%, and -4.5 to -16% respectively, Table 3.4c). The SPARTACUS-Urban model overestimates $a_{Wall+Roof}$ for all θ_0 and α (Figure 3.10c, f, i), with nMAE and nMBE between 6.3% and 15% (Table 3.4c) when using the two-exponential, with similar errors using the single-exponential. Using $\alpha = 0.1$ increases the nBE in both $SW_{\uparrow}$ and a_{Ground} to -7% and -21% respectively (Table 3.C.3).

Table 3.4: Evaluation of SPARTACUS-Urban (relative to DART) for (a) $F_{Lon,\ L}$, (b) $F_{Lon,H}$, and (c) $F_{Ind,H}$ (Table 3.1) using the single (Eq. 3.2) and two-exponential (Eq. 3.3) fit methods for urban geometry, for three solar zenith angles (θ_0: 0, 45, 75°) and one albedo (α: 0.5). Upwelling and downwelling clear air shortwave flux profiles ($SW_{\uparrow}$ and $SW_{\downarrow}$) assessed with the normalized bias error (nBE, Eq. 3.14) and wall and roof absorption (a_{Wall}, a_{Roof}) profiles assessed with the normalized mean absolute error (nMAE, Eq. 3.12) and the normalized mean-bias error (nMBE, Eq. 3.13)

θ_0 (°)	Scene Albedo ($z = H_{max}$)			a_{Ground}			a_{Wall}				a_{Roof}			
	DART	Single	Two	DART	Single	Two	Single	Two	Single	Two	Single	Two	Single	Two
		nBE (%)			nBE (%)		nMAE (%)		nMBE (%)		nMAE (%)		nMBE (%)	
(a) $F_{Lon,L}$														
0	0.378	-0.70	-3.4	0.293	0.18	0.41	10	6.7	-3.8	4.3	7.8	7.8	1.3	1.3
45	0.372	-6.3	-6.9	0.171	7.4	6.0	5.2	7.3	4.9	6.7	9.3	9.4	-3.1	-3.2
75	0.355	-8.6	-5.5	0.0796	-13	6.2	13	4.9	13	4.8	13	12	-6.3	-4.3

θ_0 (°)	Scene Albedo ($z = H_{max}$)			a_{Ground}			$a_{Wall+Roof}$			
	DART	Single	Two	DART	Single	Two	Single		Two	
		nBE (%)			nBE (%)		nMAE (%)	nMBE (%)	nMAE (%)	nMBE (%)
(b) $F_{Lon,H}$										
0	0.360	3.7	1.6	0.254	-10	-9.8	6.6	2.7	6.8	4.3
45	0.353	-1.9	-2.5	0.172	-21	-22	9.0	8.2	9.3	8.9
75	0.342	-5.9	-3.4	0.0794	-39	-27	12	8.4	12	5.3
(c) $F_{Ind,H}$										
0	0.426	1.2	0.32	0.351	-4.6	-4.5	11	4.9	11	6.3
45	0.420	-1.7	-2.4	0.310	-8.5	-9.1	13	12	14	14
75	0.394	-4.2	-3.7	0.226	-17	-16	15	14	15	13

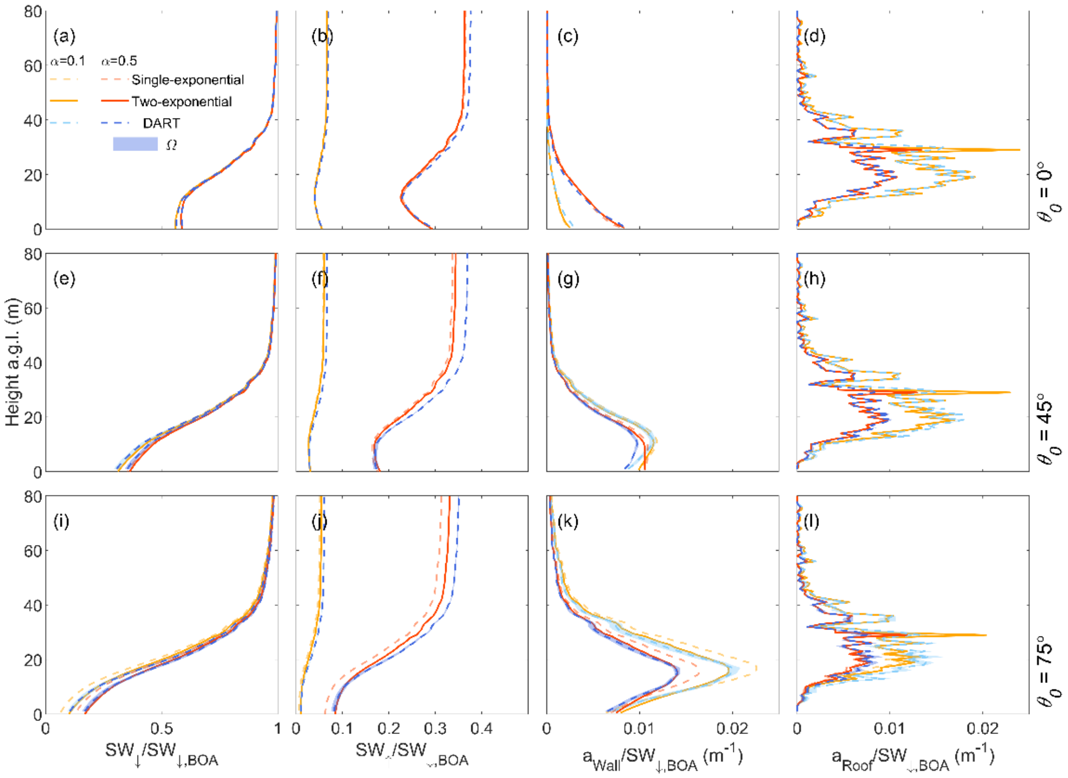

Figure 3.8: Fluxes for a 2 × 2 km^2 area of central London with a low LOD ($F_{Lon,\,L}$), using single- (dashed) and two-exponential (solid) fits, normalized by the BOA flux ($SW_{\downarrow,BOA}$) with height, simulated with SPARTACUS-Urban (orange) and DART (blue), for two albedos (α: 0.1, 0.5) and three solar zenith angles (θ_0: 0°, 45°, 75°): (a, e, i) downwelling clear air flux ($SW_{\downarrow}$), (b, f, j) upwelling clear air flux ($SW_{\uparrow}$), (c, g, k) wall absorption (a_{Wall}), (d, h, l) roof absorption (a_{Roof}) with solar azimuth angle (Ω) dependence in DART (shading)

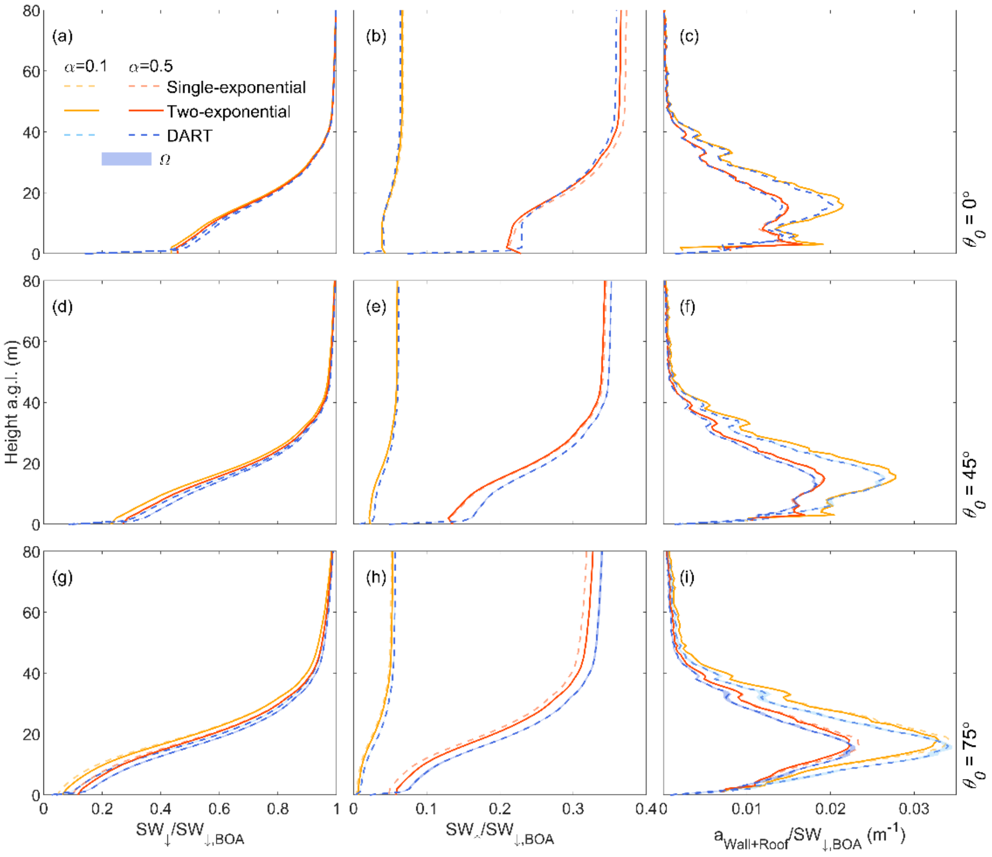

Figure 3.9: Fluxes normalized by the BOA flux ($SW_{\downarrow,BOA}$) for a high LOD 2 × 2 km^2 domain in central London ($F_{Lon,\,H}$, Table 3.1), using SPARTACUS-Urban (orange) and DART (blue) for two albedos (α: 0.1 and 0.5) and three solar zenith angles (θ_0: 0°, 45°, 75°) with solar azimuth angle (Ω) variation in DART (shading): (a, d, g) downwelling clear air flux ($SW_{\downarrow}$), (b, e, h) upwelling clear air flux ($SW_{\uparrow}$), (c, f, i) wall-plus-roof absorption ($a_{Wall+Roof}$). The SPARTACUS-Urban model's radiative fluxes are computed using both single (Eq. 3.2, orange solid) and two- (Eq. 3.3, orange dashed) exponential fits

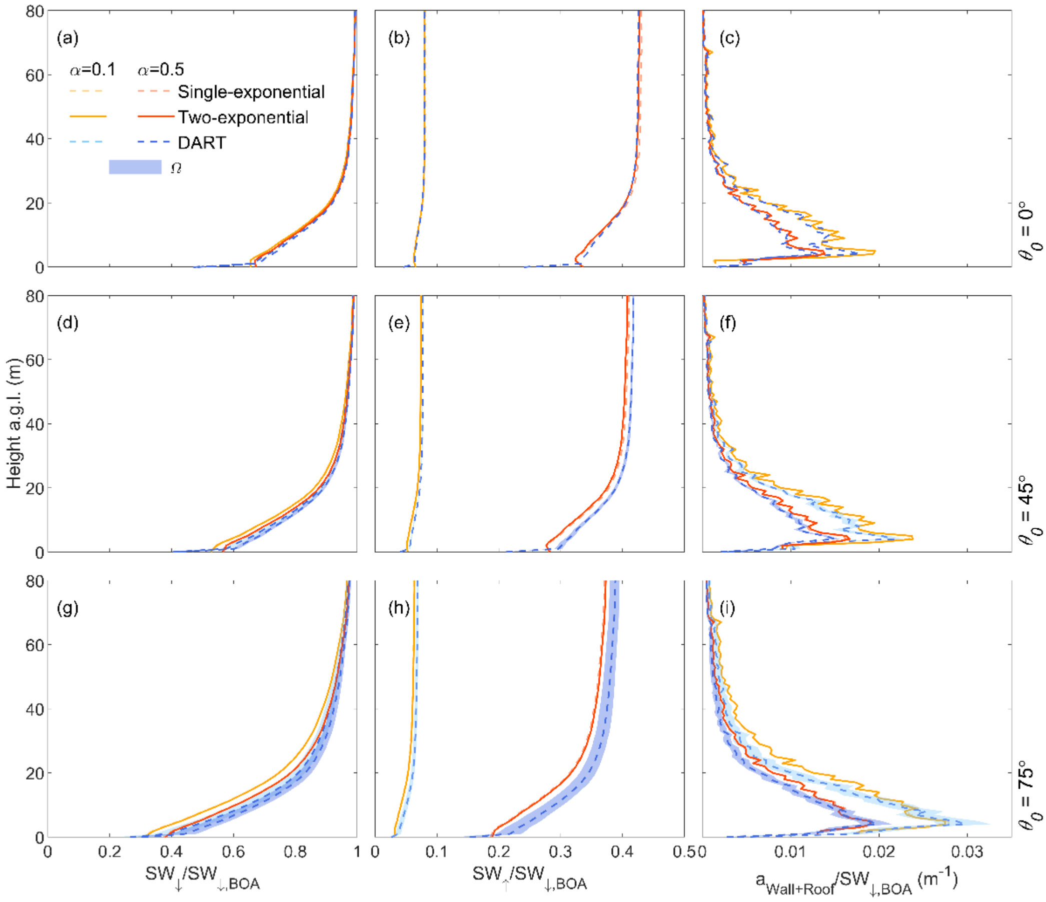

Figure 3.10: Fluxes normalized by the BOA flux ($SW_{\downarrow,BOA}$) for a high LOD 2 × 2 km^2 domain in Indianapolis ($F_{Ind,\,H}$, Table 3.1), using SPARTACUS-Urban (orange) and DART (blue) for two albedos (α: 0.1 and 0.5) and three solar zenith angles (θ_0: 0°, 45°, 75°) with solar azimuth angle (Ω) variation in DART (shading): (a, d, g) downwelling clear air flux ($SW_{\downarrow}$), (b, e, h) upwelling clear air flux ($SW_{\uparrow}$), (c, f, i) wall-plus-roof absorption ($a_{Wall+Roof}$). The SPARTACUS-Urban model's radiative fluxes are computed using both single (Eq. 3.2, orange solid) and two- (Eq. 3.3, orange dashed) exponential fits

3.7 Comparison to the Single-Layer Infinite Street-Canyon Assumption

Given the current urban models within NWP models commonly assume an urban form consisting of an infinite canyon with buildings of the same height and flat roofs, we assess SPARTACUS-Urban relative to one model of this type, Harman et al. (2004). This solves a small system of linear equations to treat any number of reflections within the canyon. Previously, Hogan (2019a) compared SPARTACUS-Urban to the Harman et al. (2004) longwave radiation by modifying the configuration, so assumptions are met for both, *viz.*: buildings all the same height, and exponential model of urban geometry (Hogan 2019b).

Hogan (2019a) found excellent agreement between SPARTACUS-Urban using eight streams, supporting the use of the discrete ordinate method for urban radiative transfer.

Here, for shortwave radiation, we compare SPARTACUS-Urban and Harman et al. (2004) against DART for cases when the assumptions of the two models are not necessarily satisfied. The Harman method is used with its usual configuration (i.e., exchange coefficients consistent in a single-layer infinite street canyon as in Sect. 3 of Hogan (2019b)), and we implement the 2 × 2 matrix inversion approach of Harman et al. (2004), as outlined in Section 4.2 and Eq. 4 of Hogan (2019a). This approach assumes two parallel infinite length buildings have constant height, H, separated by street of constant width, W, with a fixed H/W.

Care is taken to ensure that in all comparisons, the total area of ground, wall, and roof is equal between the three models. For the Harman simulations, the height H is set equal to $\overline{H}$ (Table 3.1), and the building fraction equal to $\lambda_p(z = 0)$. The value of H/W is calculated using the operational method in Eq. 3.3 of Hertwig et al. (2020),

$$\frac{H}{W} = \frac{\pi}{2}\frac{\lambda_f}{\left(1-\lambda_p\right)}, \tag{3.15}$$

where λ_f is calculated for each domain using Eq. 3.1 with the true wall area of the domain calculated from Δz and $L(z)$. From Eq. 3.15 we obtain W using $\overline{H}$. For SPARTACUS-Urban, we use the two-exponential form. Analysis is undertaken for both random cuboid and real-world scenes.

Unlike SPARTACUS-Urban, the Harman et al. method cannot predict vertical profiles, so the comparison of wall and roof absorptions is limited to vertically integrated quantities. Values of $\mathrm{SW}_{\uparrow}$ at the top of the canopy are calculated for the H_{max} in each scene for DART and SPARTACUS-Urban. These are compared using nBE (Eq. 3.14). We expand on results for an albedo of 0.5 here, with results of the comparison for an albedo of 0.1 in Figure 3.C.3. Run times for five SPARTACUS-Urban configurations are compared. These have varying numbers of diffuse streams per hemisphere (N = 1 to 8) and layers: n = 1 (i.e., as Harman et al. (2004)) to 6 (e.g., reasonable for operational NWP), to 151 (i.e., this work). The computer time of a single-threaded run for a SPARTACUS-Urban profile with the most basic configuration (N = 1, n = 1) is fast (12 µs) but six times longer than for the Harman model (Table 3.5). The $\mathrm{F}_{\mathrm{Lon,L}}$ scenes (Section 3.6.3; SPARTACUS-Urban configuration: N = 8, n = 151) have a much longer run time

(9.2 ms) but SPARTACUS-Urban is ~2.5 million times faster than DART despite DART using 14 parallel threads (Table 3.5).

Overall, Harman et al. (2004) has the best agreement with DART $SW_{\uparrow}$ (nBE < 6.3%, Figure 3.11) but generally overestimates a_{Wall}, a_{Roof}, and $a_{Wall+Roof}$. The best agreement between Harman et al. (2004) and DART is found for F_{RAND} scenes (Figure 3.11), however, SPARTACUS-Urban performs better (cf. Harman). Harman absorption errors increase with θ_0, with nBE up to 18% or 32% (a_{Wall} and a_{Roof} respectively), compared with nBE for SPARTACUS-Urban (up to 13.7% or 0.8%).

For real-world domains, SPARTACUS-Urban performs better than the Harman approach, particularly for low θ_0 (Figure 3.11). The $nBE_{SPARTACUS}$ are in the range 1.3–14.3% for a_{Roof}, a_{Wall}, and $a_{Wall+Roof}$, while nBE_{Harman} is 0.3–31% for the same quantities. a_{Roof} is overestimated by both models in all cases, except for the SPARTACUS-Urban model for $F_{Lon,L}$ at 45° and 75° (magnitudes of $nBE_{SPARTACUS}$ < 4.3%, Figure 3.11, cf. nBE_{Harman} < 21.8%), which is expected for the Harman approach as roof shadowing is neglected. Both models predict $SW_{\uparrow}$ well (nBE all < 7%), but the SPARTACUS-Urban model almost always performs better (Figure 3.11). The worst performance for both models is for a_{Ground}, with both models generally underestimating it (nBE of 0.4–26.6% for SPARTACUS-Urban and 1.2–56.4% for the Harman method). Overall, using SPARTACUS-Urban has a smaller nBE (cf. Harman) when evaluated using DART. For scenes where nBE_{Harman} (cf. DART) are lower than $nBE_{SPARTACUS}$ (i.e., better performance), the differences in nBE are < 5%.

Table 3.5: Absolute run-time of the three models (Harman, SPARTACUS-Urban, and DART) for the low LOD London domain ($F_{Lon,L}$, Table 3.1) with the indicated number of layers (*n*) and (for SPARTACUS-Urban) diffuse streams per hemisphere (*N*). The versions of SPARTACUS-Urban and Harman compared are both within the open-source SPARTACUS-Surface version 0.7.3 compiled with gfortran (O3 optimization). The runs are undertaken in a single-threaded Linux environment on a dual Xeon E5-2667 v3 processor with 256 GB of RAM. DART version 5.7.5 build number 1126 is run in the same Linux environment with 14 parallel threads using 32 CPU

Model	*n*	*N*	Time (s)
Harman	1	-	1.8×10^{-6}
SPARTACUS-Urban	1	1	1.2×10^{-5}
	6	1	5.0×10^{-5}
	151	1	1.1×10^{-3}
	151	4	3.0×10^{-3}
	151	8	9.2×10^{-3}
DART	151	-	2.5×10^{4}

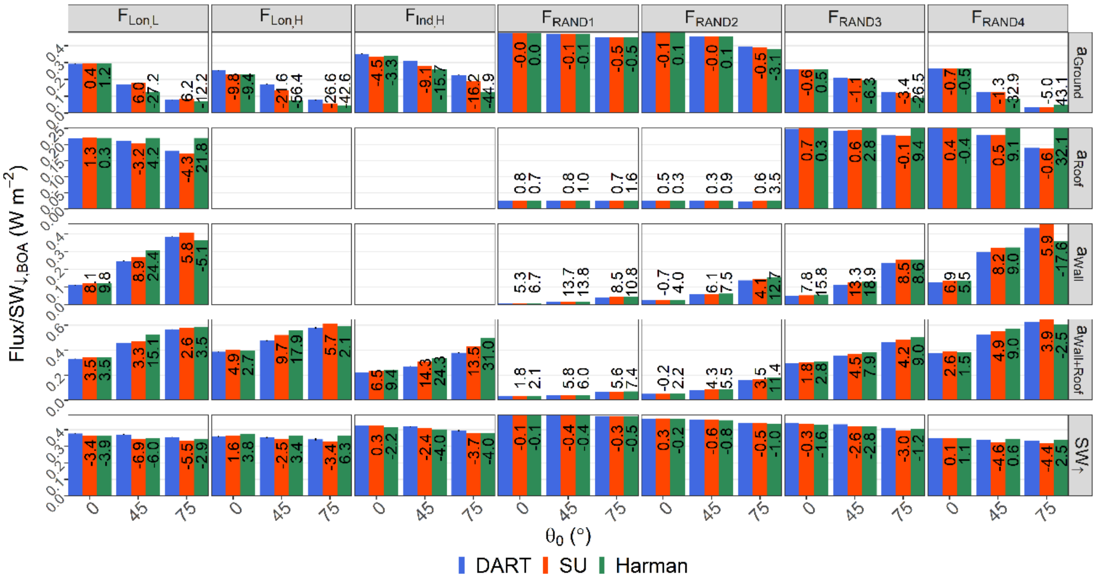

Figure 3.11: Comparison of SPARTACUS-Urban, Harman et al. (2004) and DART values for real-world scenes at low and high LOD ($F_{Lon,L}$, $F_{Lon,H}$, $F_{Ind,H}$), and random cuboid scenes (F_{RAND}) for three solar zenith angles (θ_0: 0°, 45°, 75°) and an albedo of 0.5: upwelling clear air flux at the top of the canopy ($SW_{\uparrow}$), and total wall, roof, and ground absorption (a_{Wall}, a_{Roof}, a_{Ground}). For high LOD scenes a_{Wall} and a_{Roof} are combined ($a_{Wall+Roof}$) for evaluation. Numbers on each bar are the nBE (Eq. 3.14) between the SPARTACUS-Urban model/Harman approach and the DART model. Error bars for DART span the range between if no correction for the energy imbalance is made, and if double this correction is made (Appendix 3.B)

3.8 Conclusions

Evaluation of the multi-layer SPARTACUS-Urban shortwave fluxes is undertaken using reference calculations from the explicit 3D radiative transfer model DART. The SPARTACUS-Urban model computes the vertical profiles of fluxes and absorption rates in urban scenes, which is crucial for vertically resolved urban energy balance models. A range of urban geometries were considered: regular arrays of cubes, cuboids with random placement and heights, to real city complexity (London and Indianapolis).

The SPARTACUS-Urban approach performs well when the SPARTACUS-Urban assumption of randomly distributed buildings is fulfilled. This is particularly evident for low building densities ($\lambda_p(z = 0) = 0.05$) where the normalized bias error (nBE) and normalized mean absolute error (nMAE) < 1%. The SPARTACUS-Urban model and the DART model agree less well as building fraction increases ($\lambda_p(z = 0) = 0.5$, nBE and nMAE < 5.5%). The largest nBE and nMAE occur when the solar zenith angle is highest ($\theta_0 = 75°$). For all random cuboid scenes presented, all nBE and nMAE are below 6%.

The shortwave radiative fluxes for real cities (London and Indianapolis) have nBE magnitudes of less than 7% for effective scene albedo, and nBE generally less than 15% for ground absorption. Exceptions to the latter occur for the high level of detail London domain when $\theta_0 = 45°$ and 75°. Errors (nMAE) for the wall and roof absorption (low LOD) are less than 7% and 12%, respectively. The combined wall and roof absorption (high LOD domains) is always overestimated by SPARTACUS-Urban (nMAE < 15%), which leads to underestimation in the effective albedo of the scene, and underestimation in the transmission of shortwave radiation at the surface. However, the structure of the vertical profiles of fluxes and absorptions are captured well by SPARTACUS-Urban. Overall, upwelling profiles are best predicted by SPARTACUS-Urban. For the low LOD London domain, shortwave downwelling is typically overestimated, and roof absorptions are generally underestimated, in contrast to the high LOD domains. The performance of SPARTACUS-Urban in Indianapolis is slightly worse than for London scenes, which could be related to the grid-like street layout being further from the random building distribution assumed by SPARTACUS-Urban. Nonetheless, the Indianapolis domain used here still contains parks and diagonally oriented streets, which make the domain and building separations sufficiently random enough that SPARTACUS-Urban still performs well.

Regular cube arrays tested have a similar form to earlier urban radiation studies. The roof absorptions modelled in SPARTACUS-Urban are exact (cf. DART), as all buildings have the same height. The smallest differences between SPARTACUS-Urban and DART are found in scene albedo and a_{Ground}, where nBE < 2.2%. This increases to < 18% for denser cube arrays. Across all scenes, the largest differences between DART and SPARTACUS-Urban are found in wall absorption, with nMBE between 1.8% and -22% (nMAE 9.9% and 31%) depending on cube density. These errors in wall absorption are greater than in the real scenes, which given the regular spacing does not meet the randomly distributed buildings SPARTACUS-Urban assumption, this result is not unexpected. It is plausible the low nMAE and nBE results may be associated with the open cube spacing reduces building shadowing effects.

A modification to the original SPARTACUS-Urban method is introduced here, relaxing the strict assumption that the distribution of building separations fits a single-exponential (Eq. 3.2). This is replaced with a two-exponential method, allowing for effective building edge length to vary with θ_0 (Eq. 3.3). This new method is proposed because Eq. 3.2 underpredicts the frequency of large building separations, and thus underpredicts the fraction of solar radiation reaching ground level. Using the two-exponential method both improves the predicted probability distributions (cf. 'true' distributions for London and Indianapolis) and reduces the SPARTACUS-Urban model's radiative flux errors by up to a factor of a half. A further correction is applied to both the single- and two-exponential methods to account for the concavity of real buildings, leading to better representation of the width of building shadows. The range of possible concavity values in real-world cities means that SPARTACUS-Urban simulations could be calibrated to fit DART simulations. For NWP, the concavity value uncertainty for an individual domain is smaller than the uncertainty in $L(z)$ itself.

There is scope to further refine SPARTACUS-Urban, including adjusting building shadowing. As SPARTACUS-Urban assumes the shadow cast by a building falls onto neighbouring buildings, or on gaps between buildings, is proportional to the roof area, this means shadows are randomly overlapped with roofs that they fall on. However, buildings often have roofs at low and high heights that are effectively next to each other when viewed from overhead. So, higher parts of a building can shadow lower roofs, rather than the street-level. Correcting this could improve the SPARTACUS-Urban performance further.

Comparison to the Harman et al. (2004) single-layer infinite street canyon model for randomly distributed cuboid, and real-world geometries found it performs best (c.f. DART) for random cuboid scenes. However, SPARTACUS-Urban generally performs better and notably in real-world scenes. The model results are most similar in their effective scene albedo predictions (nBE generally < 7%). The Harman approach overestimates the roof absorption, which is expected as the single-layer infinite street approach neglects roof shadowing.

Overall, our results show the SPARTACUS multi-layer approach to modelling radiative transfer in urban areas agrees well with the more complex and computationally demanding radiative transfer model DART when modelling real-world cities. The SPARTACUS-Urban model is the first multi-layer urban radiation model to achieve this, whilst being computationally cheap enough to be incorporated into weather and climate models (Hogan 2019a). This work surpasses previous evaluations that compare radiative transfer models to small scale observations or to more simplistic radiative transfer models (e.g., Harman et al. 2004; Krayenhoff and Voogt 2007; Aoyagi and Takahashi 2012; Krayenhoff et al. 2014). The single-exponential distribution that underpins SPARTACUS-Urban performs well but can be improved by using a two-exponential method. It is not yet certain if the extra complexity of implementing this two-exponential is justified, given the uncertainty in urban morphology datasets. Such datasets are required to compute required model inputs for SPARTACUS-Urban to describe the urban form (i.e., vertical descriptions of the urban canopy), which would be required if SPARTACUS-Urban is to be applied into a large-scale model.

Further investigation is needed to ascertain the amount of data required to describe building geometry worldwide, and how this impacts radiative fluxes. Further evaluation should be completed with SPARTACUS-Urban in the longwave, as this is a significant term in the urban surface energy balance (Oke 1988). As SPARTACUS-Urban can be integrated within existing urban surface energy budget models, the results of this shortwave evaluation provide a promising start to improving the treatment of the complex urban structure in NWP models.

Acknowledgements

The authors acknowledge the funding and support from the Scenario NERC Doctoral Training Partnership Grant, EPSRC 2130186, EPRSC DARE (EP/P002331/1), ERC *urbisphere (855005)*, and Newton Fund/Met Office CSSP China NGC. All data and code have been archived

at https://zenodo.org/10.5281/zenodo.5145851.

Appendix 3.A: Building concavity in real-world cities

As outlined in Section 3.2.2, a correction is made in SPARTACUS-Urban to account for the building concavity in real-world cities. Real-world buildings tend to not be convex, which means the relation between the building perimeter length given to SPARTACUS-Urban and the rate of radiation exchange is not correct. Therefore, we correct for this concavity by applying a constant scaling factor to L at each height level using a concavity parameter (C, Eq. 3.11). This allows us to approximately obtain the perimeter of the convex hull of each building. Here, three real-world domains are analyzed (in London and Indianapolis) at two levels of detail (LOD, low and high) ($F_{\mathrm{Lon,L}}$, $F_{\mathrm{Lon,H}}$, $F_{\mathrm{Ind,H}}$, Table 3.1), derived from building footprints (Table 3.1).

For the London domains, C ranges between 1.04 and 1.66 at each height interval, with smaller values for the low ($F_{\mathrm{Lon,L}}$) than high ($F_{\mathrm{Lon,H}}$) LOD domain (Figure 3.A.1). Generally, C decreases with height in real cities (Figure 3.A.1), because individual buildings in an area of the city may be short and wide, or tall and narrow, and so cast different sized shadows. Cross-sections of the high LOD London domain support this, with low height levels, where the building density is high, having a larger C (cf. higher heights where smaller, taller building occur) (Figure 3.C.4d). Given this, we calculate C at all heights, and use median C from all heights above $\overline{H}$, applying this as the scaling factor to $L(z)$ (black, Figure 3.A.1). Values below $\overline{H}$ are excluded given both the presence of courtyards, and that taller buildings will shadow shorter buildings (rather than vice versa).

We examine the impact on the shortwave fluxes, with C from 1.1 to 1.7 but constant with height. Across the three solar zenith angles (Figure 3.A.2), the C value has the greatest impact on the $SW_{\uparrow}$ profiles for the $F_{\mathrm{Lon,H}}$ domain, and less impact on the $SW_{\downarrow}$ and $a_{Wall+Roof}$ profiles.

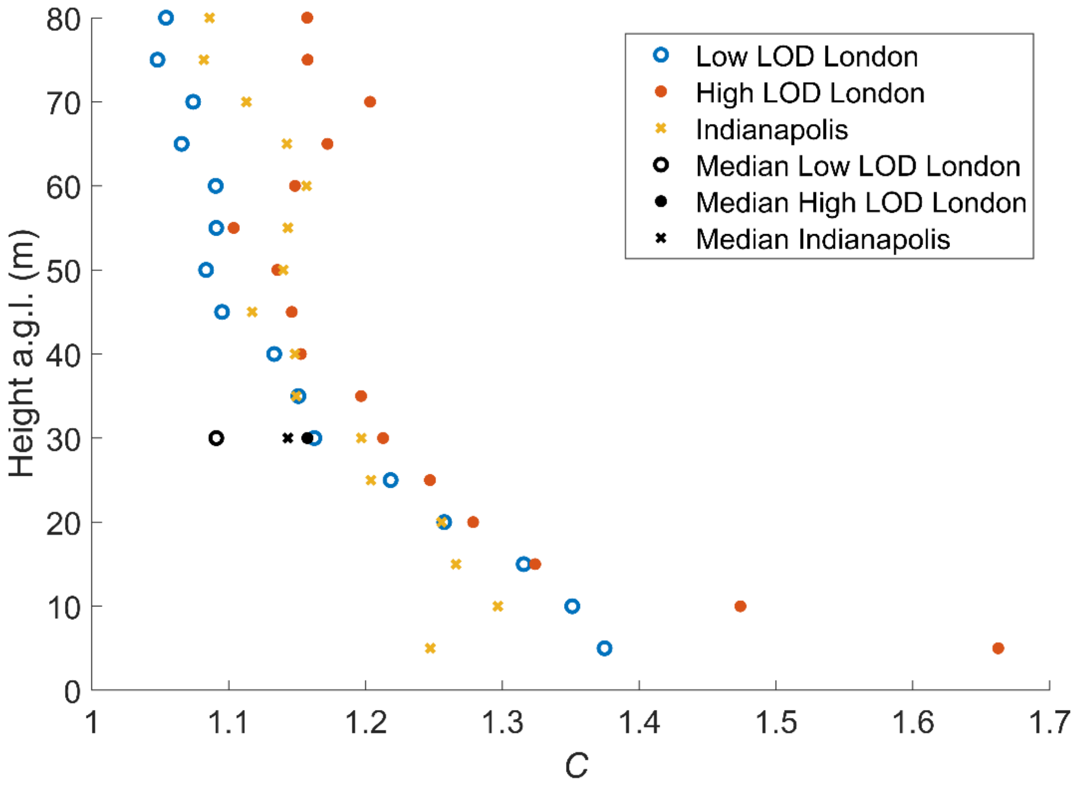

Figure 3.A.1 Variation of the concavity parameter (*C*) (Section 3.2.2). in two real cities (London and Indianapolis) for two LOD (Section 3.4.1) with height. The median values of *C* above $\overline{H}$ for each of the three domains, used as the scaling factor the building edge length (*L*) are shown in black

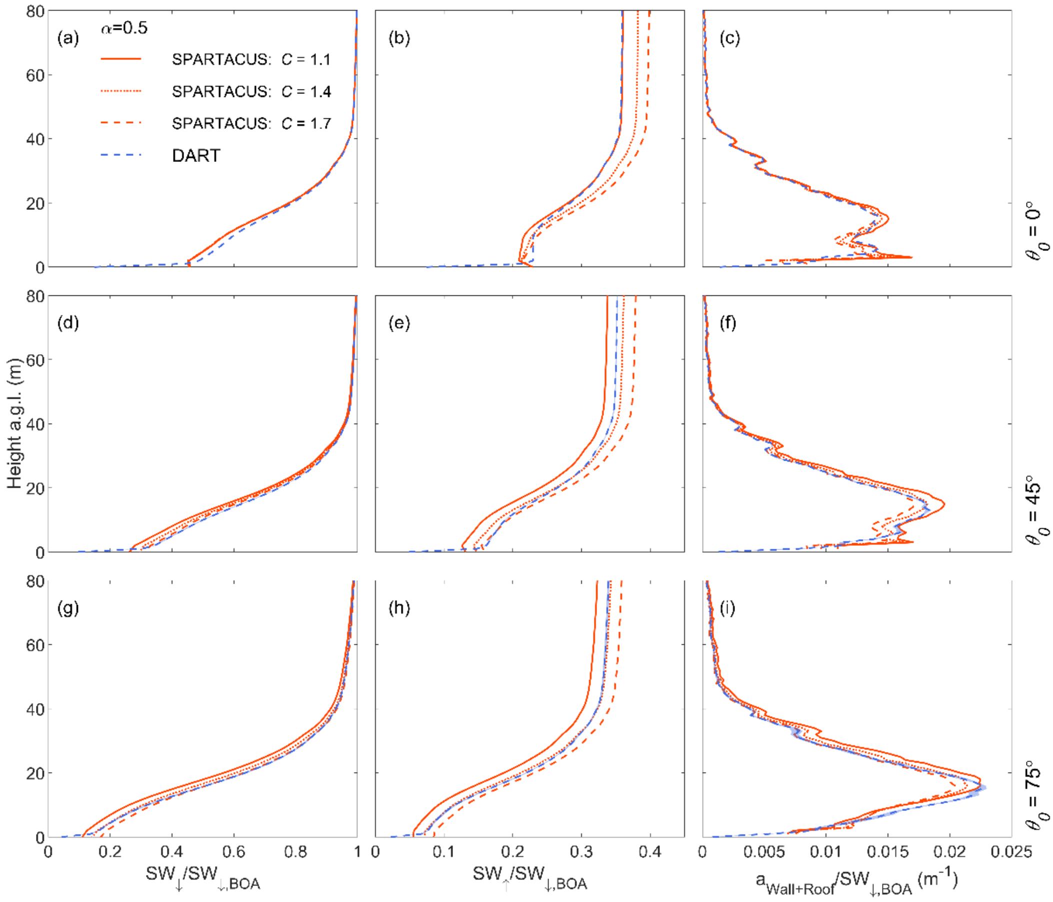

Figure 3.A.2: Fluxes normalized by the BOA flux ($SW_{\downarrow,BOA}$) for a high LOD 2 × 2 km^2 domain in central London ($F_{Lon,\ H}$, Table 3.1), using SPARTACUS-Urban (orange) and DART (blue) for two albedos (α: 0.1 and 0.5) and three solar zenith angles (θ_0: 0°, 45°, 75°) with solar azimuth angle (Ω) variation in DART (shading): (a, d, g) downwelling clear air flux ($SW_{\downarrow}$), (b, e, h) upwelling clear air flux ($SW_{\uparrow}$), (c, f, i) wall-plus-roof absorption ($a_{Wall+Roof}$). SPARTACUS-Urban profiles indicate the variation from using a concavity parameter of 1.1 (solid), 1.4 (dotted), and 1.7 (dashed). SPARTACUS-Urban uses the two-exponential (Eq. 3.3) only

Appendix 3.B: Distribution of lost energy in the DART model output

We calculate energy imbalance (E, W m^{-2}/W m^{-2}) for each DART run, using:

$$E = 1 - (a_{Wall} + a_{Roof} + a_{Ground} + SW_{\uparrow,top}) \qquad (3.16)$$

where the total wall, ground and roof absorption are given by a_{Wall}, a_{Ground} and a_{Roof}, respectively and $SW_{\uparrow,top}$ is the shortwave upwelling clear air flux at the top of the canopy. $E = 0$ for a perfectly conserving model.

The DART energy imbalance is always less than 2%, and usually less than 1% (Figure 3.B.1b). Generally, energy conservation is highest for overhead sun conditions ($\theta_0 = 0°$)

and decreases with geometry complexity to be lowest for the real-world domains (F_{Lon}, F_{Ind}). F_{REG} (Table 3.1) domains have a lower voxel resolution, so do not follow this relation, as DART energy conservation tends to improve as voxel resolution increases (e.g., 1 m → 0.5 m).

Processes identified that contribute to energy loss are (Figure 3.B.2):

(1) rays passing ‘underground’ of the domain when there are holes in the 3D building model,

(2) rays hitting internal walls of buildings

Both can occur from the domain periodic boundary conditions, if buildings and topography are cut at the domain edge (Wang et al. 2020). The F_{RAND}, $F_{Lon,H}$ and $F_{Ind,H}$ (Table 3.1) 3D building models contain some buildings that cross the domain edge. As the domain cuts though it creates ‘open’ buildings allowing rays to pass directly underneath the building footprint model or interact with the ‘internal’ walls of the buildings (Figure 3.B.2b). With non-flat topography (e.g., $F_{Lon,H}$ and $F_{Ind,H}$) the periodic boundary conditions create gaps through which rays can pass (Figure 3.B.2a). F_{REG} scenes have neither of these features, whereas F_{RAND} scenes have only building split, hence energy loss increases with increasing domain complexity. As the real-world scenes have the largest energy loss, the DART missing energy is assumed to be lost through the building walls and the ground, attributed to processes (1) and (2) above.

For high LOD scenes, we redistribute lost energy into the walls (Figure 3.B.2b, d) first as a ratio of total λ_W to total a_{Wall}. The approximated ($\lambda_{W,edges}$) wall area missing at the edge of the domain is used to calculate the average wall absorption:

$$a_{Wall,edges} = A\lambda_{W,edges}\frac{a_{Wall}}{\lambda_W}. \tag{3.17}$$

We note $\lambda_{W,edges}$ is an overestimate, as building walls in the repeated units may overlap. We assume $a_{Wall,edges}$ is the amount of energy absorbed by these extra walls. The amount of total energy available for exchange by the wall processes (E_{Wall}) in Figure 3.B.2d is equal to $a_{Wall,edges}/(1-\alpha)$. This energy is split between $SW_{\uparrow}$, a_{Wall}, and a_{Ground} (Figure 3.B.2d). The remainder of the lost energy is attributed to the ground process (E_{Ground}) (Figure 3.B.2a), and is redistributed (Figure 3.B.2c) into a_{Ground}, a_{Wall}, and $SW_{\uparrow}$, where the two-thirds of the radiation reflected from the ground is distributed into a_{Wall}. Combining these processes (Figure 3.B.2) leads to the total added energy.

This is distributed at all height levels using a scaling factor (e.g., $a_{Wall}/a_{wall,extra}$). For $F_{Lon,L}$, the buildings at the edge of the domain have complete walls with flat topography, so we distribute lost energy through both the wall and ground processes (Figure 3.B.2) equally, assuming $E_{Wall} = E_{Ground}$. Although we redistribute the energy through these processes, we note this may not match the true DART results if external walls and topography are corrected. The uncertainty in these numbers is less than the range if solar azimuth angle is varied, and so it not shown in the vertical flux profiles compared in Section 3.6. In Section 3.7, this uncertainty is shown by an error bar across: the fluxes if no correction for the energy imbalance is made, and the fluxes if double the correction is made.

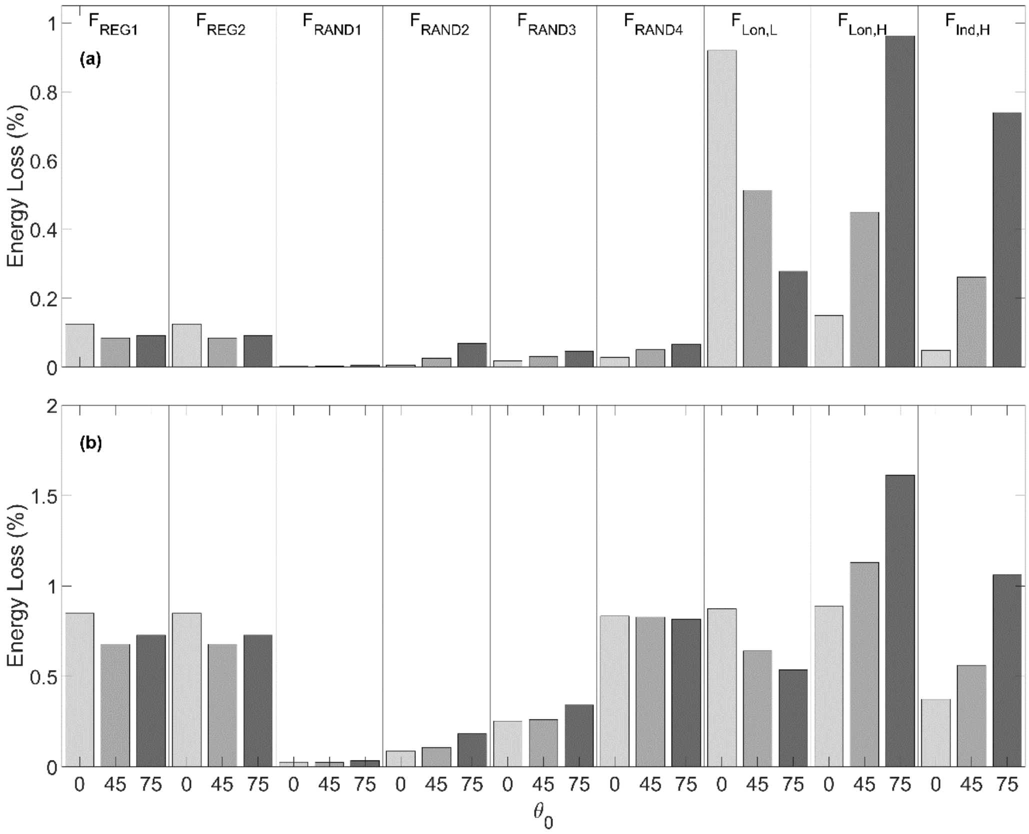

Figure 3.B.1: Energy loss (Eq. 3.16) in DART scenes (Table 3.1) for three solar zenith angles (θ_0: 0°, 45°, 75°) for albedos: (a) 0.1, and (b) 0.5, for all F_{REG}, $F_{RAND1-4}$, and real-world ($F_{Lon,L}$, $F_{Lon,H}$, $F_{Ind,H}$) scenes tested (Section 3.4.1)

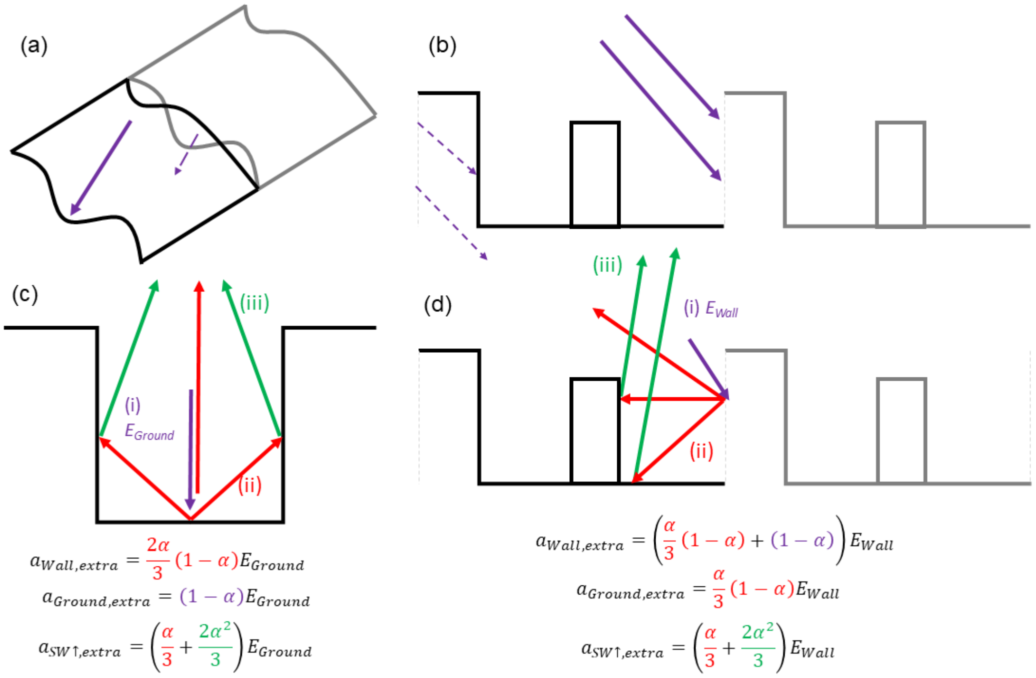

Figure 3.B.2: Energy lost in DART occurs at the edge of periodic model domains (grey) if there is (a) unmatched topography, and/or (b) buildings missing external walls. To distribute the energy through the (c) ground (E_{Ground}), and (d) walls (E_{Wall}), where the purple arrows (i) represent the extra energy into the ground and walls, and the red (ii) and green (iii) represent the first and second reflections of shortwave radiation, to determine the total extra shortwave radiation into the walls, ground, and upwelling ($a_{Wall,extra}$, $a_{Ground,extra}$, and $\mathrm{SW}_{\uparrow,\mathrm{extra}}$)

Appendix 3.C: Supplementary material for Chapter 3

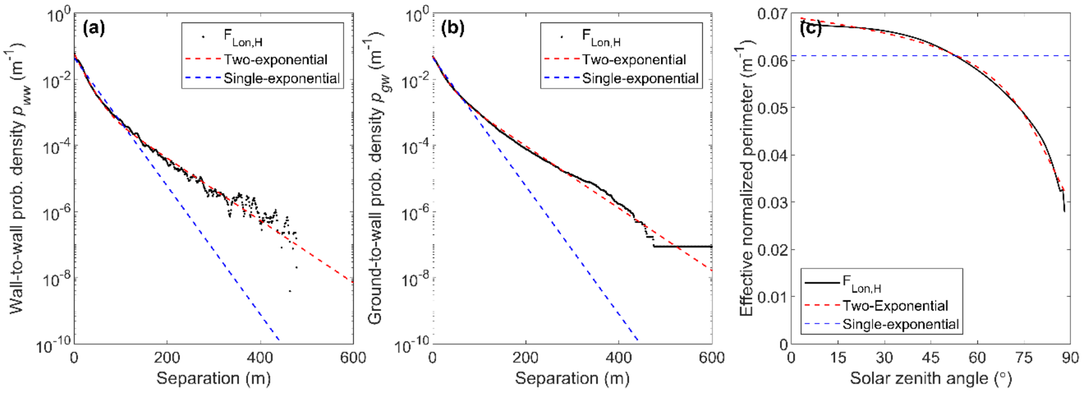

Figure 3.C.1*:* For a 2 × 2 km^2 area of central London at high LOD ($\mathrm{F}_{\mathrm{Lon,H}}$): (a) wall-to-wall and (b) ground-to-wall probability distribution, with single- (Eq. 3.2, blue) and two-exponential fit (Eq. 3.3 where X_1 = 21.6 m, X_2 = 57.4 m and G_{gw} = 0.534, red), and (c) corresponding effective normalized perimeter length at the surface as a function of solar zenith angle, $\hat{L}(z = 0, \theta_0)$, as predicted by Eq. 3.9 when applied to the actual data (black) and fitted (red) ground-to-wall probability distributions, and the true perimeter length at the surface (blue)

Table 3.C.1: Evaluation of SPARTACUS-Urban (relative to DART) for F_{REG} scenes (Table 3.1) (a) F_{REG1} and (b) F_{REG2}, for three solar zenith angles (θ_0: 0, 45, 75°) and one albedo (α: 0.1). Upwelling and downwelling clear air shortwave flux profiles ($SW_\uparrow$ and $SW_\downarrow$) assessed with the normalized bias error (nBE, Eq. 3.14) and wall and roof absorption (a_{Wall}, a_{Roof}) profiles assessed with the normalized mean absolute error (nMAE, Eq. 3.12) and the normalized mean-bias error (nMBE, Eq. 3.13)

θ_0 (°)	Scene Albedo (z = 5.5 m)		a_{Ground}		a_{Wall}	
	DART	*nBE* (%)	DART	*nBE* (%)	*nMAE* (%)	*nMBE* (%)
(a) F_{REG1}						
0	0.0889	1.8	0.844	-0.011	20	-10
45	0.0869	0.59	0.779	0.44	11	0.78
75	0.0795	0.93	0.614	3.7	19	-7.1
(b) F_{REG2}						
0	0.0674	14	0.676	-0.044	30	-23
45	0.0620	13	0.411	21	35	-26
75	0.0590	2.6	0.170	30	31	-11

Table 3.C.2: Evaluation of SPARTACUS-Urban (relative to DART) for the remainder of the F_{RAND} scenes (Table 3.1) for θ_0 = 75° and one albedo (α: 0.5). Upwelling and downwelling clear air shortwave flux profiles ($SW_\uparrow$ and $SW_\downarrow$) assessed with the normalized bias error (nBE, Eq. 3.14) and wall and roof absorption (a_{Wall}, a_{Roof}) profiles assessed with the normalized mean absolute error (nMAE, Eq. 3.12) and the normalized mean-bias error (nMBE, Eq. 3.13) with H_{max} the maximum building height in DART

F_{RAND}	λ_p(z = 0)	$\bar{H}$ (m)	H_{max} (m)	Scene Albedo (z = H_{max})		a_{Ground}		a_{Wall}		a_{Roof}	
				DART	*nBE* (%)	DART	*nBE* (%)	*nMAE* (%)	*nMBE* (%)	*nMAE* (%)	*nMBE* (%)
5	0.05	15	34	0.466	-0.75	0.426	-0.61	3.0	2.8	2.2	0.71
6	0.5	15	59	0.362	-4.2	0.0673	-5.8	5.4	5.3	4.6	0.20
7	0.15	7	22	0.456	-1.6	0.360	-1.1	2.7	2.6	0.97	0.46
8	0.15	15	61	0.414	-2.0	0.301	-1.5	3.5	3.4	2.0	0.90
9	0.15	25	85	0.373	-2.4	0.237	-0.57	3.0	2.9	3.4	-0.77
10	0.35	7	27	0.420	-3.0	0.210	-2.7	3.8	3.8	2.1	0.43
11	0.35	15	45	0.367	-3.8	0.136	-3.3	4.4	4.4	2.2	0.40
12	0.35	25	83	0.329	-4.1	0.0817	-2.6	4.4	4.4	3.3	-0.040

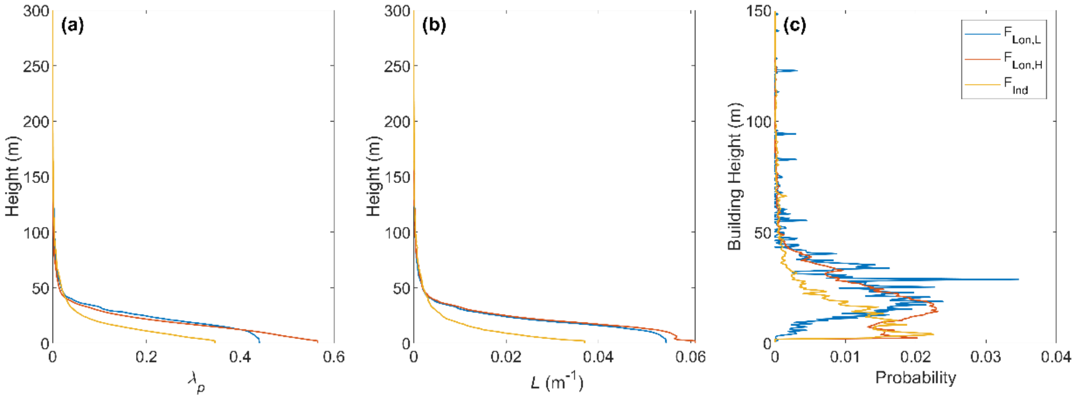

Figure 3.C.2*:* Vertical profiles of (a) building fraction (λ_p), (b) normalized building edge length (L), and (c) distribution of building heights, for central London domains ($F_{Lon,L}$, $F_{Lon, H}$) and Indianapolis (F_{Ind}) (Table 3.1)

Table 3.C.3: Evaluation of SPARTACUS-Urban (relative to DART) for (a) $F_{Lon,L}$, (b) $F_{Lon,H}$, and (c) $F_{Ind,H}$ (Table 3.1) using the single (Eq. 3.2) and two-exponential (Eq. 3.3) fit methods for urban geometry, for three solar zenith angles (θ_0: 0, 45, 75°) and one albedo (α: 0.1). Upwelling and downwelling clear air shortwave flux profiles ($SW_{\uparrow}$ and $SW_{\downarrow}$) assessed with the normalized bias error (nBE, Eq. 3.14) and wall and roof absorption (a_{Wall}, a_{Roof}) profiles assessed with the normalized mean absolute error (nMAE, Eq. 3.12) and the normalized mean-bias error (nMBE, Eq. 3.13)

θ_0 (°)	Scene Albedo ($z = H_{max}$)			a_{Ground}			a_{Wall}				a_{Roof}			
	DART	Single	Two	DART	Single	Two	Single	Two	Single	Two	Single	Two	Single	Two
		nBE (%)			*nBE* (%)		*nMAE* (%)		*nMBE* (%)		*nMAE* (%)		*nMBE* (%)	
(a) $F_{Lon,L}$														
0	0.0697	-1.6	-4.7	0.502	0.37	0.39	18	12	-16	-10	7.6	7.6	0.94	0.94
45	0.0671	-9.3	-9.9	0.265	7.4	5.7	3.5	3.5	-0.76	0.95	10	10	-4.2	-4.3
75	0.0617	-13	-9.9	0.0861	-24	4.9	10	5.0	10	3.6	17	14	-9.4	-6.9
θ_0 (°)	Scene Albedo ($z = H_{max}$)			a_{Ground}			$a_{Wall+Roof}$							
	DART	Single	Two	DART	Single	Two	Single				Two			
		nBE (%)			*nBE* (%)		*nMAE* (%)		*nMBE* (%)		*nMAE* (%)		*nMBE* (%)	
(b) $F_{Lon,H}$														
0	0.0643	5.9	3.6	0.424	-7.5	-7.5	10		5.7		10		5.9	
45	0.0618	-2.3	-3.0	0.266	-21	-22	9.9		8.2		10		8.7	
75	0.0576	-8.5	-5.7	0.0902	-53	-36	15		6.0		14		4.0	
(c) $F_{Ind,H}$														
0	0.0800	1.6	0.38	0.610	-3.4	-3.4	15		6.9		15		7.1	
45	0.0779	-3.3	-4.1	0.525	-9.0	-9.8	15		12		15		14	
75	0.0699	-7.9	-7.3	0.351	-22	-21	17		14		17		13	

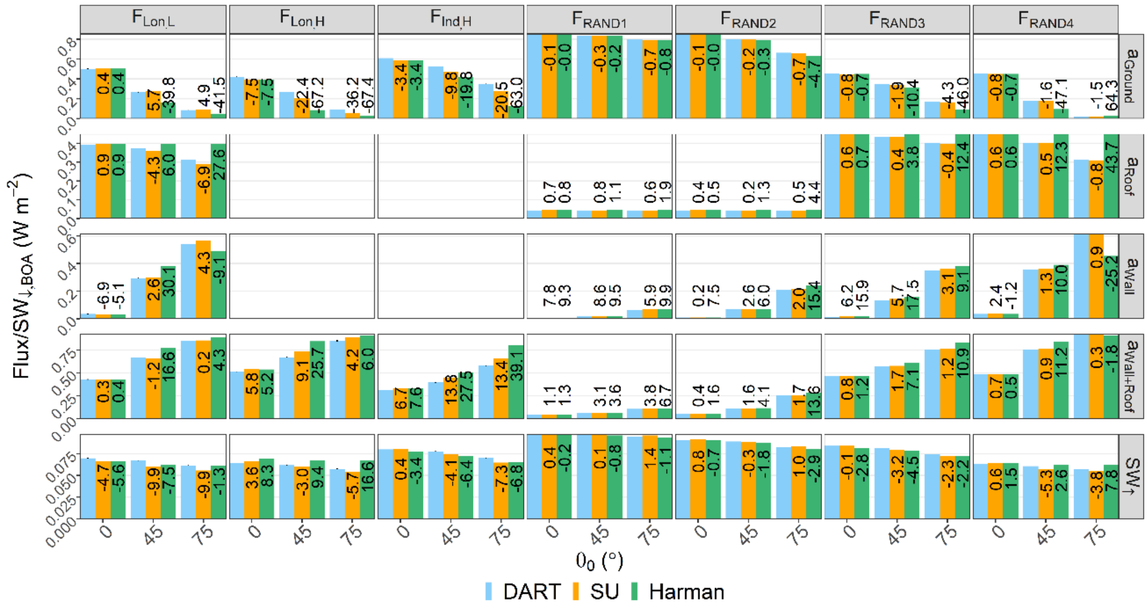

Figure 3.C.3*:* Comparison of SPARTACUS-Urban, Harman et al. (2004) and DART values for real-world scenes at low and high LOD ($F_{Lon,L}$, $F_{Lon,H}$, $F_{Ind,H}$), and random cuboid scenes (F_{RAND}) for three solar zenith angles (θ_0*:* 0°, 45°, 75°) and an albedo of 0.1: upwelling clear air flux at the top of the canopy ($SW_{\uparrow}$), and total wall, roof, and ground absorption (a_{Wall}, a_{Roof}, a_{Ground}). For high LOD scenes a_{Wall} and a_{Roof} are combined ($a_{Wall+Roof}$) for evaluation. Numbers on each bar are the nBE (Eq. 3.14) between the SPARTACUS-Urban model/Harman approach and the DART model. Error bars for DART span the range between if no correction for the energy imbalance is made, and if double this correction is made (Appendix 3.B)

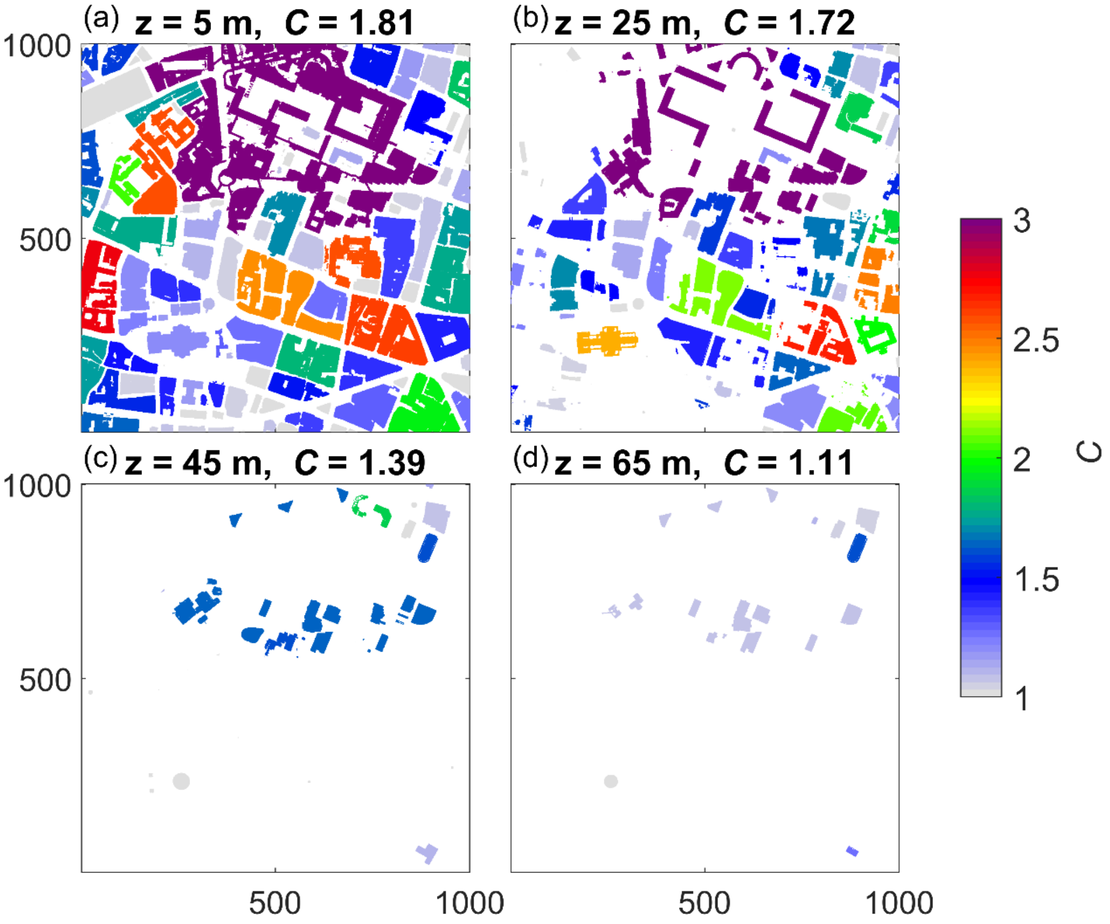

Figure 3.C.4: Variation of the concavity parameter (*C*, Eq. 3.11) for slices of individual buildings in a subset (1000 × 1000 m^2) of the high LOD London scene, at four height levels: (a) 5 m, (b) 25 m, (c) 45 m, (d) 65 m

Chapter 4 Evaluation of vertically resolved longwave radiation in SPARTACUS-Urban 0.7.3 and the sensitivity to urban surface temperatures

Abstract

Cities materials and urban form impact radiative exchanges, and surface and air temperatures. Here, the ‘SPARTACUS’ multi-layer approach to modelling longwave radiation in urban areas (SPARTACUS-Urban) is evaluated using the explicit DART (Discrete Anisotropic Radiative Transfer) model. SPARTACUS-Urban describes realistic 3D urban geometry statistically, rather than assuming an infinite street canyon. Longwave flux profiles are compared across an August day for a 2 km × 2 km domain in central London. Simulations are conducted with multiple temperature configurations, including realistic temperature profiles derived from thermal camera observations. The SPARTACUS-Urban model performs well (cf. DART) when all facets are prescribed a single temperature, with normalised bias errors (nBE) < 2.5% for downwelling fluxes, and < 0.5% for top-of-canopy upwelling fluxes. Errors are larger (nBE < 8%) for net longwave fluxes from walls and roofs. Using more realistic surface temperatures, varying depending on surface shading, the nBE in upwelling longwave increases to ~2%. Errors in roof and wall net longwave fluxes increase through the day, but nBE are still 8–11%. This increase in nBE occurs because SPARTACUS-Urban represents vertical, but not horizontal, surface temperature variation within a domain. Additionally, SPARTACUS-Urban outperforms the Harman single-layer canyon approach, particularly in the longwave interception by roofs. We conclude that SPARTACUS-Urban accurately predicts longwave fluxes, requiring less computational time cf. DART, but with larger errors when surface temperatures vary due to shading. SPARTACUS-Urban could enhance multi-layer urban energy balance schemes prediction of within-canopy temperatures and fluxes.

4.1 Introduction

The differences in energy exchanges between urban and rural areas leads to canopy layer air temperature differences of 3-10°C (Oke 1987). This phenomenon, known as the canopy layer urban heat island effect (CL-UHI), has been studied and observed worldwide (Oke 1982a; Zhang et al. 2012; Wu et al. 2014; Guo et al. 2016; Dou and Miao 2017; Gaitani et al. 2017). The CL-UHI is driven by contrasting radiative exchanges between urban and rural environments, resulting from the heterogeneous nature of cities (Aida and Gotoh 1982; Oke 1982a; Kondo et al. 2001; Harman and Belcher 2006; Ao et al. 2016). With increasing urbanization, and more people residing in cities than rural areas since 2007 (Heaviside et al. 2017), there is greater exposure of vulnerable people to extreme weather, such as heatwaves, with the severity of such events potentially exacerbated by the CL-UHI.

The heterogenous 3D structures of urban areas lead to changes in the surface energy balance, and diurnal temperatures (Souch and Grimmond 2006; Masson et al. 2008), due to the resultant differential shortwave (SW) input and radiative cooling across a city. The crenulated urban morphology and resultant deep canyons cause an uneven exposure to the sky and an increased surface area available for exchange (cf. rural areas), which increases the SW absorption throughout the day. This differential solar irradiance drives temperature variations between facets, including vertical gradients (Oke 1981; Blankenstein and Kuttler 2004; Harman and Belcher 2006; Hénon et al. 2012; Hu and Wendel 2019).

The spatial variation of facet temperatures is highest during the daytime, due to variations in the absorption and reflection of the dynamic solar radiation (Myint et al. 2013; Crum and Jenerette 2017; Antoniou et al. 2019). However, temperatures remain high overnight from the morphology reducing exposure to the sky therefore increasing radiative trapping and slowing cooling rates, and lowering effective albedo. Facet materials (e.g., concrete, tarmac) can have low albedo, high heat capacities and high thermal inertia (Bohnenstengel et al. 2011). This results in large daytime heat storage into the urban volume, which is released slowly at night (Meyn and Oke 2009; Kershaw and Millward 2012).

These impacts on the radiative and other energy exchanges need to be parameterised within numerical weather prediction (NWP) land surface schemes (Masson 2006). A common approach to simplifying the 3D structure of cities is to treat the urban form as a single canyon between buildings of equal height (Nunez and Oke 1977). Initially, in some standalone models, some complexity was considered, e.g., allowing intersections (e.g., Aida 1982; Arnfield 1982a, 1988), when modelling urban radiative exchanges. But, with

NWP computer resource limitations an infinite canyon was assumed, simplifying view factor geometry and computations (e.g., Masson 2000; Harman et al. 2004), an approach which has been adopted for other energy balance fluxes (e.g., Masson 2000; Kusaka et al. 2001a; Lee and Park 2008). Many of these models calculate the fluxes for individual facets (wall, roof, and ground) (Masson 2006). However, assuming a constant building height and lack of intersections neglects the variability of urban geometry (e.g., clusters of tall buildings, courtyards) that influence shadowing and trapping of radiation, and wind fields (e.g., Hertwig et al. 2019, 2021).

Sub-facet differences (e.g., roof orientation, and slopes, high/low parts of walls, wall orientation, sunlit/shaded pavement) can create surface temperature variability, which is not captured if represented by a single mean surface temperature in an urban energy balance scheme (Hilland and Voogt 2020). For example, diurnal variations of wall temperature are linked to their orientation relative to the sun, and additionally to inter-building interactions (e.g. shadows) (Nazarian and Kleissl 2015; Antoniou et al. 2019). This is important as 12-50% of the urban surface is comprised of walls (Voogt et al. 1997; Grimmond and Oke 1999b; Hénon et al. 2012). Similarly, roofs differ from walls, with high incident SW radiation (Harman and Belcher 2006; Morrison et al. 2018), and ground surfaces in deep urban canyons may have dampened diurnal temperature variability (Hu and Wendel 2019). Inclusion of the vertical variability of the urban form may allow such features to be captured by models, unlike within the infinite homogenous canyon approach.

Some of these features can be addressed by utilising multi-layer radiative transfer models, allowing more nuanced radiative trapping and realistic vertical temperature distributions (e.g. Seoul National University Canopy Model (Ryu and Baik 2012; Ryu et al. 2013), Building Effect Parameterisation (BEP, Martilli et al. (2002); Schubert et al. (2012)), the Town Energy Balance model (TEB, Hamdi and Masson (2008)), and SPARTACUS-Urban (Hogan 2019a)). Most assume a canyon geometry, those with varying building heights permitting more realistic inter-building shading (e.g., Schubert et al. (2012)). SPARTACUS-Urban assumes buildings are distributed randomly in the horizontal plane, with geometry describable by vertical profiles of building plan area and building edge length, allowing radiative exchanges simulations fast enough for NWP accounting for atmospheric absorption, emission, and scattering between buildings. The approach provides a more accurate description of radiation exchange than single layer street-canyon approaches (Hogan 2019b). The shortwave (SW) simulations for realistic urban domains have good agreement to an explicit radiative transfer model (Stretton et al. 2022).

In this study, the longwave (LW) capabilities are evaluated for the first time. SPARTACUS-Urban's performance is compared to both the explicit scheme DART (Discrete Anisotropic Radiative Transfer, Gastellu-Etchegorry et al. (2015)) and to a common approach used in operational NWP and climate modelling, Harman et al. (2004) (Section 4.2). To examine SPARTACUS-Urban's LW fluxes we simulate an area in central London, with facet temperatures available from thermal camera observations (Morrison et al. 2020, 2021) that can be prescribed with varying levels of complexity for the evaluation (Section 4.3). Comparison of SPARTACUS-Urban to DART (Section 4.4) and to Harman et al. (2004) street canyon radiation (Section 4.5) is made, with the conclusions presented in Section 4.6).

4.2 Radiative transfer models

4.2.1 SPARTACUS-Urban

The SPARTACUS approach, developed to model radiative exchange within cloud fields (Hogan et al. 2016), has been applied to both vegetated (Hogan et al. 2018a) and built areas (Hogan 2019a). Obstacles to radiation are assumed to be randomly distributed within the horizontal plane, allowing simulation of a mean radiation field with height. We use SPARTACUS-Surface open-source software (Hogan 2021) which includes both SPARTACUS-Urban and SPARTACUS-Vegetation. Given our buildings focus (i.e., excluding urban vegetation), we refer to this as "SPARTACUS-Urban". Previously, we used DART to evaluate SPARTACUS-Urban SW for multiple urban geometry configurations (Chapter 3).

A discrete-ordinate method is used to solve coupled ordinary-differential equations for $2N$ radiation streams (N streams per hemisphere, here $N = 8$). Radiative fluxes are calculated per height interval, z, for layers split into clear-air and building 'regions' in the horizontal plane. The incoming and outgoing fluxes (W m^{-2}), and absorption (W m^{-3}) profiles are calculated for three facets (wall, roof, and ground). SPARTACUS-Urban characterises each model grid cell simulated using its morphology, emissivity (ε), and surface temperature (T). For morphology the plan area fraction (λ_p), building edge length (L), are required as a vertical profile that varies with height (z). These, like other morphology parameters, can be derived from building footprint data (Martilli 2009; Kent et al. 2019; Stretton et al. 2022). SPARTACUS-Urban allows vertical variation of facet temperatures to be prescribed with one facet T per height level.

Although we assume a vacuum, SPARTACUS-Urban can account for atmospheric absorption. For this paper, we assume a wavelength of 10 μm (where atmospheric absorption is weak), so the emission rate in SPARTACUS-Urban (and DART) makes use of the Plank function at 10 μm, with a top-of-canopy downwelling longwave spectral flux at that wavelength ($LW_{\downarrow}$).

4.2.2 DART

The DART (Discrete Anisotropic Radiative Transfer) model (Gastellu-Etchegorry et al. 2015) can simulate variability of radiative exchanges across one SPARTACUS-Urban grid cell in detail using a 3D digital surface model (DSM) with vegetation, buildings and atmosphere. Each voxel (or grid box) size has a user-prescribed resolution. The model domain's elements (e.g., vegetation, buildings) within a voxel can interact with each other. The per-voxel radiative budget products are stored after each numerical iteration. DART scene elements are often represented by flat ‘triangles’ making up building walls and roofs or leaves on trees. Each triangle has an area, orientation, and optical properties. Alternatively, DART can represent vegetation as ‘turbid media’ (or volumes filled with randomly distributed infinitely small facets) characterised by an angular distribution and an area volume density.

To model the urban LW field in DART, both a 3D building model and a 3D field of surface temperatures are required. The latter can be prescribed based on solar irradiance state (e.g., currently sunlit, shaded). Here, each building’s triangles are categorised based on facet type (e.g., roof, wall) and orientation (e.g., west, east) to allow realistic spatial values. As a triangle can have only one temperature, if a triangle covers a whole wall (i.e., vertical building facet) there is no vertical variation.

Given DART is an explicit radiative transfer model it has more detailed radiative interactions than the simpler radiative transfer models (e.g., SPARTACUS, Harman). DART has been evaluated in vegetated areas using thermal infrared observations (Sobrino et al. 2011) and relative to other models in the RAMI intercomparison project (Widlowski et al. 2015). The DART version including buildings (Gastellu-Etchegorry et al. 2015) has not been explicitly evaluated in urban areas, but has been used to assess urban SW and LW radiation and albedo (Chrysoulakis et al. 2018; Landier et al. 2018), variations in urban surface temperatures (Morrison et al. 2020, 2021), and mean radiant temperature (Dissegna et al. 2021), and to assess simpler radiative transfer models (e.g., SPARTACUS-Urban, Chapter 3).

4.2.3 Harman et al. (2004)

Harman et al. (2004) use a system of linear equations to compute the exact LW radiative transfer from one temperature per facet (e.g., one for walls). Hogan (2019b), after modifying Harman's horizontal geometry to have an exponential distribution, to be consistent with SPARTACUS's assumptions, finds agreement between the two models for the net outward LW flux from the ground and walls when SPARTACUS uses more than 4 streams. Here, the SPARTACUS-Surface software package (see Section 4.2 of (Hogan 2019a)) implementation of Harman is used for the simulations.

Harman assumes two parallel buildings of infinite length with constant height (*H)* separated by a constant street width (*W).* For this comparison, the real-world domain (Section 4.2.3) total area of the ground, walls, and roofs (i.e., building fraction at the surface ($\lambda_p(z = 0)$), and mean building height ($\overline{H} = H$) are used. *H/W* is calculated using (Hertwig et al. (2020), their Eq. 3):

$$\frac{H}{W} = \frac{\pi}{2}\frac{\lambda_f}{(1 - \lambda_p)} \tag{4.1}$$

where the frontal area index (λ_f) is calculated from the total normalised wall area ($\lambda_w = \lambda_f \pi$) using from the vertical profile of normalised building edge length (L) derived the from vertical profile:

$$\lambda_W = \sum_{i}^{n} L_i \Delta z_i\,. \tag{4.2}$$

All Harman simulations have only one temperature (i.e., not a profile) per facet (i.e., wall, roof, ground).

4.3 Methodology

4.3.1 Model domain

The evaluation is undertaken for a 2 km × 2 km area in central London, with residential and commercial buildings of varying horizontal extent and height (Figure 4.1a). The

DSM and digital elevation model (DEM) are derived from "Virtual London" building footprint dataset (Evans et al. 2006). To simplify buildings so they have flat both roofs and walls, for each building the 25th percentile of the DEM and 75th percentile of the DSM heights are used. For DART, the resulting 3D building roof DSM and ground DEM are used. The Chapter 3 3D building model is improved slightly (e.g. shift in vertical plane, removal of some internal walls). The DART voxel resolution used is 1 m vertically and 5.206 m horizontally. For SPARTACUS-Urban the same vertical resolution as DART (1 m) is used. To remove internal walls between buildings, the SPARTACUS-Urban vertical profiles of λ_p and L are derived from a 1 m × 1 m building footprint raster.

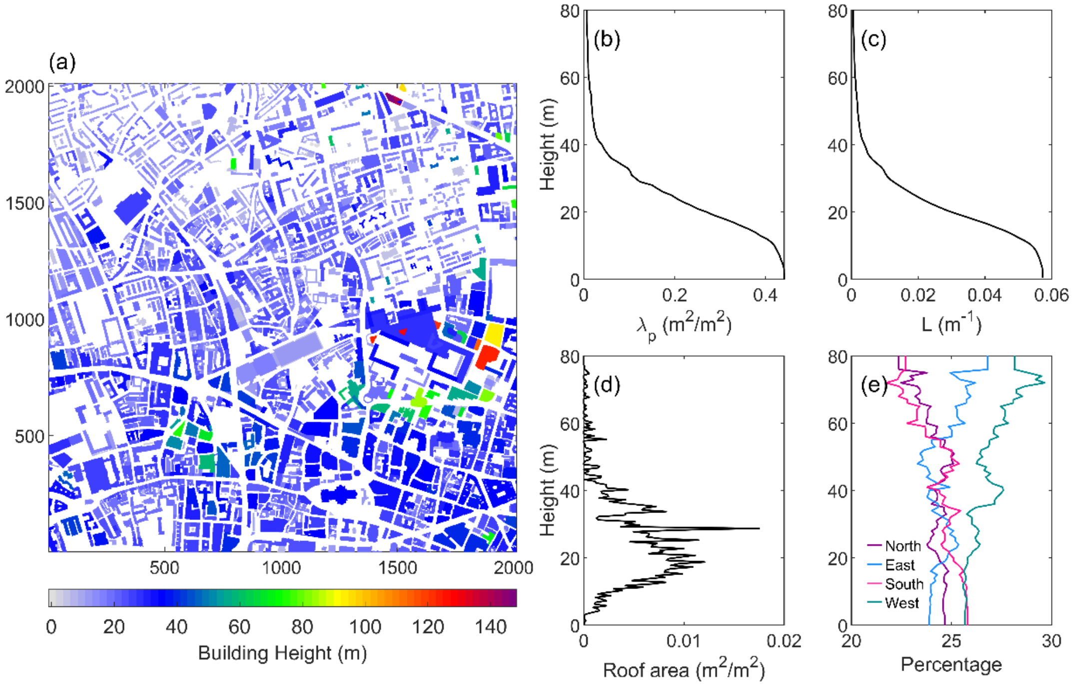

Figure 4.1: Low level of detail central London domain (i.e., flat roofs): (a) building heights, (b) building plan area fraction (λ_p) with height, (c) normalised building edge length (L) with height (Eq. 4.2), (d) roof area with height, (e) wall orientation distributions calculated from surface-classified DART emission output

4.3.2 Observations used for radiative transfer inputs

In the model domain, three observation sites are present (Table 4.1). We focus on a day (27th August 2017) with detailed surface temperature observations and almost clear skies (< 45-min cloud mid-afternoon) (Morrison et al. 2020).

Given computational constraints, DART is run for a single wavelength (10 µm). We choose 10 µm, as it is approximately central to the LW infrared band, hence some additional uncertainty arises in SPARTACUS-Urban results for other wavelengths and broadband longwave flux measurements cannot be used. Instead, we rerun the ECMWF atmospheric radiation scheme using pressure, temperature and humidity profiles for the site 0.25° grid-cell from ERA5 (Hersbach et al. 2020) for that day (Figure 4.2), and extract bottom-of-atmosphere (BOA) clear-sky downwelling spectral flux at 10 μm. For the SPARTACUS-Urban and Harman et al. (2004) simulations, SPARTACUS-Surface is modified to calculate the single spectral wavelength emission. SPARTACUS-Surface requires T_{Air}, but as we simulate radiative fluxes in a vacuum, it is set to 0 K. Each model requires an emissivity (ε) per surface. We assume homogenous value of 0.93, based on the mean urban value in the Kotthaus et al. (2014b) spectral library.

Facet surface temperatures are prescribed using thermal camera imagery (Optris PI-160 LW infrared cameras) observed for a 420 m × 420 m area within this domain (Morrison et al. 2020, 2021) (Figure 4.3). Detailed modelling has categorised these observations by facet type, sunlit/shaded, and orientation (Morrison et al. 2020, 2021). Surface temperatures are split into roof, ground, and cardinal wall orientation (*etc.*) types. Although we evaluate SPARTACUS-Urban across the whole day, to demonstrate the performance for multiple surface temperature configurations, we select times with distinct temperature profiles (e.g., just after sunrise, with no facet temperature range) and summarise the general model performance. As surface temperature processing constraints (Morrison et al. 2020) gives observations from 5:45 UTC (sunrise: 5:04 UTC), the models are runs for every hour from then to end of the day. The mid-afternoon cloud period is discarded, as no sunlit/shaded temperature range is observed (Figure 4.3).

Table 4.1: Sensors used from within domain (Figure 4.1a). Meteorological time series, and further details of observations within this domain can be found in Morrison et al. (2021)

Site	Full name	Latitude °N	Longitude °W	Instruments
BCT	Barbican Cromwell Tower	51.5206	0.09230	Davis weather station
IMU	Islington Michael Cliffe House Upper	51.526	0.1061	Davis weather station Kipp and Zonen CNR1 radiometer Optris Pi160 infrared thermal camera
WCT	Wycliffe Court Tower	51.5267	0.1036	Optris Pi160 infrared thermal camera

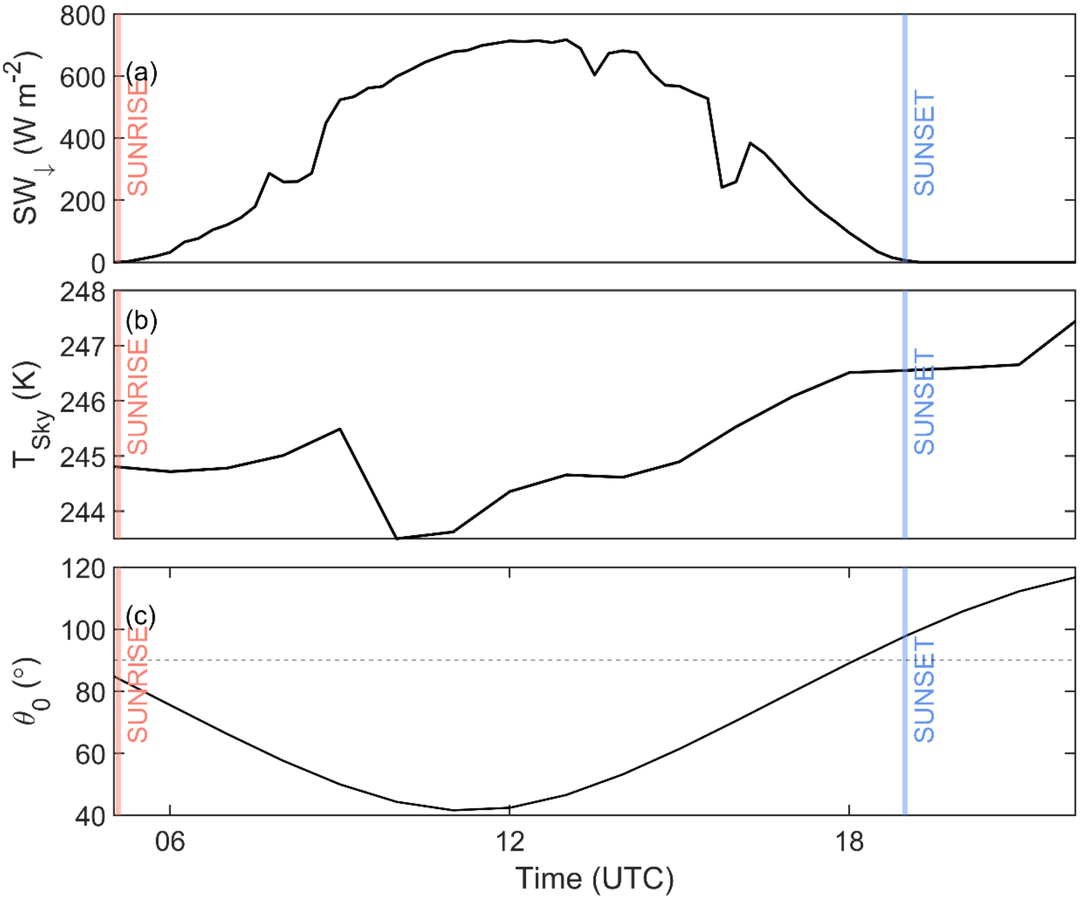

Figure 4.2: Diurnal timeseries for 27th August 2017 of (a) downwelling shortwave (SW$_\downarrow$) observations from a Kipp and Zonen CNR1 radiometer located at IMU, (b) clear-sky 10-µm brightness temperatures calculated from ERA5, and (c) solar zenith angle (θ_0). Additional meteorological observations for the day of interest are shown in Morrison et al. (2021)

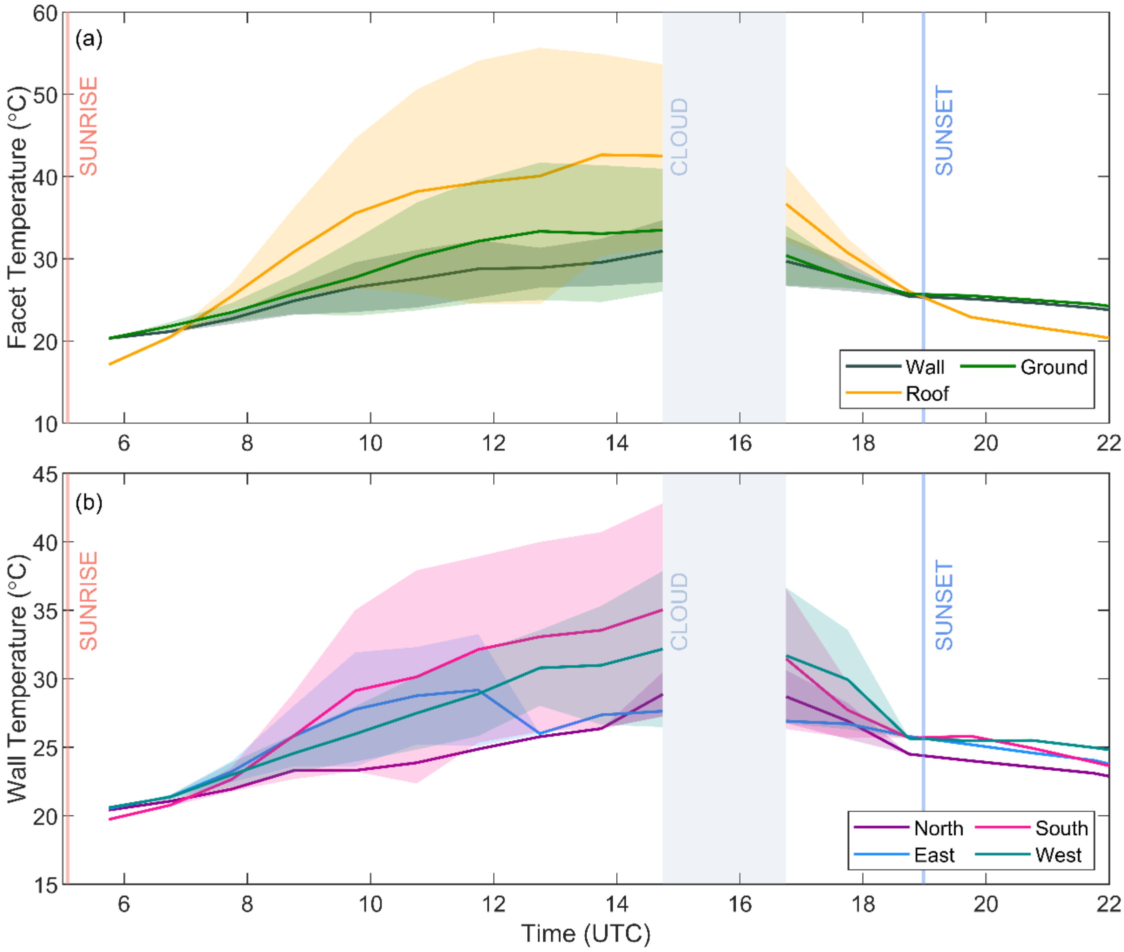

Figure 4.3: Observed mean (line) and range (shading, [between sunlit to shaded areas]) temperature on 27th August 2017 (Morrison et al. 2021) for each (a) facet type (walls – all weighted equally) and (b) wall azimuthal orientation

4.3.3 Model surface temperature (*T*) prescription

The three radiative transfer models (Section 4.2) require different *T* inputs. To assess the sources of error between SPARTACUS-Urban and DART (i.e., radiation calculation or surface temperature values), two complexities of model runs are undertaken.

First, simulations assume an isothermal temperature within each surface type, with DART surfaces prescribed the single mean *T* from the camera observations (Figure 4.3a, line). To match this, SPARTACUS-Urban roofs and ground are prescribed the mean DART input temperature. For SPARTACUS-Urban T_{Wall}, each wall orientation is weighted equally (**Figure 4.A.1**), following the SPARTACUS-Urban assumption that walls equally face in all directions, such that:

$$T_{Wall} = (T_{Wall\,N} + T_{Wall\,E} + T_{Wall\,S} + T_{Wall\,W})/4 \qquad (4.3)$$

where $T_{,Wall\ N\text{-}E\text{-}S\text{-}W}$ are one of the four cardinal directions. For Harman, the same temperatures as SPARTACUS-Urban are used.

Non-isothermal surface temperatures varying by sunlit – shaded status allow for horizontal and vertically differences by facet type. These can be represented in multi-layer energy exchange schemes. A temperature range can be prescribed in DART allowing sunlit-shaded variations. However, given level of detail of the surface model used (Figure 4.1) the observed surface temperatures are not directly usable as camera pixels has much higher resolution than the DART triangles. DART SW simulations are used to determine whether each facet triangle is sunlit or shaded, and therefore which temperature (maximum/minimum) range (Figure 4.3) is assigned by type (e.g., roof, west facing wall, east facing wall). As noted, as DART triangles may have whole wall resolution but only one prescribed temperature.

As it is complex to extract the vertical profile of temperature for each surface type from DART, solar zenith angle (θ_0) dependent SW SPARTACUS-Urban simulations are used to estimate the sunlit fraction for the walls ($F_{Sun,Wall,i}$) and roofs $F_{Sun,Roof,i}$) by height interval, and for the ground ($F_{Sun,Ground}$). The shaded fractions are obtained by difference ($F_{Sh,Wall,i} = 1 - F_{Sun,Wall,i}$). The appropriate DART sunlit (shaded) temperatures are assigned to SPARTACUS-Urbans sunlit (shaded) fraction. Similarly, the sunlit and shaded roof temperatures ($T_{Sun,Roof}$, $T_{Sh,Roof}$) are weighted at each height by the appropriate sunlit and shaded fractions to obtain $T_{Roof,i}$ and at $z = 0$ for the ground ($T_{Ground,sun}$, $T_{Ground,sh}$). Thus, enabling SPARTACUS-Urban to capture the horizontal surface temperature variations.

As the four wall orientations have different temperatures depending on their shadow history (Morrison et al. 2021), for SPARTACUS-Urban we weight them to obtain one average sunlit and shaded wall temperature ($T_{Wall,sun}$, $T_{Wall,sh}$). Given the SPARTACUS-Urban assumption that walls face equally in all directions, we weight the sunlit and shaded temperatures (as Eq. 4.3), but use the solar azimuth angle (Ω) to determine the 'dominant' sunlit wall orientation. The dominant sunlit facing surface (e.g., south) temperature (in this example, $T_{Sun,South}$) is double weighted in Eq. 4.3 (i.e., replacing $T_{Sun,North}$) assuming the wall 180° (i.e., north facing surfaces in example) are shaded. The opposite is done for the $T_{,Sh,Wall}$, obtaining (for this example):

$$T_{Sun,Wall} = 0.0 \cdot T_{Sun,Wall\,N} + 0.25 \cdot T_{Sun,Wall\,E} + 0.25 \cdot T_{Sun,Wall\,W} + 0.5 \cdot T_{Sun,Wall\,S}, \tag{4.4}$$

$$T_{Sh,Wall} = 0.5 \cdot T_{Sh,Wall\,N} + 0.25 \cdot T_{Sh,Wall\,E} + 0.25 \cdot T_{Sh,Wall\,W} + 0.0 \cdot T_{Sh,Wall\,S}. \tag{4.5}$$

The $T_{Wall,sh}$ and $T_{Wall,sun}$ are weighted using $F_{Sun,Wall,i}$ and $F_{Sh,Wall,i}$ to determine the $T_{Wall,i}$ for each height:

$$T_{Wall,i} = F_{Wall,sun,i} T_{Wall,sun} + F_{Wall,sh,i} T_{Wall,sh}. \tag{4.6}$$

To visualise this at several times see **Figure 4.A.1**. Combining $F_{Sun,Wall,i}$ and $F_{Sun,Roof,i}$ gives a larger weight to warmer sunlit surface temperatures in the simulations, better matching the emission from the DART model scenes.

For the Harman et al. (2004) simulations, area-weighted surface temperatures from the SPARTACUS-Urban profiles are used:

$$T_{Wall} = \sum_{i}^{n} T_{Wall,i} \left(\lambda_{Wall,i} / \lambda_{Wall}\right) \tag{4.7}$$

where $\lambda_{Wall,i}$ is the exposed normalised wall area at each height, which is normalised by the total wall area, λ_W. Eq. 4.7 is also applied to roofs. This ensures that warmer surfaces at the top of the canopy with small areas are not overweighted.

4.3.4 Evaluation metrics

We evaluate SPARTACUS-Urban using DART by comparing the profiles of LW upwelling and downwelling clear-air spectral fluxes ($LW_{\uparrow}$, $LW_{\downarrow}$), and the intercepted, outgoing, and net (= incoming – outgoing, relevant for facet temperature evolution) flux into walls, roofs, and ground (i.e., $LW_{In,Wall}$, $LW_{Out,Wall}$, LW^*_{Wall}). The LW clear-air fluxes have units of W m^{-2} μm^{-1} of the entire horizontal scene, while the fluxes from walls and roofs have units W m^{-3} μm^{-1}, as we divide by the layer thickness (1 m) to obtain a resolution independent flux.

For the comparison between SPARTACUS-Urban and DART, we examine the downwelling longwave at the base of the canopy, and the upwelling longwave at the top of the canopy in DART (H_{max}) to obtain a normalised bias error. The $LW_{\uparrow}$ flux profiles are evaluated using the normalized bias error at a specified height (*nBE*), expressed as a percentage of the DART flux:

$$nBE = \frac{LW_{SU} - LW_{\mathrm{DART}}}{LW_{\mathrm{DART}}} 100\%. \tag{4.8}$$

We compare the differences in the wall and roof fluxes between the two models by using a nBE in the total interception, emission, and net LW flux, calculated from 1 m to H_{max}.

4.4 Results

4.4.1 Prescribed surface temperatures

The $F_{Sun,Wall,i}$ and $F_{Sun,Roof,i}$ are calculated from SPARTACUS-Urban SW simulations for each time period (Figure 4.4). The sunlit fraction into the canopy increases as zenith angle, θ_0, decreases until about 11:45 UTC (Figure 4.2). As more walls become illuminated within the canopy, there is an increase in T_{Wall} (Figure 4.3, Figure 4.4). As θ_0 increases again (Figure 4.2c), the within-canopy surfaces become more shaded than sunlit.

From combining the F_{Sh} and F_{Sun} profiles with the DART prescribed facet T (Eq. 4.4-4.6) the T_{Wall} and T_{Roof} profiles are obtained (Figure 4.5). At 5:45 UTC all DART temperatures are the same, so all temperature configurations and SPARTACUS-Urban temperatures are equal. At 7:45 UTC, the first vertical variations in temperature occur with sunlit roof facets higher in the canopy causing warmer temperatures above. Both 11:45 UTC and 13:45 UTC share similar T_{Wall} profiles, and do not have much influence from the warmer south facing walls despite their greater weighting. The most different T_{Roof} profile, spanning the widest temperature range, occurs at 17:45 UTC.

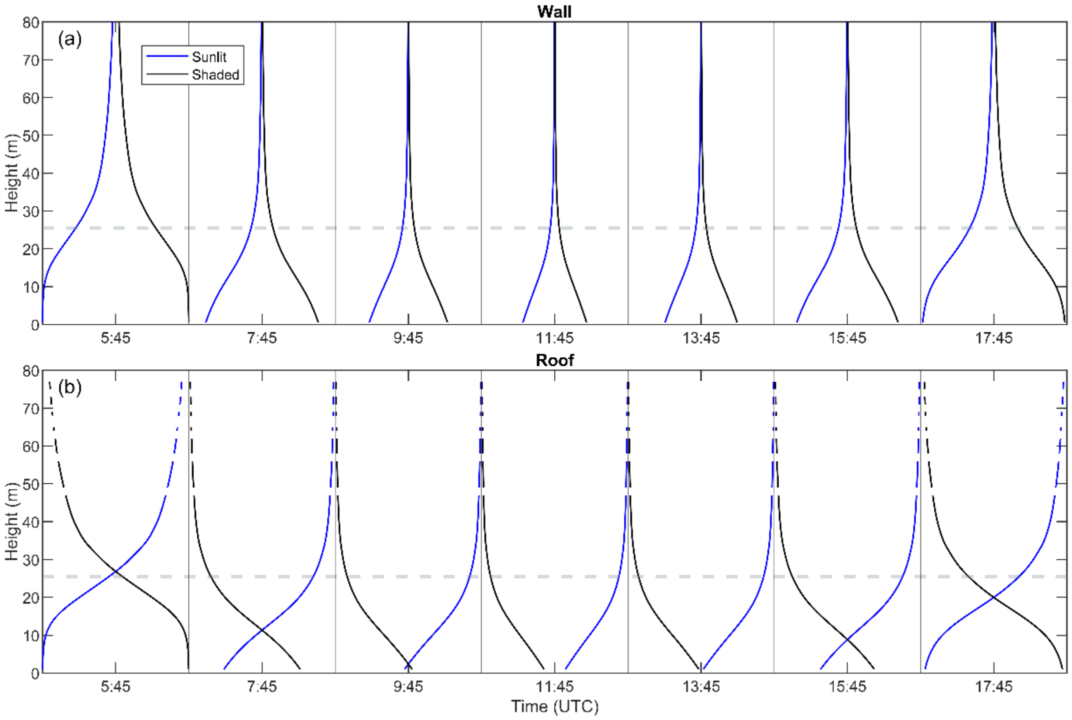

Figure 4.4: Sunlit (blue) and shaded (black) fraction of (a) walls and (b) roofs during the study day from SPARTACUS-Urban shortwave simulations using solar zenith angles (Figure 4.2). Lines are shown as dashed when no roofs occurs at a height. Mean building height ($\overline{H}$= 25.5 m, grey dashed).

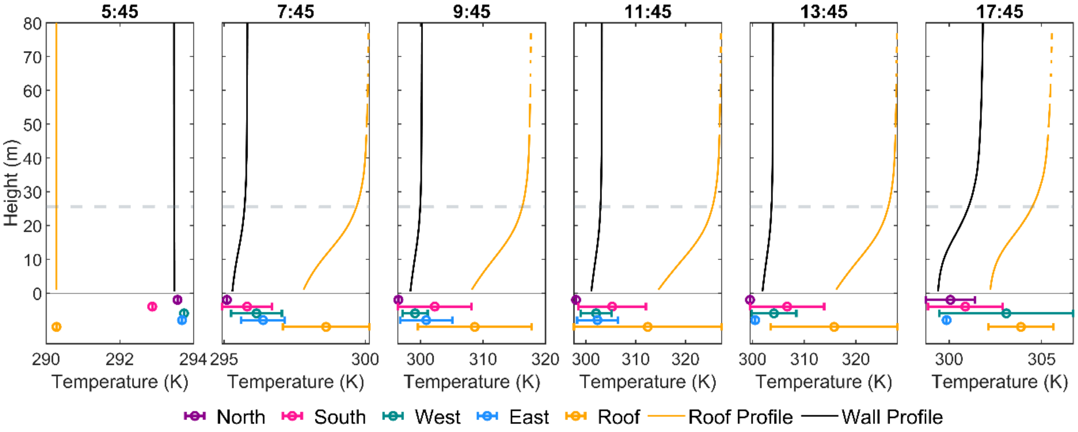

Figure 4.5: Temperature profiles at six times (UTC) used in SPARTACUS-Urban simulations (averaging methods, Section 4.3.3) with temperatures prescribed to DART surface types given in the error bars below each set of temperature profiles, with the mean temperature denoted by open circles, and sunlit-shaded range given (Figure 4.3). Note x-axes differ between panels.

4.4.2 Comparison of SPARTACUS-Urban and DART: One facet temperature (*T*)

First, when *T* does not have sunlit-shaded variations, there is good agreement between SPARTACUS-Urban and DART. There is good agreement for both $LW_{\uparrow}$ at the top of the canopy (nBE < 0.5% across the whole day,

Table 4.2, Figure 4.6, Figure 4.B.1 - Figure 4.B.5), and for $LW_{\downarrow}$ across the day (nBE ~2%). The $LW_{Out,Wall}$ nBE is < 0.1%, and the nBE for LW^*_{Wall} is 8-11%. The nBE is less when T_{Wall} is warmer (i.e., middle of day). The larger error in LW^*_{Wall} is caused by a small net flux as $LW_{In,Wall}$ and $LW_{Out,Wall}$ cancel each other thus small errors result in large nBE.

SPARTACUS-Urban slightly underestimates $LW_{In,Wall}$ and $LW_{Out,Wall}$ (Figure 4.6) at the base of the canopy, therefore LW^*_{Wall} is slightly overestimated. SPARTACUS-Urban overestimates $LW_{In,Roof}$ below $\overline{H}$. With just one T_{Roof} per time interval, $LW_{Out,Roof}$ error is small (nBE ~3%), causing underestimates of LW^*_{Roof} and larger nBE (5.5 to 8.5 %).

Across the multiple cases for different facet T and with different differences between facet T (e.g., magnitude of $T_{Roof} > T_{Wall}$), the agreement is consistent between the two models. These differences may have arisen due to the geometry assumptions in SPARTACUS-Urban or the wall temperature averaging, but despite this, their magnitudes remain low.

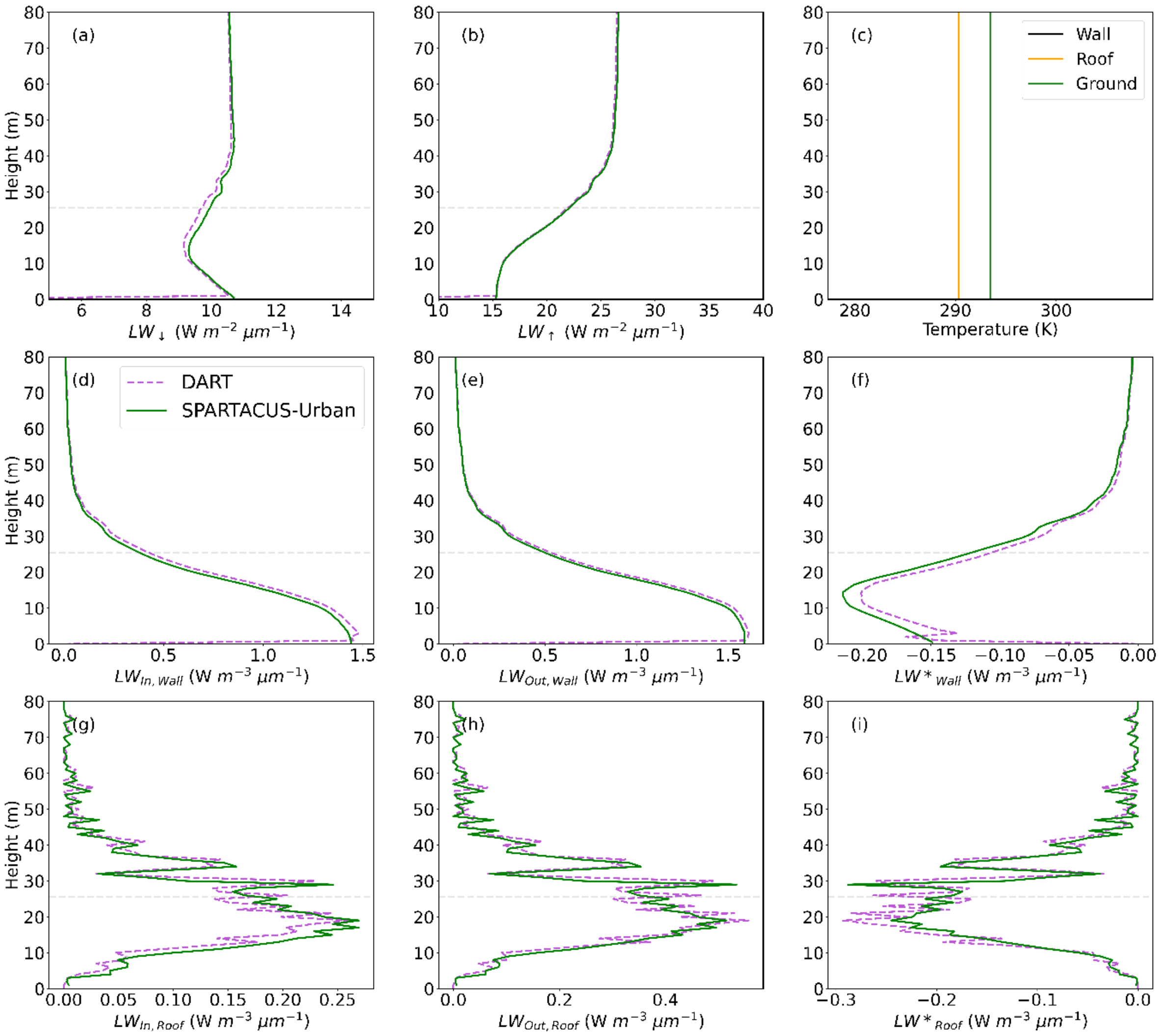

Figure 4.6: Longwave fluxes (LW) for a 2 km × 2 km domain in central London (Figure 4.1) simulated with SPARTACUS-Urban (green) and DART (purple) with an emissivity of 0.93 at 5:45 UTC on the 27th August 2017 with (c) single facet T: (a) downwelling clear air flux ($LW_\downarrow$), (b) upwelling clear air flux ($LW_\uparrow$), (d-f) wall interception, outgoing and net flux ($LW_{In,Wall}$, $LW_{Out,Wall}$, $LW*_{Wall}$), (g- i) roof interception, outgoing and net flux ($LW_{In,Roof}$, $LW_{Out,Roof}$, $LW*_{Roof}$). Prescribed facet temperatures using: a single temperature per surface type for DART, and (c) single temperatures per facet type for SPARTACUS-Urban.

Table 4.2: Evaluation of SPARTACUS-Urban (cf. DART) for a 2 km × 2 km domain in central London on an August day, for facets prescribed a single surface temperature. Upwelling and downwelling clear-air fluxes (LW$_{\downarrow}$, LW$_{\uparrow}$), and the total outgoing and net flux into each urban facet (wall, roof, ground, e.g., LW$_{\mathrm{Out,Wall}}$, LW*$_{\mathrm{Wall}}$), assessed using the normalised bias error (nBE, Eq. 4.8).

Time (UTC)	LW$_{\downarrow}$, z = 1		LW$_{\uparrow}$, $z = H_{max}$		LW*$_{\mathrm{Wall}}$	LW*$_{\mathrm{Roof}}$	LW*$_{\mathrm{Ground}}$	LW$_{\mathrm{Out,Wall}}$	LW$_{\mathrm{Out,Roof}}$	LW$_{\mathrm{Out,Ground}}$
	DART	nBE (%)	DART	nBE (%)	nBE (%)	nBE (%)	nBE (%)	nBE (%)	nBE (%)	nBE (%)
5:45	10.5	2.2	26.6	0.47	11	-8.2	-3.3	0.047	-3.3	-0.24
7:45	10.9	2.2	28.9	0.19	9.8	-6.9	-3.1	0.023	-3.1	-0.24
9:45	11.3	2.3	32.0	-0.099	8.5	-6.0	-2.9	0.0073	-2.9	-0.24
11:45	11.6	2.4	33.7	-0.18	8.5	-5.8	-2.7	0.0052	-2.7	-0.24
13:45	11.8	2.4	34.7	-0.27	8.2	-5.5	-2.7	-0.0043	-2.7	-0.24
17:45	11.6	2.4	31.2	0.20	9.9	-6.9	-3.3	0.029	-3.3	-0.23
19:45	11.3	2.2	29.1	0.40	11	-7.9	-3.1	0.047	-3.1	-0.24
21:45	11.2	2.2	28.4	0.45	11	-8.2	-3.2	0.047	-3.2	-0.24

4.4.3 Comparison of SPARTACUS-Urban and DART: Varying facet temperature with solar irradiance

Second, we compare the two models when facets are prescribed a T range. Here, SPARTACUS-Urban has good agreement with DART for LW$_{\downarrow}$ at the base of the canopy (nBE 1.7- 2.9%, Table 4.3), and at the top of the canopy, for all times (Figure 4.2, Figure 4.7- 4.8, Figure 4.B.6 - Figure 4.B.10). There are some disagreements towards the centre of the canopy (~10 – 40 m), at all times, where SPARTACUS-Urban overestimates the LW$_{\downarrow}$. There is also good agreement in LW$_{\uparrow}$ up to ~ 40 m. SPARTACUS-Urban has good agreement (nBE < 0.5%) at the start and end of the day when there is a small range in facet T (Figure 4.5), and so temperature averaging (i.e., wall orientation) has little impact. The nBE in LW$_{\uparrow}$ is poorest in middle of the day (11:45 – 14:45 UTC) when the facets have a large range in temperature but is still < 2.5 %.

The largest errors occur in the LW roof fluxes. SPARTACUS-Urban overestimates all the LW$_{\mathrm{In,Roof}}$ below the $\overline{H}$ (as in Section 4.4.2). However, LW$_{\mathrm{Out,Roof}}$ is similar between SPARTACUS-Urban and DART (nBE ~ 3%), suggesting the $T_{Sun,Roof}$ and $T_{Sh,Roof}$ averaging method provides a good approximation to DART. Hence, SPARTACUS-Urban underestimates the LW*$_{\mathrm{Roof}}$ below the $\overline{H}$, with nBE 6 – 8 %. These differences may be associated with the 1 m vertical resolution used in SPARTACUS-Urban cf. DART's roof fluxes being aggregated to each voxel top. Despite this, the vertical profiles of LW$_{\mathrm{Roof}}$ fluxes in SPARTACUS-Urban and DART are still close (Figure 4.7g-i).

SPARTACUS-Urban LW wall fluxes generally compare well to DART. There are slight differences in the LW$_{\mathrm{In,Wall}}$ close to the surface, which likely is attributable to removal of the internal building walls (Section 4.3.1). For all surface temperature configurations, the LW$_{\mathrm{Out,Wall}}$ the nBE is ~8% throughout the day. Through the day LW*$_{\mathrm{Wall}}$ nBE varies from 0 – 10%. It is smallest when the T_{Wall} variation is largest (11:45 – 14:45 UTC, Figure 4.3). The good agreement in LW$_{\mathrm{Out,Ground,}}$ suggests the averaging method for sunlit and shaded temperatures performs well. SPARTACUS-Urban underestimates LW*$_{\mathrm{Ground}}$ but with low nBE (2 - 5 %).

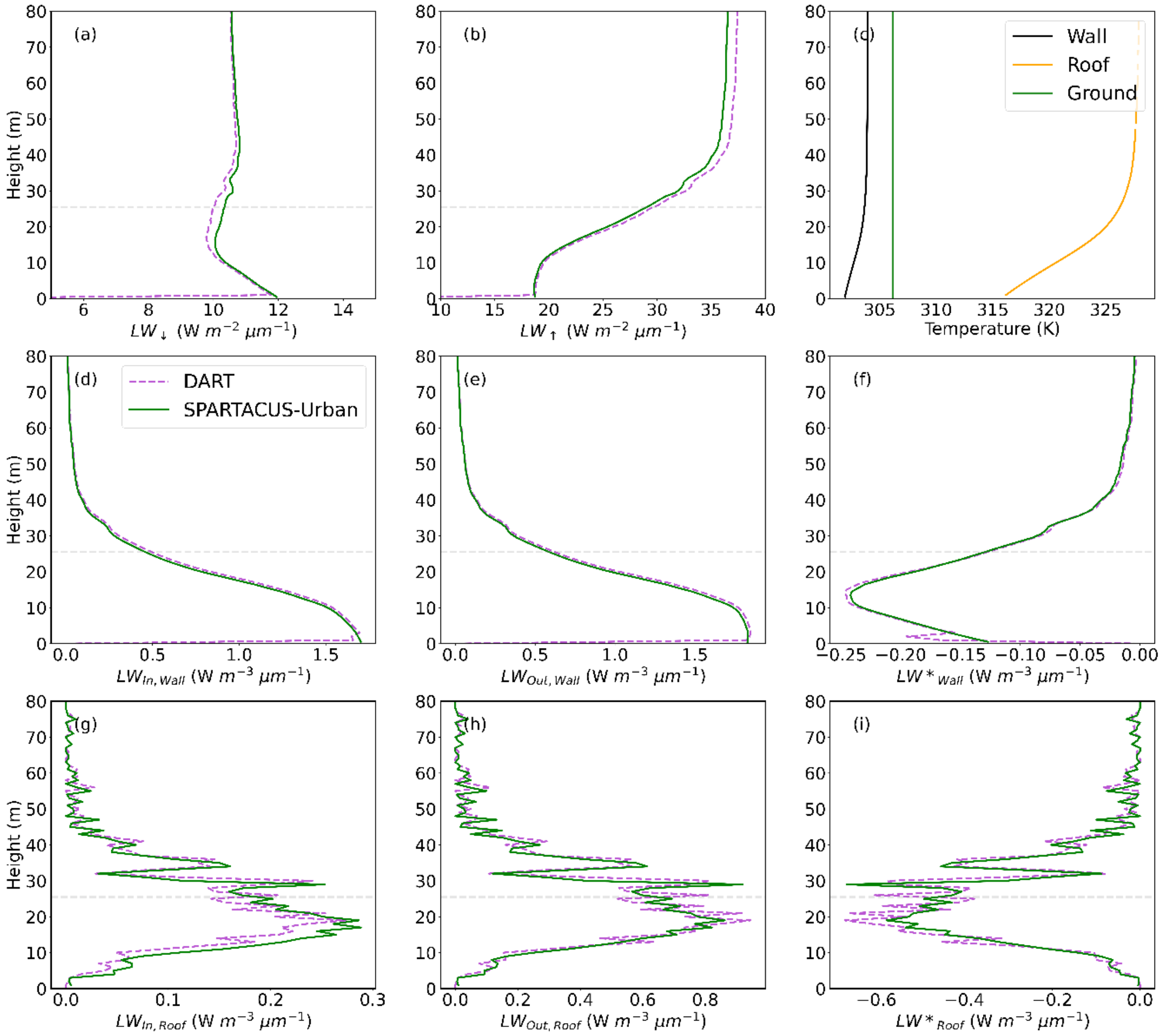

Figure 4.7: Longwave fluxes (LW) for a 2 km × 2 km domain in central London (Figure 4.1) simulated with SPARTACUS-Urban (green) and DART (purple) with an emissivity of 0.93 at 13:45 UTC on the 27th August 2017: (a) downwelling clear air flux (LW$_{\downarrow}$), (b) upwelling clear air flux (LW$_{\uparrow}$), (d-f) wall interception, outgoing and net flux (LW$_{\mathrm{In,Wall}}$, LW$_{\mathrm{Out,Wall}}$, LW*$_{\mathrm{Wall}}$), (g-i) roof interception, outgoing and net flux (LW$_{\mathrm{In,Roof}}$, LW$_{\mathrm{Out,Roof}}$, LW*$_{\mathrm{Roof}}$). Prescribed facet temperatures based on SW simulations at 13:45 using: a full 3D temperature field for DART, and (c) temperature profiles per facet type for SPARTACUS-Urban.

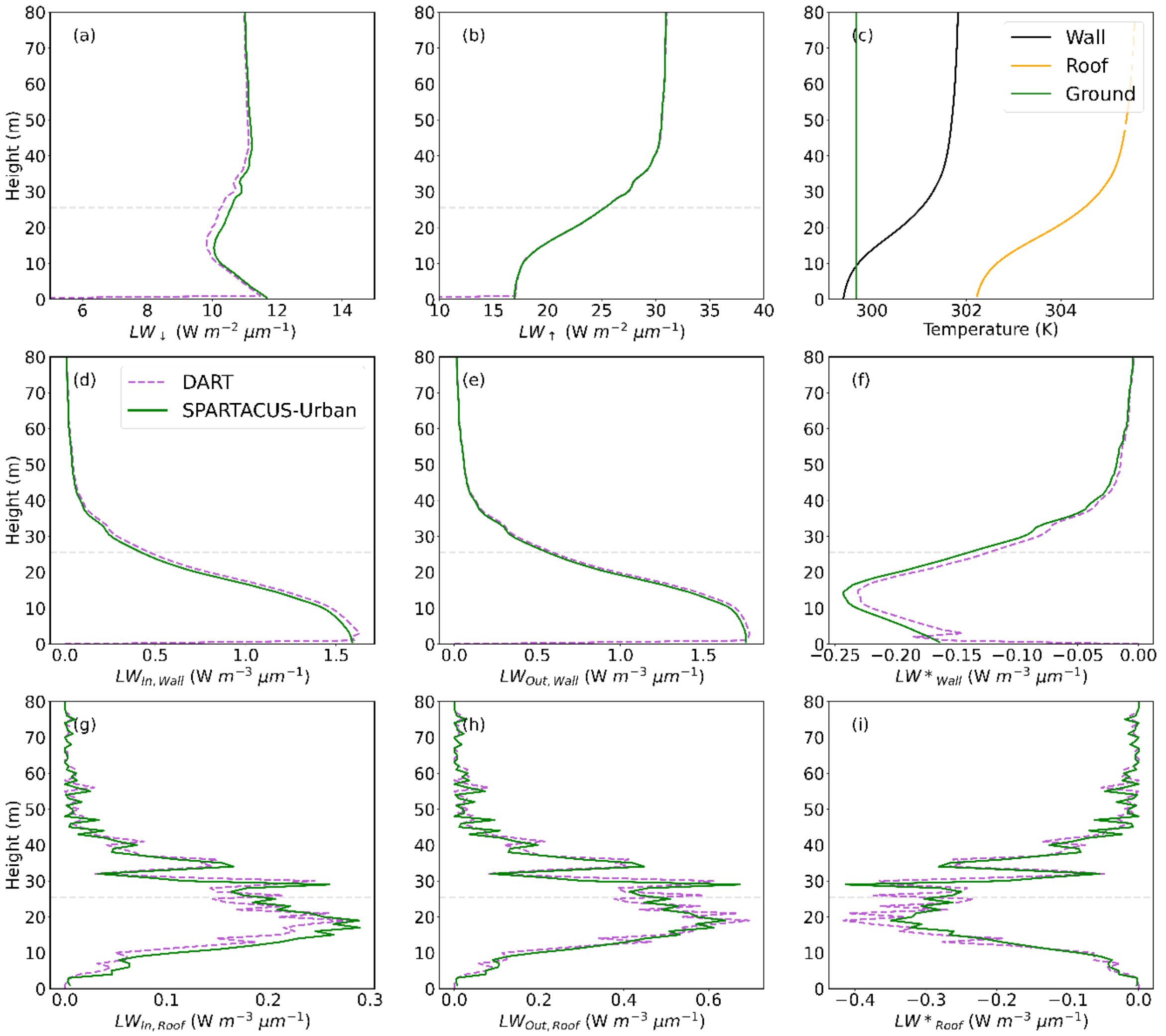

Figure 4.8: Longwave fluxes (LW) for a 2 km × 2 km domain in central London (Figure 4.1) simulated with SPARTACUS-Urban (green) and DART (purple) with an emissivity of 0.93 at 17:45 UTC on the 27th August 2017: (a) downwelling clear air flux ($LW_\downarrow$), (b) upwelling clear air flux ($LW_\uparrow$), (d-f) wall interception, outgoing and net flux ($LW_{In,Wall}$, $LW_{Out,Wall}$, $LW*_{Wall}$), (g-i) roof interception, outgoing and net flux ($LW_{In,Roof}$, $LW_{Out,Roof}$, $LW*_{Roof}$). Facet temperatures used are prescribed based on SW simulations at 17:45, with DART using a full 3D temperature field and (c) SPARTACUS-Urban using temperature profiles for each facet type

Table 4.3: Evaluation of SPARTACUS-Urban (cf. DART) for a domain in central London on an August day, for SPARTACUS-Urban facets prescribed a surface temperature profile based

on SW simulations, and DART using a full temperature field. Upwelling and downwelling clear-air fluxes ($LW_{\downarrow}$, $LW_{\uparrow}$), and the total outgoing and net flux into each urban facet (wall, roof, ground, e.g., $LW_{Out,Wall}$, LW^*_{Wall}), assessed using the normalised bias error (nBE, Eq. 4.8).

Time (UTC)	$LW_{\downarrow}$, $z = 1$		$LW_{\uparrow}$, $z = H_{max}$		LW^*_{Wall}	LW^*_{Roof}	LW^*_{Ground}	$LW_{Out,Wall}$	$LW_{Out,Roof}$	$LW_{Out,Ground}$
	DART	*nBE* (%)	DART	nBE (%)	nBE (%)	nBE (%)	nBE (%)	nBE (%)	nBE (%)	nBE (%)
7:45	10.8	1.9	29.1	-0.31	8.0	-7.3	-3.3	0.047	-3.3	-0.23
9:45	11.3	1.7	33.9	-2.0	1.7	-7.3	-3.1	-0.38	-3.1	-0.42
11:45	11.6	2.7	37.2	-2.2	4.0	-6.6	-2.0	-1.6	-2.0	-0.28
12:45	11.7	2.2	37.9	-2.5	0.62	-6.8	-4.8	-1.5	-4.8	-0.923
13:45	11.8	2.3	37.6	-2.4	0.13	-6.9	-3.0	-1.7	-3.0	-0.48
14:45	11.8	2.9	37.3	-2.3	5.2	-7.7	-2.0	-1.7	-2.0	-0.032
17:45	11.5	2.4	31.2	-0.15	10	-7.8	-5.0	-2.0	-5.0	-0.70

4.4.4 Impact of surface temperature prescription in SPARTACUS-Urban

As SPARTACUS-Urban performs well (cf. DART) for both temperature scenarios (Section 4.4.2, 4.4.3), we examine differences between using a single facet temperatures (Section 4.4.2) or a profile ($T_{Profile}$, Section 4.4.3). To ensure the average emission is the same in each, the single temperature SPARTACUS-Urban simulations use weighted mean vertical profiles of T_{Wall} and T_{Roof} (Eq. 7, as for Harman).

There are negligible differences between the $LW_{\uparrow}$ and $LW_{\downarrow}$ within the canopy, for both simulations (Figure 4.9). As the geometry is identical between simulations, the $LW_{In,Roof}$ and $LW_{In,Wall}$ are also the same. The nBE in the $LW_{Out,Roof}$ and $LW_{Out,Wall}$ are small (< -0.2%), but larger for $LW_{Out,Ground}$ (nBE < 4%) (Table 4.4, Figure 4.B.11). The largest nBE are for LW^*_{Wall} (nBE < -3%) and LW^*_{Ground} (nBE < 4.8%). The $LW_{Out,Wall}$ switches from an over- to underestimate in the single T simulation at ~12 m, corresponding to where the single wall temperature over- and then underestimates the T profile. This impacts the LW^*_{Wall} profile. These changes in wall and roof temperature profiles mimic the cumulative profiles in the wall and roof fraction (Figure 4.B.12).

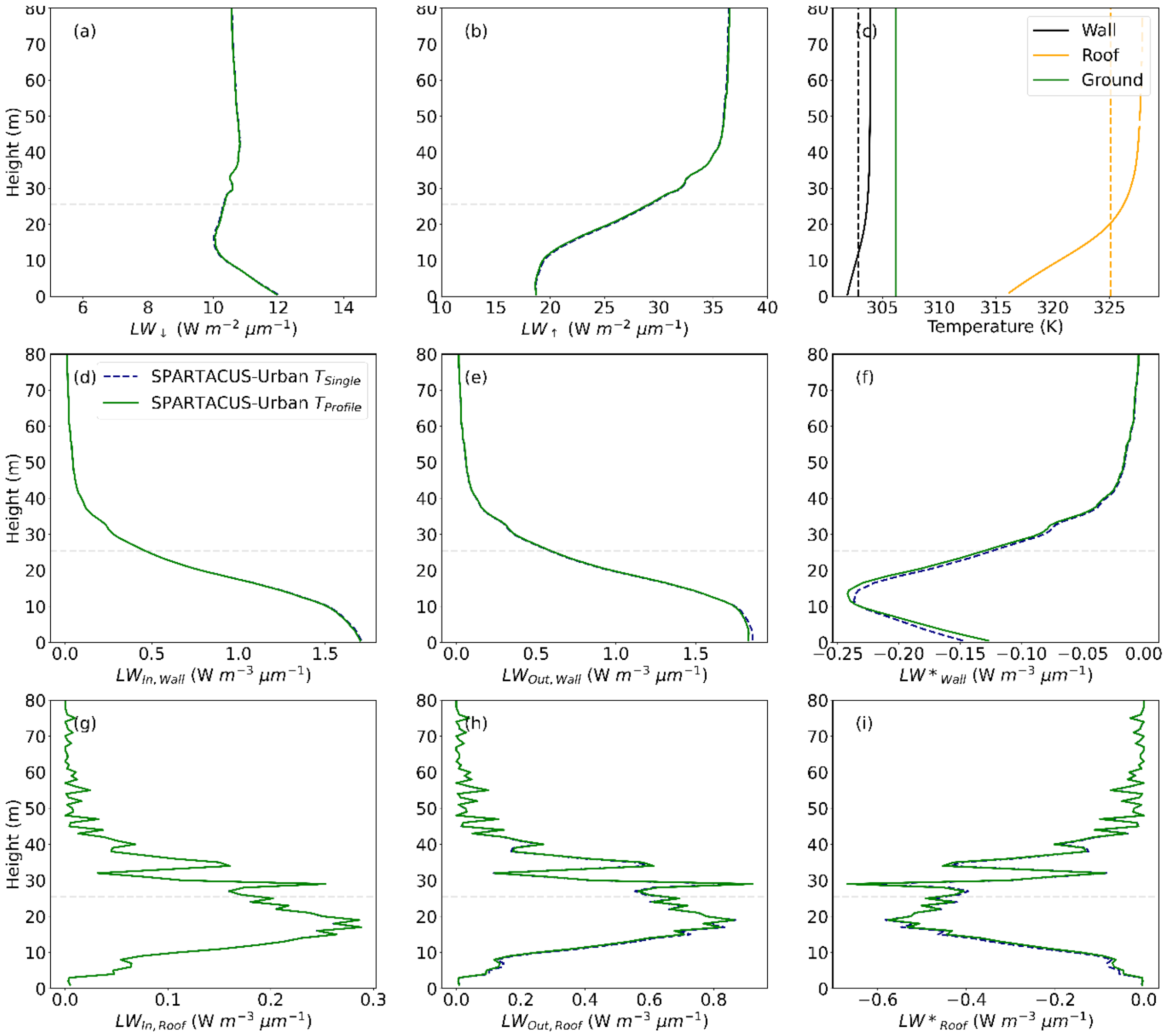

Figure 4.9: Longwave (LW) SPARTACUS-Urban simulations for a 2 km × 2 km domain in central London (Figure 4.1) with an emissivity of 0.93 for 13:45 UTC on the 27th August 2017: (a) downwelling clear air flux ($LW_{\downarrow}$), (b) upwelling clear air flux ($LW_{\uparrow}$), (d-f) wall interception, outgoing and net flux ($LW_{\mathrm{In,Wall}}$, $LW_{\mathrm{Out,Wall}}$, LW^{*}_{Wall}), (g-i) roof interception, outgoing and net flux ($LW_{\mathrm{In,Roof}}$, $LW_{\mathrm{Out,Roof}}$, LW^{*}_{Roof}). Facet temperatures prescribed are (c) a single temperature per facet (T_{Single}, black dashed) and using temperature profiles for each facet type (T_{Profile}, green)

Table 4.4: Comparison between SPARTACUS-Urban simulations for one central London grid-cell (for 27th August) with surface temperature profile assigned based on SW simulations ($T_{Profile}$) and single facet temperatures (T_{Single}), assessed using the normalised bias error (nBE, Eq. 4.8) for upwelling and downwelling clear-air fluxes ($\mathrm{LW}_{\downarrow}$, $\mathrm{LW}_{\uparrow}$), and the total outgoing and net flux into each urban facet (wall, roof, ground, e.g., $\mathrm{LW}_{\mathrm{Out,Wall}}$, $\mathrm{LW}^{*}_{\mathrm{Wall}}$)

Time	$\mathrm{LW}_{\downarrow}$, z = 1		$\mathrm{LW}_{\uparrow}$, $z = H_{max}$		$\mathrm{LW}^{*}_{\mathrm{Wall}}$	$\mathrm{LW}^{*}_{\mathrm{Roof}}$	$\mathrm{LW}^{*}_{\mathrm{Ground}}$	$\mathrm{LW}_{\mathrm{Out,Wall}}$	$\mathrm{LW}_{\mathrm{Out,Roof}}$	$\mathrm{LW}_{\mathrm{Out,Ground}}$
	$\mathrm{T}_{\mathrm{Profile}}$	*nBE* (%)	$\mathrm{T}_{\mathrm{Profile}}$	nBE (%)	nBE (%)	nBE (%)	nBE (%)	nBE (%)	nBE (%)	nBE (%)
7:45	11.0	0	29.0	0	-1.7	0.036	2.9	0.031	2.9	1.0
9:45	11.5	0	33.2	0	-1.9	0.063	1.2	-0.017	1.2	0.65
11:45	11.9	0	36.4	0	0.43	-0.072	-4.1	-0.12	-4.1	-1.2
13:45	12.0	0	36.7	0	-1.4	0.0045	-0.54	-0.11	-3.7	-1.1
17:45	11.7	0	31.1	0	-3.0	0.29	4.8	-0.054	-0.54	0.067

4.5 Comparison with the Harman et al. (2004) approach

Finally, SPARTACUS-Urban, DART and Harman et al. (2004) are applied to a case with an infinitely long canyon surrounded by buildings of equal height, with area-weighted SPARTACUS-Urban temperature profiles used in Harman (Eq. 4.7). For the more realistic temperature configurations, SPARTACUS-Urban single-layer and Harman have similar run-times (Table 4.5). This increases by a factor of 10^2 when realistic geometry is used in SPARTACUS-Urban. The full-temperature DART runs are 10^7 times slower than the most complex SPARTACUS-Urban simulations.

For single surface temperatures per facet simulations (cf. temperature profile), $\mathrm{LW}_{\uparrow}$ at the top-of canopy (H_{max}) Harman et al. (2004) is more similar to DART, with 5:45 UTC approximately equal (Figure 4.10). The poorest Harman - DART agreement is for $\mathrm{LW}_{\mathrm{In,Roof}}$ and $\mathrm{LW}^{*}_{\mathrm{Wall}}$. Although, at 5:45 UTC, the nBE $\mathrm{LW}^{*}_{\mathrm{Wall}}$ is approximately the same for SPARTACUS-Urban and Harman (Figure 4.10). This may be because no walls exist above $\overline{H}$, so roofs cannot intercept radiation from above, leading to an underestimate in $\mathrm{LW}_{\mathrm{In,Roof}}$. When DART simulations use a T range, the Harman performance is similar to the single facet T simulations (Figure 4.11). However, the nBE are generally higher, except for the $\mathrm{LW}^{*}_{\mathrm{Roof}}$ and the $\mathrm{LW}_{\mathrm{Wall}}$ fluxes (e.g., 13:45 UTC).

Generally, SPARTACUS-Urban agrees more closely to DART than Harman et al. (2004). In the varied facet T simulations, SPARTACUS-Urban and Harman approach are similar for $\mathrm{LW}_{\uparrow}$ and $\mathrm{LW}_{\mathrm{In,Roof}}$, with nBE < 3%. The two models are similar for $\mathrm{LW}_{\mathrm{Out,Ground}}$ and $\mathrm{LW}_{\mathrm{Out,Wall}}$ throughout the day, with the smallest nBE (Figure 4.B.13-Figure 4.B.14). Largest differences are seen for $\mathrm{LW}^{*}_{\mathrm{Ground}}$ (SPARTACUS nBE 2-5%, cf. Harman nBE > 20%) and $\mathrm{LW}^{*}_{\mathrm{Wall}}$ (SPARTACUS nBE 0-10% cf. 8-16%).

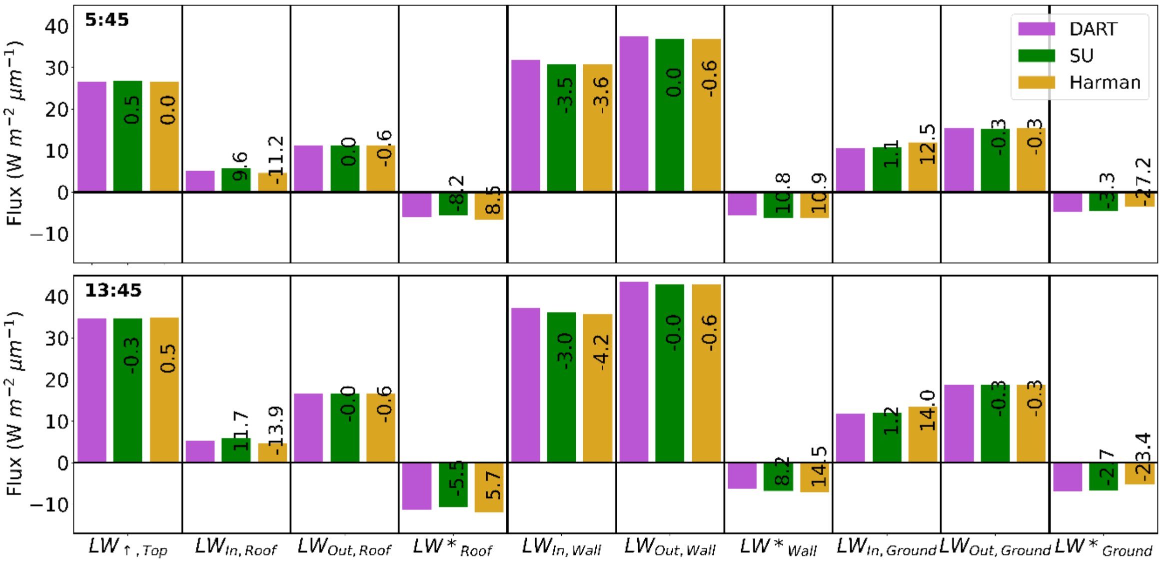

Figure 4.10: Comparison of simulations for one grid-cell in central London on 27th August using nBE (values, Eq. 4.8) relative to realistic world DART, for SPARTACUS-Urban (SU) and Harman et al. (2004) longwave fluxes with isothermal facet temperatures (Section 4.3.3): upwelling clear air flux at the top of the canopy ($LW_{\uparrow}$), and the roof, wall, and ground total interception, outgoing, and net flux, for two times (rows)

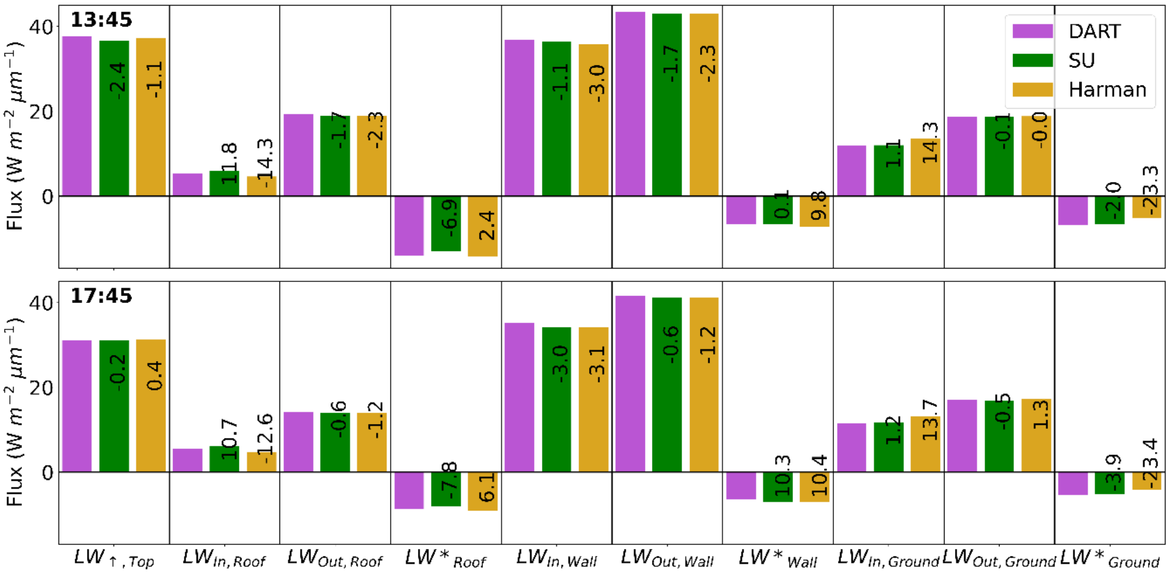

Figure 4.11: Comparison of simulations for one grid-cell in central London on 27th August using nBE (values, Eq. 4.8) relative to realistic world DART, for SPARTACUS-Urban (SU) and Harman et al. (2004) longwave fluxes with facet temperatures prescribed based on SW simulations (Section 4.3.3), upwelling clear air flux at the top of the canopy ($LW_{\uparrow}$), and the roof, wall, and ground total interception, outgoing, and net flux, for two times (rows)

Table 4.5: Absolute run-time of Harman (Section 4.2.3), SPARTACUS-Urban (open-source version 0.7.3 compiled with gfortran, O3 optimization), and DART (version 5.7.5 build number 1126) for simulations with *n* vertical layers, and *N* diffuse streams per hemisphere. All runs undertaken in a Linux environment on a dual Xeon E5-2667 v3 processor with 256 GB of RAM, with a single-thread for Harman and SPARTACUS-Urban, but for DART 14 parallel threads using 32 CPU

Model	*n*	*N*	Time (s)	Time relative to Harman
Harman	1	-	2×10^{-5}	-
SPARTACUS-Urban	1	8	3×10^{-5}	1.5
	6	8	4×10^{-4}	20
	151	1	2×10^{-3}	100
	151	4	2×10^{-3}	100
	151	8	2×10^{-3}	100
DART	151	-	6.6×10^{4}	3.3×10^{9}

4.6 Conclusions

Here, the longwave capabilities of the multi-layer radiative transfer model SPARTACUS-Urban are assessed using the explicit radiative transfer model, DART. DART resolves radiative interactions between individual facets of buildings, whereas SPARTACUS-Urban models the mean radiation field with height using building fraction and wall area at each height. Real-world geometry is considered using prescribed categorised observed surface temperatures (*T*) measured in London (Morrison et al. 2020, 2021).

Longwave (LW) fluxes are predicted well when one surface *T* is prescribed per facet type (or sub-facet, e.g., wall orientation). The clear-air upwelling and downwelling fluxes are predicted well, although there is some disagreement in the mid-canopy. SPARTACUS-Urban underestimates the net LW roof flux (normalised bias errors (nBE) -5.5 – -8.2%), suggesting too much emission from surrounding walls. Errors in this configuration could be from the SPARTACUS-Urban geometry assumptions, or the wall-temperature averaging methods.

Similar agreement is found when facets are prescribed a temperature range based on shortwave simulations. The clear-air fluxes are in good agreement, with nBE < 3% for all times assessed. The net wall LW is overestimated (nBE ≤ 10%) at times with low intra-facet temperature variability (e.g., early morning and evening). Roof interception also is overestimated nearer the ground, leading to an underestimation in the net roof LW. However, all nBE < 11%. This suggests the average *T* profiles, informed by shortwave geometry are acceptable approximations of the true *T* field. However, we note the sub-facet wall *T* range is small, which may differ in different conditions (e.g. atmospheric, geometry).

SPARTACUS-Urban outperforms the frequently used infinite street canyon approach (Harman et al. 2004) (cf. DART). Both are similar if single *T* facets are used, except for the intercepted roof and net wall LW, when SPARTACUS-Urban is better. When using a facet temperature range the performance for both models is poorer. Harman notably underestimates roof interception, most likely linked to the absence of downward emission from walls higher in the canopy, given all are same height.

The impact of vertically varying *T* is small to SPARTACUS-Urban, with little impact on the net LW fluxes. However, only one summer day in central London is considered, possibly with small variations in wall *T*. In other geometries or climates (e.g., subtropical city with taller buildings), the impact of *T* profile (single, varied) application on the results still needs to be assessed and could be explored in future research.

Overall, this offline evaluation suggests SPARTACUS-Urban's longwave fluxes agree well relative to the more complex, computationally and data demanding DART model. Alongside the evaluation of SPARTACUS-Urban for shortwave radiation (Stretton et al. 2022), good model performance is shown here, indicating it is suitable for implementing into a multi-layer urban model. Testing is underway with SPARTACUS-Urban coupled to the Surface Urban Energy and Water balance Scheme (SUEWS, Järvi et al. (2011, 2014); Ward et al. (2016); Omidvar et al. (2022)), to predict the vertical profile of fluxes, surface temperatures, and heat stress metrics within the canopy, with future work including an online evaluation of SPARTACUS-Urban within SUEWS. Further, comparisons could be made between existing single- and multi-layer urban radiative transfer schemes, such as done in the RAMI intercomparison for vegetation (Widlowski et al. 2015), or urban energy balance intercomparisons (Grimmond et al. 2010b, 2011; Lipson et al. 2023). Such models require high resolution building geometry information (i.e., vertical descriptions of the urban canopy), which are unavailable for most cities. Therefore, to supplement these implementations an assessment should be made on how realistically available data influences model outputs, e.g., vertically distributed fluxes and temperatures.

Acknowledgements

The authors acknowledge the funding and support from the Scenario NERC Doctoral Training Partnership Grant, EPSRC 2130186, EPRSC DARE EP/P002331/1, ERC Synergy *urbisphere (855005)*, and Newton Fund/Met Office CSSP China NGC.

Data availability statement

The Fortran SPARTACUS-Surface package is available under an open-source license from https://github.com/ecmwf/spartacus-surface. The DART model is available from https://dart.omp.eu. All code and data used for this study are archived at 10.5281/zenodo.6798640

Appendix 4.A: Determining temperature profiles for SPARTACUS-Urban

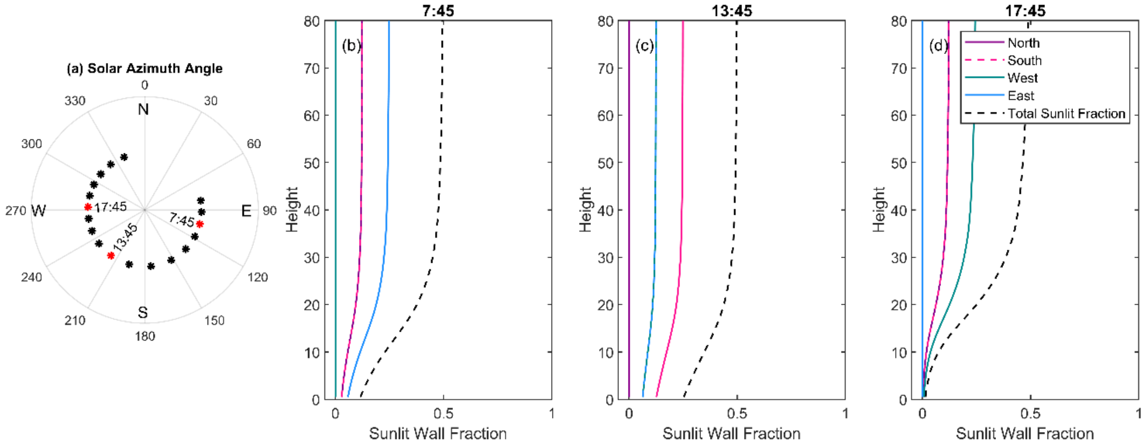

Figure 4.A.1: Demonstration of the T_{Wall} averaging method used for SPARTACUS-Urban simulations (Section 4.3.3). Wall types are weighted using (a) solar azimuth angle for each time as in Eq. 4.4 and Eq. 4.5, resulting in (b-d) sunlit fraction profiles for each time step that are used to weight the sunlit-shaded temperatures (Figure 4.3) to determine profiles in Figure 5. Red scatter in (a) shows azimuth angle of times used in further panels

Appendix 4.B: Additional comparisons between SPARTACUS-Urban and DART

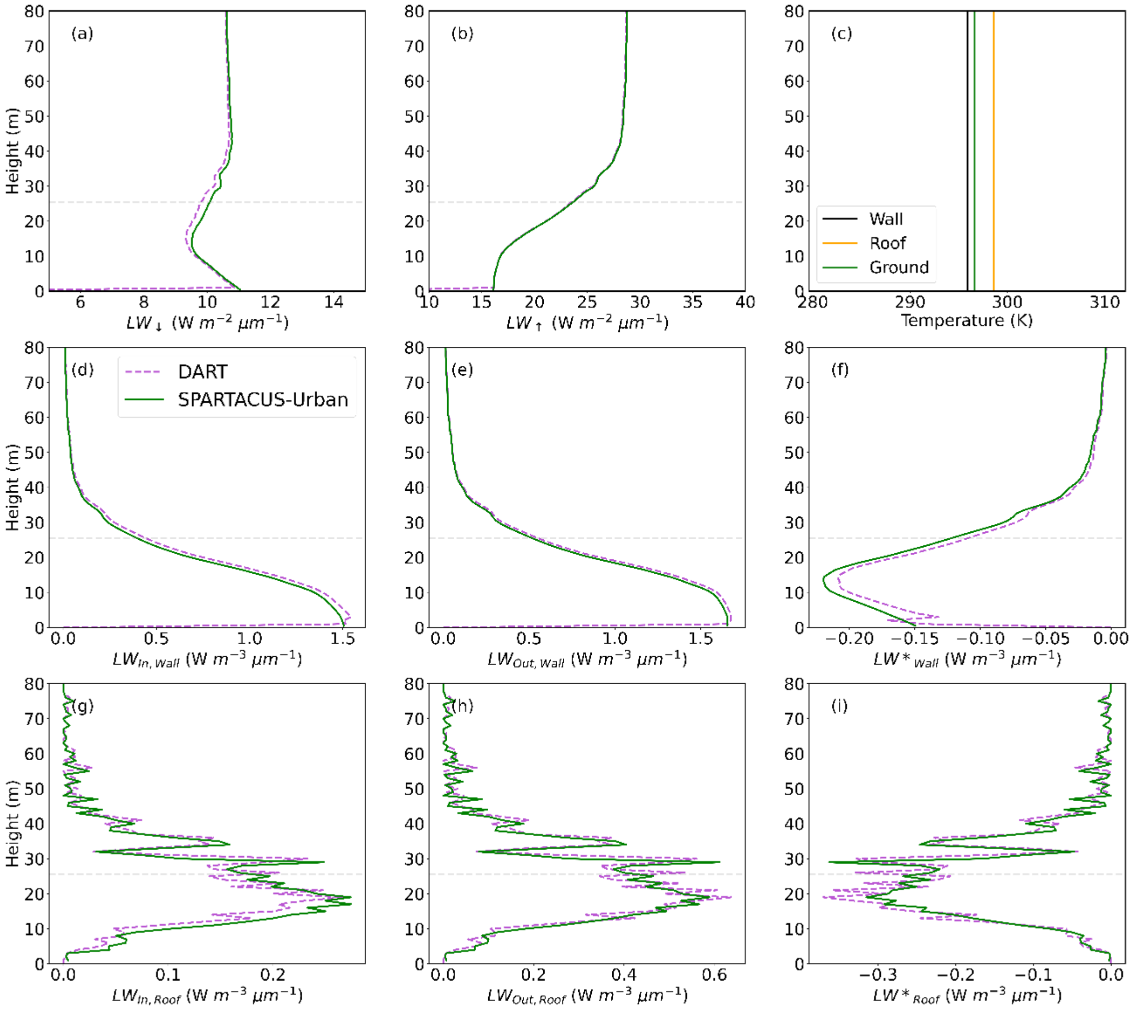

Figure 4.B.1: Longwave fluxes (LW) for a 2 km × 2 km domain in central London (Figure 4.1) simulated with SPARTACUS-Urban (green) and DART (purple) with an emissivity of 0.93 at 7:45 UTC on the 27th August 2017 with (c) single facet *T*: (a) downwelling clear air flux ($LW_{\downarrow}$), (b) upwelling clear air flux ($LW_{\uparrow}$), (d-f) wall interception, outgoing and net flux ($LW_{In,Wall}$, $LW_{Out,Wall}$, LW^{*}_{Wall}), (g,-i) roof interception, outgoing and net flux ($LW_{In,Roof}$, $LW_{Out,Roof}$, LW^{*}_{Roof}). Prescribed facet temperatures using: a single temperature per surface type for DART, and (c) single temperatures per facet type for SPARTACUS-Urban

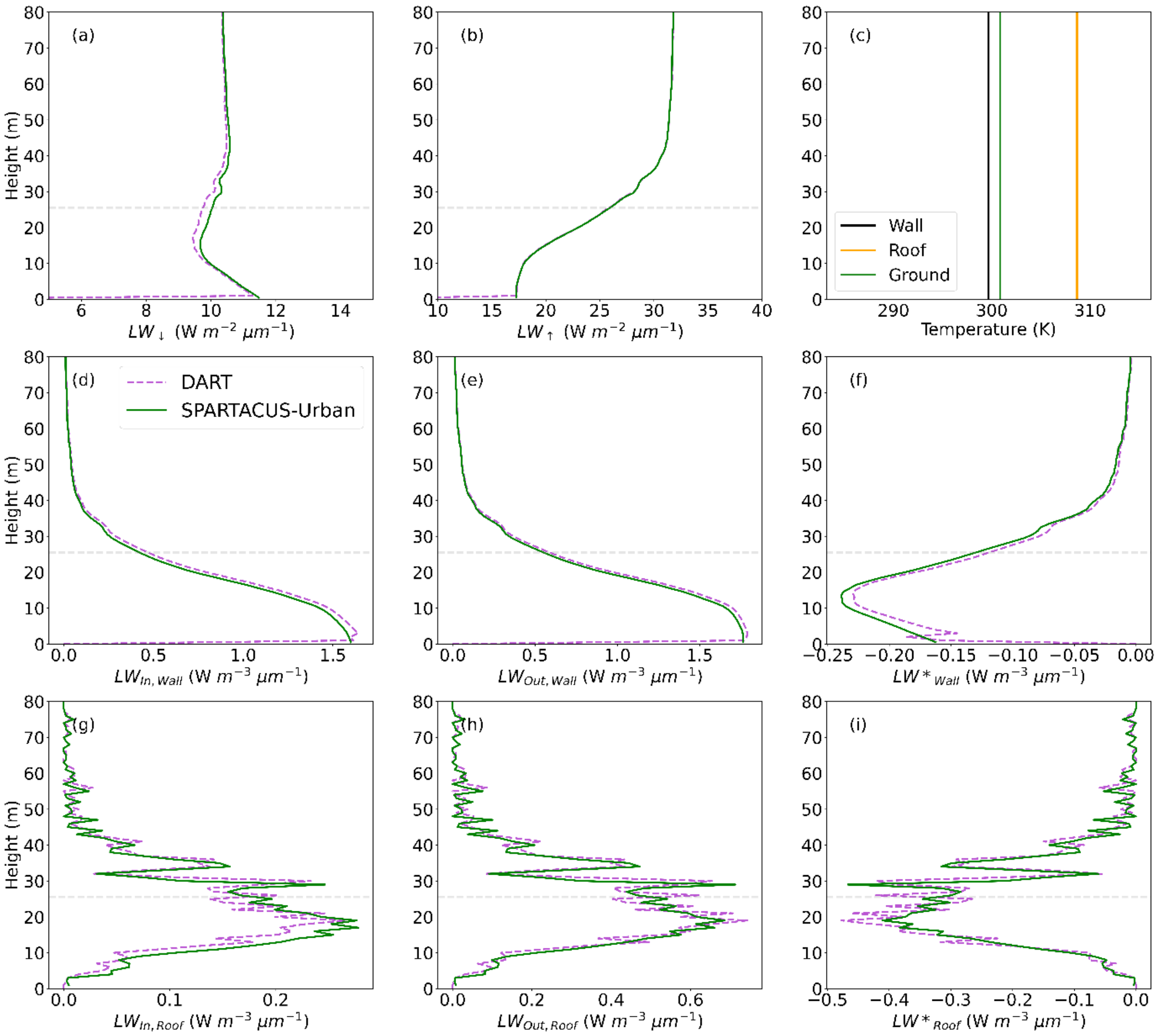

Figure 4.B.2*:* Longwave fluxes (LW) for a 2 km × 2 km domain in central London (Figure 4.1) simulated with SPARTACUS-Urban (green) and DART (purple) with an emissivity of 0.93 at 9:45 UTC on the 27th August 2017 with (c) single facet *T*: (a) downwelling clear air flux ($LW_\downarrow$), (b) upwelling clear air flux ($LW_\uparrow$), (d-f) wall interception, outgoing and net flux ($LW_{In,Wall}$, $LW_{Out,Wall}$, $LW*_{Wall}$), (g-i) roof interception, outgoing and net flux ($LW_{In,Roof}$, $LW_{Out,Roof}$, $LW*_{Roof}$). Prescribed facet temperatures using: a single temperature per surface type for DART, and (c) single temperatures per facet type for SPARTACUS-Urban

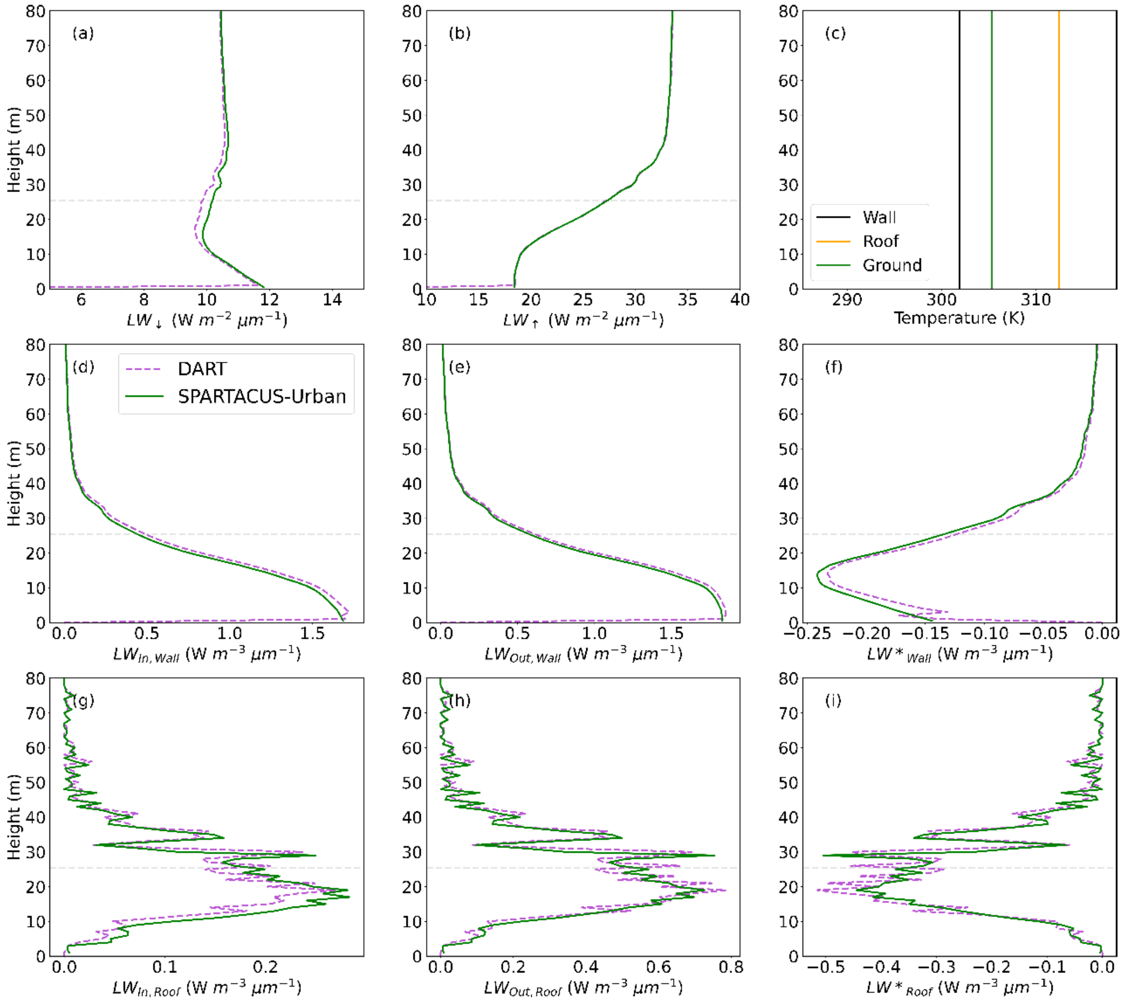

Figure 4.B.3*:* Longwave fluxes (LW) for a 2 km × 2 km domain in central London (Figure 4.1) simulated with SPARTACUS-Urban (green) and DART (purple) with an emissivity of 0.93 at 11:45 UTC on the 27th August 2017 with (c) single facet *T*: (a) downwelling clear air flux ($LW_{\downarrow}$), (b) upwelling clear air flux ($LW_{\uparrow}$), (d-f) wall interception, outgoing and net flux ($LW_{\text{In,Wall}}$, $LW_{\text{Out,Wall}}$, LW^{*}_{Wall}), (g-i) roof interception, outgoing and net flux ($LW_{\text{In,Roof}}$, $LW_{\text{Out,Roof}}$, LW^{*}_{Roof}). Prescribed facet temperatures using: a single temperature per surface type for DART, and (c) single temperatures per facet type for SPARTACUS-Urban

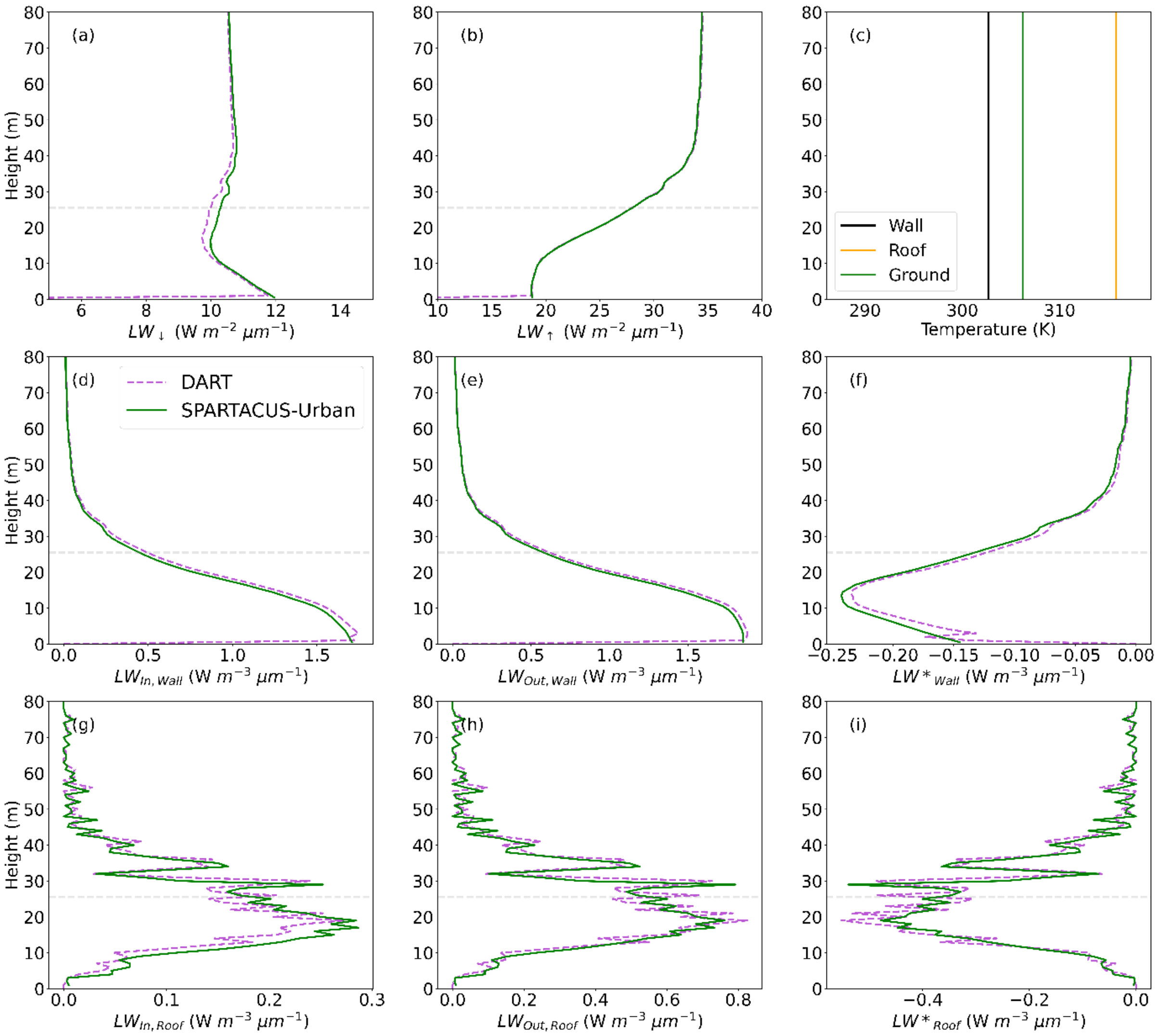

Figure 4.B.4: Longwave fluxes (LW) for a 2 km × 2 km domain in central London (Figure 4.1) simulated with SPARTACUS-Urban (green) and DART (purple) with an emissivity of 0.93 at 13:45 UTC on the 27th August 2017 with (c) single facet T: (a) downwelling clear air flux ($LW_\downarrow$), (b) upwelling clear air flux ($LW_\uparrow$), (d-f) wall interception, outgoing and net flux ($LW_{In,Wall}$, $LW_{Out,Wall}$, $LW*_{Wall}$), (g-i) roof interception, outgoing and net flux ($LW_{In,Roof}$, $LW_{Out,Roof}$, $LW*_{Roof}$). Prescribed facet temperatures using: a single temperature per surface type for DART, and (c) single temperatures per facet type for SPARTACUS-Urban

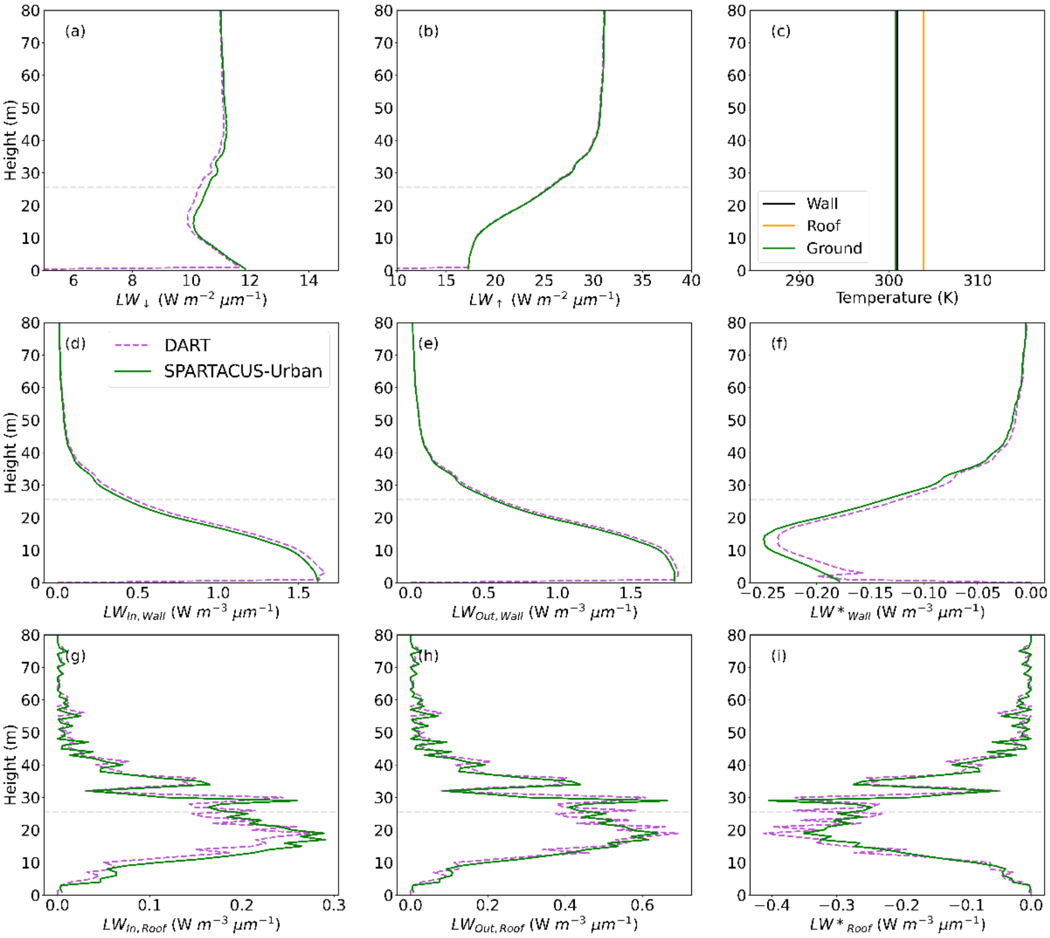

Figure 4.B.5*:* Longwave fluxes (LW) for a 2 km × 2 km domain in central London (Figure 4.1) simulated with SPARTACUS-Urban (green) and DART (purple) with an emissivity of 0.93 at 17:45 UTC on the 27th August 2017 with (c) single facet *T*: (a) downwelling clear air flux ($LW_\downarrow$), (b) upwelling clear air flux ($LW_\uparrow$), (d-f) wall interception, outgoing and net flux ($LW_{In,Wall}$, $LW_{Out,Wall}$, $LW*_{Wall}$), (g-i) roof interception, outgoing and net flux ($LW_{In,Roof}$, $LW_{Out,Roof}$, $LW*_{Roof}$). Prescribed facet temperatures using: a single temperature per surface type for DART, and (c) single temperatures per facet type for SPARTACUS-Urban.

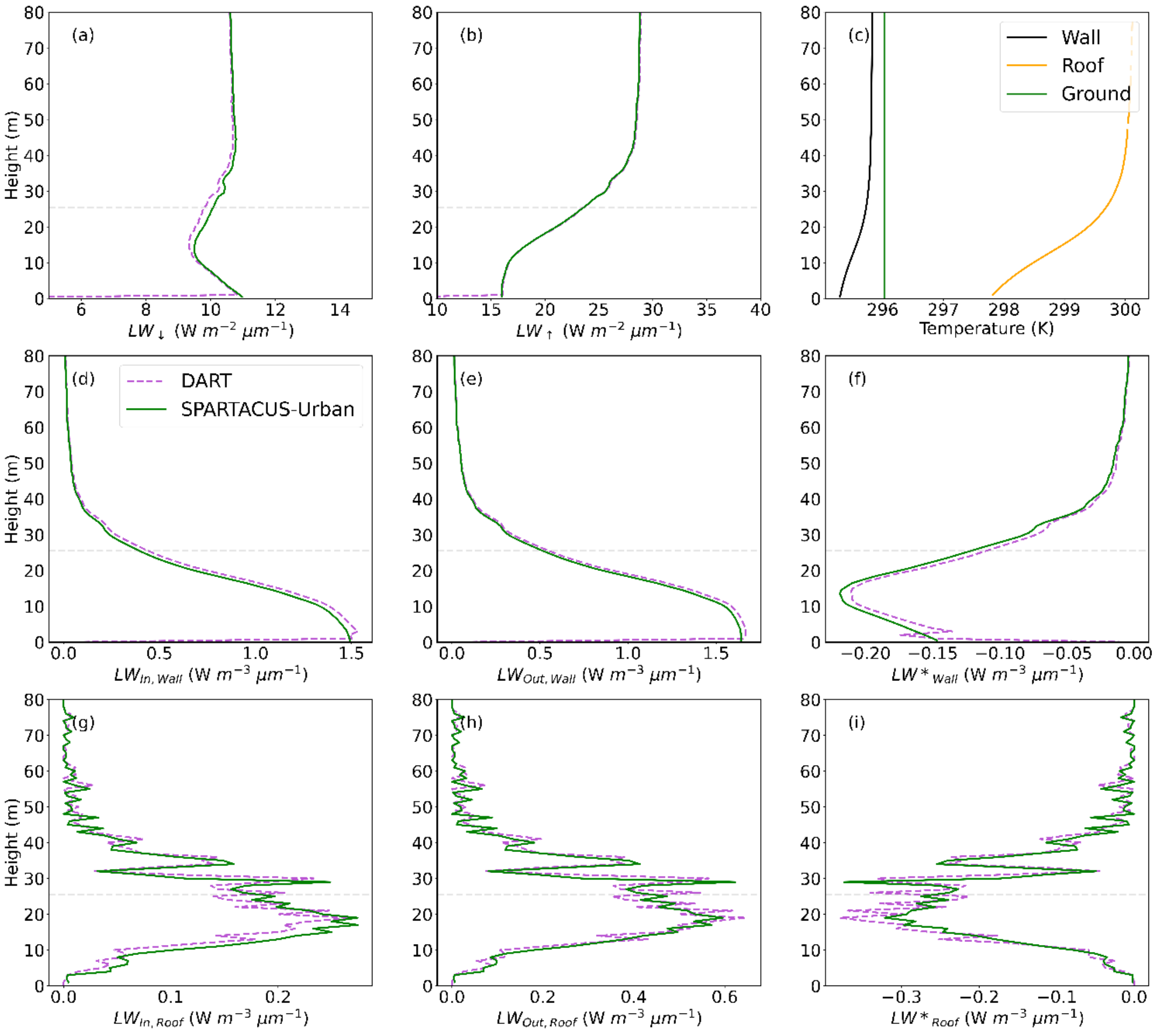

Figure 4.B.6: Longwave fluxes (LW) for a 2 km × 2 km domain in central London (Figure 4.1) simulated with SPARTACUS-Urban (green) and DART (purple) with an emissivity of 0.93 at 7:45 UTC on the 27th August 2017: (a) downwelling clear air flux ($LW_{\downarrow}$), (b) upwelling clear air flux ($LW_{\uparrow}$), (d-f) wall interception, outgoing and net flux ($LW_{In,Wall}$, $LW_{Out,Wall}$, $LW*_{Wall}$), (g-i) roof interception, outgoing and net flux ($LW_{In,Roof}$, $LW_{Out,Roof}$, $LW*_{Roof}$). Prescribed facet temperatures based on SW simulations at 7:45 using: a full 3D temperature field for DART, and (c) temperature profiles per facet type for SPARTACUS-Urban.

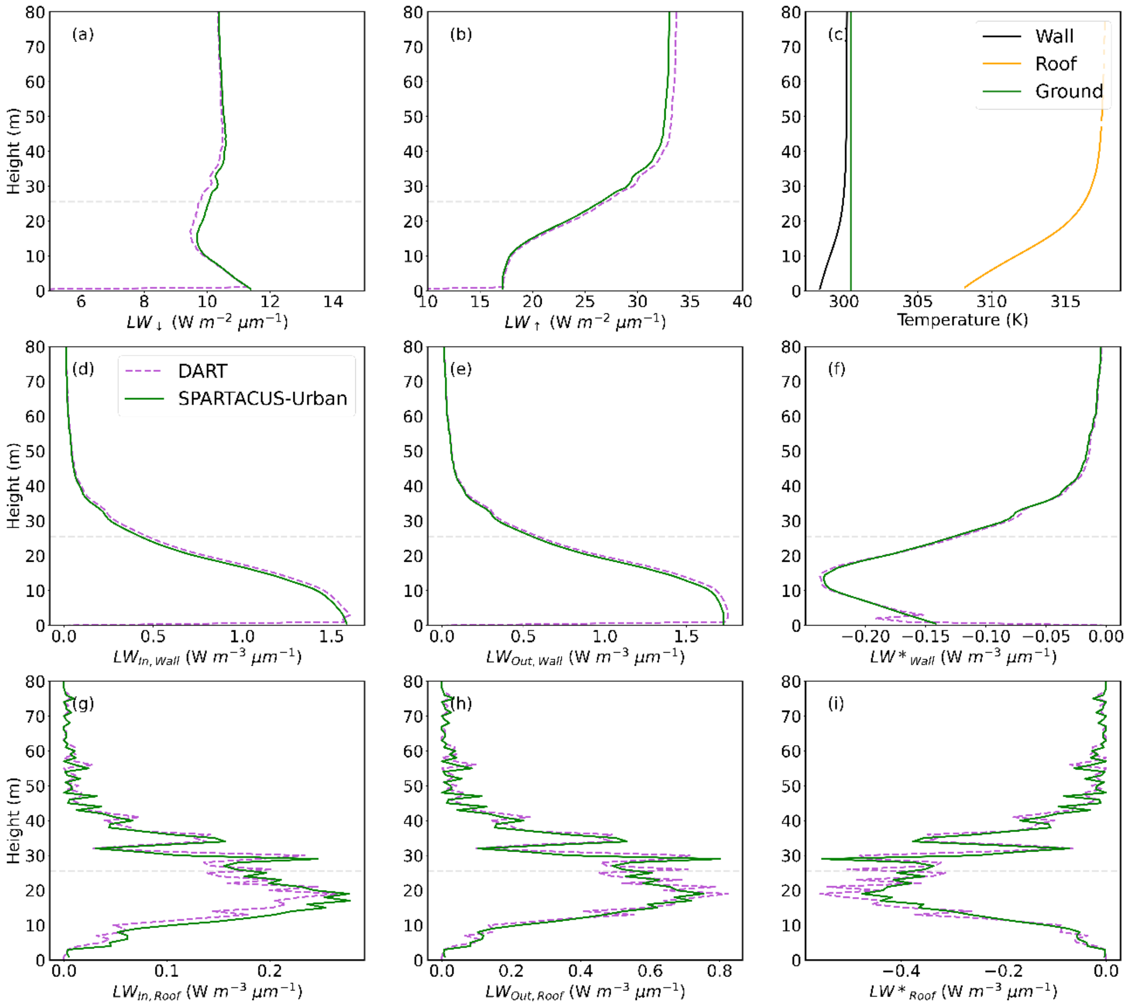

Figure 4.B.7: Longwave fluxes (LW) for a 2 km × 2 km domain in central London (Figure 4.1) simulated with SPARTACUS-Urban (green) and DART (purple) with an emissivity of 0.93 at 9:45 UTC on the 27th August 2017: (a) downwelling clear air flux ($LW_\downarrow$), (b) upwelling clear air flux ($LW_\uparrow$), (d-f) wall interception, outgoing and net flux ($LW_{In,Wall}$, $LW_{Out,Wall}$, $LW*_{Wall}$), (g-i) roof interception, outgoing and net flux ($LW_{In,Roof}$, $LW_{Out,Roof}$, $LW*_{Roof}$). Prescribed facet temperatures based on SW simulations at 9:45 using: a full 3D temperature field for DART, and (c) temperature profiles per facet type for SPARTACUS-Urban

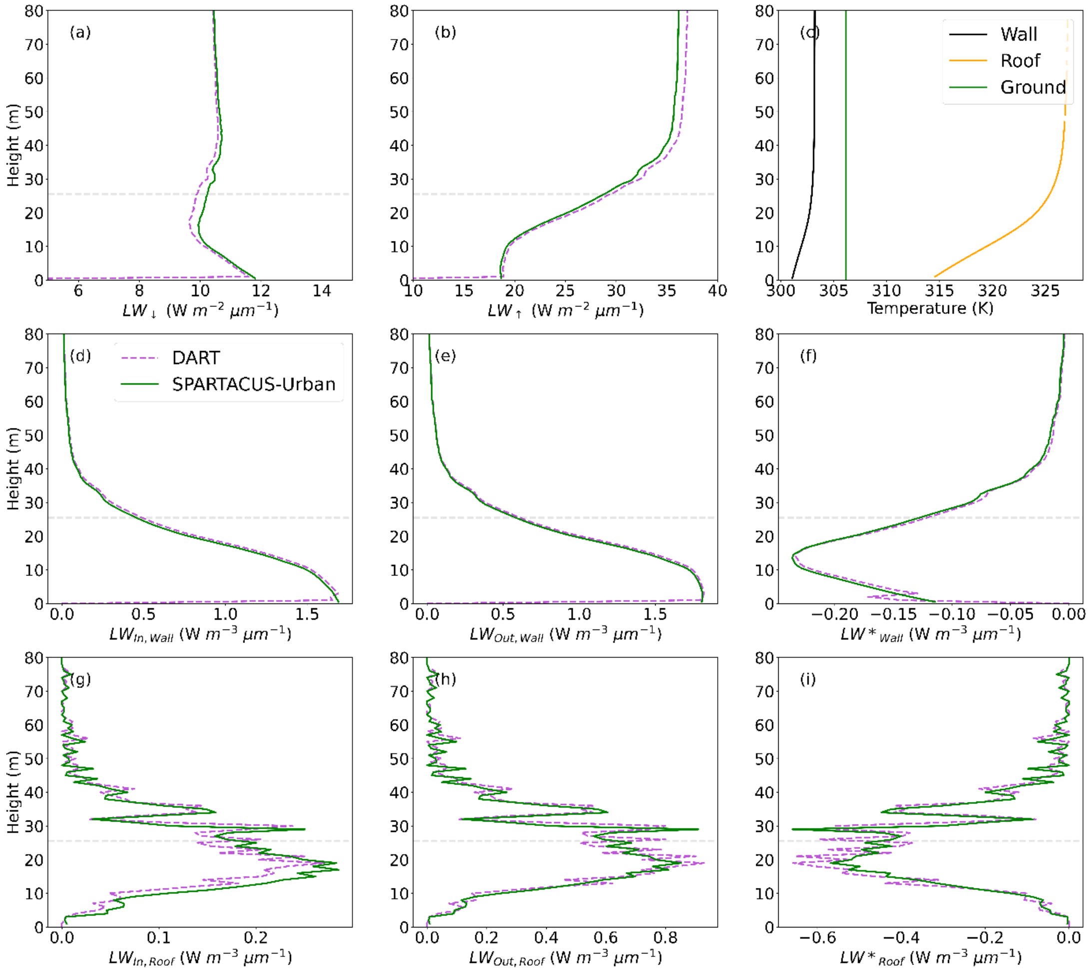

Figure 4.B.8: Longwave fluxes (LW) for a 2 km × 2 km domain in central London (Figure 4.1) simulated with SPARTACUS-Urban (green) and DART (purple) with an emissivity of 0.93 at 11:45 UTC on the 27th August 2017: (a) downwelling clear air flux ($LW_{\downarrow}$), (b) upwelling clear air flux ($LW_{\uparrow}$), (d-f) wall interception, outgoing and net flux ($LW_{In,Wall}$, $LW_{Out,Wall}$, $LW*_{Wall}$), (g-i) roof interception, outgoing and net flux ($LW_{In,Roof}$, $LW_{Out,Roof}$, $LW*_{Roof}$). Prescribed facet temperatures based on SW simulations at 11:45 using: a full 3D temperature field for DART, and (c) temperature profiles per facet type for SPARTACUS-Urban

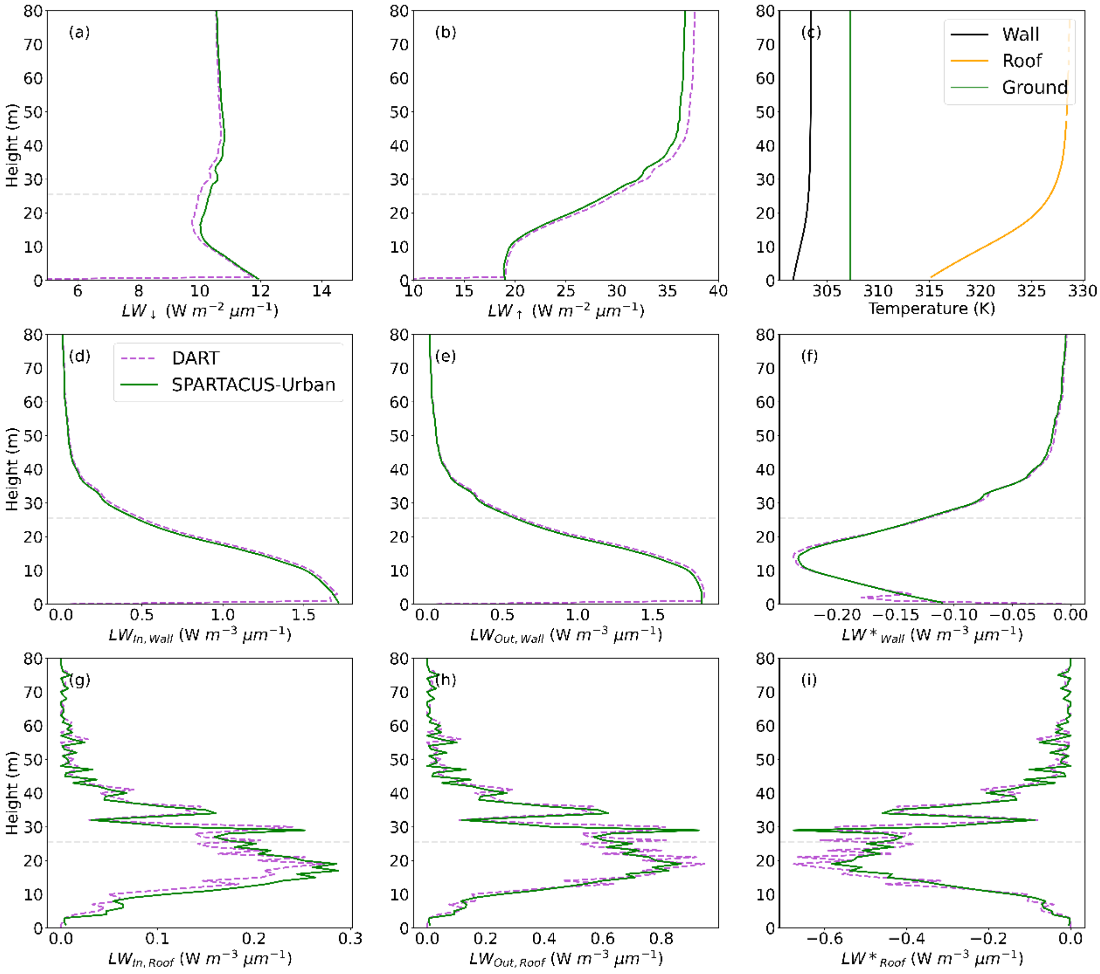

Figure 4.B.9: Longwave fluxes (LW) for a 2 km × 2 km domain in central London (Figure 4.1) simulated with SPARTACUS-Urban (green) and DART (purple) with an emissivity of 0.93 at 12:45 UTC on the 27th August 2017: (a) downwelling clear air flux ($LW_{\downarrow}$), (b) upwelling clear air flux ($LW_{\uparrow}$), (d-f) wall interception, outgoing and net flux ($LW_{In,Wall}$, $LW_{Out,Wall}$, $LW*_{Wall}$), (g-i) roof interception, outgoing and net flux ($LW_{In,Roof}$, $LW_{Out,Roof}$, $LW*_{Roof}$). Prescribed facet temperatures based on SW simulations at 12:45 using: a full 3D temperature field for DART, and (c) temperature profiles per facet type for SPARTACUS-Urban

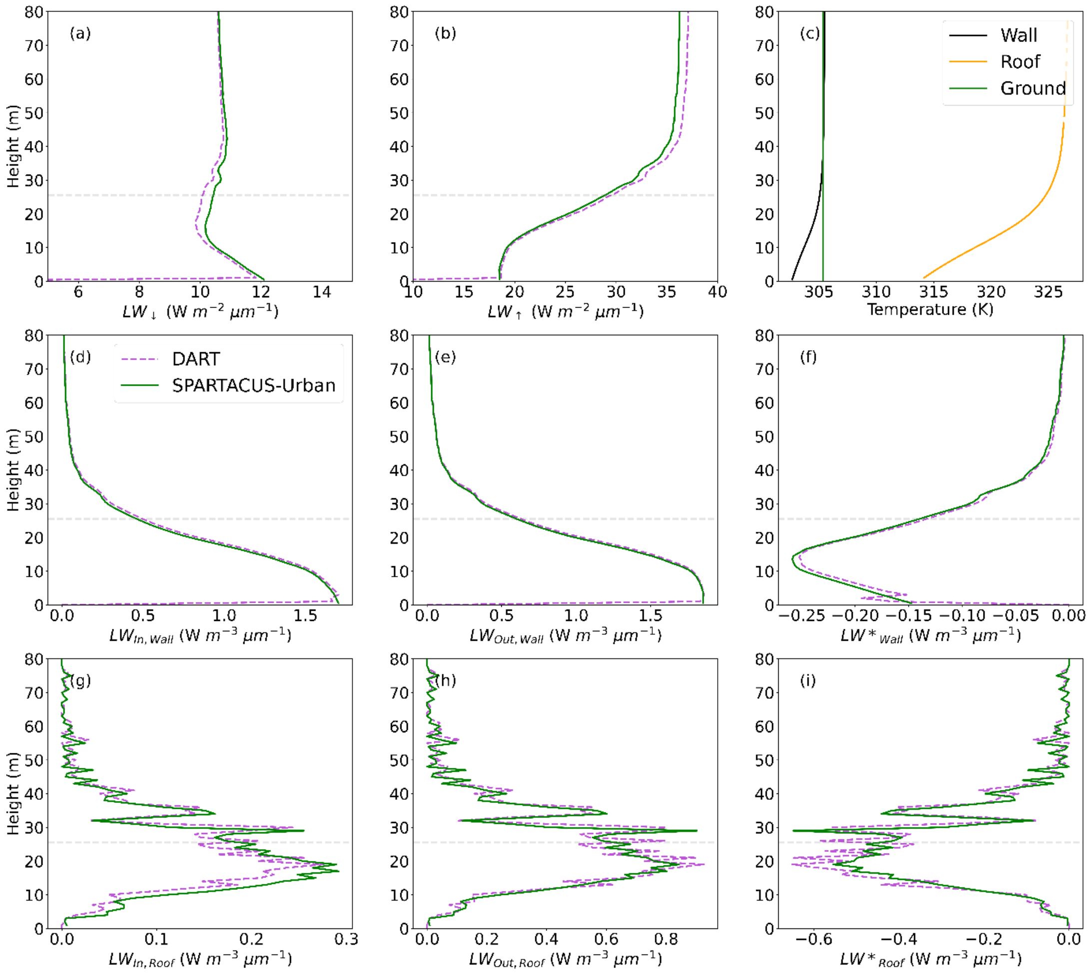

Figure 4.B.10: Longwave fluxes (LW) for a 2 km × 2 km domain in central London (Figure 4.1) simulated with SPARTACUS-Urban (green) and DART (purple) with an emissivity of 0.93 at 14:45 UTC on the 27th August 2017: (a) downwelling clear air flux ($LW_{\downarrow}$), (b) upwelling clear air flux ($LW_{\uparrow}$), (d-f) wall interception, outgoing and net flux ($LW_{In,Wall}$, $LW_{Out,Wall}$, $LW*_{Wall}$), (g-i) roof interception, outgoing and net flux ($LW_{In,Roof}$, $LW_{Out,Roof}$, $LW*_{Roof}$). Prescribed facet temperatures based on SW simulations at 14:45 using: a full 3D temperature field for DART, and (c) temperature profiles per facet type for SPARTACUS-Urban

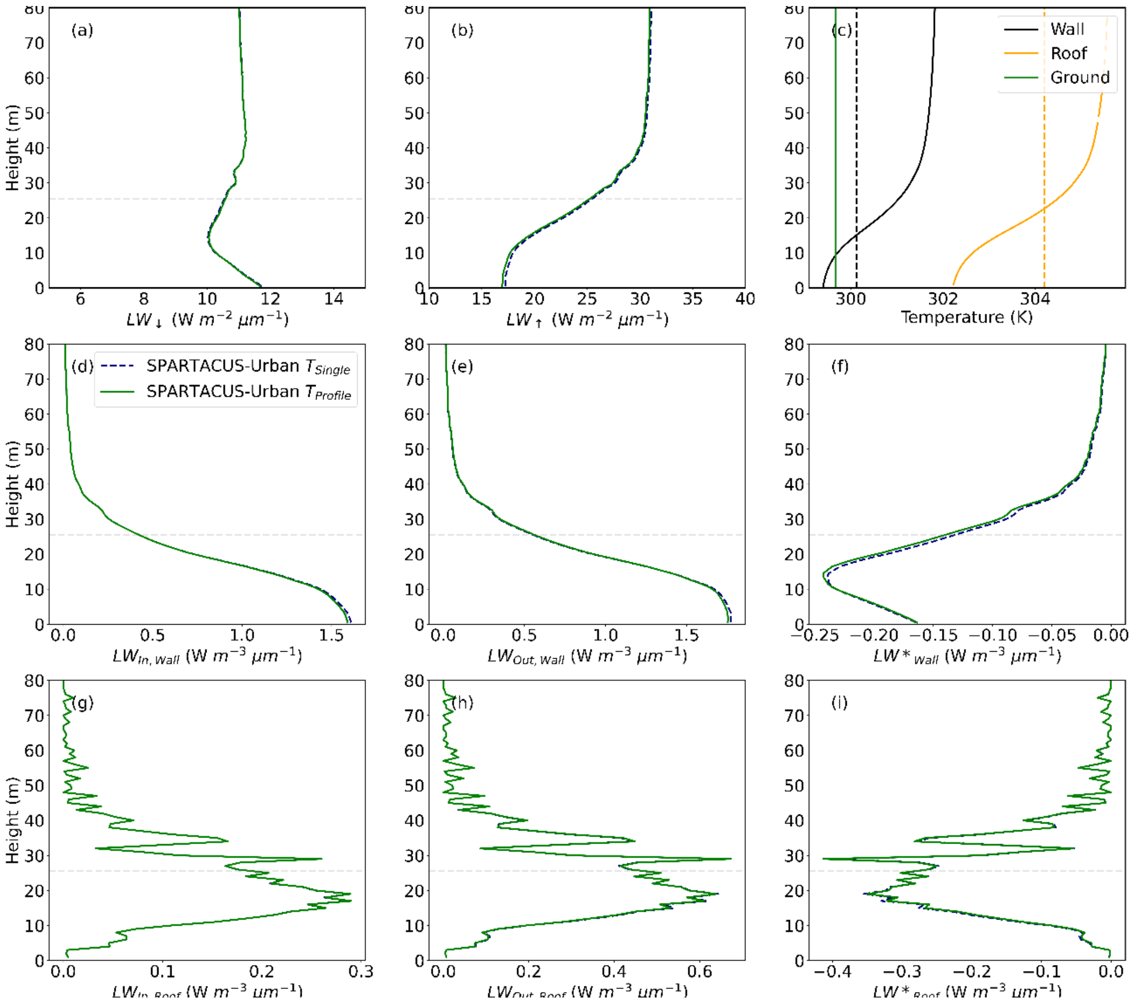

Figure 4.B.11: Longwave (LW) SPARTACUS-Urban simulations for a 2 km × 2 km domain in central London (Figure 4.1) with an emissivity of 0.93 for 17:45 UTC on the 27th August 2017 for: (a) downwelling clear air flux ($LW_{\downarrow}$), (b) upwelling clear air flux ($LW_{\uparrow}$), (d-f) wall interception, outgoing and net flux ($LW_{In,Wall}$, $LW_{Out,Wall}$, LW^{*}_{Wall}), (g-i) roof interception, outgoing and net flux ($LW_{In,Roof}$, $LW_{Out,Roof}$, LW^{*}_{Roof}). Facet temperatures prescribed are (c) a single temperature per facet (T_{Single}, black dashed) and using temperature profiles for each facet type ($T_{Profile}$, green)

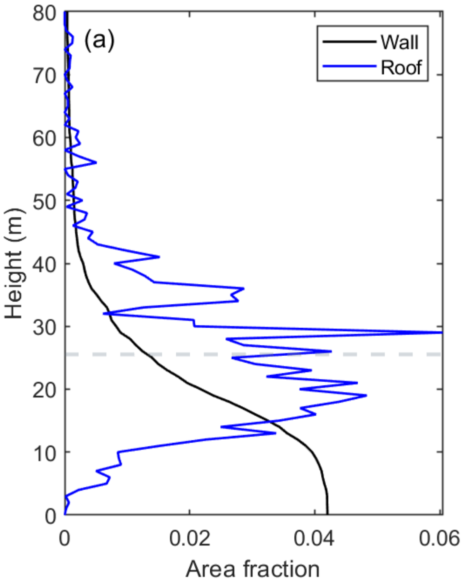

Figure 4.B.12: Vertical profiles for a 2 km × 2 km domain in central London of (a) fractional wall (black) and roof (blue) area and (b) cumulative fraction. Dashed grey lines denote the mean building height. Dotted blue and grey lines show the heights where cumulative fraction reaches 50%

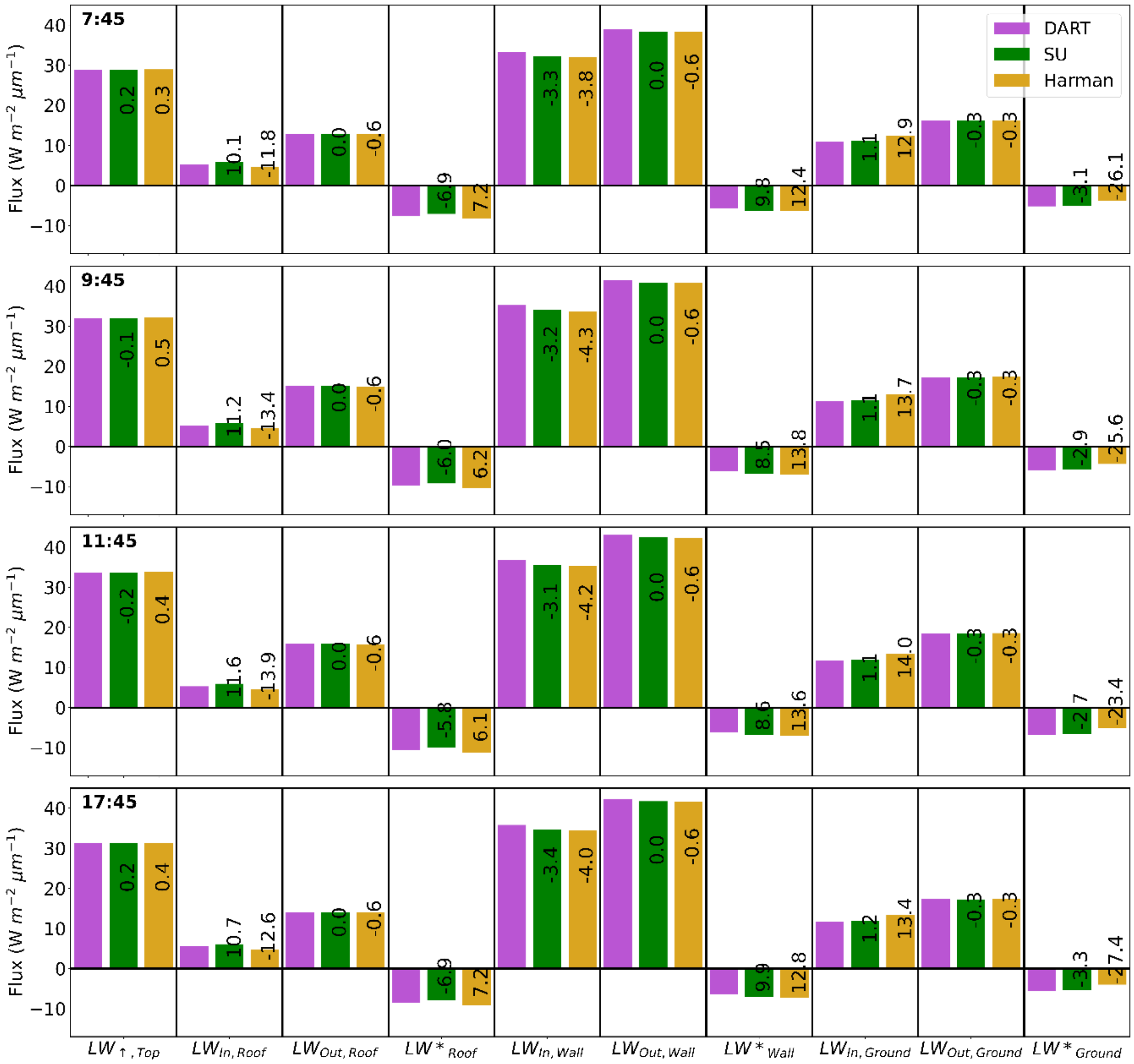

Figure 4.B.13: Comparison of simulations for one grid-cell in central London on 27th August using nBE (values, Eq. 4.8) relative to realistic world DART, for SPARTACUS-Urban (SU) and Harman et al. (2004) longwave fluxes with isothermal facet temperatures (Section 4.3.3): upwelling clear air flux at the top of the canopy ($LW_{\uparrow}$), and the roof, wall, and ground total interception, outgoing, and net flux, for four times (rows)

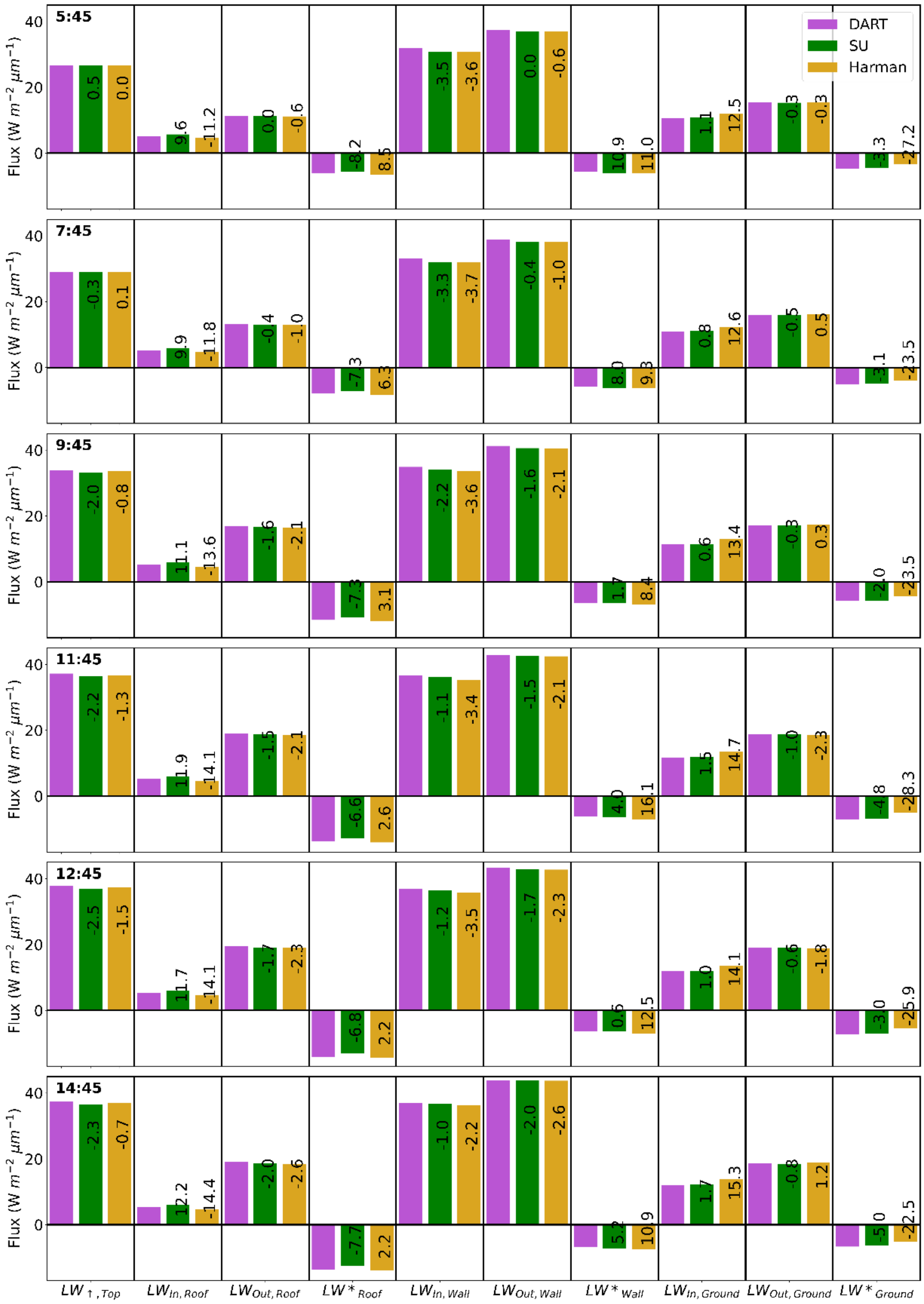

Figure 4.B.14*:* Comparison of simulations for one grid-cell in central London on 27th August using nBE (values, Eq. 4.8) relative to realistic world DART, for SPARTACUS-Urban (SU) and Harman et al. (2004) longwave fluxes with facet temperatures prescribed based on SW simulations (Section 4.3.3), upwelling clear air flux at the top of the canopy ($LW_{\uparrow}$), and the roof, wall, and ground total interception, outgoing, and net flux, for six times (rows)

Chapter 5 Characterising the vertical structure of buildings in cities for use in atmospheric models

Abstract

Urban schemes for numerical weather prediction (NWP) often assume an infinite street canyon with constant height and width, impacting turbulent and radiative fluxes. We develop parameterisations for urban morphology profiles, with five complexity levels, using data from six cities at 2 km × 2 km resolution. Comparisons of parameterised building plan area to these ‘true’ data show that 90% of building fraction profiles have bias errors (BE) at any height of < 0.03. An effective building diameter (*D*) is used to characterise the proportionality between building plan area and building normalised perimeter length. The six-city mean *D* is 21 m. Relations for *D* have normalised BE (nBE) $< 16\%$, increasing to 26% when total wall area is assumed to be unknown. Impacts from using these new morphology relations are tested with SPARTACUS-Urban radiative transfer simulations. The effective shortwave albedo has a nBE 2-10% (cf. ‘true’). Within-canyon absorption have larger nBEs, suggesting the bulk albedo hides within-canopy errors. Overall, nBE increase as less morphology data are provided, notably when omitting total wall area. We conclude that urban vertical variability using the proposed relations are acceptable for NWP, requiring only: surface building plan area, mean building height, and effective building diameter.

5.1 Introduction

High population densities in cities can expose large numbers of people to extreme weather events such as heatwaves, whose effects can be exacerbated by poor air quality and the impacts of climate change. With urban areas being home to 54% of the world’s population and rising ($> 60\%$ by 2030) (United Nations 2018), these extreme events threaten public health and may cause severe economic loss. Because of this, there is a need for increasing accuracy and spatial resolution in weather forecasting and climate projections for urban areas (Grimmond et al. 2020).

Cities contain a heterogenous mix of buildings and trees with varying heights and densities. The material properties vary between and within the impervious (e.g., buildings, roads, sidewalks) and pervious (vegetated) areas. These characteristics influence the absorption and loss of shortwave and longwave radiation, while also impacting ventilation within the urban canopy (Guo et al. 2016; Kent et al. 2019). These effects cause trapping of heat (impacting local temperatures), influence the surface energy balance, and can affect precipitation and thunderstorm intensities (Shepherd 2005; Collier 2006; Liang et al. 2018).

Therefore, the 3D structure of cities should be treated with appropriate assumptions in order to understand the impacts of urban areas on the shortwave and longwave radiation (Arnfield 1982b; Masson 2000; Martilli et al. 2003). Within numerical weather prediction (NWP) models, surface obstacles (e.g., buildings, vegetation) and the interactions between them need to be parameterised, due to computational and data constraints (among others) that limit surface schemes. NWP urban morphology often assumes an ‘urban canyon’, consisting of flat roofed buildings of the same height with constant width, that are characterised by the building height to canyon width (*H*/*W*) ratio (e.g. Arnfield and Grimmond 1998; Kusaka et al. 2001; Porson et al. 2010).

Morphometric parameters are key for accurate modelling of urban weather and climate, and include: building heights (Zhu et al. 2019; Masson et al. 2020a) and their probability distribution (e.g., Temperatures of Urban Facets (TUF), Krayenhoff et al. (2014)), building plan area, wall area, and *H*/*W* (e.g., Town Energy Balance (TEB), Masson (2000); Lemonsu et al. (2012)) with vertical structure of cities additionally vital (Wentz et al. 2018). One reason why urban NWP schemes remain simple is a lack of global data to describe this vertical structure of cities. If global data for all buildings were available, the required parameters for modelling (e.g., building fraction, wall area) could be derived at any NWP grid resolution without parameterisations.

An additional reason for NWP urban schemes simplicity is a lack of accurate but computationally efficient methods to represent vertically resolved energy exchanges within urban canopies. Model developments, such as the SPARTACUS-Urban radiation scheme (Hogan 2019b), the Building Effect Parameterization scheme for turbulent fluxes (Martilli et al. 2002; Salamanca et al. 2011; Schubert et al. 2012), Seoul National University Urban Canopy Model (Ryu and Baik 2012; Ryu et al. 2013), and NJUC-UM-M (Kondo et al. 2005), have potential use in NWP. These consider a multi-layer approach, resolving multi-layer fluxes within the urban canyon, taking into account varying building heights and often vegetation.

Often building footprints, sometimes with height information, are available from municipal sources. Airborne stereophotography, photogrammetry or LiDAR data are used to develop digital elevation models (DEMs) and digital surface models (DSMs) (Gamba and Houshmand 2002; Xu et al. 2017). These allow high resolution (< 1 m) characterisation of individual cities (Holland et al. 2008; Goodwin et al. 2009; Lindberg and Grimmond 2011a,b; Gage and Cooper 2017). However, these data are unavailable for all cities worldwide due to the expense of data collection, storage and processing (Kent et al. 2019). Community volunteer projects (e.g., OpenStreetMap) collect building footprints, which may also have building height attributes provided (e.g., Microsoft providing U.S. cities, Heris et al. (2020)), or derived from other new techniques (e.g., using surrounding building information (Bernard et al. 2022)).

Building heights can be derived from remote sensing observations (Rao 1972; Champeaux et al. 2005) but few satellite missions have both the coverage and sufficient resolution to provide individual building heights for large areas (Frantz et al. 2021). Datasets have also been derived from combining multiple satellite sources (e.g., Frantz et al. (2021)), and additionally with local building footprint data (e.g., Milojevic-Dupont et al. (2020)), but studies such as these may only cover a single continent, or few cities, and/or rely on the availability of open-source building footprints.

Across the range of current morphology dataset creation studies, methodologies are inconsistent and need to be standardised before building information (e.g., height) can be provided across large areas. Hence, providing parameterisations that use publicly available data to estimate the vertical structure of cities at resolutions suitable for NWP would be beneficial, until better datasets become available globally. Such relations have been developed for urban areas (e.g., plan area fraction of buildings, mean building height, frontal area index) and are used operationally, e.g., UK Met Office use the Bohnenstengel et al. (2011) within the UKV (Hertwig et al. 2020). These parameterisations often require inputs that are not widely available (e.g., urban land cover), are derived from a single city but applied globally, and/or assume very limited variability e.g., one mean building height per built (‘urban’) fraction with saturation (i.e., tall dense city centres are the same as other areas). Intra-city urban form variability has been included using the Stewart and Oke (2012) local climate zones (LCZ) which provide representative ranges of values of parameters (e.g. plan area fraction of buildings or paved surfaces, roughness element height, and frontal area index) for each class, with datasets available to use as urban model inputs (Demuzere et al. 2022b), and integration with models, e.g., within the Weather Research and Forecasting model with a single layer urban canopy model (Brousse et al. 2016; Molnár et al. 2019) with analysis on urban air temperatures.

Given the importance of radiation to surface energy exchange, this work, and multi-layer modelling generally, is motivated by the need to reduce the sources of error in urban radiation calculations, which are from:

(1) the radiation scheme, even if the urban morphology is known exactly
(2) approximating the morphology from a few parameters (e.g., plan area or building cover fraction, mean building height and total building wall area)
(3) incomplete knowledge of the parameters in any given city.

Stretton et al. (2022) addressed the first of these, evaluating the SPARTACUS-Urban shortwave radiation scheme. They demonstrated that SPARTACUS-Urban accurately predicts profiles of absorption into urban facets (mean absolute error < 16%), and the effective albedo at the top of the canopy (normalised bias error < 6%) for real-world scenes. Overall, errors for all variables are largest when the sun is low in the sky, when the impact of the underlying assumptions on building geometry are largest.

The specific objective of this paper is to address (2) by identifying and parameterising key vertical profiles of the urban form, using methods and coefficients that can be used globally, while retaining some of the realistic intra-city variability. Given the range of urban forms (within and between cities) and the sparsity of data, the relations developed here ideally need to be both simple and universal. We focus on input parameters including building: height, plan area fraction (with height), and wall area (with height), as they define the area of roof and walls exposed for energy exchange with height. Problem (3) is partially addressed here by giving a range of typical values of parameters for six cities. However, the parameterisations developed in this paper will become more applicable once datasets of building cover and mean building height are available globally.

The parameters to describe the urban form are selected and defined (section 5.2) and used within this study's various methods (section 5.3). The proposed parameterisations are assessed with 'true' urban morphology (section 5.4), combined (section 5.4.4), and used with SPARTACUS-Urban (Hogan 2019a) (Chapter 3) to simulate absorbed shortwave radiation into the three facets (walls, roof, and ground) (Secct. 5.5). The conclusions drawn are given in Section 5.6.

5.2 Definitions of multi-layer urban form parameters

5.2.1 Plan area fraction (λ_p)

The plan area fraction of buildings (λ_p) is the ratio of the total area covered by buildings to the 'grid-cell' or total horizontal area of interest. Typically, λ_p is assumed to be constant with height, ($\lambda_p(z)$), from the surface ($\lambda_p(z = 0)$), unlike real buildings which rarely have equal heights in an area or an individual model grid-cell. Whilst we often model arrays of regular cubes (Kanda et al. 2005a; Morrison et al. 2018), e.g., Chapter 3. Rather, $\lambda_p(z)$ varies (Figure 5.1a) resulting in variations in sunlit and shaded surfaces (e.g., roofs) at any given height, allowing interception of radiation reflected from higher surfaces, increasing the radiation trapping with a canopy.

$\lambda_p(z)$ can be related to $\lambda_p(z = 0)$ if the area-weighted mean building height ($\overline{H}$) is known (e.g., determined from building data in real cities), assuming:

$$\lambda_p(z) = \lambda_p(z = 0)y(z/\overline{H}), \tag{5.1}$$

where $y(z/\overline{H})$ is a universal function with the properties: $y(0) = 1$, $y(\infty) = 0$, and the vertical integral of y must equal 1. A functional form for y is proposed in Section 5.3.2.

5.2.2 Wall area: building perimeter length (L)

The wall area relates to the normalised building perimeter length, L, at any given height ($L(z)$) (Chapter 3). L is the total building perimeter (m) normalised by the total area of the grid-cell (m^2). Thus, if the canopy is divided into n layers and layer i has thickness Δz_i, then:

$$\lambda_W = \sum_i^n L_i \Delta z_i \, , \tag{5.2}$$

with λ_W the total wall area divided by the grid-cell area (Masson et al. 2020a). If all wall orientations are assumed to be equally probable within a grid-cell, then $\lambda_w = \lambda_f \pi$ (Hogan and Shonk 2013), where λ_f is the frontal area index – the total projected wall area for a particular wind (or azimuth) direction, relative to the grid-cell area. λ_f is often used to parameterise aerodynamic drag of roughness elements (Raupach 1992; Grimmond and Oke 1999c; Sützl et al. 2020).

5.2.3 Effective building diameter (*D*)

Assuming both narrow and wide buildings have an equal probability of extending to any height (Figure 5.1a), L is proportional to λ_p. We use this to define an effective building diameter (*D*) that is independent of height:

$$L(z) = \frac{4\lambda_p(z)}{D}. \tag{3}$$

This is analogous to the relations used between perimeter length and area of clouds and trees (Jensen et al. 2008; Hogan et al. 2018b). The *D* parameter can be thought of as the diameter (or width) of buildings in an equivalent idealized city, with the same properties (λ_p and *L*) as a real city (Figure 5.1b), where all buildings are identical cylinders (or cubes). Note that we neither assume buildings have a particular shape, nor that they are all the same size in a real city. Rather, *D* quantifies the assumed proportionality between *L* and λ_p in Eq. 5.3, while having a simple physical interpretation.

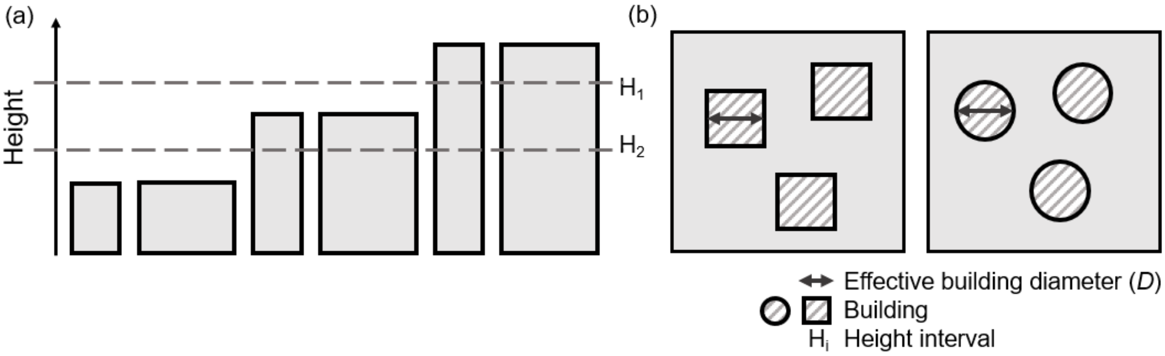

Figure 5.1: Effective building diameter (*D*): (a) assumption it is constant with height (Eq. 5.3) implies an equal probability of both large and small buildings extending to different heights (cross section); and (b) plan view of two equivalent areas with buildings that are either cuboids of width *D* or cylinders of diameter *D*

5.3 Methods

5.3.1 Deriving $\lambda_p(z)$ and $L(z)$ from high resolution reference data

Profiles of λ_p and *L* are derived from high resolution reference data from six cities with differing characteristics (e.g., morphology, city layout) (Table 5.1). The cities chosen are Auckland, New Zealand; Berlin, Germany; Birmingham, UK; London, UK; New York City (NYC), US; and Sao Paulo, Brazil. Multiple global cities are used to capture the variation in building and land-use types seen exhibited across urban areas.

For London, Berlin, and Birmingham, building footprints (Umweltatlas Berlin 2010; EMU Analytics 2018)[2] are used to create a 1 m × 1 m raster with mean height assigned to each building. Therefore, buildings have flat roofs and non-tapering vertical walls without building features (e.g., pitched roofs) above the mean height. During rasterization, "false walls" between adjoining (e.g., terraced) and overlapping buildings are removed. Building information for Auckland, NYC, and Sao Paulo are LiDAR datasets provided as 4 m × 4 m raster (Kent et al. 2019). Although some differences in building morphology may arise from the raster resolution chosen (Figure 5.A.1, Table 5.A.1), by using the highest resolution available (i.e., not coarsening to the 4 m × 4 m resolution of some datasets) allows the parameterisations to be closer to 'true' data. Buildings/pixels with height values below 2.5 m (mean storey height in the UK (OPDC 2018)) or without height information are discarded for consistency across all datasets. For all grid-cells in all cities, the topography is assumed to be flat.

Each city dataset is split into 2 km × 2 km grid-cells, to have a similar resolution to operational limited-area NWP models (e.g. Met Office 1.5 km UKV model (Tang et al. 2013), DWD 2.8 km COSMO-DE model (Baldauf et al. 2011)). At this scale, most grid-cells will have many buildings with different heights, but are less likely to contain multiple neighbourhoods with very different characteristics. Grid-cells with incomplete (i.e., missing) building data (determined from visual inspection of aerial imagery) and/or any areas with extremely small building coverage ($\lambda_p(z = 0) < 0.001$) are removed. Profiles are calculated using a height interval (Δz) of 0.5 m.

---

[2] EMU Analytics data combine building polygons from Ordnance Survey Open Map and heights from Environment Agency LiDAR data from 2014 and 2015.

Table 5.1: Cities and high-resolution reference data used to evaluate urban form parameterisations. City area (A_{city}) from Demographia World Urban Areas (2020), US Gazetteer (2021) as basis for the whole city area, an area can be > 100% if it contains areas outside of the city, or areas of water. The 2 km × 2 km parameters are derived from either raster (rDSM) or vector (vDSM) digital surface models with the horizontal resolution (Δx) indicated

City	City		Whole city mean building			Data			
	Number of grid-cells	Fraction of A_{city}	Edge length $L(z=0)$ (m^{-1})	Surface fraction $\lambda_p(z=0)$	Building height $\overline{H}$ (m)	Date	Type	Δx (m)	Source
Auckland	59	0.45	0.051	0.21	5.98	Jul-Nov 2013	rDSM	4	Kent et al. (2019)
Berlin	198	0.58	0.022	0.10	8.86	2009-2010	vDSM	1	Umweltatlas Berlin (2010)
Birmingham	177	1.18	0.020	0.082	5.87	Jan-1998 – Sep-2014	vDSM	1	EMU Analytics (2018)
London	415	0.96	0.029	0.13	7.32		vDSM	1	
New York City	251	1.29	0.033	0.17	12.68	2014	rDSM	4	Kent et al. (2019)
Sao Paulo	329	0.41	0.046	0.24	5.97	2007	rDSM	4	

5.3.2 Deriving globally obtainable parameterisations for $\lambda_p(z)$ and $L(z)$

The profiles of λ_p and L are parameterised for the six cities (Table 5.1). The parameterisations developed for $\lambda_p(z)$ and $L(z)$ are used in five combinations of increasing complexity, with differing input data requirements. These are evaluated against the high-resolution reference datasets (P0). The parameterisations (P#) of $\lambda_p(z)$ and $L(z)$ are given increasing numbers (#, 1 → 5) as the input requirements decrease (i.e., with the intention they are more globally applicable) (Table 5.2):

P1 the most data demanding (e.g., from high-resolution raster data, Section 5.3.1), parameterisation, uses non-globally available (yet) λ_W and $\lambda_p(z)$. An effective building diameter, D, is used to predict $L(z)$ to ensure the latter satisfies Eq. 5.2 (Table 5.2). This can be achieved if λ_w is known, by:

$$D = \frac{4}{\lambda_W} \sum_{z=0}^{i} \lambda_{p,i}\, \Delta z = \frac{4}{\lambda_W} \mathrm{V}, \tag{5.4}$$

where the normalised building volume, V, is the ratio of building volume and grid-cell area, related to building plan area and mean building height ($\overline{H}$) by $V = \lambda_p(\mathrm{z}=0)\overline{H}$ (parameterisation: *Wall area conserved (CWA) D*, Table 5.2).

P2 uses λ_W as in P1 but parameterises $\lambda_p(z)$ from $\lambda_p(z=0)$, and mean building height ($\overline{H}$) using Eq. 5.1, with:

$$y(x) = [1 + (ax)^b]^{-1}, \tag{5.5}$$

where $x = z/\overline{H}$, a is a function of b that ensures the integral of y from zero to infinity is one. Figure 5.A.2 demonstrates that this functional form is a good fit to the median building-fraction profile from real cities worldwide. Value of the best-fit parameter, b, derived from the high-resolution reference data have smaller values when there is larger variation in building heights within a grid-cell. To determine b, we take $\lambda_p(z)$, and normalise each axis by $\overline{H}$ and $\lambda_p(z = 0)$, such that the resultant curve represents the $y(x)$ function from Eq. 5.4 (Figure 5.A.2). The normalised curves are interpolated using a common vertical normalised height interval of 0.05, prior to determining the median profile (Figure 5.A.2a, b).

For the $\lambda_p(z)$ *variable b* parameterisation (Table 5.2), grid-cells are categorised in $\overline{H}$ intervals. Values of b are derived using median normalised profiles for each $\overline{H}$ interval calculated from all cities.

P3 is P2 but for $\lambda_p(z)$ the *fixed b* parameterisation (Table 5.2) is used with $b = 4.7$ (Eq. 5.4) across all $\overline{H}$ for all grid-cells. This value is derived from the multi-city median $y(x)$. Using one b value allows assessment of cities similarity, and if parameterisations perform better (less error in radiation fluxes) if more data are included.

P4 requires only grid-cell values of $\lambda_p(z = 0)$ and $\overline{H}$. $\lambda_p(z)$ is obtained as in P2 and derives L from calculating an effective building diameter (D) from:

$$D = p\overline{H} + q\lambda_p(\mathrm{z} = 0) + r, \tag{5.6}$$

where the constants p, q, and r ($p = 0.847$, $q = 5.17$, $r = 11.96$) are derived by fitting D to $\lambda_p(z = 0)$ and $\overline{H}$ across all cities (Table 5.1, Table 5.2). This is referred to as *linear-fit D* (Table 5.2).

P5 the simplest case uses only $\lambda_p(z = 0)$ and $\overline{H}$, so requires the least data. It parameterises $\lambda_p(z)$ as in P3. To obtain L, with D set to 20.93 m for all cities (*fixed D*, Table 5.2) and λ_w is assumed proportional to V (Eq. 5.4).

All the 2 km × 2 km grid-cells available are used to derive parameters for the $L(z)$ and *fixed b* parameterisations. For the *variable b* parameterisations (P2, P4), for each height interval a bootstrapped random sample (Padiyedath Gopalan et al. 2019) of 1000 is used to ensure all intervals have the same sample size.

Table 5.2: Combinations of morphology parameterisations to determine building fraction (λ_p), normalised building edge length (L) from D (Figure 5.1b) (assumed constant with height), evaluated relative to the actual 'true' profiles of λ_p and L (P0, section 5.3.1), mean building height, $\overline{H}$, and building fraction at the surface, $\lambda_p(z = 0)$, are required inputs for all parameterisations

Code	Inputs required	$\lambda_p(z)$ parameterisation	$L(z)$ parameterisation
P0	$\lambda_p(z)$ and $L(z)$ profiles	Known	Known
P1	$\lambda_p(z)$ profile; λ_w; $\overline{H}$	Known	Wall area conserved D: Eq. 5.5
P2	$\lambda_p(z=0)$; λ_w; $\overline{H}$	Variable b: Eq. 5.1 & 5.4 with $b(\overline{H})$	Wall area conserved D: Eq. 5.5
P3	$\lambda_p(z=0)$; λ_w; $\overline{H}$	Fixed b: Eq. 5.1 & 5.4 with b=4.7	Wall area conserved D: Eq. 5.5
P4	$\lambda_p(z=0)$; $\overline{H}$	Variable b: Eq. 5.1 & 5.4 with $b(\overline{H})$	Linear-fit D: Eq. 6: $D[\lambda_p(z=0), \overline{H}]$
P5	$\lambda_p(z=0)$; $\overline{H}$	Fixed b: Eq. 5.1 & 5.4 with b=4.7	Fixed D: D=20.93 m

5.3.3 SPARTACUS-Urban radiative transfer model

The original SPARTACUS (Speedy Algorithm for Radiative Transfer through Cloud Sides) 3D radiative exchange model for complex cloud fields simulates lateral radiative exchange between clear and cloudy regions in proportion to the cloud edge length per unit area of a NWP grid-cell, using cloud fraction and cloud edge length (Hogan et al. 2016). A similar approach has been applied to forest vegetation (Hogan et al. 2018) and city buildings (Hogan 2019a). All three assume any obstacles to radiation are randomly distributed within a horizontal plane, allowing the mean radiation field to be modelled as a function of height. The open-source software SPARTACUS-Surface combines SPARTACUS-Urban and SPARTACUS-Vegetation. As we focus only on buildings, we refer to it as SPARTACUS-Urban.

SPARTACUS-Urban is underpinned by the 1D discrete-ordinate method, solving coupled ordinary differential equations for $2N$ streams of radiation, with N streams per hemisphere. The radiation field is described more accurately as N increases, but with added computational cost. In this work, 16 streams are used (i.e., $N = 8$). A scene (any combination of building geometry, solar zenith angle, and albedo) is split into n layers to calculate radiative interactions per level. Each layer has regions of clear-air and buildings. SPARTACUS-Urban computes the radiative interactions between the three facets (wall, roof, and ground) using the vertical profiles of L and λ_p to characterise the urban form with z within a grid-cell. If vegetation is included, it also needs to be accounted for in each layer.

To compute radiative fluxes, SPARTACUS-Urban uses a prescribed albedo (α). Here, we assign 0.2 to all facets (wall, roof, ground), based on literature for a range of urban form synthesised by Oke et al. (2017): 0.08-0.25 for roofs, 0.2-0.25 for walls and 0.08-0.25 for the ground (Grimmond and Oke 1995; Feigenwinter et al. 1999; Grimmond et al. 2004; Lemonsu et al. 2004; Offerle et al. 2005b; Balogun et al. 2009; Bergeron and Strachan 2012). This is constant between facets to isolate any radiative errors due to the changes in morphology. SPARTACUS-Urban treats determines both direct and diffuse radiation, but does not separate sunlit and shaded surfaces. For this study, we assume all incoming radiation is direct radiation (i.e., no diffuse) with the normal solar flux at the top of the canopy set to 1000 W m^{-2}. We model for three solar zenith angles (θ_0): overhead (nadir) sun (0°), 45°, and low-sun (75°). Under overhead sun ($\theta_0 = 0°$) we expect fluxes to be sensitive primarily to differences in the λ_p parameterisations (P2, P3), and for low sun simulations ($\theta_0 = 75°$) to respond to differences in L parameterisations (P4, P5).

5.3.4 Metrics to evaluate parameterisations against high resolution reference datasets

The parameterisations (P1→P5, Table 5.2) are evaluated using the bias error ($BE_i = P\#_i - P0_i$) between the 'true' (P0) and parameterised profiles for building fraction and building edge length. The BE of individual λ_p and L vertical profiles across each city are analysed using the median, mean, and 5th - 95th percentiles.

Similarly, the λ_w for L parameterisations is evaluated using the mean BE (MBE). The mean λ_w is also evaluated using a normalised MBE (nMBE), computed by dividing the MBE by the 'true' mean λ_w computed from the P0 data, and multiplying by 100 to give a percentage. The mean absolute error ($MAE = \Sigma(|P\#_i - P0_i|)/n$) for λ_w for each parameterisation is calculated for the number of grid-cells per city (n), to examine the performance across all data.

The impact of the parameterisations to the vertically integrated shortwave absorption into the walls (a_{Wall}), roof (a_{Roof}) and ground (a_{Ground}) per unit area of the entire horizontal grid-cell (W m^{-2}) is assessed using the MBE, nMBE, and MAE as above. The total absorption is also assessed for each grid-cell using the normalised BE (nBE). Similarly, we examine the impact on the shortwave bulk albedo for each grid-cell as above.

5.4 Results and Discussion

5.4.1 Spatial variation of morphology in high resolution reference datasets

For all six cities, the largest values of both plan area fraction at the surface ($\lambda_p(z = 0)$) and mean height ($\overline{H}$) are found near the city centre or central business district (CBD) (Figure 5.2). The largest $\overline{H}$ values occur in NYC (e.g., Manhattan) (~ 30 m for 2 km × 2 km grid-cells) and Berlin. The lower values in other cities may be due to large variations in building types within a grid-cell, e.g., in Sao Paulo very tall buildings are often surrounded by areas of smaller buildings within the same grid-cells. Values of $\lambda_p(z = 0)$ are higher in NYC, Sao Paulo, and Auckland. Similar values of $L(z = 0)$ are found across each individual city, lowest in Berlin, Birmingham, and London (< 0.05 m^{-1}) and largest in Auckland, NYC, and Sao Paulo (0.05-0.1 m^{-1}). These could be impacted by fraction of the whole city analysed and the definitions used (Table 5.1), as this varies between 45% and > 100%. For example, in Auckland, a smaller fraction (0.45) of the city is analysed, so likely less variability in land-use and building type are characterised. However, each city has grid-cells that contain parks, residential areas, and parts of the

CBD. Although only six cities are analysed, they cover a wide range of λ_p and $\overline{H}$ combinations, city layouts, locations, employment types/industries, and demographic characteristics. However, as other cities are analysed the result details will vary.

Across all cities the 2 km × 2 km grid-cells generally have a $\overline{H}$ of < 30 m (colour bar, Figure 5.3). The few grid-cells with $\overline{H} > 40$ m often have larger $\lambda_p(z = 0)$ values. This suggests that grid-cells are not dominated by a large number of tall buildings, although this depends on the exact grid-cell location. Effective building diameter (D) values are always > 8 m but mostly < 40 m (Figure 5.3). Values of D tends to increase with $\lambda_p(z = 0)$ (between 10 and 20 m, when surface building fractions are 0.0 to 0.5) in grid-cells with low values of $\overline{H}$ (< 10 m) (Figure 5.3). Grid-cells with large values of D (up to 100 m) tend to have smaller $\lambda_p(z = 0)$.

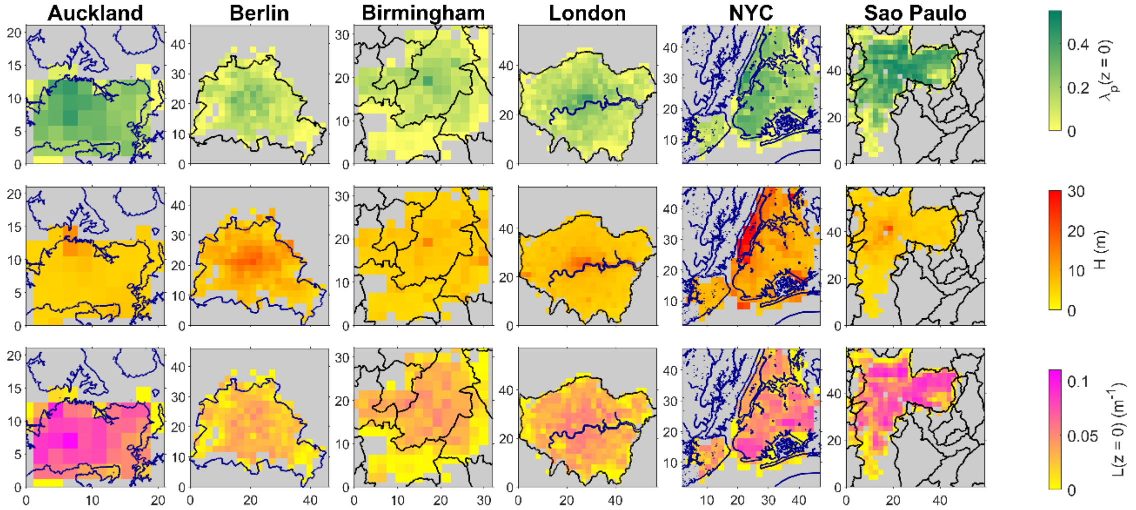

Figure 5.2: Parameters derived from building data (Table 5.1) at 2 km × 2 km resolution for (columns) six cities: (row 1) building fraction at the surface ($\lambda_p(z = 0)$), (row 2) mean building height ($\overline{H}$), and (row 3) normalised building perimeter length at the surface ($L(z = 0)$) (Eq. 5.3); with city boundaries (black) and water bodies (blue) shown. Data sources are given in Table 5.1

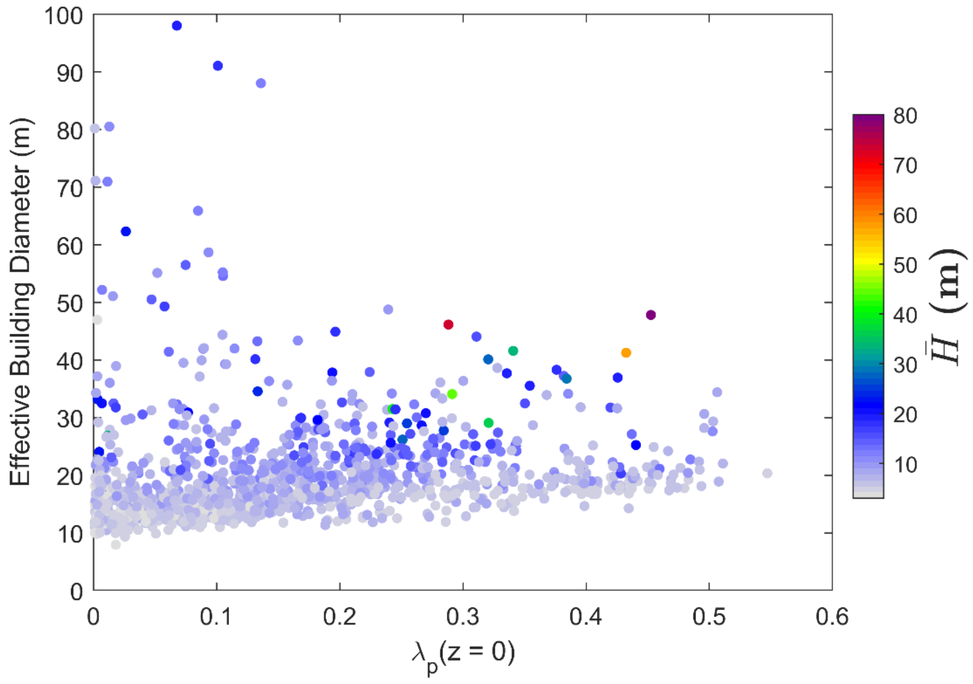

Figure 5.3: Relation between the three parameters used in the 'linear-fit D' parameterisation (Table 5.2) for all grid-cells (N = 1429): building fraction at the surface ($\lambda_p(z = 0)$), effective building diameter (D) calculated using normalised wall area (λ_w) and mean building height ($\overline{H}$) (colour)

5.4.2 Evaluation of parameterisations for normalised perimeter length (*L*)

We assess if the assumption that the effective building diameter (D) is constant with height (z) (Section 5.3.2) is appropriate. Within and between cities, D varies with z (Figure 5.4). The mean and median D values across each city appear to follow similar vertical relations, with the mean D at each height larger than the median, especially with increasing height. In Birmingham, London, and NYC, D is approximately constant with height between 7 and 10 m, and at ~25 m (Birmingham and London), and ~35 m (NYC). Similar behaviour is seen in Berlin, although the mean and median D values are much closer in magnitude. In Sao Paulo, D is roughly constant with height above 20 m. In Auckland, D decreases with height, with $D > 20$ m until $z > 50$ m; but Auckland has both the fewest grid-cells (only 59) and smallest fraction of the city analysed (Table 5.1).

As the vertical variation of D is much smaller than the vertical variation of plan area fraction of buildings (λ_p, Figure 5.4), we test the consequence of assuming D is constant with height. In four of the six cities, wider buildings tend to extend higher into the urban canopy (not Auckland or Sao Paulo). Auckland appears to be an outlier (cf. other cities), possibly because of the smaller fraction of the city assessed (0.45, Table 5.1). In grid-cells with taller buildings (larger mean $\overline{H}$), the assumption of a constant D is appropriate, but could be replaced with values obtained from two (or more) height intervals to better characterise the vertical profile; however, this additional complexity is not introduced here.

Examining the normalised perimeter length at each height level ($L(z)$, Eq. 5.3, Table 5.2) parameterisations derived using the high-resolution reference dataset λ_p profile for each grid-cell, an increase in $L(z)$ bias error (BE) between the *linear-fit D* and *fixed D* parameterisations is evident (Figure 5.5). In most cities there is a tendency to overestimate $L(z)$ higher in the canopy (Figure 5.4, Figure 5.5), indicating an under-estimation in effective building diameter (i.e., from Eq. 5.3). Hence, buildings with a larger horizontal size are more likely to be taller.

The λ_w nMBE for the *linear-fit D* parameterisation are lowest in NYC (0.01%), and largest in Auckland (-15%) (Table 5.3). The *fixed D* parameterisation of λ_w have larger nMBE than the *linear-fit D* parameterisation, with values between -6.4% (Berlin) and -26% (Auckland). Generally, all nMBE indicate λ_w is underestimated when using both *linear-fit D* and the *fixed D* parameterisations for $L(z)$ (Table 5.3). For Auckland, London, and Birmingham, the *linear-fit D* parameterisation performance is always better than the *fixed D* parameterisation. The distribution of BE in $L(z)$ (Figure 5.5) for both the *linear-fit D* and *fixed D* parameterisations, indicate the median is < 0.005 m^{-1} (mean $L(z = 0)$ spans 0.02 - 0.05 m^{-1}). Exceptions to this include the *fixed D* parameterisation in Auckland. The 5th – 95th percentiles of profiles (shading, Figure 5.5) for Berlin, London, and Birmingham do not exceed 0.04 m^{-1} at any height but are slightly larger for the remaining cities.

Both UK cities (London and Birmingham) have similar shaped BE profiles, suggesting a similar urban structure. In London, the L skill changes with height from an underestimation ($z <$ ~7 m) to overestimation (z > ~9 m) (Figure 5.4). This could result from the larger $\overline{H}$ variation across the city (Figure 5.2), cf. Birmingham which has lower $\overline{H}$ with less variation, as the CBD covers fewer grid-cells. NYC has the largest $L(z)$ differences of the six cities, with the *fixed D* parameterisation median BE and MBE generally smaller than the *linear-fit D* parameterisation for $z \leq 10$ m. For all cities the largest $L(z)$ errors occur for $z < 10$ m, with most overestimating $L(z)$ for both parameterisations below 5 m.

Table 5.3: Evaluation of mean normalized wall area (λ_w) using the linear-fit D and fixed D parameterisations (Table 5.2) using the Conserved wall area D parameterisation for each city assessed with metrics (section 5.4.4): mean bias error (MBE), normalised mean bias error (nMBE, %) and mean absolute error (MAE). Table 5.1 gives number of grid-cells analysed per city

City	*Conserved wall area D*	Linear-fit *D*			Fixed *D*		
	$\overline{\lambda_W}$ (m^2/m^2)	MBE (m^{-1})	nMBE (%)	MAE (m^{-1})	MBE (m^{-1})	nMBE (%)	MAE (m^{-1})
Auckland	0.482	-0.054	-15	-0.054	-0.082	-26	-0.082
Birmingham	0.165	-0.0025	1.5	-0.0025	-0.018	-14	-0.018
Berlin	0.187	-0.0073	-3.3	-0.0073	0.0071	-6.4	0.0071
London	0.250	-0.011	-4.8	-0.011	-0.016	-13	-0.016
NYC	0.302	-0.043	0.013	-0.043	0.074	13	0.074
Sao Paulo	0.287	0.0061	5.8	0.0061	-0.015	-7.6	-0.015

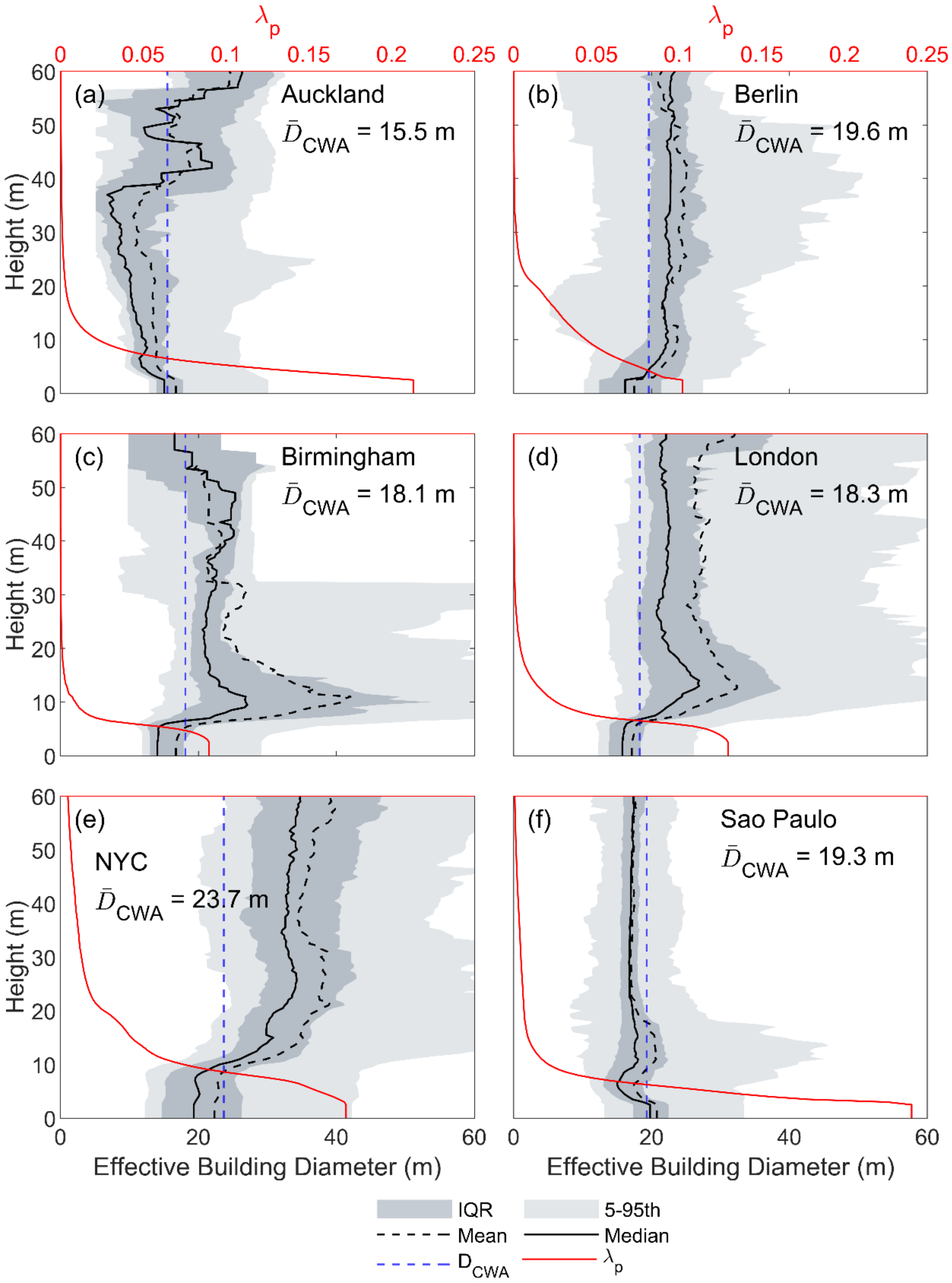

Figure 5.4: Vertical profiles of effective building diameter (*D*) calculated from the true building data (P0, Table 5.2) [mean (dashed), median (solid), inter-quartile range (IQR, shading), 5th and 95th percentile (shading)], building fraction (λ_p) [red, mean weighted by number of grid-cells ($\lambda_p > 0.001$) per height level] and mean 'wall area conserved D' (CWA) parameterisation (blue dashed) for each city: (a) Auckland, (b) Berlin, (c) Birmingham, (d) London, (e) NYC, and (f) Sao Paulo

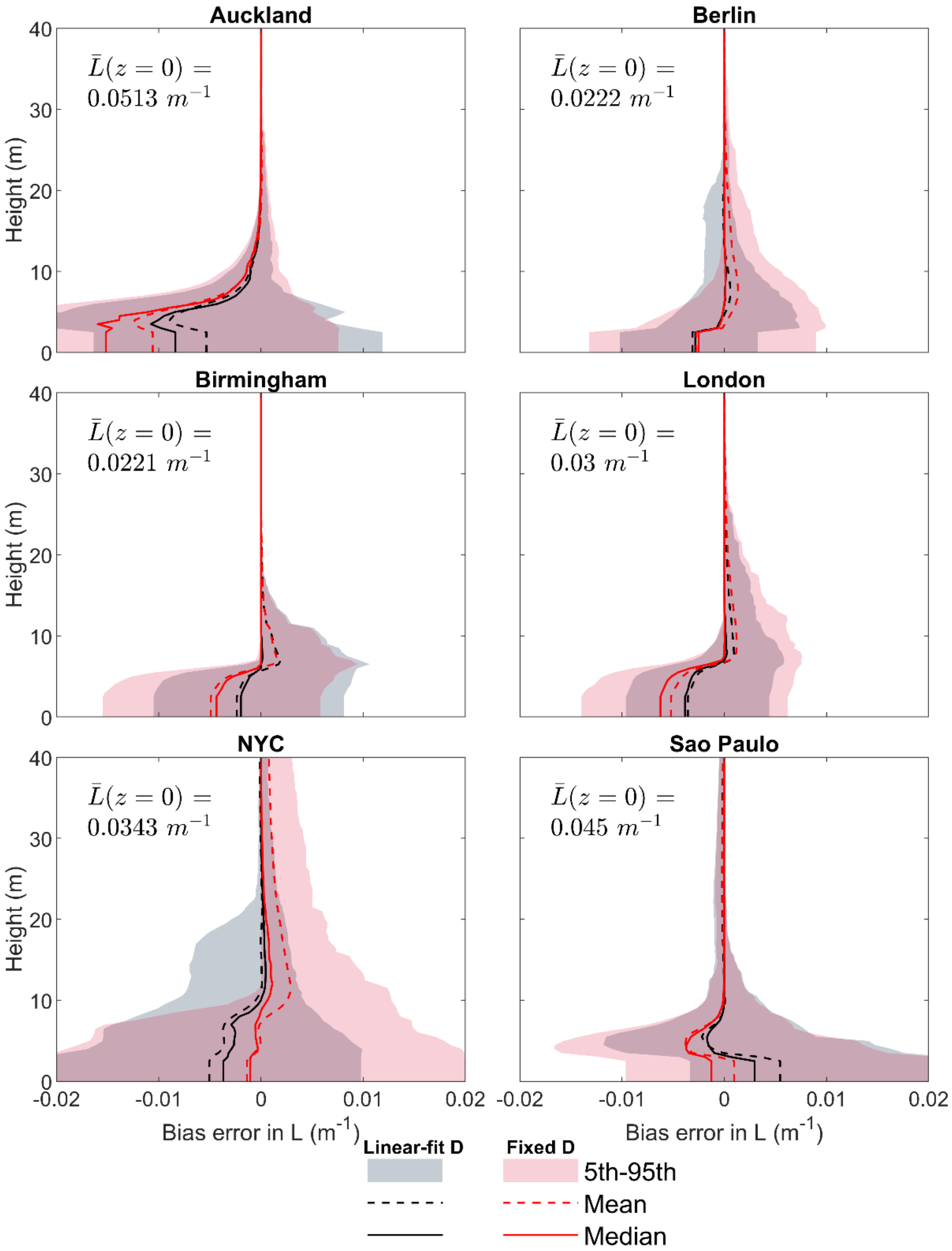

Figure 5.5: Mean building edge length at the surface ($\overline{L(0)}$) and vertical profiles of bias error (BE, section 5.3.4) of normalised building edge length (L) determined using the 'linear-fit D' parameterisation (grey) and 'fixed D' parameterisation (red) (Table 5.2) for (a) Auckland, (b) Berlin, (c) Birmingham, (d) London, (e) NYC, and (f) Sao Paulo

5.4.3 Evaluation of parameterisations for plan area fraction of buildings (λ_p)

Parameterisation methods for λ_p (*variable b* and *fixed b*, Table 5.2), are evaluated using the $\lambda_p(z)$ vertical profiles from the high-resolution reference datasets (P0, Table 5.2) for each grid-cell (Figure 5.2). For the *variable b* parameterisation, b varies with $\overline{H}$ intervals ($b = 2.1 – 6.5$, Figure 5.6), whereas *fixed b* uses one multi-city value ($b = 4.7$) independent of city. As both parameterisations assume $\lambda_p(z = 0)$ is known, they agree with the 'truth' at the surface.

Generally, b decreases when mean building heights exceed 7 m (Figure 5.6). The multi-city *fixed b* is approximately equivalent to the *variable b* parameterisation value of b at ~7 m. Grid-cells with the lowest $\overline{H}$ have the smallest variation in building heights and are associated with the largest b values. Areas with low $\overline{H}$ are often found in suburbs, dominated by two-storey buildings. This contrasts with the CBD, where a wider variation of building heights occurs, with lower values of b.

The variability around the median multi-city curve (black, Figure 5.6) shows the variability in b is higher when $\overline{H}$ is larger (whiskers, Figure 5.6), which may be associated with smaller sample sizes. The multi-city b with $\overline{H}$ relation follows NYC closely (green, Figure 5.6), as NYC has the most grid-cells sampled. Differences between the multi-city median and the NYC b at $\overline{H} = 40$ m arise as extra grid-cells from other cities (i.e., with < 5 grid-cells) are included. Auckland and Sao Paulo have b values are most different from both other cities and the multi-city relation (Figure 5.6). The UK cities, London and Birmingham, are similar to ~10 m but differ above this as London has higher $\overline{H}$. Other cities with different variations in morphology may lie either side, or elsewhere in relation to this multi-city curve, e.g., taller cities (Asian megacities) may sit with Sao Paulo, or more with NYC.

Using the *variable b* and *fixed b* parameterisations (Table 5.2) gives absolute BE for λ_p of < 0.025 for all heights in all cities (black lines, Figure 5.7), except Sao Paulo. There is little difference between the two parameterisations. Generally, 90% of the data (5^{th} - 95^{th} percentile, shading Figure 5.7) in each city are within 0.03 of the 'true' values at each height. These results suggest Eq. 5.1 is applicable to real-world cities.

Focusing on individual cities, the UK cities have similar vertical profiles (Figure 5.7), as expected given their similar b values (Figure 5.6). For Auckland and Sao Paulo, λ_p is underestimated below 10 m and overestimated above, the opposite to London and

Birmingham. For NYC, large errors extend to higher building heights, especially for the *fixed b* parameterisation. In Sao Paulo the largest BE (> 0.05) occur when $z < 10$ m. Berlin, up to 20 m, has the second largest maximum magnitude of BE (~0.06), but low mean and median absolute BE (< 0.02).

Overall, the *fixed b* parameterisation *b* (Eq. 5.4) gives a reasonable fit in all cities. Comparing both parameterisations (*variable b*, *fixed b*) shows that only small improvements when *b* values are dependent on mean building height.

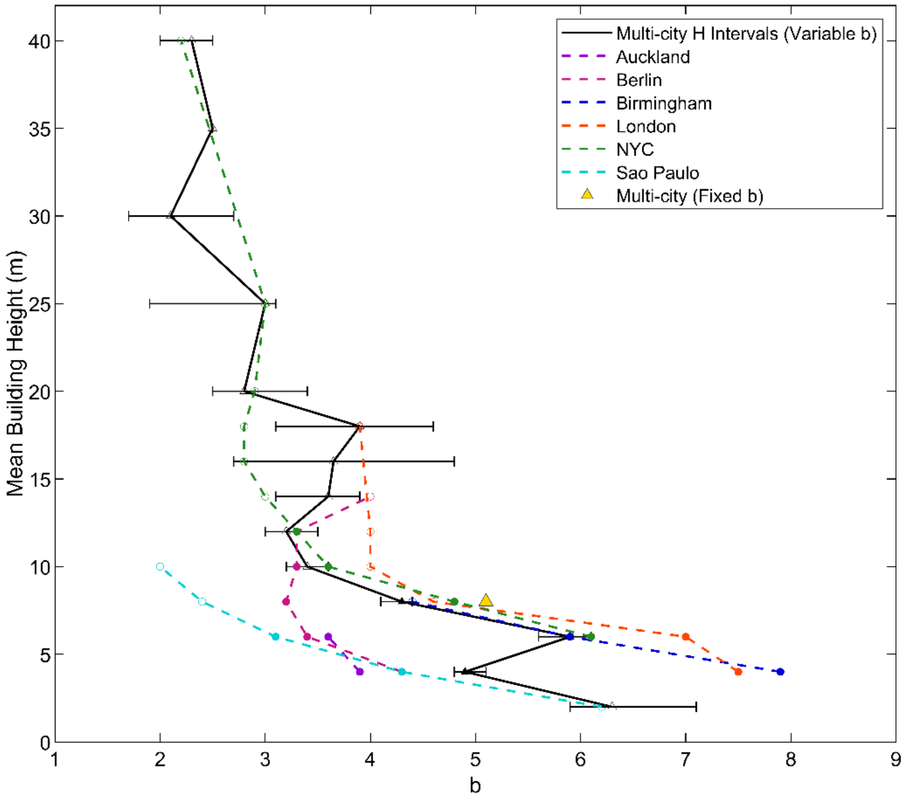

Figure 5.6: Relation between b (Eq. 5.4) and mean building height ($\overline{H}$) for each city (Table 5.1) and across all cities, for $\overline{H}$ intervals (2 m: 2-20 m, 5 m: 20-40 m). $\overline{H}$ intervals with sample size ≥ 5, containing > 10% of individual city grid-cells or across all (multi-city) (filled, otherwise open) the 'variable b' spread (whiskers) in median b with height are calculated from 1000 bootstrap samples, random with repetition to the same sample size of each interval, for the full dataset (P0, Table 5.2)

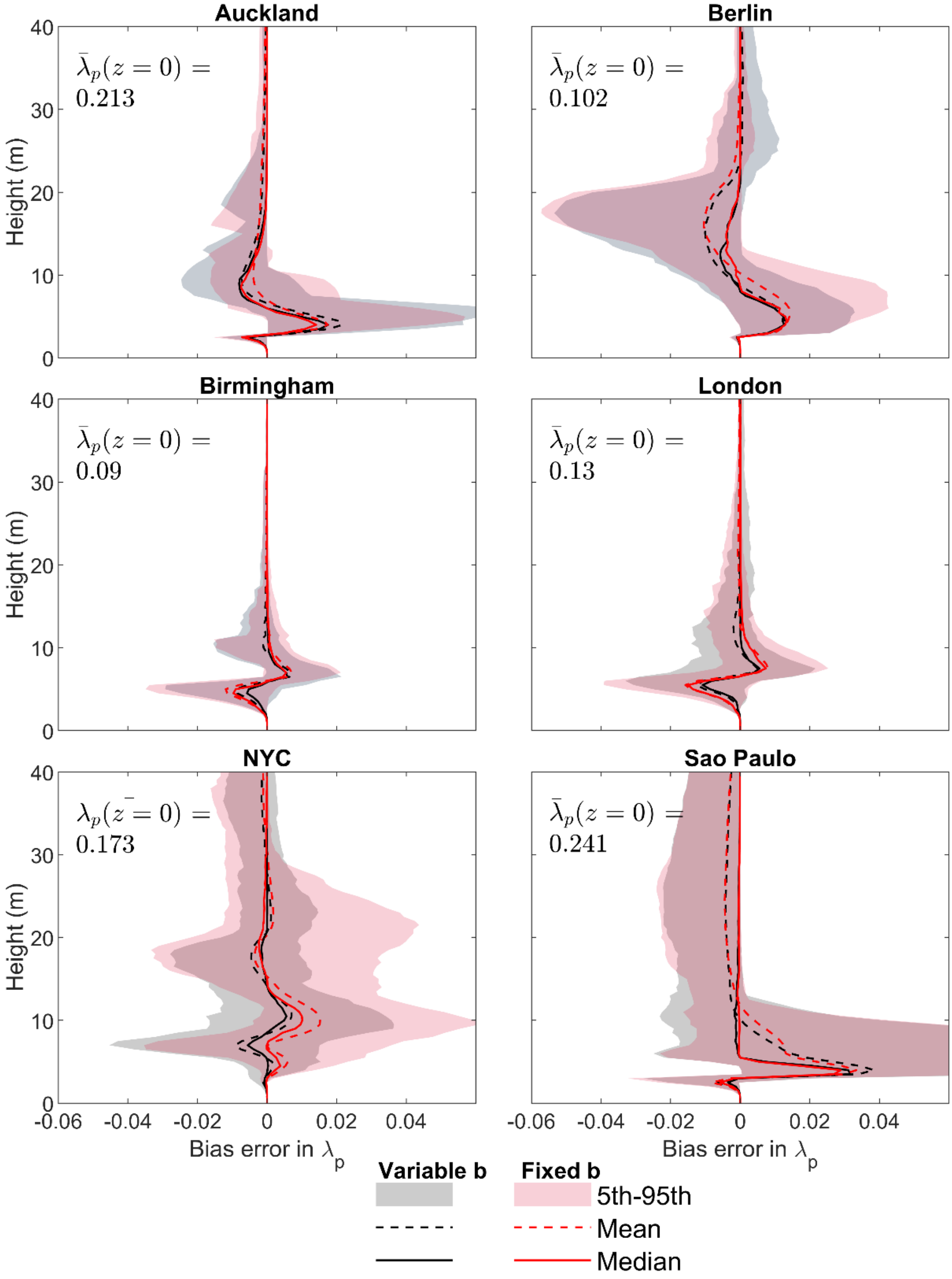

Figure 5.7: Mean city plan area building fraction at the surface ($\overline{\lambda_{p,0}}$) and vertical profiles of bias error (BE) of plan area fraction (λ_p) determined using the 'variable b' (grey) and 'fixed b' (red) (Table 5.2)

5.4.4 Evaluation of combined parameterisations

The combined $L(z)$ and λ_p parameterisations (P1 → P5, Table 5.2) are evaluated using the P0 high resolution reference profiles for each city. This evaluation also assesses λ_w for parameterisations of L.

MBE for λ_w is smallest if more city-specific information is used (Table 5.2). For mean λ_w, the nMBE are < 2.5% for P2 and P3, but up to -17% for P4 (Table 5.4). The largest nMBE occur in Auckland and Berlin, and smallest in Birmingham and London. Using *fixed* coefficients (P5) has the largest nMBE in all cities, with Auckland the poorest (-27%).

For P2 and P3, profiles of $L(z)$ have similar BE in all cities (Figure 5.8). In NYC, P3 tends to underestimate $L(z)$, and P2 overestimate $L(z)$, least. Across all cities, 90% (5-95th percentile, shading Figure 5.8) of both the P2 and P3 profiles are < 0.01 m^{-1} different from P0, except for Sao Paulo between 5 and 10 m. In London and Birmingham, both P2 and P3 overestimate $L(z)$ below z = 5 m but underestimate $L(z)$ above, while in Sao Paulo and Auckland the opposite occurs. Overall, the largest errors occur in Sao Paulo.

Consistent with the errors in total λ_w (Table 5.4), P4 and P5 perform the poorest for $L(z)$ (Figure 5.9), Generally, the $L(z)$ absolute value of BE are < 0.01 for P4 (black) and P5 (red, Figure 5.9) with close to 90% of the profiles being within magnitude of 0.02 of P0. For all cities when P5 is used, the range of the 5 - 95th percentile of profiles is wider.

Table 5.4: Evaluation of mean normalized wall area (λ_w) for six cities calculated using P2-P5 (Table 5.2) assessed using P0 with bias and normalised bias error (MBE and nMBE, section 5.3.4). Table 5.1 gives number of grid-cells analysed per city

City	P0	P2			P3			P4			P5		
	λ_w (m^2/m^2)	MBE (m^2/m^2)	nMBE (%)	MAE (m^{-1})	MBE (m^2/m^2)	nMBE (%)	MAE (m^{-1})	MBE (m^{-1})	nMBE (%)	MAE (m^{-1})	MBE (m^{-1})	MBE (%)	MAE (m^{-1})
Auckland	0.482	-0.0078	-2.3	-0.0078	-0.0077	-2.3	-0.0077	-0.060	-17	-0.0603	-0.088	-27	-0.088
Birmingham	0.165	-0.0030	-2.2	-0.0029	-0.0029	-2.2	-0.0029	-0.0054	-0.75	-0.0054	-0.020	-15	-0.020
Berlin	0.187	-0.0044	-2.1	-0.0044	-0.0045	-2.1	-0.0045	-0.012	-5.3	-0.012	0.0025	-8.4	0.0025
London	0.250	-0.0051	-2.2	-0.0050	-0.0050	-2.2	-0.0050	-0.016	-6.9	-0.016	-0.021	-15	-0.021
NYC	0.302	-0.011	-2.4	-0.011	-0.0067	-2.1	-0.0067	-0.053	-2.3	-0.053	0.069	11	0.069
Sao Paulo	0.287	-0.0069	-2.1	-0.0069	-0.0068	-2.0	-0.0068	-0.00088	3.7	-0.00088	-0.021	-9.5	-0.021

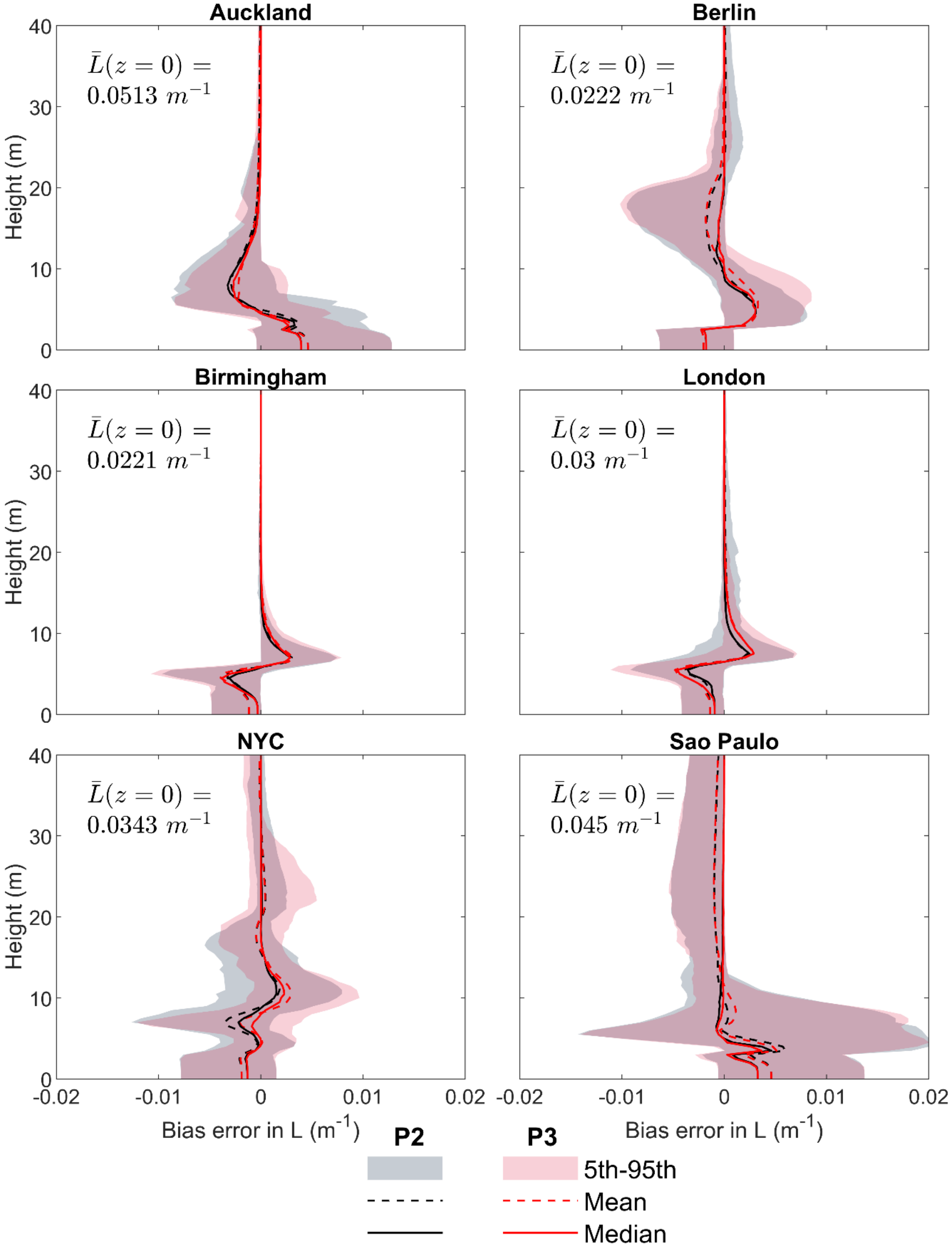

Figure 5.8: Mean building edge length at the surface ($\overline{L(0)}$) and vertical profiles of bias error (BE, section 5.3.4) of normalised building edge length (L) determined using P2 (grey) and P3 (red) (Table 5.2)

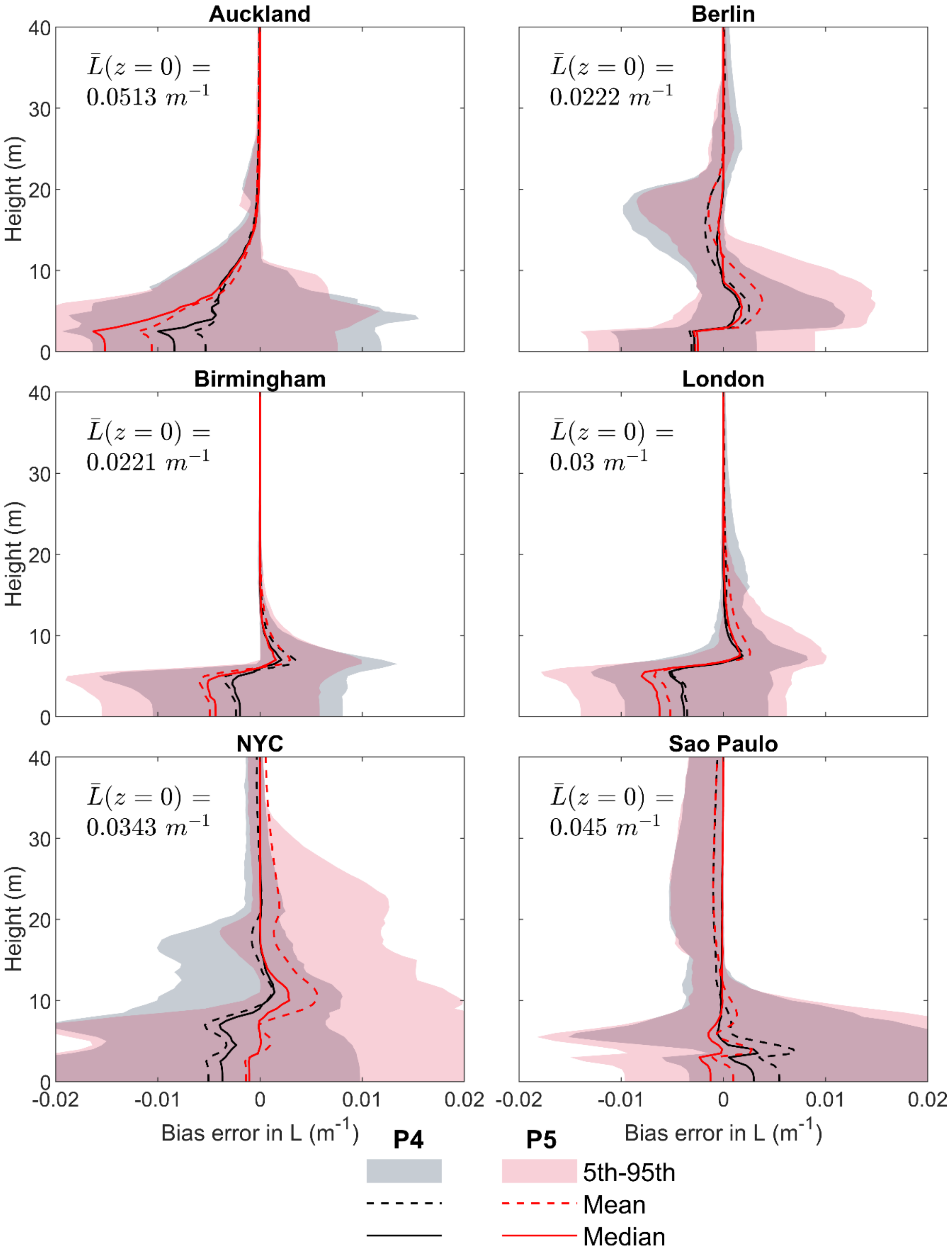

Figure 5.9: Mean building edge length at the surface ($\overline{L(0)}$) and vertical profiles of bias error (BE, section 5.3.4) of normalised building edge length (L) determined using P4 (grey) and P5 (red) (Table 5.2)

5.5 Impacts of applying parameterisations for λ_p and L in the SPARTACUS-Urban radiative transfer model

5.5.1 Impact on vertically integrated absorbed shortwave radiation

To assess the impact of approximating the urban morphology using parameterisations (P2-P5, Table 5.2) on simulated (section 5.3.3) total integrated shortwave absorption into urban facets, results are compared to the P0 in each grid-cell. Although three solar zenith angles (θ_0) are simulated, as θ_0 = 75° has the largest normalised bias errors (nBE) we focus on these, with the θ_0 = 0° and 45° results given in Figure 5.A.3 – Figure 5.A.6.

The SPARTACUS-Urban simulated wall absorption (a_{Wall}) with a θ_0 = 75°, generally have nMBE magnitudes > 3% for P2 (cf. > 15% as complexity increases to P5, Table 5.5) across all cities. Given poorer skill of the urban form parameterisations in Auckland (Section 5.4.4), the poorest a_{Wall} performance is consistent (P4 15%; P5 25%) (Table 5.5). The largest nBE in a_{Wall} occur when using P1-P3 in Auckland, NYC, and Sao Paulo, in areas with the largest $\lambda_p(z = 0)$ and $L(z =0)$ (Figure 5.2, cf. Figure 5.10). However, for P4 and P5 no clear relation is evident between grid-cell morphology and a_{Wall} nBE. Generally, P1 - P3 underestimate the absorption of radiation by walls (Table 5.5), which is consistent with the morphology results (Table 5.4).

Simulated a_{Roof}, using P2-P5 morphology, have all cities have a mean nBE < 5% (Table 5.5), and across all grid-cells the largest nBE magnitudes < 25% (Figure 5.11). Given the skill in morphology parameterisations (section 5.4), Sao Paulo and Auckland overestimate a_{Roof}, while London and Birmingham underestimate a_{Roof}. The highest nBE occur in areas with the largest $\lambda_p(z = 0)$ (e.g., CBD, industrial), and therefore P0 a_{Roof} is highest.

Across all parameterisations, many cities have an absolute value of nMBE in mean a_{Ground} of < 2% (Table 5.5), apart from P5 in Auckland (7.5%) and NYC (9%). The spatial patterns of a_{Ground} show underestimates in Auckland and Sao Paulo, but overestimates in the other cities when using P1-P3 (Figure 5.12).

Overall, the lowest nMBE occur when θ_0 = 0° with a_{Roof} and a_{Ground} nBE < 1% for all cities (Table 5.A.3); but with larger nMBE for a_{Wall} (2-5% for P1-P3, up to 50% for P4 and P5, Figure 5.A.3). When θ_0 = 45° the nMBE for a_{Wall} are similar to θ_0 = 0° (P1-P3 < 5%, and P4 and P5 > 50%; Table 5.A.2, Figure 5.A.4) and a_{Roof} (2-5%) with the largest nBE associated with larger $\lambda_p(z = 0)$. The $\theta_0 = 45°$ a_{Ground} values have nBE that are less than 10% (Table 5.A.2, Figure 5.A.6).

Table 5.5: Evaluation of SPARTACUS-Urban simulated total absorption when the solar zenith angle is 75° for (a) walls, (b) roof, and (c) ground facets assessed using P0 with bias and normalised bias error (MBE and nMBE, section 5.3.4). Table 5.1 gives number of grid-cells analysed per city

City	P0	P2			P3			P4			P5		
(a) Wall	Absorption (W m^{-2})	MBE (W m^{-2})	nMBE (%)	MAE (W m^{-2})	MBE (W m^{-2})	nMBE (%)	MAE (W m^{-2})	MBE (W m^{-2})	nMBE (%)	MAE (W m^{-2})	MBE (W m^{-2})	nMBE (%)	MAE (W m^{-2})
Auckland	68.3	-2.1	-2.7	-2.1	-2.02	-2.6	-2.0	-10	-15	-10	-16	-25	-16
Birmingham	31.9	-0.55	-1.9	-0.55	-0.53	-1.8	-0.53	-1.5	-1.1	-1.5	-4.9	-15	-4.9
Berlin	44.6	-0.74	-1.9	-0.74	-0.9	-2.0	-0.90	-2.1	-5.1	-2.1	-1.2	-9.4	-1.2
London	47.8	-0.68	-1.7	-0.68	-0.72	-1.7	-0.72	-3.2	-6.3	-3.2	-5.6	-14	-5.6
NYC	73.2	-0.89	-1.5	-0.89	-1.59	-2.1	-1.6	-4.8	-0.78	-4.8	0.22	5.4	0.22
Sao Paulo	62.5	-2.7	-3.3	-2.7	-2.66	-3.2	-2.7	-1.4	1.3	-1.4	-5.5	-10	-5.5
(b) Roof													
Auckland	37.9	1.8	3.5	1.8	1.7	3.2	1.7	2.4	4.7	2.4	2.6	5.2	2.6
Birmingham	18.0	-0.24	-0.95	-0.24	-0.31	-1.2	-0.31	-0.28	-0.92	-0.28	-0.28	-0.85	-0.28
Berlin	19.0	0.18	0.83	0.18	0.5	1.7	0.50	0.21	0.98	0.21	0.37	1.5	0.37
London	25.3	-0.47	-1.3	-0.47	-0.46	-1.5	-0.46	-0.46	-1.14	-0.46	-0.45	-1.1	-0.45
NYC	30.3	-0.31	-0.74	-0.31	0.8	1.9	0.80	0.12	0.39	0.12	0.21	0.51	0.21
Sao Paulo	41.4	3.0	5.0	3.0	2.8	4.9	2.8	2.9	5.0	2.9	2.9	5.2	2.9
(c) Ground													
Auckland	111	-0.31	-0.46	-0.097	-0.10	-0.40	0.0070	0.0070	-0.32	6.2	6.2	7.5	10
Birmingham	162	0.11	0.086	0.70	0.70	0.51	0.75	0.75	0.55	1.5	1.5	0.86	4.3
Berlin	150	0.066	0.043	0.44	0.44	0.40	0.25	0.25	0.17	1.5	1.5	1.4	0.58
London	140	0.15	0.16	1.0	1.0	1.0	1.1	1.1	0.95	3.1	3.1	2.4	5.1
NYC	115	0.26	0.36	1.1	1.1	1.7	0.53	0.53	0.12	4.0	4.0	9.0	-0.47
Sao Paulo	113	-0.40	-0.83	-0.72	-0.72	-1.8	-0.58	-0.58	-1.6	-1.7	-1.7	-2.4	1.6

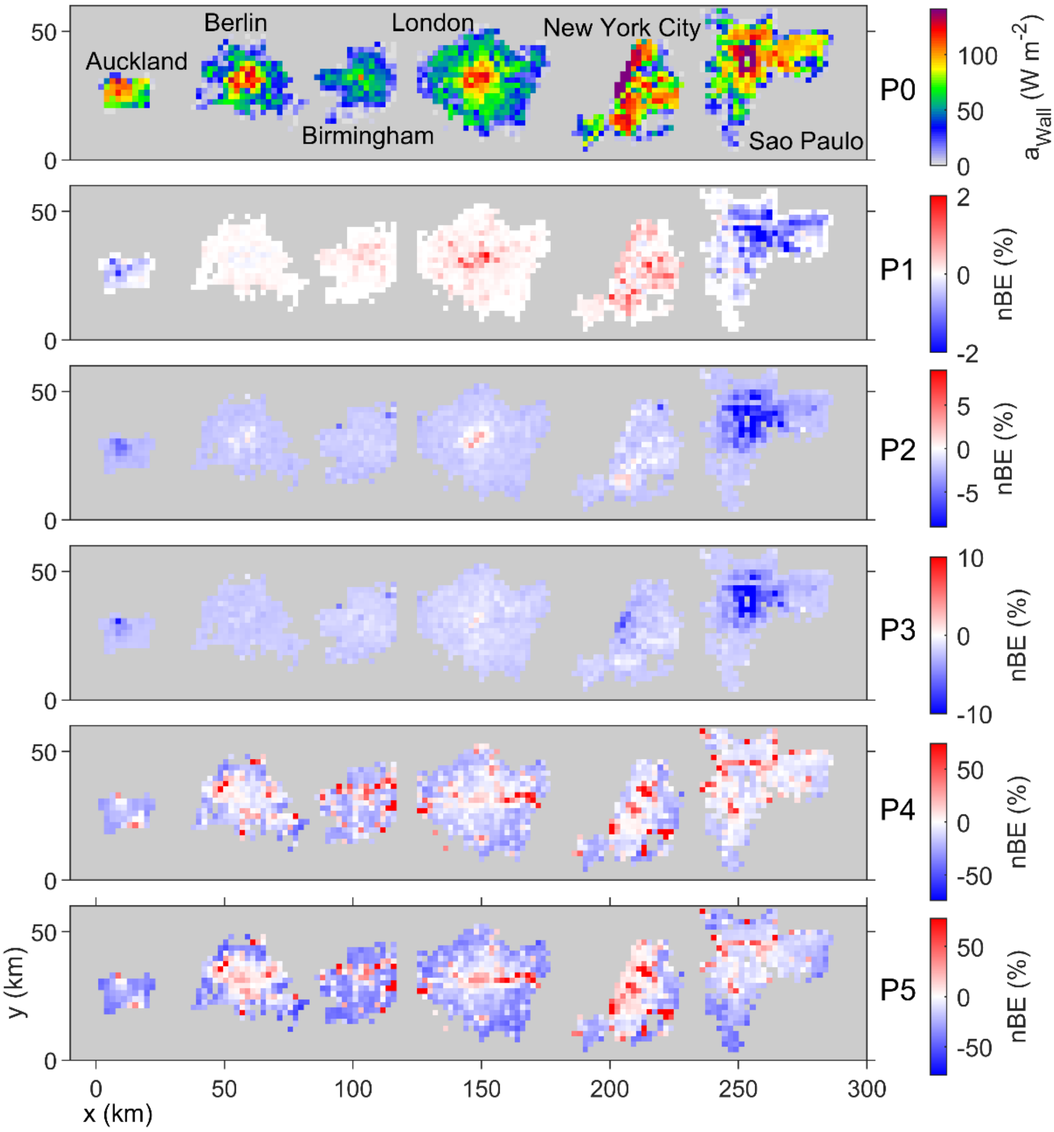

Figure 5.10: Total absorbed shortwave radiation into walls (a_{Wall}) modelled with SPARTACUS-Urban for a solar zenith angle (θ_0) of 75° for six cities using 'true' building fraction and building edge length vertical profiles (P0, Table 5.2), and normalised bias error (nBE, section 5.3.4) when using parameterised profiles (P1-P5). Note scales differ between rows. See Figure 5.A.3 for $\theta_0 = 0°$ and Figure 5.A.4 for $\theta_0 = 45°$

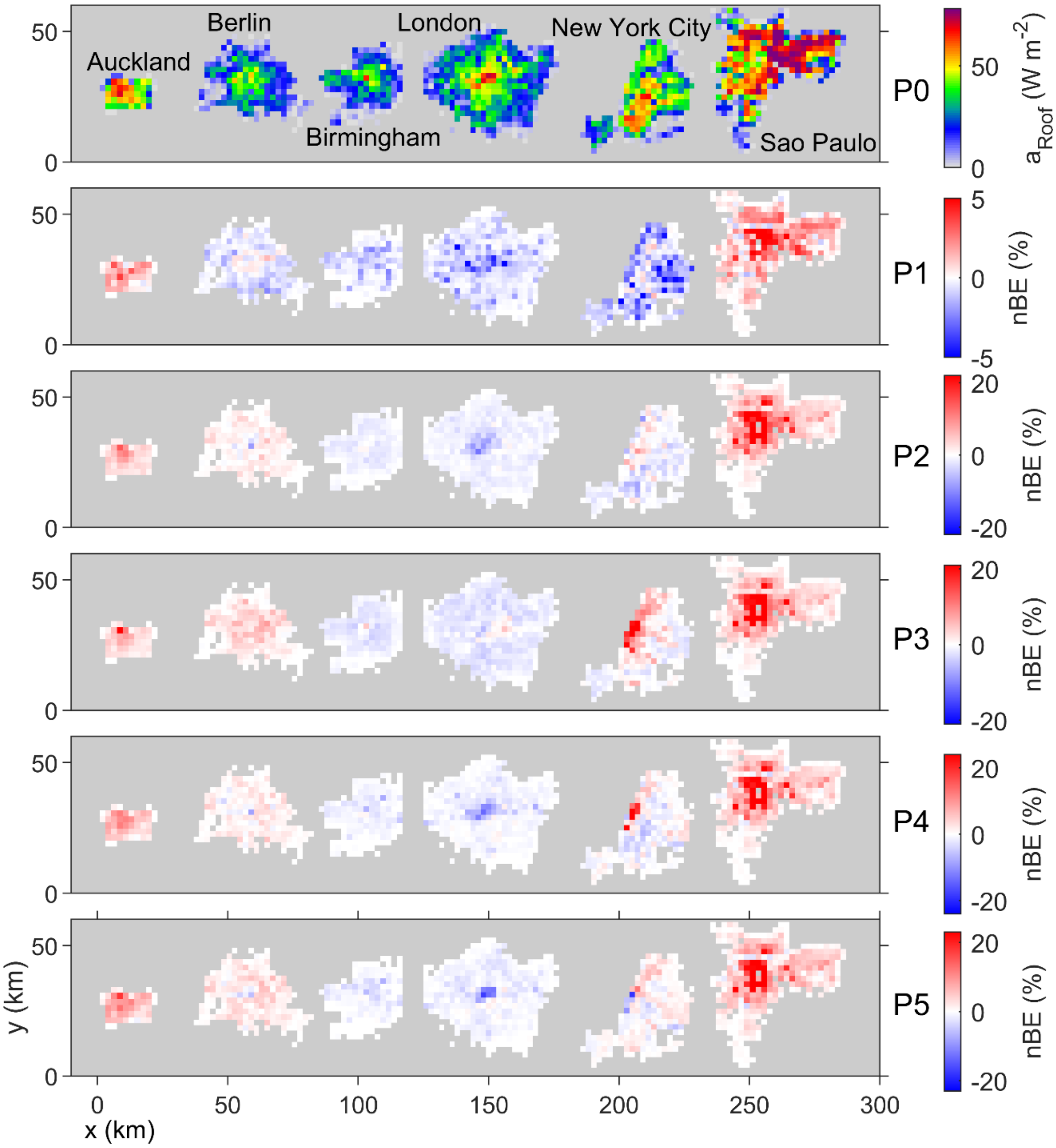

Figure 5.11: Total absorbed shortwave radiation into roofs (a_{Roof}) modelled with SPARTACUS-Urban for a solar zenith angle (θ_0) of 75° for six cities using 'true' building fraction and building edge length vertical profiles (P0, Table 5.2), and normalised bias error (nBE, section 5.3.4) when using parameterised profiles (P1-P5). Note scales differ between rows. See Figure 5.A.5 for $\theta_0 = 45°$

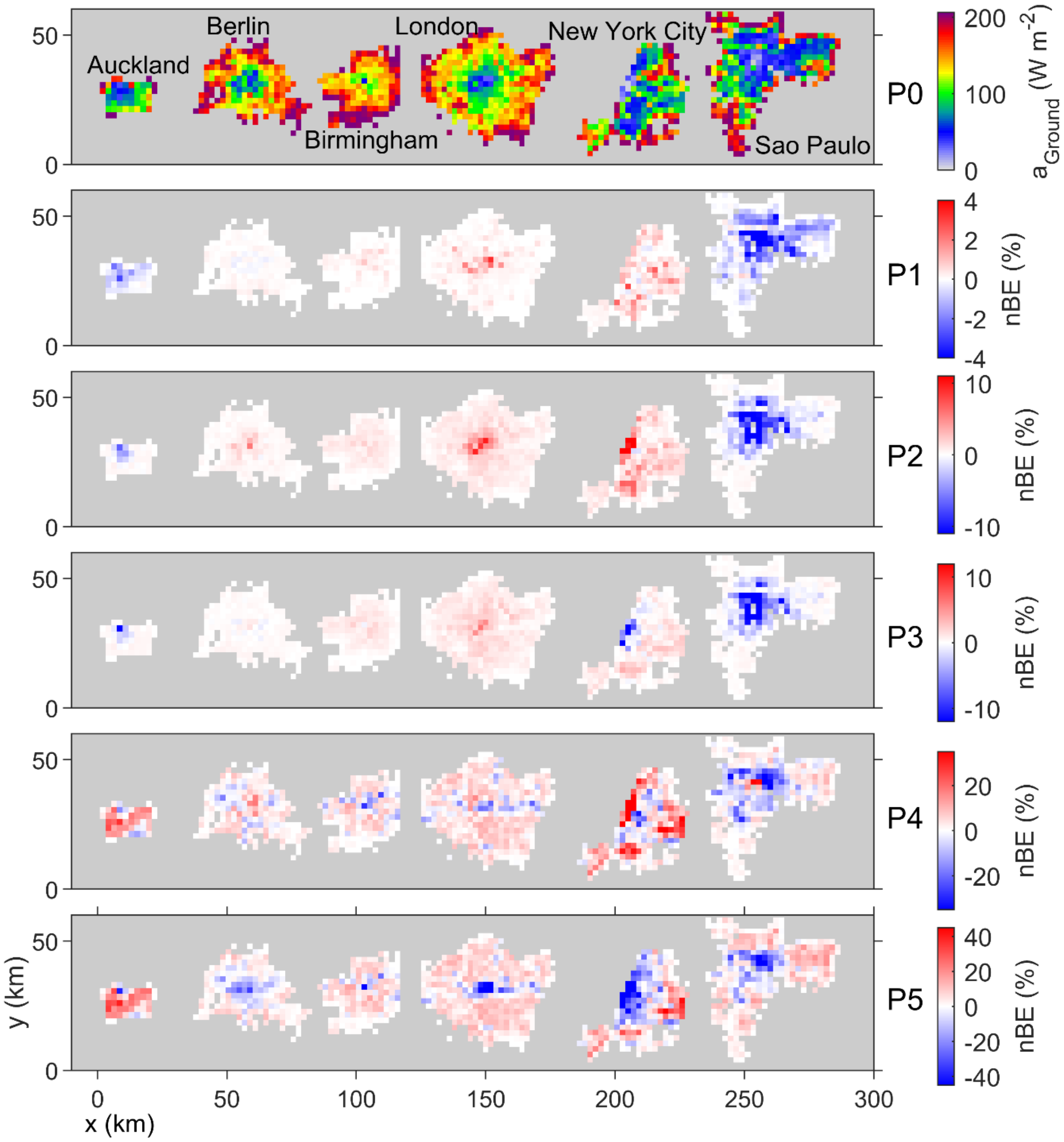

Figure 5.12: Total absorbed shortwave radiation into the ground (a_{Ground}) modelled with SPARTACUS-Urban for a solar zenith angle (θ_0) of 75° for six cities using 'true' building fraction and building edge length vertical profiles (P0, Table 5.2), and normalised bias error (nBE, section 5.3.4) when using parameterised profiles (P1-P5). Note scales differ between rows. See Figure 5.A.6 for $\theta_0 = 45°$

5.5.2 Impact on shortwave bulk albedo

We additionally assess the error in approximating the urban morphology using P2-P5 on the simulated bulk albedo for each grid-cell (i.e., ratio of upwelling to downwelling shortwave radiation at the top of the urban canopy). For all θ_0 values tested, the nBE have similar magnitudes across the six cities, so we focus on $\theta_0 = 45°$. The nBE results for $\theta_0 = 75°$ are slightly larger (Figure 5.A.7).

Simulated bulk albedo generally increases with parameterisation complexity (i.e., P1-P5), but all have an absolute nBE < 10% (Figure 5.13). This is smaller than the total facets absorption nBE (Figure 5.10 - Figure 5.12) that have a maximum of ±20-50% for P5 (largest for a_{Wall}). This suggests bulk effects result from within canopy compensation (i.e., some absorption overestimates and underestimates). The net result is a good approximation of the shortwave bulk albedo for all parameterisations. Unlike absorption, albedo has a similar trend for all six cities, being overestimated for P1-P3 in all grid-cells and for P4-P5 in most grid-cells. For the latter, notably P5, the albedo is underestimated in areas with the higher surface building fractions (Figure 5.2).

Hence, the crudest assumptions about urban form have low impact on the bulk albedo. However, this contrasts with the error in shortwave absorption (Section 5.5.1), suggesting that the within-canopy impacts work to cancel one another out.

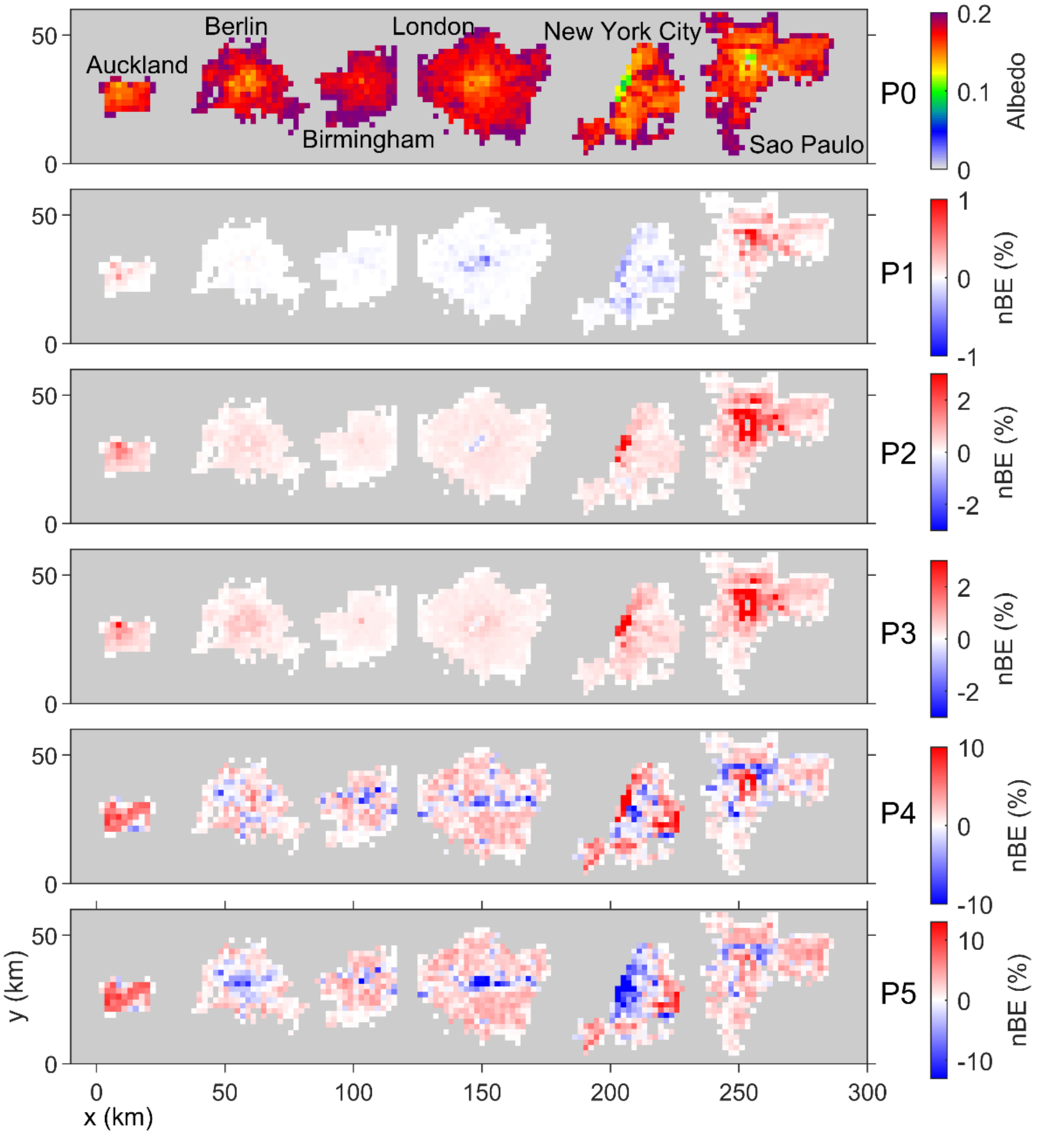

Figure 5.13: Bulk albedo modelled with SPARTACUS-Urban for a solar zenith angle (θ_0) of 45° for six cities using 'true' building fraction and building edge length vertical profiles (P0, Table 5.2), and normalised bias error (nBE, section 5.3.4) when using parameterised profiles (P1-P5). Note scales differ between rows. See Figure 5.A.7 for $\theta_0 = 75°$

5.6 Conclusions

Given the challenges in collecting urban morphology data (Masson et al. 2020a; Frantz et al. 2021), that are critical to simulating meteorological processes in cities (e.g. Hogan 2019b; Krayenhoff et al. 2020), we propose methods to parameterise vertical profiles of building plan area fraction (λ_p) and normalised building perimeter length (L). The latter is simply the vertically resolved normalised wall area.

Although profiles can be derived from high resolution building height data, few datasets with large spatial extent exist. Here, data are analysed for six cities (in Europe, North

America, Oceania, and South America) to derive both city specific and multi-city parameters, and to evaluate model skill.

The impact of parameter uncertainty is assessed using SPARTACUS-Surface (Hogan 2019a), shortwave radiation simulations of albedo, and shortwave radiation absorption by three urban facets (roof, walls, ground). The grid-cell bulk albedo has an absolute normalised bias error of ≤ 10% when using the urban form parameterisations. Albedo is more likely to be underestimated in high-density central-city areas when the most assumptions are made about the urban morphology. Reducing the assumptions made, and therefore increasing the knowledge of the urban morphology used within the parameterisation, decreases the absolute value of normalised bias errors to ≤ 2% for all areas of cities.

The low error in bulk albedo hides errors within the urban canopy introduced by the parameterisations, as errors in shortwave absorption appear to cancel out. This may make the parameterisations acceptable for use with more complex models. Generally, low (< 20%) absolute values of normalised errors in absorption occur at when the sun is overhead, when building fraction parameterisation is more influential (cf. wall area parameterisation). The largest normalised bias errors (up to 50%) occur in wall absorption for larger solar zenith angles, when wall area is assumed unknown (Section 5.4.4, 5.5.1). Thus, trying to overcome a lack of urban form data through parameterisations introduces larger errors. Hence, if vertical profiles of radiation absorption are the focus, appropriate wall area data are critical.

We conclude that building height variations can be approximated using a function of mean building height and surface λ_p. Parameters are derived for both all-cities and each city. Overall, 90% of the profiles have building fraction error < $\pm$0.03 at any height (cf. ‘true’ data). As there is little difference between the two methods in four out of six cities analysed, it suggests the multi-city approach may be acceptable.

Additionally, we find intra-city building horizontal extent can be approximated using an effective building diameter D derived either as function of mean building height and λ_p, or from the ‘true’ wall area. The latter is most constrained by data availability. Although we treat D as constant with height, we find evidence suggesting two values may improve representation of vertical variability. The near ground (for areas with $\lambda_p > 0.05$) mean D across all six cities is ~21 m. For all methods used to determine D, the absolute value of median bias error is < 6%, with the magnitude of bias error of 90% of all profiles < 0.02 m^{-1} (cf. 0.02-0.05 m^{-1} at the surface).

The proposed parameterisations can be combined to give a full description of the vertical morphology, with five combinations used here, with decreasing data requirements. Little skill is lost from using a more general (cf. detailed) parameterisation for λ_p. Parameterisation of L has a larger impact on wall area. If wall area is known but λ_p is parameterised, the mean total wall area is calculated within 3% for all cities, whereas if wall area is unknown this error can increase by up to an order of magnitude. The parameterisations for the six cities perform best in areas with both low λ_p and L (e.g., suburban areas). In denser areas, errors are generally larger and increase without knowledge of wall area. Additionally, in denser areas the errors in absorbed shortwave and bulk albedo may have opposite signs of those in the outer city.

Overall, as our parameterisations can characterise vertical profiles of λ_p and L they have utility in multi-layer urban canopy models (e.g., SPARTACUS-Urban, BEP, TEB). However, the uncertainty in radiative fluxes shown here will impact other modelled fluxes (e.g., storage and sensible heat fluxes) so future work should assess these cascading effects. Alongside this, as the morphology within a given grid cell influences the surface roughness, future work could include assessing the impact of the parameterisations developed here on the momentum transfer. Here, only λ_p and mean building height data are used to approximate urban form. Including building wall area information would improve this, but it is the most challenging of the three variables to obtain. Additionally, we note that the coefficients and best-fit parameters derived here, which impact absorption and albedo, may change as the range and mean of cities properties are expanded and analysed at different scales.

If only mean building height and plan area fraction are available for a city at grid resolution, building height and λ_p can be derived from existing empirical relations, such as Bohnenstengel et al. (2011), that are currently applied globally, despite being developed from data from a single city. But, these relations require input data (i.e., built or ‘urban’ [*sic*] fraction). Thus, there is a clear and increasing need to improve global datasets of urban morphological parameters for weather and climate models, but also for a wide range of other applications that use the outputs from these models for decision making and managing cities day-to-day, in emergencies and for the long-term changes (both climate and urban).

Acknowledgements

Funding from the NERC Scenario Doctoral Training Partnership Grant, EPSRC 2130186, EPRSC DARE EP/P002331/1, ERC Synergy *urbisphere (855005)*, and Newton Fund/Met Office CSSP China NGC (SG). Processed data for Berlin: Karthik Reddy, Andreas Christen, Environmental Atlas Berlin; Auckland, New York City, and Sao Paulo: Christoph Kent for rasterised data. All data and code are archived at https://zenodo.org/10.5281/zenodo.5851021.

Appendix 5.A: Supplementary material for Chapter 5

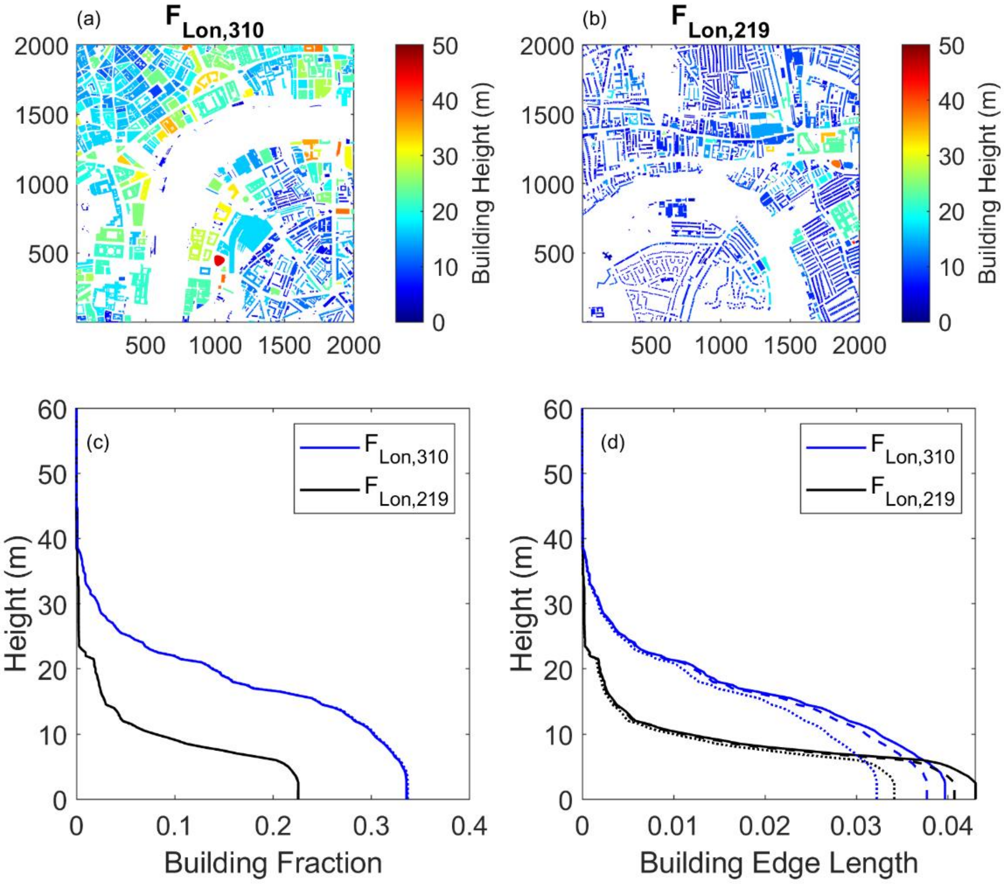

Figure 5.A.1: Morphology for two 2 km × 2 km grid boxes in central London ($F_{Lon,310}$, $F_{Lon,219}$), with (a, b) building height maps, and profiles of building (c) plan area fraction and (d) normalised edge length Profiles are for the two 2 km × 2 km areas when rasterised at 1 m (solid), 4 m (dashed) and 10 m (dotted) for $F_{Lon,310}$ (blue) and $F_{Lon,219}$ (black)

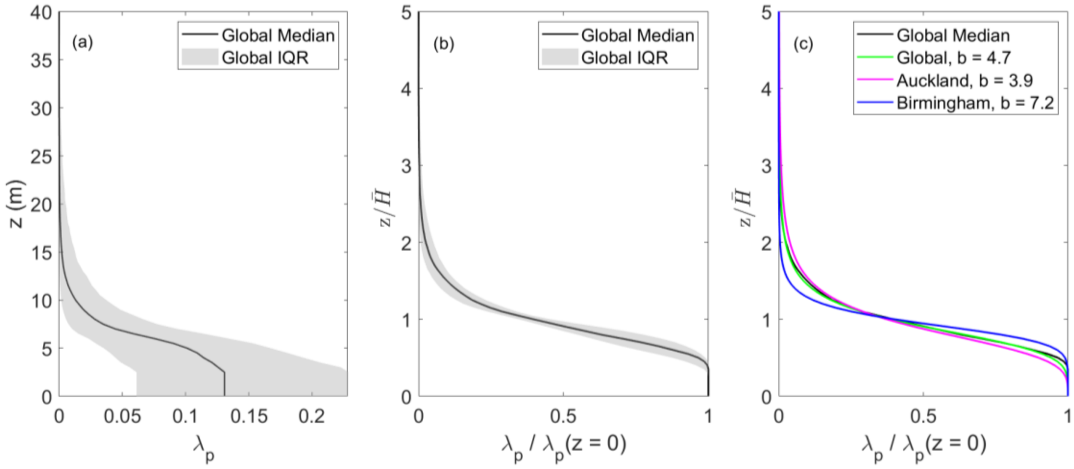

Figure 5.A.2*:* Demonstration of the methods to parameterised plan area fraction (λ_p) for both *variable b* and *fixed b* parameterisations: (a) vertical profiles of λ_p from all cities (Table 5.1) with multi-city median (line) and inter-quartile range (IQR, shading), (b) vertical profiles normalised by $\overline{H}$ and $\lambda_p(z = 0)$ to obtain y(x) in Eq. 5.2, (c) normalised vertical profiles (Eq. 5.2) with curves (Eq. 5.4) with *b* values derived from real-world city data (Table 5.2) including global ('fixed b')

Table 5.A.1: Comparison of surface building fraction ($\lambda_p(z = 0)$), surface normalised edge length ($L(z = 0)$), and mean building height ($\overline{H}$) for two London grid-cells ($F_{Lon,310}$, F_{Lon219}, Figure 5.A.1) when rasterised at 1 m, 4 m, and 10 m

	$\lambda_p(z = 0)$			$\overline{H}$ (m)			L(z = 0)		
	1 m	4 m	10 m	1 m	4 m	10 m	1 m	4 m	10 m
$F_{Lon,310}$	0.336	0.336	0.337	18.7	18.7	18.7	0.0397	0.0377	0.0322
$F_{Lon,219}$	0.226	0.225	0.226	10.2	10.2	10.2	0.0430	0.0407	0.0341

Table 5.A.2: Evaluation of SPARTACUS-Urban simulated total absorption when the solar zenith angle is 45° for (a) walls, (b) roof, and (c) ground facets assessed using P0 with bias and normalised bias error (MBE and nMBE, section 5.3.4). Table 5.1 gives number of grid-cells analysed per city

City	Total Absorption P0 (W m^{-2})	P2			P3			P4			P5		
		MBE (W m^{-2})	nMBE (%)	MAE (W m^{-2})	MBE (W m^{-2})	nMBE (%)	MAE (W m^{-2})	MBE (W m^{-2})	nMBE (%)	MAE (W m^{-2})	MBE (W m^{-2})	nMBE (%)	MAE (W m^{-2})
(a) Wall													
Auckland	73.0	-1.9	-2.4	-1.9	-1.9	-2.4	-1.9	-12	-17	-12	-18	-27	-18
Birmingham	30.8	-0.62	-2.1	-0.62	-0.6	-2.0	-0.60	-1.3	-0.9	-1.3	-4.7	-15	-4.7
Berlin	45.1	-0.87	-2.0	-0.87	-0.95	-2.1	-0.95	-2.3	-5.2	-2.3	-0.19	-8.8	-0.19
London	50.1	-0.94	-2.0	-0.94	-0.96	-2.0	-0.96	-3.4	-6.7	-3.4	-5.2	-15	-5.2
NYC	82.3	-1.7	-2.0	-1.7	-1.8	-2.1	-1.8	-8.2	-1.8	-8.2	4.6	8.1	4.6
Sao Paulo	67.7	-2.1	-2.5	-2.1	-2.1	-2.5	-2.1	-0.71	2.8	-0.71	-5.2	-9.9	-5.2
(b) Roof													
Auckland	116	1.5	0.94	1.5	1.4	0.86	1.4	2.0	1.3	2.0	2.2	1.4	2.2
Birmingham	50.3	-0.18	-0.26	-0.18	-0.23	-0.33	-0.23	-0.22	-0.25	-0.22	-0.22	-0.23	-0.22
Berlin	56.0	0.18	0.25	0.18	0.45	0.49	0.45	0.21	0.3	0.21	0.33	0.44	0.33
London	72.1	-0.37	-0.35	-0.37	-0.35	-0.4	-0.35	-0.38	-0.32	-0.38	-0.38	-0.31	-0.38
NYC	92.8	-0.17	-0.15	-0.17	0.96	0.62	0.96	0.36	0.21	0.36	0.14	0.12	0.14
Sao Paulo	129	2.6	1.3	2.6	2.5	1.3	2.5	2.6	1.3	2.6	2.6	1.4	2.6
(c) Ground													
Auckland	398	-0.26	-0.12	-0.26	-0.17	-0.10	-0.17	6.7	1.9	6.7	11	3.0	11
Birmingham	494	0.62	0.14	0.62	0.67	0.15	0.67	1.1	0.19	1.1	3.4	0.66	3.4
Berlin	478	0.45	0.11	0.45	0.22	0.047	0.22	1.4	0.35	1.4	-0.38	-0.24	-0.38
London	458	1.1	0.28	1.1	1.1	0.26	1.1	2.8	0.61	2.8	3.9	0.71	3.9
NYC	414	1.5	0.50	1.5	0.3	-0.068	0.30	5.9	2.3	5.9	-4.1	-2.1	-4.1
Sao Paulo	388	-1.3	-0.55	-1.3	-1.2	-0.52	-1.2	-2.2	-0.77	-2.2	0.93	0.05	0.93

Table 5.A.3: Evaluation of SPARTACUS-Urban simulated total absorption when the solar zenith angle is 0° for (a) walls, (b) roof, and (c) ground facets assessed using P0 with bias and normalised bias error (MBE and nMBE, section 5.3.4). Table 5.1 gives number of grid-cells analysed per city

City	Total Absorption P0 (W m^{-2})	P2			P3			P4			P5		
		MBE (W m^{-2})	nMBE (%)	MAE (W m^{-2})	MBE (W m^{-2})	nMBE (%)	MAE (W m^{-2})	MBE (W m^{-2})	nMBE (%)	MAE (W m^{-2})	MBE (W m^{-2})	nMBE (%)	MAE (W m^{-2})
(a) Wall													
Auckland	22.0	-0.6	-2.5	-0.60	-0.59	-2.5	-0.59	-3.5	-16.1	-3.5	-5.2	-26	-5.2
Birmingham	9.73	-0.18	-2.0	-0.18	-0.17	-1.9	-0.17	-0.42	-1.0	-0.42	-1.5	-15	-1.5
Berlin	13.9	-0.25	-1.9	-0.25	-0.28	-2.0	-0.28	-0.68	-5.1	-0.68	-0.2	-8.9	-0.18
London	15.5	-0.25	-1.8	-0.25	-0.26	-1.8	-0.26	-1.0	-6.5	-1.0	-1.6	-14	-1.6
NYC	24.4	-0.44	-1.8	-0.44	-0.51	-2.0	-0.51	-2.2	-1.6	-2.1	1.1	7.1	1.1
Sao Paulo	20.3	-0.71	-2.8	-0.71	-0.70	-2.7	-0.70	-0.31	2.2	-0.31	-1.6	-10	-1.6
(b) Roof													
Auckland	170	-0.041	-0.018	-0.041	-0.038	-0.016	-0.038	-0.0493	-0.021	-0.049	-0.052	-0.023	-0.052
Birmingham	71.8	0.0062	0.0063	0.0062	0.0081	0.0081	0.0081	0.0067	0.0060	0.0067	0.007	0.006	0.0070
Berlin	81.6	-0.0055	-0.0057	-0.0055	-0.013	-0.010	-0.013	-0.0058	-0.0062	-0.0058	-0.012	-0.0104	-0.012
London	104	0.011	0.0077	0.0112	0.011	0.0094	0.011	0.011	0.0070	0.011	0.0097	0.007	0.0097
NYC	138	0.0074	0.0044	0.0075	-0.018	-0.0075	-0.018	0.0039	0.0026	0.0039	-0.017	-0.0069	-0.017
Sao Paulo	193	-0.070	-0.023	-0.070	-0.065	-0.022	-0.065	-0.069	-0.023	-0.06	-0.068	-0.023	-0.068
(c) Ground													
Auckland	631	-0.0047	-0.00062	-0.0047	-0.0066	-0.00094	-0.0066	-0.16	-0.027	-0.16	-0.26	-0.044	-0.26
Birmingham	728	-0.017	-0.0025	-0.017	-0.0183	-0.0026	-0.018	-0.039	-0.0049	-0.039	-0.114	-0.015	-0.11
Berlin	719	-0.011	-0.0015	-0.010	-0.0074	-0.0010	-0.0074	-0.039	-0.0053	-0.039	-0.022	-0.0019	-0.022
London	697	-0.024	-0.0036	-0.024	-0.025	-0.0037	-0.025	-0.077	-0.011	-0.077	-0.13	-0.018	-0.13
NYC	663	-0.025	-0.004	-0.025	-0.016	-0.0025	-0.016	-0.095	-0.015	-0.095	0.012	0.0029	0.012
Sao Paulo	608	0.007	0.0017	0.0070	0.0044	0.0012	0.0044	0.031	0.0062	0.031	-0.052	-0.0079	-0.052

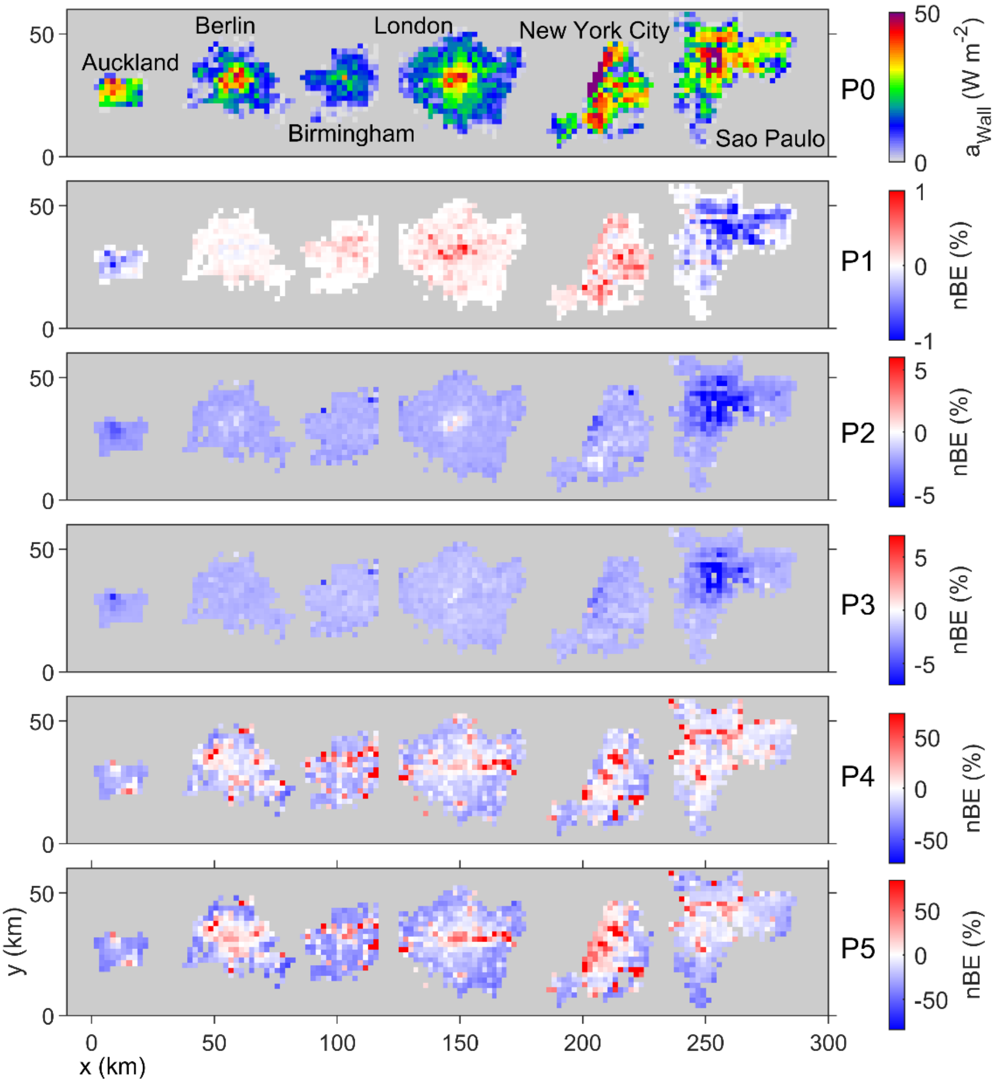

Figure 5.A.3: Total absorbed shortwave radiation into walls (a_{Wall}) modelled with SPARTACUS-Urban for a solar zenith angle (θ_0) of 0° for six cities using 'true' building fraction and building edge length vertical profiles (P0, Table 5.2), and normalised bias error (nBE, section 5.3.4) when using parameterised profiles (P1-P5). Note scales differ between rows

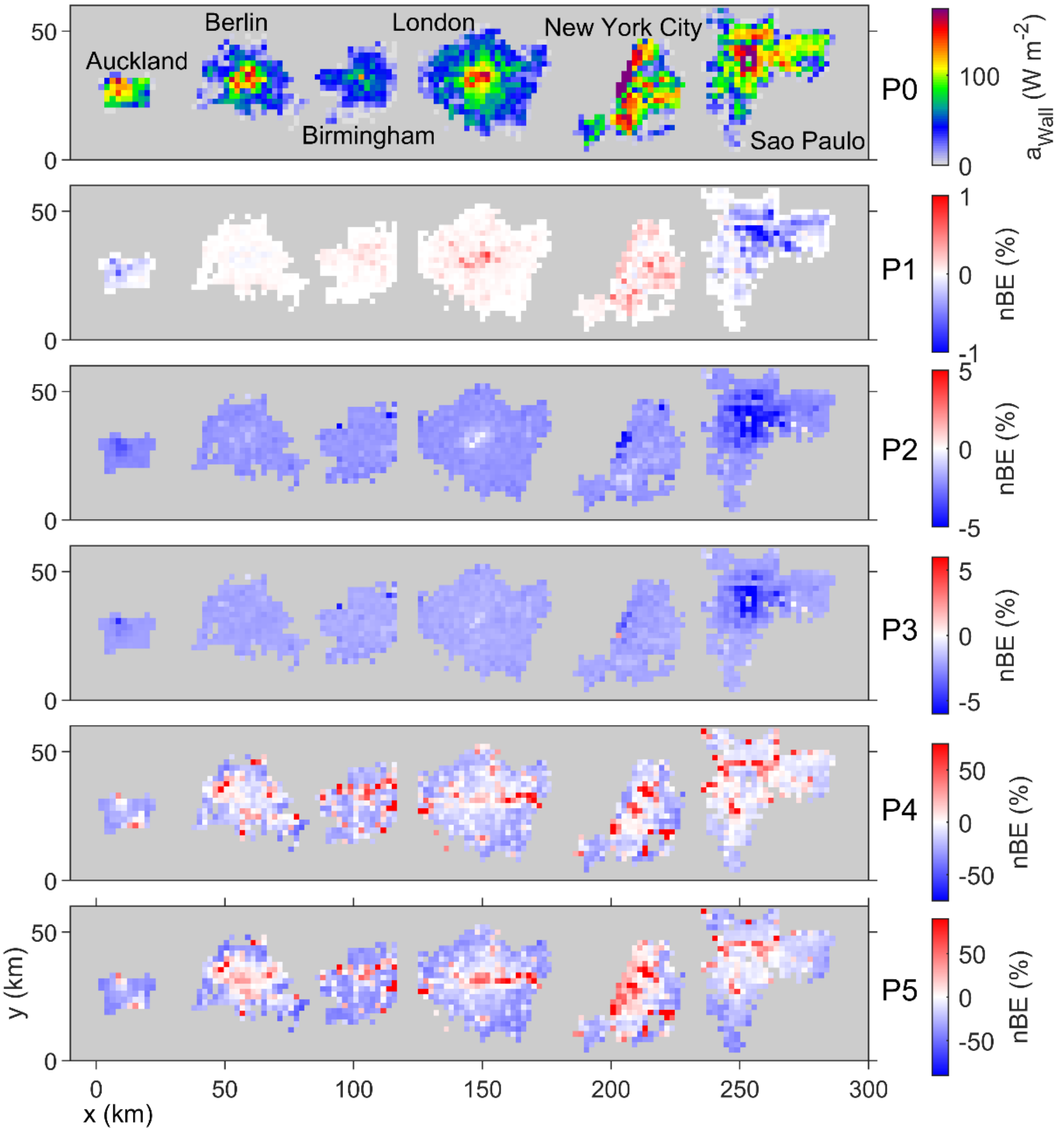

Figure 5.A.4: Total absorbed shortwave radiation into walls (a_{Wall}) modelled with SPARTACUS-Urban for a solar zenith angle (θ_0) of 45° for six cities using 'true' building fraction and building edge length vertical profiles (P0, Table 5.2), and normalised bias error (nBE, section 5.3.4) when using parameterised profiles (P1-P5). Note scales differ between rows

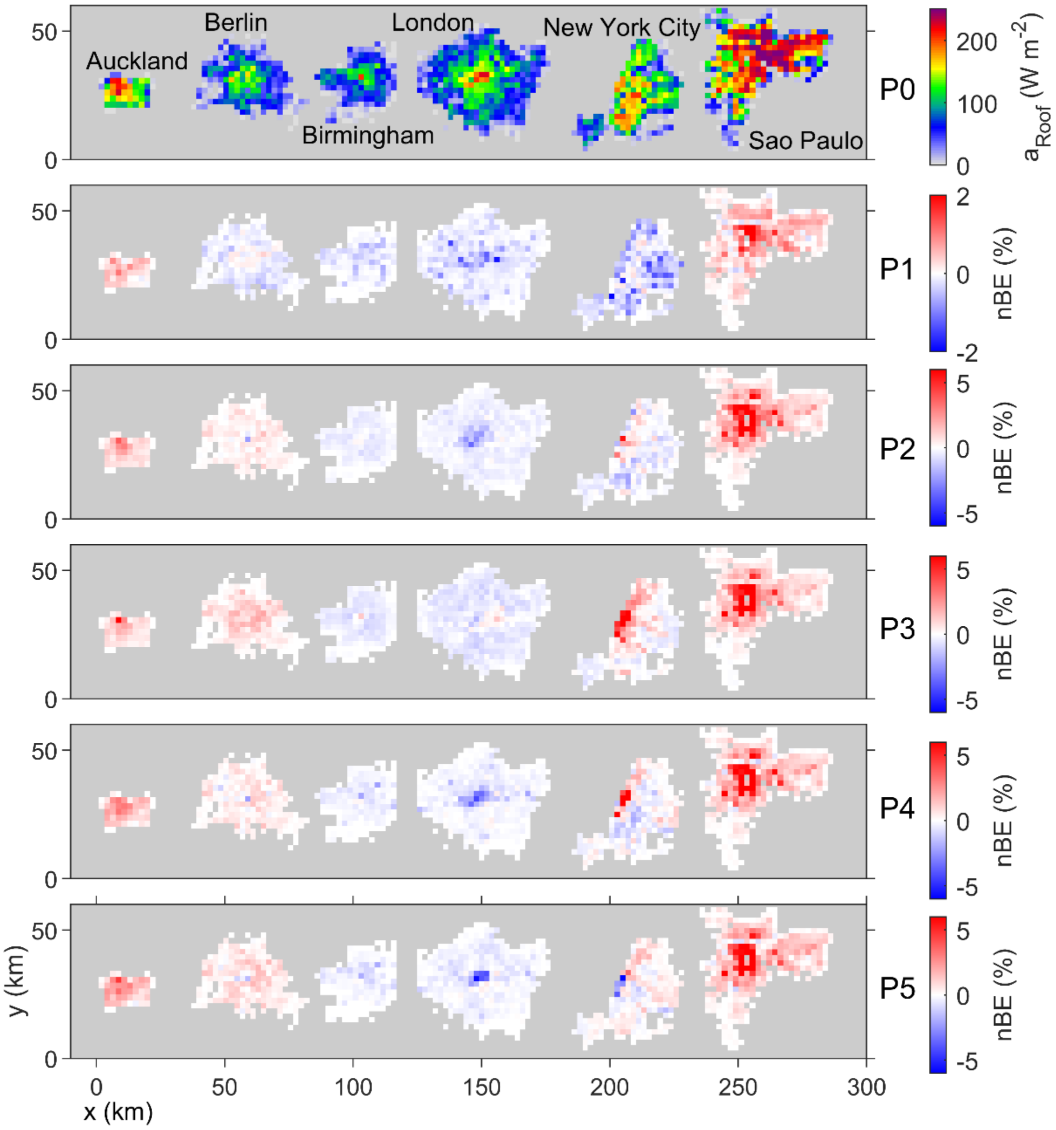

Figure 5.A.5: Total absorbed shortwave radiation into roofs (a_{Roof}) modelled with SPARTACUS-Urban for a solar zenith angle (θ_0) of 45° for six cities using 'true' building fraction and building edge length vertical profiles (P0, Table 5.2), and normalised bias error (nBE, section 5.3.4) when using parameterised profiles (P1-P5). Note scales differ between rows

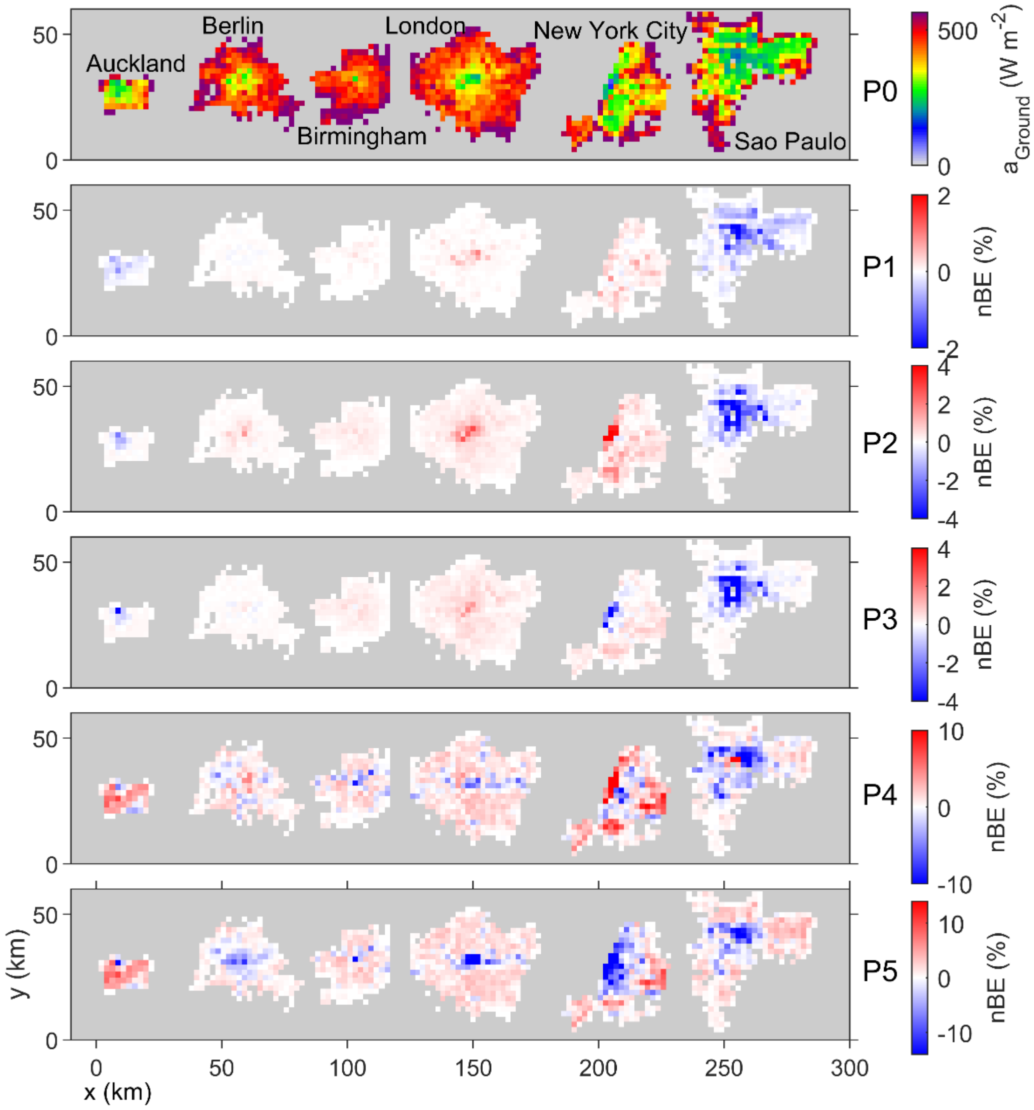

Figure 5.A.6*:* Total absorbed shortwave radiation into the ground (a_{Ground}) modelled with SPARTACUS-Urban for a solar zenith angle (θ_0) of 45° for six cities using 'true' building fraction and building edge length vertical profiles (P0, Table 5.2), and normalised bias error (nBE, section 5.3.4) when using parameterised profiles (P1-P5). Note scales differ between rows

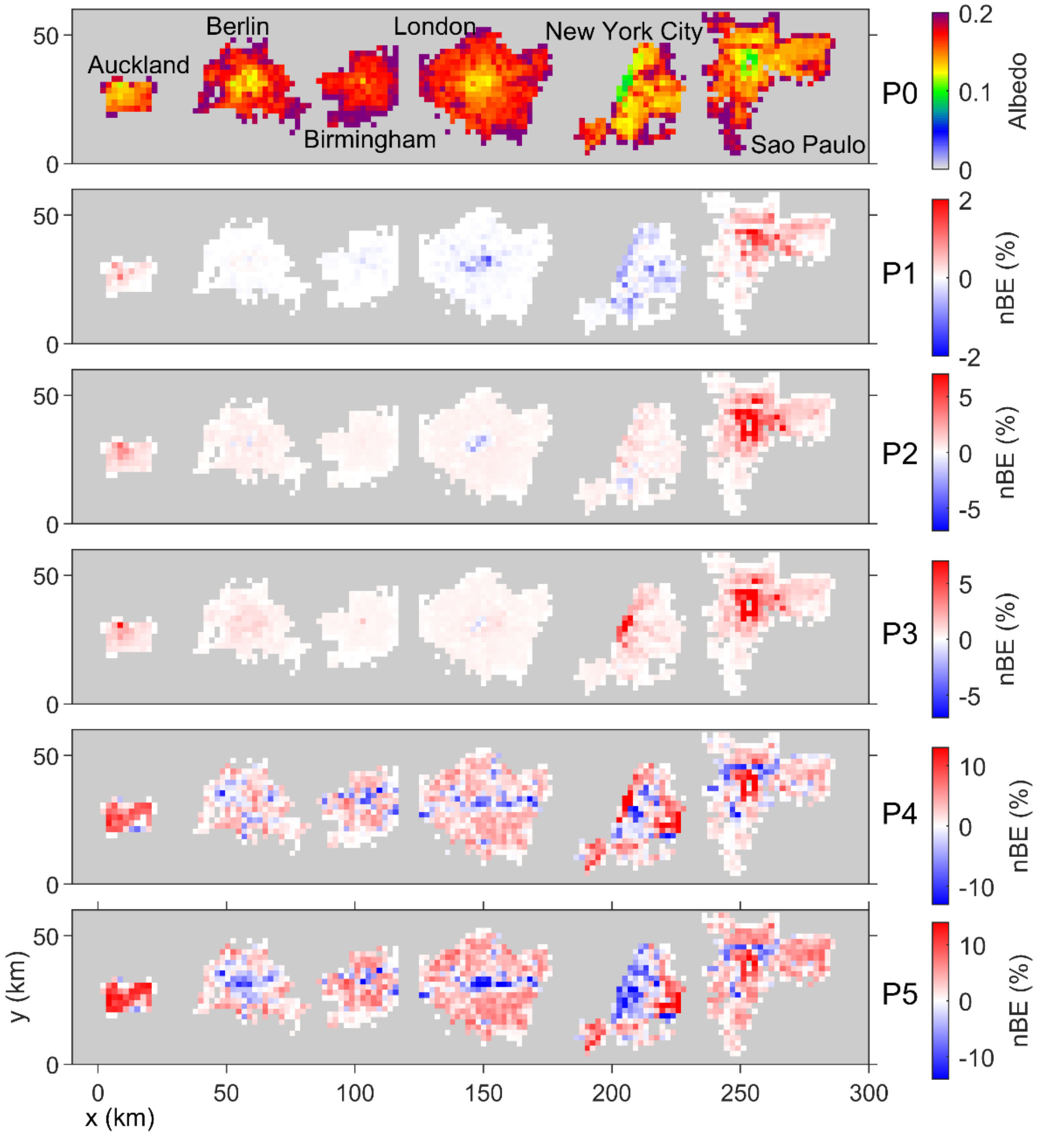

Figure 5.A.7: Bulk albedo modelled with SPARTACUS-Urban for a solar zenith angle (θ_0) of 75° for six cities using 'true' building fraction and building edge length vertical profiles (P0, Table 5.2), and normalised bias error (nBE, section 5.3.4) when using parameterised profiles (P1-P5). Note scales differ between rows

Chapter 6 Vertical variability of urban morphology: implications for modelling surface fluxes and temperatures[3]

Abstract

The variable nature of urban morphology and materials, in both the horizontal and vertical plane, influence heat exchanges and urban facet (e.g., wall, roof) temperature evolution. In this study, SUEWS (Surface Energy and Water balance Scheme) and the multi-layer radiation model SPARTACUS-Surface are coupled to a new multi-layer explicit heat conduction scheme (mEHC) for deriving the storage heat flux (hereafter SUEWS-SS-mEHC). The developed model is evaluated and tested in both single- and multi-layer configurations. Using surface temperature observations for a summer day in central London, it is concluded that using SUEWS-SS-mEHC with multiple layers (nine spanning 0 – 100 m) improves the simulated mean roof temperature, with an ~ 5 °C reduction cf. single-layer (layer up to 25.5 m). However, the multi-layer simulation gives warmer daytime wall temperatures cf. single-layer and observations. Although, sensitivity studies show that this could be strongly driven by choice of thermal material parameters. Nine areas with realistic urban morphology are simulated using multiple-layers in SUEWS-SS-mEHC. Comparing across the nine areas, when building cover is low (plan area fraction < 0.1) the effective bulk albedo is higher, ground temperatures warmer, and cooling rates higher (cf. denser morphologies). The relations between morphology and fluxes become complex as mean building height increases, and as building height variability increases. Although vertical gradients in facet temperature are small, even with a range < 10 °C, large differences in simulated storage and sensible heat fluxes occur, indicating the importance and impacts of vertically resolving the urban canopy.

6.1 Introduction

Most numerical weather prediction (NWP) models have a basic representation of cities, but with increasing computer resources, developers are considering increasing horizontal resolution (Barlow et al. 2017; Lean et al. 2019). With more detail, there is a need to

---

[3] This chapter is in preparation for submission with the following co-authors: Megan Stretton, Ting Sun, Sue Grimmond, Robin Hogan, Lewis Blunn, Ruidong Li, William Morrison, Denise Hertwig

improve process parameterisation and features (e.g., tall buildings, building height variability) (Hertwig et al. 2021), allowing better prediction and monitoring of conditions (e.g., heat stress, air quality) that impact the increasing urban population. This is particularly critical with predicted increases in both the frequency and intensity of heatwave events (IPCC 2014a).

Interactions between cities and the atmosphere are modified by factors such as building density, building materials and human activities. These are constrained by the surface energy balance (SEB) (Oke et al. 2017):

$$Q^* + Q_F = Q_H + Q_E + \Delta Q_S, \tag{6.1}$$

where Q_F is the anthropogenic heat flux, Q_H is the sensible heat flux, Q_E the latent heat flux, ΔQ_S the net storage flux, and Q^* is the net all-wave radiation. Some areas within cities may have low Q_E when vegetated fractions are small, allowing increased Q_H (Christen and Vogt 2004; Rotach et al. 2005; Offerle et al. 2006b). In densely built areas, Q_H may remain positive throughout the night, because of the release of the large ΔQ_S and low sky view factors (ψ_{Sky}) (Grimmond et al. 1991; Grimmond and Oke 1999a; Harman and Belcher 2006; Kawai and Kanda 2010).

The Q^* combines the net shortwave (SW*) and longwave (LW*) radiative fluxes:

$$\mathrm{Q}^* = \mathrm{SW}^* + \mathrm{LW}^* = \mathrm{SW}_\downarrow - \mathrm{SW}_\uparrow + \mathrm{LW}_\downarrow - \mathrm{LW}_\uparrow, \tag{6.2}$$

which result from the upwelling (e.g., $\mathrm{SW}_\uparrow$) and downwelling (e.g., $\mathrm{SW}_\downarrow$) components. In low latitude cities, Q^* is the predominate SEB source term. But at high latitudes in winter, Q_F may dominate (Ichinose et al. 1999). As with any environment, Q^* is driven by daytime SW fluxes and LW fluxes at night. Combinations of both urban materials with high heat capacities, albedos (α) and emissivities (ε) (e.g., tarmac, concrete (Oke 1987; Kotthaus et al. 2014)), and urban morphology (e.g., corrugated structure, street orientation, building separation) influence the trapping and absorption of SW and LW radiation. Morphology influences shadow patterns, causing sub-facet variations in $\mathrm{SW}_\downarrow$ influencing surface temperatures (T) (Lindberg and Grimmond 2011b; Yang and Li 2015; Morrison et al. 2018, 2021). Surface temperature is required to calculate $LW_\uparrow$, ΔQ_S and Q_H, and therefore impacts fluxes into the boundary layer.

Within-canopy (ground, walls) surfaces and roofs exhibit different SEB (Harman and Belcher 2006) as they have different ψ_{Sky}, which influences their receipt and loss of SW and LW radiation (Oke 1981; Arnfield 1990; Voogt et al. 1997). Roofs have both the highest daytime surface temperatures (*T*) and highest overnight cooling rates (Morrison et al. 2021), and are a key interface between the urban canopy layer and the urban boundary layer (Mills 1993; Loridan et al. 2010), potentially influencing large-scale conditions. However, within-canopy fluxes influence the conditions experienced by pedestrians, and so are of interest for many applications.

Canopy flux exchange processes need to be parameterised for NWP (Masson 2006). Despite such fluxes being impacted by heterogeneity, NWP simplifies the geometry in a given area, such as assuming one mean building height (e.g., Masson (2000); Harman et al. (2004); Porson et al. (2010)). For radiation this neglects vertical variation of SW and LW (Chapter 3, Chapter 4), and the role of wall area critical for simulation of ΔQ_S (Lindberg et al. 2020). Multi-layer models with different approaches to represent the urban structure are being adopted for radiation (e.g., Schubert et al. (2012); Hogan (2019)), airflow (e.g., Martilli et al. (2002); Krayenhoff et al. (2020); Tang et al. (2021)), and energy balance fluxes (e.g. Hamdi and Masson (2008)).

For this work, the SUEWS (Surface Urban Energy and Water balance Scheme, (Järvi et al. 2011, 2014; Ward et al. 2016) is coupled to the SPARTACUS-Surface (SS) multi-layer radiative transfer model (Hogan 2019a) and new multi-layer heat explicit conduction (mEHC), hereafter SUEWS-SS-mEHC. SPARTACUS-Surface's skill has been evaluated using the DART explicit radiative transfer model (Gastellu-Etchegorry et al. 2015) for both SW (Chapter 3) and LW (Chapter 4) for real-world morphologies. The facet absorption profiles, and cooling rates are shown to be simulated well (normalised bias errors < 6 % for bulk albedo, normalised mean absolute error < 15 % for absorption). By incorporating SPARTACUS-Surface into a state-of-the-art urban energy balance model there is capacity to simulate vertical profiles of surface temperatures within different urban neighbourhood with realistic sunlit and shaded partitioning, rapidly (i.e., minimal computer resources). In turn, this should improve provision of integrated urban services (WMO 2019; Grimmond et al. 2020), such as health related heat stress metrics.

Details of the new coupled modelling approach, and the model settings used are given (Section 6.2.1). One study period (Section 6.2.2) is used to simulate urban geometries spanning real-world cities, that are also compared to the widely used local climate zone (LCZ) framework (Stewart and Oke 2012) (Section 6.2.4). Both the new radiation physics option (Section 6.3.3), and morphological impact (Section 6.3.4) on fluxes and temperatures are assessed.

6.2 Methodology

6.2.1 Model description

SUEWS can simulate energy (Järvi et al. 2011; Ward et al. 2016), water (Grimmond and Oke 1986, 1991), and carbon (Järvi et al. 2012, 2019) balance fluxes for both urban and non-urban areas (Omidvar et al. 2022). To do this, each grid-cell can have up to seven surface cover types (paved, buildings, trees – deciduous and coniferous, grass, soil, and water) with properties that can vary between grid-cells.

SUEWS has multiple physics options for Q^* (Offerle et al. 2003; Lindberg et al. 2008, 2015), ΔQ_S (Grimmond et al. 1991; Offerle et al. 2005a; Lindberg et al. 2020; Sun et al. 2017) and Q_F (Sailor and Vasireddy 2006; Järvi et al. 2011; Ward et al. 2016; Ao et al. 2018; Capel-Timms et al. 2020). The model and various options have been evaluated (Järvi et al. 2011, 2014; Alexander et al. 2015; Karsisto et al. 2016; Ward et al. 2016; Ao et al. 2018; Kokkonen et al. 2018) and used for investigating the influences of parameter prescription in energy balance modelling (Demuzere et al. 2017), and urban land-use and land-cover changes (Ward and Grimmond 2017).

The simplest radiation scheme, SUEWS-NARP (Net All-Wave Radiation Parameterisation, (Offerle et al. 2003; Loridan et al. 2011)), provides the fluxes for bulk urban surfaces. SUEWS-BEERS (Building Envelope Energy Radiation Scheme) provides radiation by facet orientation based on the SEBE scheme (Solar Energy on Building Envelopes, Lindberg et al. (2015)) and SOLWEIG (Solar Longwave Environmental Irradiance Geometry model, Lindberg et al. (2008); Lindberg and Grimmond (2011)). The ΔQ_S schemes include: OHM (Objective Hysteresis Model, Grimmond et al. (1991); Grimmond and Oke (1999)), ESTM (Element Surface Temperature Method, Offerle et al. (2005a); Lindberg et al. (2020)) and AnOHM (Analytical OHM, Sun et al. (2017)).

Here, the SPARTACUS-Surface radiation scheme (Hogan 2019a) is coupled to SUEWS v2020b. To obtain the surface temperatures, a new multi-layer heat storage module (mEHC) is used, which allows vertical variations for the ΔQ_S calculation. Further model details can be found in the online repository (Sun 2023).

6.2.1.1 SPARTACUS-Surface (SS)

The SPARTACUS (Speedy Algorithm for Radiative Transfer through Cloud Sides) approach models radiative exchanges for cloud fields (Hogan et al. 2016), vegetation (Hogan et al. 2018), and urban areas (Hogan 2019b). The underpinning assumption is that the obstacles are randomly distributed within the horizontal plane of a model grid-cell, allowing the simulation of the mean radiation field with height, with outputs that include vertically distributed upwelling and downwelling clear-air fluxes, and facet absorption profiles. SPARTACUS-Surface (i.e., SPARTACUS-Urban and SPARTACUS-Vegetation) is coupled to SUEWS.

SPARTACUS-Surface solves ordinary differential equations for $2N$ streams of radiation (where N is number of streams per hemisphere) for a given scene or NWP grid-cell (combination of morphology, materials, and meteorology) with a combination of regions of buildings, vegetation, and clear-air, to model lateral radiative exchanges between these. SPARTACUS then computes the clear-air upwelling and downwelling fluxes, alongside the shortwave and longwave fluxes into each of the urban facets.

For each grid-cell, the plan area fraction of buildings (λ_p) and vegetation (λ_v) and their respective edge length normalised by the grid-cell area (L) are required as a function of height (i.e., $\lambda_p(z)$ and $L(z)$). This allows the roof area to vary with height, enabling a more realistic distribution of sunlit surfaces within the urban canopy, and for roofs to be shadowed by taller buildings. The $L(z)$ and $\lambda_p(z)$ can be related using an effective building diameter (D):

$$L(z) = \frac{4\lambda_p(z)}{D}. \tag{6.3}$$

providing a measure of building size (Figure 5.1, Chapter 5).

6.2.1.2 Multiple-layer explicit heat conduction (mEHC) scheme

In this study, a new module (hereafter mEHC) is developed to allow multi-layer approach to calculate heat storage and surface temperatures by facet (e.g., wall). This uses a 1D heat conduction equation (Gao et al. 2003) with an explicit scheme to resolve the heat storage and temperature with external surface heat flux and internal surface temperature as the upper and lower boundary conditions, respectively. The calculations are conducted for both the ground surfaces of standard SUEWS land covers (e.g., paved, grass, bare soil, etc.) and heterogenous building facets (i.e., roofs and walls at different vertical levels).

For consistency and to save computing time, the mEHC and SS *vertical-layers* both have a grid-cell limit of 15 to be consistent with the SUEWS-RSL (roughness sub-layer) profile module limit of 30 (Tang et al. 2021). Hence, allowing the minimum assumption of the urban canopy layer being half the depth of the top of the RSL, where the inertial sub-layer (ISL) occurs. This 15/30 limit can be increased. The user-prescribed vertical layer heights (z) for each grid-cell (SS, mEHC) do not have to be evenly spaced, unlike in the RSL scheme, but are matched between the SS and the mEHC.

The building facets products are output for each facet and also combined into one area-weighted single 'building' flux, to match SUEWS surface types. As SS only has a single 'ground' facet, when vegetation is neglected, ground-level surfaces (e.g., paved, grass, bare soil) are linearly weighted by surface fraction to give one ΔQ_S flux and T after each timestep. Then, all SUEWS surface type fluxes are aggregated to obtain the overall ΔQ_S (ISL). Each facet (e.g., wall, roof, ground) can have up to five layers with different thermal parameters prescribed per grid-cell (Section 6.2.3, 6.3.2).

6.2.1.3 Model coupling

SPARTACUS-Surface (SS) is integrated with SUEWS-EHC through surface temperatures (T) using an iterative method (Figure 6.1). The process differs between the first and subsequent iterations.

During the first iteration the initial states are set for each facet (f) at all vertical levels (z):

- For the first SS radiation calculations, user prescribed initial (s=j-1; where s is the step to obtain a surface temperature, and j is the number within it) $T_{(s=j-1)}(f, z)$ values are used (e.g., air temperature, T_{Air}).
- For the initial mEHC, the external surface conductive heat flux, $Q_G(f, z)$, and the user prescribed internal (or deep) temperatures are set. The former is set initially as $0.1 \cdot Q^*(f, z)$ using the net radiation from SS. Whether the internal building temperatures are held constant or not, has implications for the Q_F. Here, internal (deep) temperatures are assumed to be constant.

In subsequent iterations and timesteps:

- Using mEHC, $T_{(s=j)}(f, z)$ and the profile of storage heat fluxes ($\Delta Q_S(f, z)$) are calculated for iteration $s=j$.
- With $Q^*_{(s=j-1)}(f, z)$ and $\Delta Q_S(f, z)$, $Q_E(f, z)$ is calculated using aerodynamic resistance(s), determined either from the wind speed profile, $U(z)$, MOST (Monin-Obukhov Similarity Theory) stability functions (Theeuwes et al. 2019; Tang et al. 2021) and roughness parameters, or with the U(ISL), MOST, and roughness parameters (r_a(ISL)); and surface resistance that accounts for the facet-specific surface wetness or soil moisture (as appropriate, e.g., if surface dry and vegetated); and in this case assume $Q_F(f, z)$ is 0 W m^{-2}. From this, by difference, $Q_H(f, z)$ is obtained.
- Using $Q_H(f, z)$, T_{Air}(ISL) and r_a(ISL) the new surface temperatures are $T_{(s=j+1)}(f, z)$ are derived.
- A weighted average ($T_{(s=j+2)}$) of $0.4 \cdot T_{(s=j)}(f, z)$ and $0.6 \cdot T_{(s=j+1)}(f, z)$ is used in next SS calculations to ensure faster convergence (Yao et al. 2021).
- In mEHC, $Q_G(f, z)$ is updated assuming energy balance closure at each f, z, allowing the next $T_{(s=j+2)}$ to be obtained for the SS radiation calculations.
- If the maximum absolute difference between $T_{(s=j+2)}(f, z)$ and $T_{(s=j+1)}(f, z)$ across all f and z is < 0.1 K, the timestep ceases; otherwise, it continues.

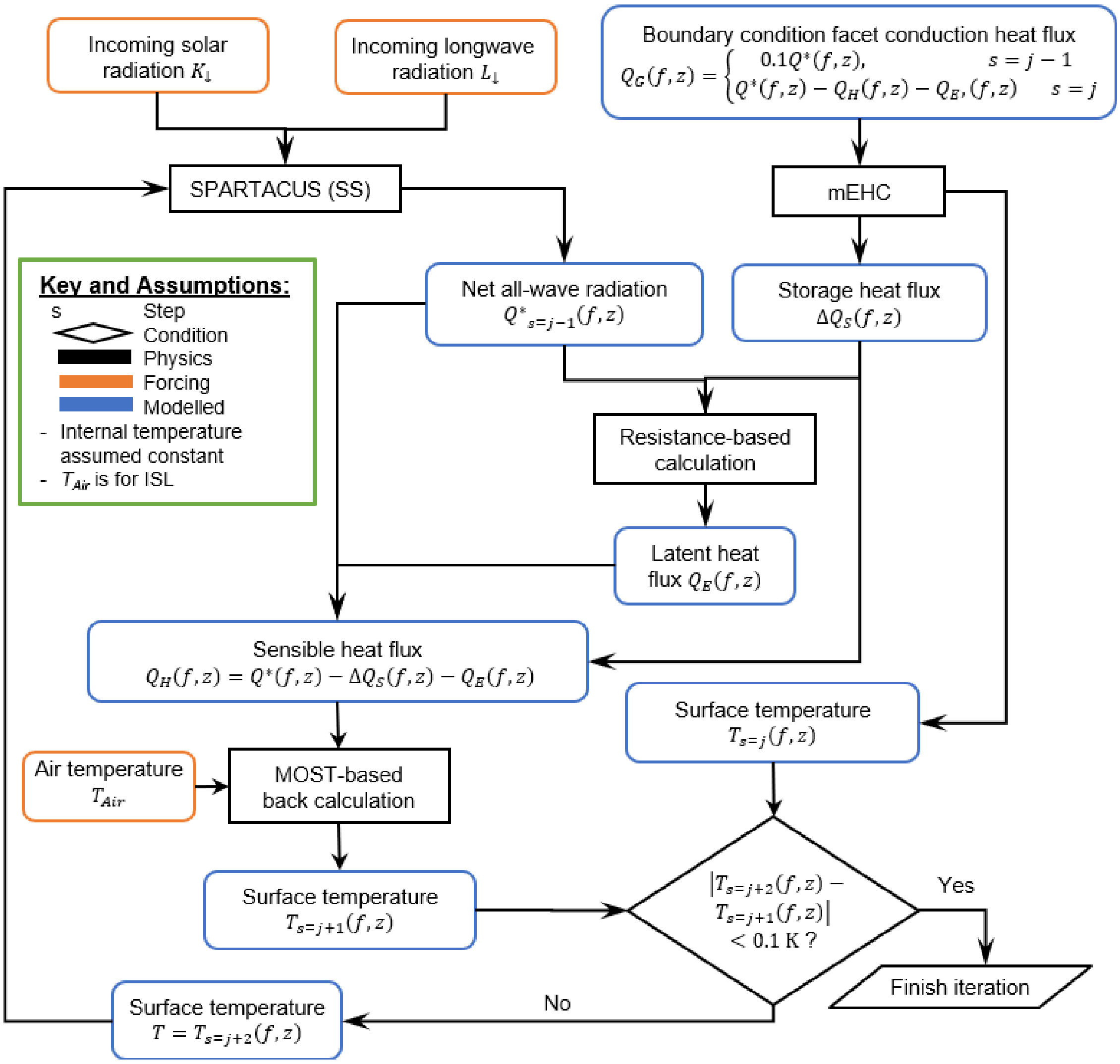

Figure 6.1: SUEWS physics options, SS and mEHC are coupled through differences in SUEWS surface temperature (T), used to assess if the iterative model solution has been satisfied, using the external surface conductive heat flux (Q_G) and the forcing T_{Air} (i.e., from inertial sub-layer (ISL)) which is assumed the same height for all grids. Fluxes are calculated for each facet, f, and vertical layer, z.

6.2.2 Study period and observations

SUEWS requires continuous (i.e., gap filled) ISL meteorological forcing of: downwelling SW radiation ($SW_\downarrow$), wind speed, T_{Air}, surface pressure and relative humidity. These can be from observations, reanalysis data (e.g., ERA5, (Hersbach et al. 2020)), or from larger scale modelling (e.g., Sun et al. (2023)). For model variable evaluation, independent data sets are needed.

Here, observations from two sites (Table 6.1, Figure 6.2) in central London are used to evaluate the surface temperature model output and to force the simulations. A 15-min forcing dataset is derived from observations from the IMU site (~74 m above ground level, a.g.l). As the mean building height of the surroundings is 25.5 m (2 km × 2 km, Table 3.1, Figure 3.1), sensors are assumed to be with the ISL (Barlow 2014). The small number of data gaps in 15-min relative humidity (n = 7) are filled using linear interpolation.

For model evaluation, surface temperature (T) data are used. The observed T are obtained from Optris PI-160 infrared cameras thermal sensors (Figure 6.2e) with processing providing data attributes including known facet type (including wall orientation) and sunlit/shaded status (Morrison et al. 2020, 2021). The processed T observations are available for the 27th August 2017 (day of year (DOY) 239) from 5:45 (sunrise: 5:04) (Morrison et al. 2020, 2021). All times referred to in this study are UTC.

Given the real-world variability of surface material across the observation area (420 m × 420 m), the assigned SUEWS-SS-mEHC parameters used to represent these cannot be fully consistent. However, whether the model can capture the variability and the magnitude can be assessed using the observations.

We focus our simulations analysis on the four-day period 24th to 27th August 2017 (DOY 236-239), after a 10-day model spin-up period (14th to 23rd August, DOY 226-235). Although the main focus is DOY 239, examining the earlier days allows fluxes to be compared with other conditions (e.g., overcast).

Table 6.1: Meteorological forcing and evaluation data are obtained from observation at two sites with building height indicated above ground level (a.g.l) (Morrison et al. 2021). All observations are used at 15-min resolution to force SUEWS

Full name (site/model)	Location	Instruments	Variable
Islington Michael Cliffe House Upper (IMU)	51.5261 °N 0.1061 °W 74 m a.g.l	Davis Vantage Pro weather station	Relative humidity Air temperature T_{Air} Wind speed U Pressure
		Kipp and Zonen CNR1 radiometer	Downwelling shortwave radiation SW↓
		Optris PI-160 infrared thermal camera	Surface temperature T
Wycliffe Court Tower (WCT)	51.5267 °N 0.1036 °W 36 m a.g.l	Optris PI-160 infrared thermal camera	Surface temperature T

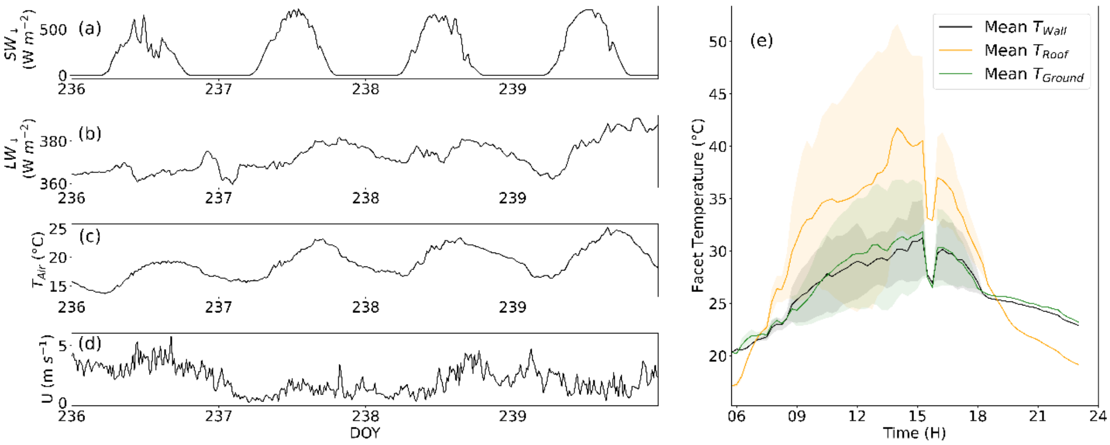

Figure 6.2: IMU meteorological data (a) downwelling shortwave flux (SW↓), (c) air temperature (T_{Air}), (d) wind speed (U).; (b) SUEWS simulated downwelling longwave flux ($LW_{\downarrow}$) and (e) Optris PI-160 infrared cameras observed mean (equally weighted sunlit and shaded, solid) and sunlit-shaded range (shading) temperature range for walls (black), roofs (orange), and ground (green) surfaces.

6.2.3 SUEWS-SS-mEHC model parameters and application

Additionally, SUEWS requires parameters to describe the site being simulated. The full range of parameters needed are given within the SUEWS code repository and documentation (Sun et al. 2022). Here, the focus is on the morphology (form) and material characteristics used in this study. The assumptions made during the simulations are also addressed.

To describe the urban form, the parameters required are: mean building height ($\overline{H}$), surface and profiles of cover fractions (building, λ_p, paved λ_i, vegetation λ_v – although unused here), frontal area index (λ_f), and profiles normalised edge length. Profiles of geometry are provided at the prescribed vertical layers (Δz). For the single-layer simulations $\Delta z = \overline{H}$ is used.

The material properties of primary interest in this study are the radiative and thermal parameters. For the former, the albedo (α) and emissivity (ε) for each facet (wall, roof, ground) with Δz are required. The material properties impacting the conduction of heat vary by facet, surface type, and material thickness. The model allows parameters for up to five layers: layer thickness (dz), volumetric heat capacity (ρc_p), thermal conductivity (k). Like with reflective materials, these can vary with SS vertical layers (i.e., height in the canopy) for both wall and roof facets.

SUEWS-SS-mEHC is used in two height modes: (1) multi-layer with variability (SS-9), and (2) single-layer with the grid-cell $\overline{H}$ (SS-1) which also impacts the surface cover fractions (e.g., buildings, $\lambda_p(z)$). To ensure wall area is conserved between SS-1 and SS-9 simulations the total normalised wall area (λ_w) is used (Masson et al. 2020a):

$$\lambda_W = \sum_{i}^{n} L_i \Delta z_i \,. \tag{6.4}$$

Assuming all wall orientations equally probable, allows a relation with the frontal area index ($\lambda_w = \lambda_f \pi$) - the total wall area for particular wind (or azimuth) direction relative to the total grid-cell area. For SS-1 simulations, the surface value of λ_p, $\lambda_p(z = 0)$ is used.

For simplicity in this study, Q_F is assumed to be 0 W m^{-2}. Similarly, snow (Järvi et al. 2014), irrigation (Ao et al. 2018) and carbon exchanges (Järvi et al. 2012) are turned off. The period is assumed to be dry (all observed rain is removed from forcing data), and the initial soil state is set to zero. All simulations are assumed to contain no vegetation (i.e., trees or grass).

The 15-min forcing data (Section 6.2.2) are linearly interpolated by SUEWS to the 5-min calculations. The model output analysed are 15-min block averages. For the SW$_\downarrow$ a constant diffuse/direct fraction is assumed, with a value of 0.45SW$_\downarrow$ (Li et al. 2015b; Fan et al. 2018). In this application, Downwelling longwave flux (LW$_\downarrow$) is modelled (NetRadiationMethod = 1003 (Loridan et al. 2011)).

The initial surface temperatures are set to be 10 °C, which is cooler than the first timestep T_{Air} (~16 °C), with tests showing increasing this did not influence the fluxes after the spin-up period. The deep soil temperature is also assumed to be 10 °C.

6.2.4 Capturing urban morphology variation

High-resolution limited-area NWP models have horizontal grid resolutions of the order of 2 km (e.g. Met Office 1.5 km UKV (Tang et al. 2013)). There are many ways to characterise the varying morphology across and between cities for NWP, including using land-use and land-cover maps (e.g., Global Urban Footprint, Esch et al. (2017)), UZE's (Urban Zones for Energy partitioning, Loridan and Grimmond (2012); Loridan et al. (2013)), Local Climate Zones (LCZ, Stewart and Oke (2012); Bechtel and Daneke (2012); Bechtel et al. (2015); Brousse et al. (2016); Demuzere et al. (2017); Molnár et al. (2019); Patel et al. (2020)). Each method requires values to be assigned for several parameters for each zone. For example, Stewart and Oke (2012) prescribe for each LCZ the range for: surface land cover fractions λ_p, λ_v, and paved, λ_i; $\overline{H}$, height to width ratio ($\overline{H}$/W), and sky view factor (ψ_{Sky}).

Here, the focus is on impervious surfaces (i.e., vegetation is excluded) to consider the implications of vertical structure in typical neighbourhoods (i.e., 2 km × 2 km grid-cells) using building data for six cities (Table 6.2). With a total of 1429 grid-cells, these cover a wide range of building densities (black scatter, Figure 6.3a) and heights, and both the Southern (Auckland, New Zealand; Sao Paulo, Brazil) and the Northern Hemispheres (Berlin, Germany; Birmingham, UK; London, UK; New York City (NYC), USA).

Using these two parameters ($\lambda_p(z = 0)$ and $\overline{H}$) for assigning grid-cells to LCZ classes (Figure 6.1) results in some LCZs being combined (LCZ 3+LCZ 8, and LCZ 5+LCZ 10). After classifying all six cities grid-cells into Stewart and Oke's (2012) LCZ using boundaries defined by $\lambda_p(z = 0)$ and $\overline{H}$, examples of all 8 combined urban LCZ’s occur (Figure 6.2b, black and grey). But not all of the 2 km × 2 km resolution grid-cells are assigned an urban LCZ because of low building densities ($\lambda_p(z = 0) < 0.2$) and this is not resolved by the ‘rural’ LCZs (Figure 6.3b, green, hereafter LCZ 0). Examining the spatial distribution of these LCZ neglected grid-cells shows they are often suburban areas (Figure 6.A.2).

Using this LCZ designation method and spatial scale, the six study cities (Table 6.2) contain up to 5 LCZs. The larger cities (e.g., NYC, Sao Paulo) have more zones (Figure 6.A.2). Beyond the LCZ 0 ($\lambda_p(z = 0) < 0.2$ or 0.1), the most common LCZs are: open mid- and low-rise’ [5 (+ LCZ 10), 6] and sparsely built’ [LCZ 9]. The few (1-2 Auckland and London, ~ 10 NYC) CBD grid-cell are generally classified as ‘compact midrise’ [LCZ 2] (Table 2, Stewart and Oke (2012a)).

To characterise the full range of the data (Table 6.2), the Stewart and Oke (2012) LCZ boundaries are revisited, considering the heights relative to building floor heights (e.g., 3 or 6 storey buildings, corresponding to 7.5 m and 15 m, if building storeys are assumed 2.5 m (OPDC 2018)). From analysing the $\lambda_p(z = 0)$ data for ‘natural’ classes, the LCZ 9 boundary is expanded to $\lambda_p(z = 0) = 0.2$ to derive nine categories (C1 – C9) spanning both high and low $\lambda_p(z = 0)$ and $\overline{H}$ (Figure 6.3a, increasing building density blue → red, increasing height darker).

These nine categories are well distributed across all six cities, with each city having a minimum of five categories (Figure 6.4) with the larger cities (e.g., London, Sao Paulo, NYC) having more categories occurring within them. Grid-cells with high $\lambda_p(z = 0)$ (red, Figure 6.3) occur in city centres, alongside slightly less dense areas with high building heights (green, Figure 6.3a). Suburban regions of cities have a lower $\lambda_p(z = 0)$ (blue, Figure 6.4). However, some suburban regions have larger $\overline{H}$, possibly indicating grid-boxes with industrial sites or airports.

As the distance between buildings (street width, W) may be skewed by areas with large open spaces, here D (Eq. 6.3) is used, which can be calculated conserving wall area using the λ_W, the layer thickness (Δz, m) and the building fraction at each height, as in Chapter 5, Eq. 5.4:

$$D = \frac{4}{\lambda_W} \sum_{z=0}^{i} \lambda_{p,i} \, \Delta z, \tag{6.5}$$

Visualisation of the D distribution calculated conserving wall area supports the suggestion that wider buildings are taller (Section 5.4.2; Figure 5.4). Categories with taller $\overline{H}$ (C3, C6, C9) having a larger building size (Figure 6.5) and a wider spread in D (cf. shorter $\overline{H}$ categories). This is consistent with suburban grid-cells having smaller $\lambda_p(z = 0)$ and $\overline{H}$.

Table 6.2: Six cities are analysed with 2 km × 2 km grid-cell resolution resulting in NGC (number of grid-cells) using raster digital surface model (rDSM) and vector DSM (vDSM) with different horizontal resolutions (Δx) from different sources. For consistency all obstacles shorter than the single floor height (OPDC 2018) (i.e., < 2.5 m) are removed

City	NGC	Type	Δx (m)	Data Source
Auckland	59	rDSM	4	Kent et al. (2019)
Berlin	198	vDSM	1	Umweltatlas Berlin (2010)
Birmingham	177	vDSM	1	EMU Analytics (2018)
London	415	vDSM	1	
	1	vDSM	1	Evans et al. (2006)
New York City	251	rDSM	4	Kent et al. (2019)
Sao Paulo	329	rDSM	4	

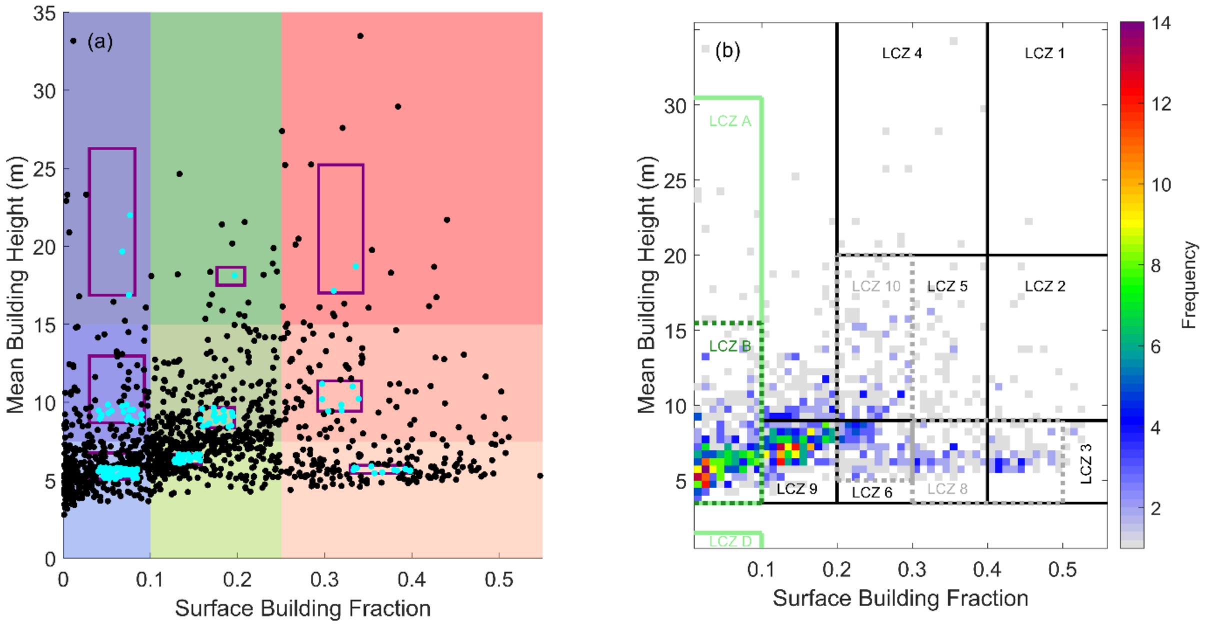

Figure 6.3: Mean building height ($\overline{H}$, m) and plan area building fraction at the surface ($\lambda_p(z = 0)$) for 1429 (2 km × 2 km) grid-cells (black scatter) from six cities (Table 6.2) (a) nine building form categories (colour) with 'median' box (35th to 65th percentile, cyan scatter). For categories with $\lambda_p(z = 0) < 0.1$ (blue shading) the boxes are modified to be $\lambda_p(z = 0) > 0.04$ and $\overline{H}$ 35th – 90th, and the (b) urban (black/grey) and rural (green) local climate zones (LCZ) (Stewart and Oke 2012; Bechtel et al. 2015) assigned based on $\overline{H}$ and $\lambda_p(z = 0)$. Colour key corresponding to categories (Figure 6.3) have reduced intensity to ensure all data points are visible

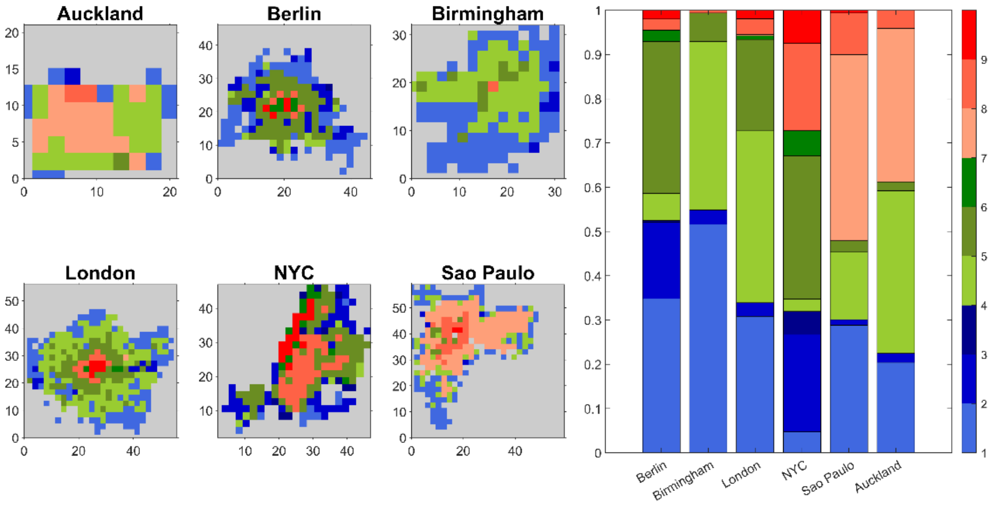

Figure 6.4: Nine urban categories (Figure 6.3) mapped onto 2 km × 2 km grid-cells from six cities: (a) location and (b) fractions per city

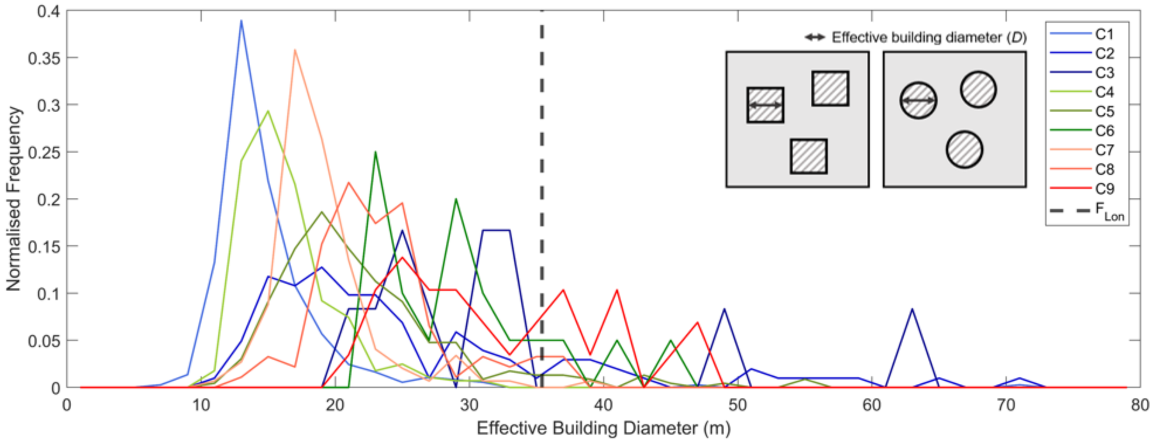

Figure 6.5: Frequency of effective building diameter (*D*, Eq. 6.3, Eq. 6.5) (bins = 2 m) in the grid-cells by category (colour, Figure 6.3) calculated conserving wall area using the vertical profiles of building fraction and normalised edge length. For a real-city reference, the London grid-cell used in this study to compare to surface temperature observations has a D = 35.4 m (dashed line, F_{Lon}) (source: Chapter 3, Chapter 4).

6.2.5 Analysis scenes, morphology, and material parameters

This work involves three main simulation types. The first is a comparison to (Offerle et al. 2005a), morphology parameters (D, λ_f) are calculated by inverting the operational method to derive $\overline{H}$/W, using Eq. 3.3 of Hertwig et al. (2020),

$$\frac{H}{W} = \frac{\pi}{2}\frac{\lambda_f}{\left(1 - \lambda_p\right)}, \tag{6.6}$$

Assuming height is equal to $\overline{H}$ to determine λ_f ($\overline{H}$/W = 0.75, Offerle et al. (2005a)'s Table 1). Then, assuming walls face in equal directions λ_W is calculated, followed by D conserving wall area (Eq. 6.5), which is then used as an input to SUEWS-SS-mEHC. This simulation is run with single-layer SUEWS-SS-mEHC.

To examine the suitability of SUEWS-SS-mEHC against observations, a single 2 km × 2 km grid-cell in central London derived from Evans et al. (2006) building footprint dataset, is used (F_{Lon}, Table 6.3) This grid has been previously used in SPARTACUS-Surface evaluations (Chapter 3, Chapter 4), and contains the location of both observation sites in Table 6.1. This morphology (as SS-1) is also used to conduct a sensitivity analysis on internal building materials.

To examine the implications of morphology on the SEB, one grid-cell per category is randomly chosen (F_{CX}, Table 6.3). In order for these to be 'representative', they are randomly chosen from grid-cells in the Figure 6.3 'median' boxes, within 35th – 65th percentile ($\lambda_p(z = 0)$ and $\overline{H}$) (cyan scatter, Figure 6.3). For the categories with $\lambda_p(z = 0) < 0.04$ (Figure 6.3a) and $\overline{H}$ is chosen between 35th – 90th percentile, choices are not random to ensure the chosen grid-cell is not anomalous (e.g., one large building).

Each grid-cell used (morphology categories, F_C, and London for comparison to observations, F_{Lon}) spans different morphometric properties (Table 6.3, Figure 6.6). Therefore, λ_p, and L profiles are derived with different Δz (and layer number). To assess the implications of utilising the multi-layer SPARTACUS configuration, the F_{Lon} domain uses both one layer, and nine layers. The F_{CX} grid-cells have between five and seven layers, to enable equal sampling of each domain. The initial layers are the same for all F_{CX} grids as λ_p is constant up to 2.5 m. Further layers are a function of mean building height starting when layer heights exceed 5.0 m (i.e., layers interfaces could be skipped) (Table 6.3).

Urban form parameters (λ_p, L, D, $\overline{H}$) are derived from rasterised building height data at variable resolution (1 m × 1 m, or 4 m × 4 m, Table 6.2). Each building has only one height, so roofs and walls are assumed flat. Any buildings with heights < 2.5 m are discarded (UK storey height, (OPDC 2018)). Building cover fractions and edge-lengths are derived at each height interval, to produce profiles (Figure 6.7). For all simulations, the λ_f required by SUEWS-SS-mEHC is calculated using λ_W (from L, Eq. 6.4) and assuming walls face equally in all directions.

To ensure the impacts of morphology are isolated, the facet ε and α need to be made consistent. To do this, all simulations use the same external and internal building materials. Both single- and multi-layer for $\mathrm{F_{Lon}}$, and all $\mathrm{F_{CX}}$ SUEWS-SS-mEHC simulations use facet $\varepsilon = 0.93$ based on Kotthaus et al. (2014)'s Appendix C, and facet $\alpha = 0.2$ from synthesised literature in Oke et al. (2017)'s Table A2.1.

The SS layer and morphology comparison conduction related properties ($\mathrm{M_X}$, Table 6.4) are prescribed from two sources. The first using UK/London values calculated for residential buildings built between 1966-1990 (varies with $\mathrm{M_X}$), which are effective values obtained as the average of all construction layers weighted by layer thickness, with materials and thicknesses obtained from CIBSE (2015) based on an analysis of UK building regulations (domestic sector) for various building periods (Smith 2009). Second, assuming a constant layer thickness with materials from Lindberg et al. (2020) (Table 6.4a, b). The materials from CIBSE (2015) assume the same materials for roofs and walls following the assumptions of MORUSES (Met Office Reading Urban Surface Exchange Scheme, Porson et al. (2010)). In the morphology and layer comparisons, all SUEWS-SS-mEHC simulations are simulated with same material properties to assess only the radiation scheme or morphology. For the comparison with observed and modelled (ESTM) fluxes for the Lipowa site ($\mathrm{F_{Lipowa}}$) in Łódź, Poland, parameters from Offerle et al. (2005a)'s Table 3 are used but spread across the five layers of mEHC ($\mathrm{M_{Lipowa}}$, Table 6.4).

Table 6.3: Morphological parameters derived for one grid-cell of each the of assigned for main (F_{Code}) used in this study, and the London grid-box where observation sites are located (F_{Lon}) simulated for different layer numbers. Including: surface plan area fraction of buildings, $\lambda_p(z = 0)$, mean building height, $\overline{H}$, surface normalised building edge length, $L(z = 0)$, and frontal area index (λ_f). A useful measure of building size within a grid is the effective building diameter, D, which is calculated conserving wall area, Eq. 6.5.

Form (F)	$\lambda_p(z = 0)$	$\overline{H}$ (m)	$L(z = 0)$ (m^{-1})	D (m)	λ_f	Layers	Layer interfaces (m)
F_{Lipowa}	0.3	10.6	-	12.11	0.33	1	10.6
F_{Lon}	0.44	25.5	0.055	35.4	0.394	1 9	25.5 5.0, 7.5, 10.0, 15.0, 25.0, 32.0, 50.0, 75.0, 100.0
F_{C1}	0.047	5.21	0.017	13.4	0.0358	5	2.5, 5.0, $0.5\overline{H}$, $0.75\overline{H}$, $\overline{H}$, $1.5\overline{H}$, $2\overline{H}$
F_{C2}	0.073	8.87	0.010	40.2	0.0569	6	
F_{C3}	0.068	19.7	0.0037	98.0	0.0703	7	
F_{C4}	0.14	6.32	0.040	14.6	0.161	5	
F_{C5}	0.17	9.13	0.036	20.6	0.465	6	
F_{C6}	0.20	18.1	0.017	44.9	0.298	7	
F_{C7}	0.35	5.90	0.29	4.34	1.36	5	
F_{C8}	0.34	10.2	0.30	4.86	4.91	7	
F_{C9}	0.34	18.7	0.040	38.1	2.75	7	

Table 6.4: Thermal parameters including internal layer thickness (dz), volumetric specific heat capacity (ρc_p), and thermal conductivity (k), from three sources (a) CIBSE (2015) (b) Lindberg et al. (2020)'s Table 2 and (c) Offerle et al. (2005a)'s Table 3. All ground materials are from Lindberg et al. (2020). If less than five layers are used, they are split into five equal layers to fit the number used by SUEWS-SS-mEHC. For multiple layer simulations, all layers are assigned the same materials. The ground thickness in (a) and (b) is the average of that in (c)

Code (M)		dz (m)			k (W m^{-1} K^{-1})			ρc_p (MJ K^{-1} m^{-3})		
		Wall	Roof	Ground	Wall	Roof	Ground	Wall	Roof	Ground
(a) CIBSE (2015)										
BBC	Brick-brick cavity	0.0551		0.87	0.567		0.64	1.1		1.23
BIB	Brick-insulation-brick	0.0571			0.394			1.06		
BICC	Brick-insulation-concrete cavity	0.0506			0.257			1.02		
BITC	Brick-insulation-timber cavity	0.0607			0.160			0.91		
CCC	Concrete-concrete cavity	0.0589			0.278			0.68		
(b) Lindberg et al. (2020)										
LDN1	Table 2, Lindberg et al. (2020)	0.055		0.87	0.85	0.63	0.64	1.29	1.06	1.23
LDN2					0.62	0.58		1.27	1.02	
LDN3					0.69	0.25		0.89	1.12	
LDN4					0.52	0.24		0.95	0.75	
LDN5					0.83	0.61		1.22	1.12	
LDN6					0.88	0.90		1.42	1.50	
(c) Offerle et al. (2005a)										
Lipowa	Table 3, Offerle et al. (2005a)	0.06	0.03, 0.04, 0.04, 0.04, 0.05	0.1, 0.25, 1.0, 1.0, 2.0	0.95	0.74, 0.93, 0.93, 0.93, 0.06	0.76, 0.74, 0.63, 0.63, 0.63	1.6	1.9, 1.5, 1.5, 1.5, 0.07	1.5, 1.9, 1.2, 1.2, 1.2

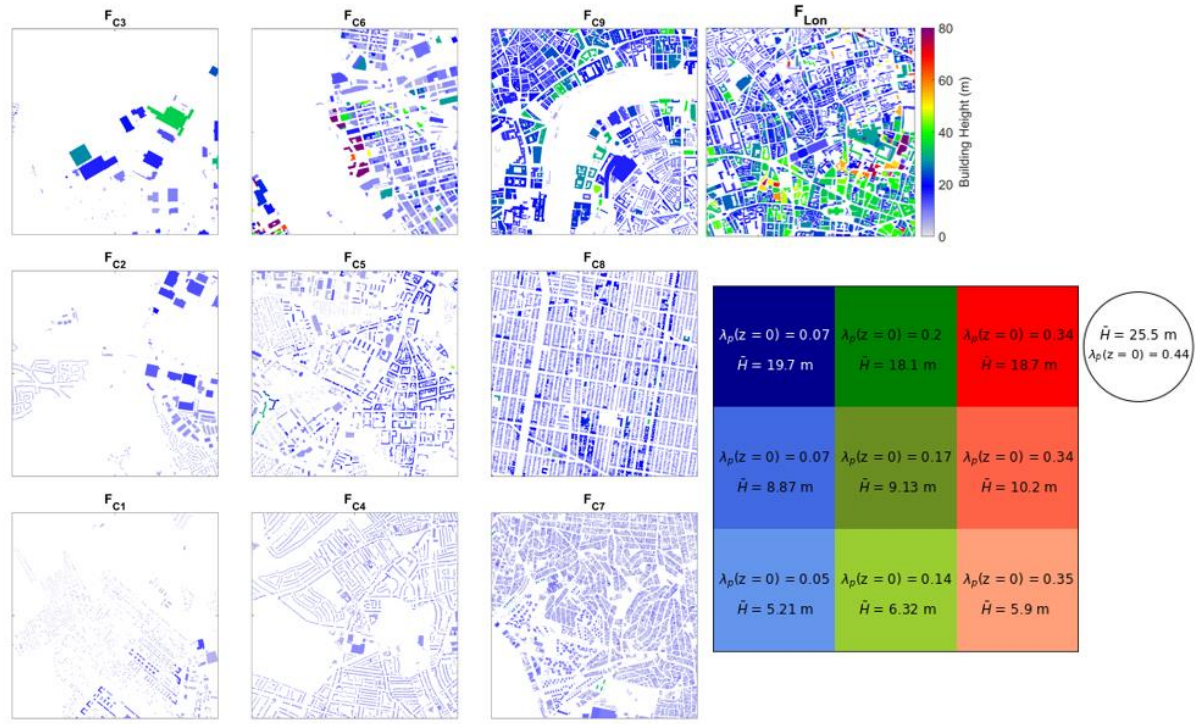

Figure 6.6: Spatial variation of building height (colour bar) in the ten 2 km × 2 km areas analysed. Key (lower right hand side) gives two parameters (surface building fraction, $\lambda_p(z = 0)$, mean building height, $\bar{H}$)

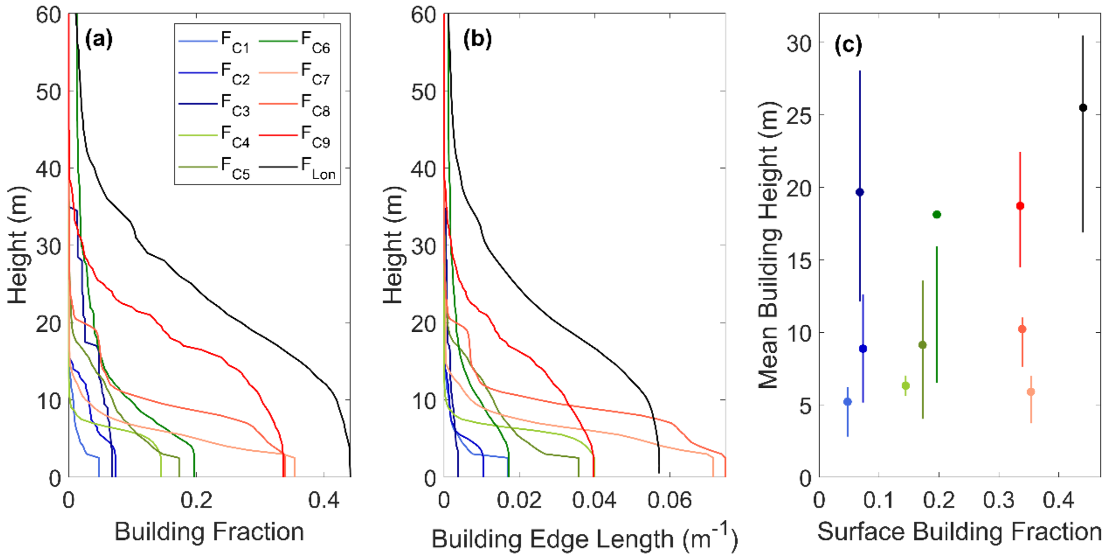

Figure 6.7: Ten study areas (Figure 6.6) vertical profiles of: (a) height and building fraction (λ_p), (b) height and normalised building edge length (L), and (c) mean building height ($\bar{H}$) (point) with inter-quartile range (whiskers), and surface λ_p, ($\lambda_p(z = 0)$)

6.2.6 Evaluation metrics

The SUEWS-SS-mEHC simulations are compared:

(1) single- (SS-1) and multi-layer (SS-9) fluxes (e.g., SW*), and

(2) surface temperatures (T_{obs}) to observations

for *n* data points, using both the mean absolute error (MAE):

$$MAE = \frac{1}{n}\sum \left| T_{sim,i} - T_{obs,i} \right| \ , \tag{6.7}$$

mean bias error (MBE):

$$MBE = \frac{1}{n}\sum (SW^{*}{}_{SS-1,i} - SW^{*}{}_{\mathrm{SS-9,i}}) \tag{6.8}$$

normalised MAE (nMAE) and nMBE:

$$nMBE = \left(MBE / \overline{SW^{*}_{SS-9}} \right) \times 100 \tag{6.9}$$

For the normalised errors a mean reference variable is used and converted to have units of percentage. Flux metrics are determined by time of day, with daytime defined as when $SW_{\downarrow}$ > 0 W m^{-2}. The temperature metrics are based for the whole period (5:45 UTC – 23:00 UTC). Subscripts are used to indicate the time of day or model configuration (e.g., $\mathrm{MBE}_{\mathrm{Day}}$, $\mathrm{MBE}_{\mathrm{SS-1}}$).

6.3 Results

6.3.1 Lipowa, Łódź, Poland ($\mathrm{F}_{\mathrm{Lipowa}}$)

First, the ability to model the Lipowa site in Łódź, Poland (Offerle et al. 2005a) morphology and materials with a single-layer configuration SUEWS-SS-mEHC. This site is chosen as there are direct observations of net all wave radiation (Q^*), both the turbulent sensible (Q_H) and latent (Q_E) heat fluxes, as well as external surface temperature (T) and internal building temperatures (Offerle et al. 2005a). The latter allowed, the net storage heat flux (ΔQ_S) to be directly determined using the ESTM (Offerle et al. 2005a) approach.

For the simulation undertaken, some of Offerle et al. (2005a)'s conditions are modified to make them consistent with later model assumptions. Notably, to remove uncertainty in the SS vegetation radiation modelling, the vegetated areas are assumed to be paved. Thus, the eddy covariance observed Q_E and Q_H (Offerle et al. 2005a) are combined for comparison purposes. As Offerle et al. (2005a) determine the anthropogenic heat flux as the residual in the SEB but we later assume it is 0 W m^{-2}, we do the same here. The simulation is run with the same meteorological forcing for London (Section 6.2.2) as used for the rest of the study with model spin-up from DOY 226, and the Lipowa morphology/form ($\mathrm{F}_{\mathrm{Lipowa}}$, Table 6.3) and the materials ($\mathrm{M}_{\mathrm{Lipowa}}$, Table 6.4).

To assess the model performance, we consider the one clear-sky day (27th August) relative to the mean July-August fluxes in Lipowa (Figure 6.8). Comparing the peak daytime fluxes for both cases: Q^* is ~450 W m^{-2}, the EC observed $Q_H + Q_E$ (Lipowa) is ~300 W m^{-2} and the simulated Q_H is ~350 W m^{-2}, the ΔQ_S both derived from observed T and simulated with mEHC is ~150 W m^{-2}. However, for the latter the timing is earlier (Figure 6.8). Thus, if no vegetation occurred, we would expect Q_H to be larger than $\Delta Q_{S.}$ This is likely enhanced by the lack of external water use for street-cleaning in this simulations, compared to observed in many cities (e.g., Marseille, Grimmond et al. (2004), and Beijing, Dou et al. (2019)).

In many dense urban areas, morning storage heat flux (ΔQ_S) is larger than the turbulent sensible heat flux (Q_H). The vertical surfaces rapid warm with Q^* but as conduction cannot transport the heat rapidly enough, later in the morning Q_H becomes greater than ΔQ_S (Grimmond et al. 2004). The large daytime ΔQ_S play an important role in sustaining a positive night-time Q_H observed (e.g., Rotach et al. 2005; Offerle et al. 2006a; Coutts et al. 2007a; Keogh et al. 2012; Kotthaus and Grimmond 2014a,b; Ward et al. 2016) and simulated (e.g., Lemonsu and Masson 2002; Kusaka and Kimura 2004). These studies cover central city areas (e.g., London, UK; Basel, Switzerland; Melbourne, Australia) as well as suburban (e.g., Swindon, UK).

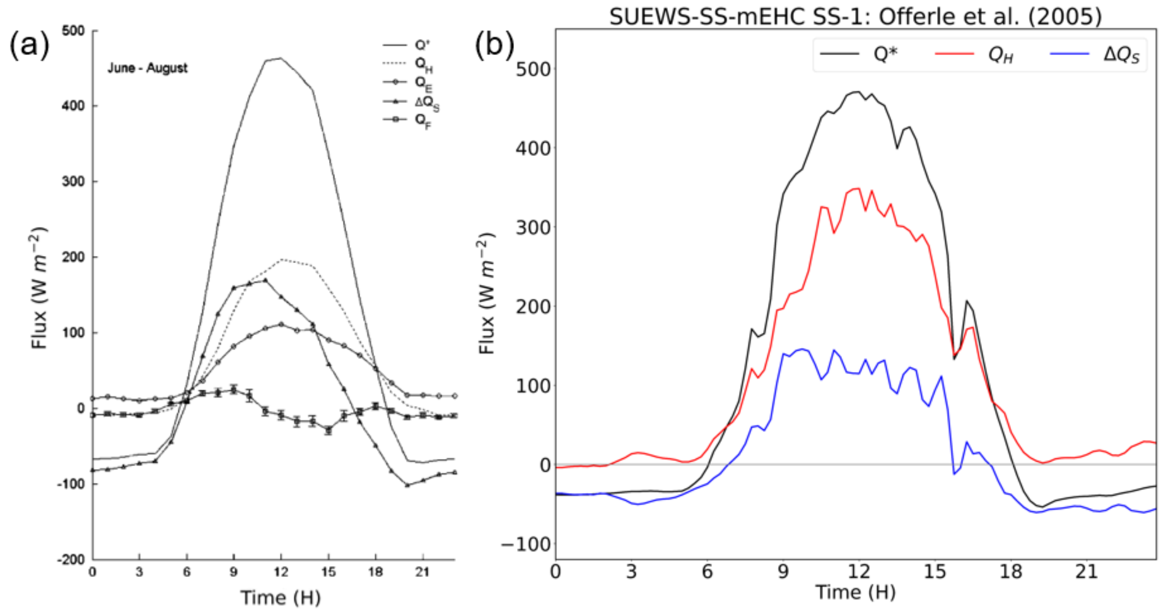

Figure 6.8: Lipowa site (Łódź, Poland), mean net all wave radiation (Q^*), turbulent sensible (Q_H) and latent (Q_E), and net storage (ΔQ_S) heat fluxes: (a) June-August, 2001-2002 observed (including T used with ESTM (Source: Figure 6 Offerle et al. (2005a)), and (b) SUEWS-SS-mEHC (15-min) simulations using London observations for 27th August 2017 (Section 6.2.2) and Lipowa parameters (F_{Lipowa}, Table 6.3, M_{Lipowa} Table 6.4) assuming all vegetation is paved (Section 6.2.5)

6.3.2 Sensitivity to thermal parameters in single layer mode

To assess the impact of parameters assigned for thermal material properties (Table 6.4a, b) used in mEHC in single layer mode (SS-1), the fluxes are compared for the 2 km × 2 km study area in central London (Figure 6.5), with all other model settings held constant (Section 6.2.3, 6.2.4). The range of parameters used include across different building types in the UK based on CIBSE (2015) and values from Lindberg et al. (2020) collected from multiple building types in London.

Simulated daytime ΔQ_S is generally higher when the heavier-duty materials (i.e., larger thermal conductivity (k), volumetric heat capacity (ρc_p) and material thickness (dz)) are used for both roofs and walls (e.g., $M_{LDN2,5,6}$ and M_{BBC} with $\rho c_p > 1.1$ MJ K^{-1} m^{-3} and $k > 0.5$ W m^{-1} K^{-1}) (Figure 6.9b). These have smaller daytime Q_H and larger daytime ΔQ_S cf. other material combinations (Figure 6.9b, c) , with differences of ~70 W m^{-2} in Q_H between the lowest (M_{LDN6}) and highest (M_{BITC}) on DOY 239 (e.g., clear-sky). These two configurations give such different fluxes due to their differences in k (> 0.7 W m^{-1} K^{-1}) and ρc_p (> 0.5 MJ K^{-1} m^{-3}) for roofs and walls.

There is less impact to Q^* from changes in the thermal properties, with differences of < 25 W m^{-2} across all materials (Figure 6.9a). Note, changes to radiative parameters (e.g., albedo) are not explored as they are well known to have large impacts. These small differences in Q^*, result in large differences in daytime surface temperatures (T). For example, the M$_{\mathrm{LDN6}}$ and M$_{\mathrm{BITC}}$ simulations (Figure 6.10), have maximum daytime differences of ~8 °C for roofs, and < 4 °C for walls. Overnight, T_{Roof} and T_{Wall} differences are generally < 5 °C. As the materials of the ground are not modified between simulations (Table 6.4), there are little difference in T_{Ground} (< 1 °C).

When, using the CIBSE (2015) thermal parameters, the roof parameters are modified to be different to those of walls (chosen here as M$_{\mathrm{LDN1}}$), both ΔQ_S and Q_H are impacted (Figure 6.A.1). Generally, the ΔQ_S increases (red, Figure 6.8) which follows as the materials then assigned to roofs have both higher k (up to four times cf. original values in Table 6.4a) and generally larger ρc_p.

Comparing all material simulations to the T observations (Morrison et al. 2020, 2021), the M$_{\mathrm{LDN6}}$ and M$_{\mathrm{LDN1}}$ are the most similar to observed T_{Wall} (day and night) (Figure 6.10). Using M$_{\mathrm{LDN6}}$ parameters gives slightly more similar results to the observed T_{Roof} during the daytime but is one of poorest of T_{Roof} overnight. Maximum differences between the M$_{\mathrm{LDN1}}$ and M$_{\mathrm{LDN6}}$ simulations across the whole day are < 0.25 °C for T_{Wall}, and < 2 °C for T_{Roof}. Given the small differences in T between the two simulations, and therefore also between each and the T observations (Figure 6.10, Figure 6.2), for the single- and multi-layer comparison and morphology analysis (Section 6.3.3, 6.3.4) the M$_{\mathrm{LDN1}}$ internal wall, roof, and ground parameters (Table 6.4) are used.

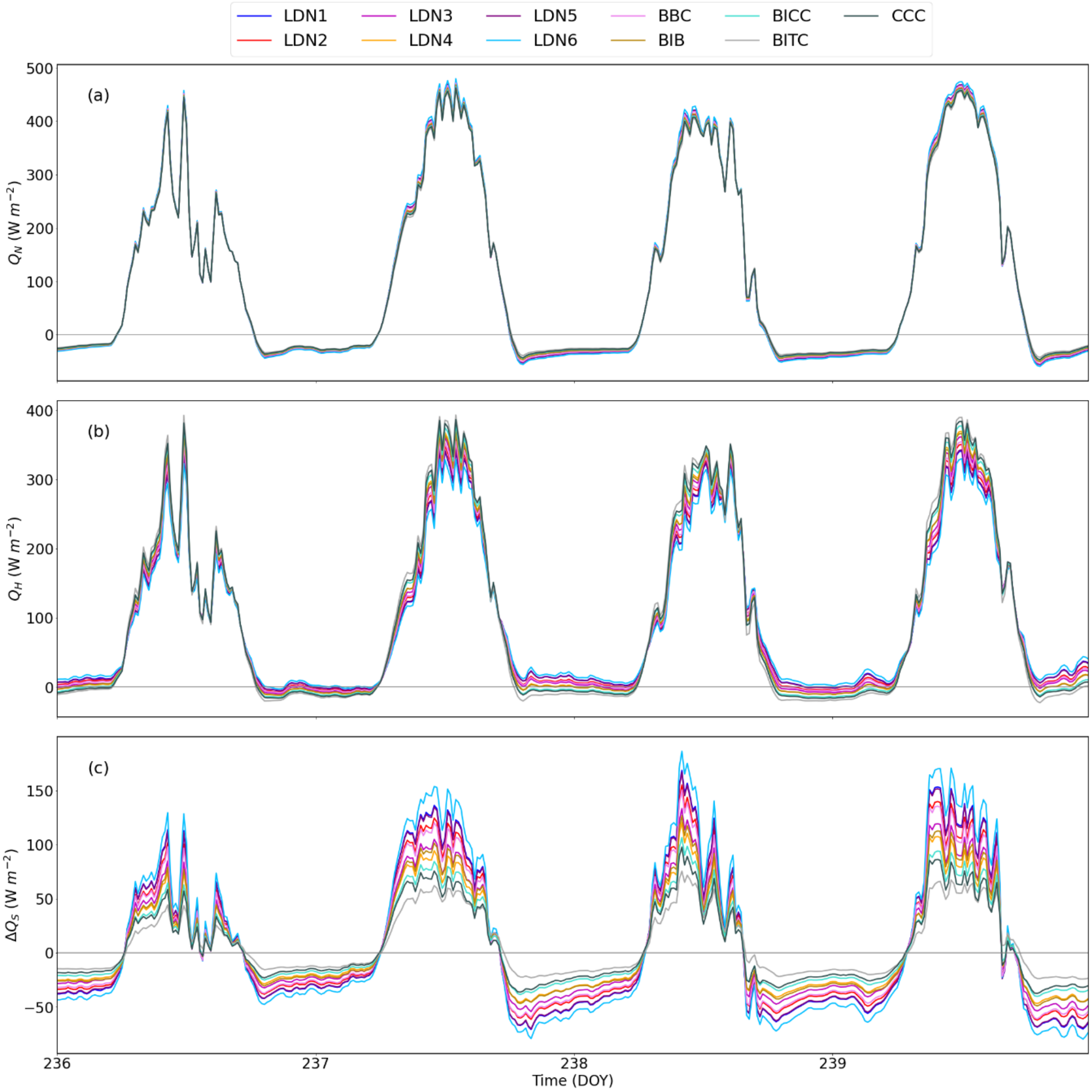

Figure 6.9: Impact of changing thermal parameters (colour, code in Table 6.4) to SUEWS-SS-mEHC SS-1 simulated surface energy balance fluxes (15-min) for four days in August 2017 (a) Q^*, (b) Q_H, and (c) ΔQ_S

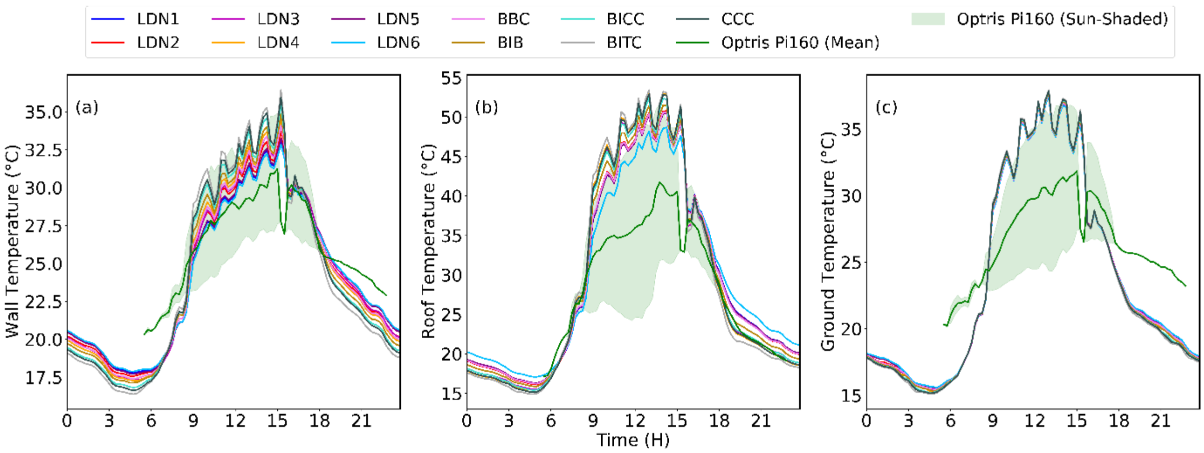

Figure 6.10: Impact of changing thermal parameters (colour, code in Table 6.4) to SUEWS-SS-mEHC SS-1 simulated surface temperatures (15-min) for DOY 239 August 2017 (a) T_{Wall}, (b) T_{Roof}, and (c) T_{Ground}

6.3.3 Single- and multi-layer (SS-1, SS-9) simulations for London (F_{Lon})

Single (SS-1) and nine layers (SS-9) SUEWS-SS-mEHC simulations are conducted for a central London area (F_{Lon}, Figure 6.6) with surface temperature observations (Section 6.2.2).

First, the simulated facet temperatures (T_{Wall}, T_{Roof}, T_{Ground}) are assessed using the observed T Morrison et al. (2021)'s for 27th August 2017 (Figure 6.11). The SS-9 results are consistent with the daytime peak mean facet T observations, despite complex real-world roof geometry (Figure 3.1, Chapter 3, and Figure 1, Morrison et al. (2021)) (Figure 6.11), and complex surface materials.

Both the diurnal pattern and magnitude of the SS-9 and SS-1 simulations agree with the wall and roof facets observations, particularly the SS-9 modelled range of temperatures. From 09:00 – 15:00 the simulated facet T are warmer than observed, but cooler after a cloud period at ~15:00. As the SS-1 simulated T_{Roof} lacks realistic roof shading, it is warmer than SS-9 ($MBE_{SS\text{-}1}$ = 4.2 °C; $MBE_{SS\text{-}9}$ = 2.8 °C, Table 6.6). During pre-sunrise and post-sunset periods, both SS-1 and SS-9 underestimate T_{Wall}, and T_{Ground} (Figure 6.11a, c), with larger differences for T_{Ground}. This suggests further sensitivity tests are needed for ground materials. As the camera measurements cover a smaller area than the F_{Lon} grid (Section 6.2.2), the selection of materials parameters (Section 6.2.5) may not be ideal.

Second, top-of-canopy short (SW), long (LW) and net all-wave (Q^*) radiative fluxes (Figure 6.A.3) are analysed. These show the expected increase over the four day-period, consistent with the forcing data (i.e., forcing peak daytime $\mathrm{SW}_{\downarrow}$ and T_{Air} increase). The SS-1 and SS-9 simulations are similar (nMBE < 1.5%) for SW*, LW* and Q^* (Table 6.5, Figure 6.A.3). As the single layer SS-1 simulations use the same α and ε as the SS-9 multi-layer configuration (Section 6.2.1.1), the SS-1 radiative fluxes are larger than the SS-9 during the day, consistent with the multi-layer simulation accounting for greater radiative trapping and shadowing during the daytime.

Third, comparing surface energy balance fluxes (i.e., Q^*, ΔQ_S, Q_H) for the four-days (Figure 6.12, Table 6.5), the results are similar between the two layer configurations (Figure 6.A.3, Figure 6.A.4). In these $\mathrm{F}_{\mathrm{Lon}}$ simulations, $Q_H > \Delta Q_S$ throughout the daytime (Figure 6.8, Figure 6.A.4). With no vegetation, no rainfall, no irrigation, and no water-bodies Q_E is effectively 0 W m^{-2}, so the Q_H is larger (Figure 6.8). Hence, although the $\Delta Q_S - Q_H$ differences and timings, differ from previous observation- and model-based studies (e.g., given in section 6.3.1), they appear to be consistent with the section 6.3.1 results.

Table 6.5: Four days in August 2017 of simulations for a 2 km × 2 km area in central London ($\mathrm{F}_{\mathrm{Lon}}$, Figure 6.7, Table 6.3) compared using 15-min model output relative to SUEWS-SS-mEHC-multi-layer (SS-9) of to SUEWS-SS-mEHC-single-layer (SS-1) for top-of-canopy net shortwave (SW*) and longwave (LW*), all-wave (Q^*) radiation, storage heat flux (ΔQ_S), and sensible heat (Q_H) fluxes for day and night using metrics discussed in secti2.6

Flux	Mean SS-9 (W m^{-2})	MBE (W m^{-2})	nMBE (%)	MAE (W m^{-2})	nMAE (%)
Day ($\mathrm{SW}_{\downarrow}$ > 0, n=585)		SS-1			
SW*	289.1	-0.8	-0.9	0.8	0.9
LW*	-88.2	-0.4	1.4	0.4	-1.4
Q^*	200.9	-1.2	-1.9	1.2	1.9
ΔQ_S	40.2	0.3	2.6	0.6	4.5
Q_H	155.1	-1.7	-3.3	1.8	3.6
Night ($\mathrm{SW}_{\downarrow}$ = 0, n=759)					
LW*	-34.3	0.01	-0.2	0.02	-0.2
Q^*	-34.3	0.01	-0.2	0.02	-0.2
ΔQ_S	-43.2	-0.3	2.5	0.3	-2.6
Q_H	6.8	0.2	14.4	0.3	15.7

Table 6.6: Four days in August 2017 of simulations for a 2 km × 2 km area in central London (F_{Lon}, Figure 6.7, Table 6.3) compared using 15-min model output relative to SUEWS-SS-mEHC-multi-layer (SS-9) of to SUEWS-SS-mEHC-single-layer (SS-1) for facet temperatures (wall – T_{Wall}, roof – T_{Roof}, ground – T_{Ground}) with the observations as reference (Optris PI-160 thermal camera, Morrison et al. (2021)) on 27th August 2017 from 5:45 – 23:00. All errors are to the mean of the sunlit and shaded temperatures, weighted equally

Facet	Mean Obs (°C)	MBE (°C)	nMBE (%)	MAE (°C)	nMAE (%)	MBE (°C)	nMBE (%)	MAE (°C)	nMAE (%)
n=70		SS-9				SS-1			
T_{Roof}	29.5	2.8	9.4	3.6	12.2	4.2	14.2	4.7	16.0
T_{Wall}	26.2	1.0	3.8	2.1	7.9	-0.3	-1.0	1.3	5.0
T_{Ground}	26.5	0.5	2.0	4.7	17.8	-0.2	-0.9	4.1	15.3

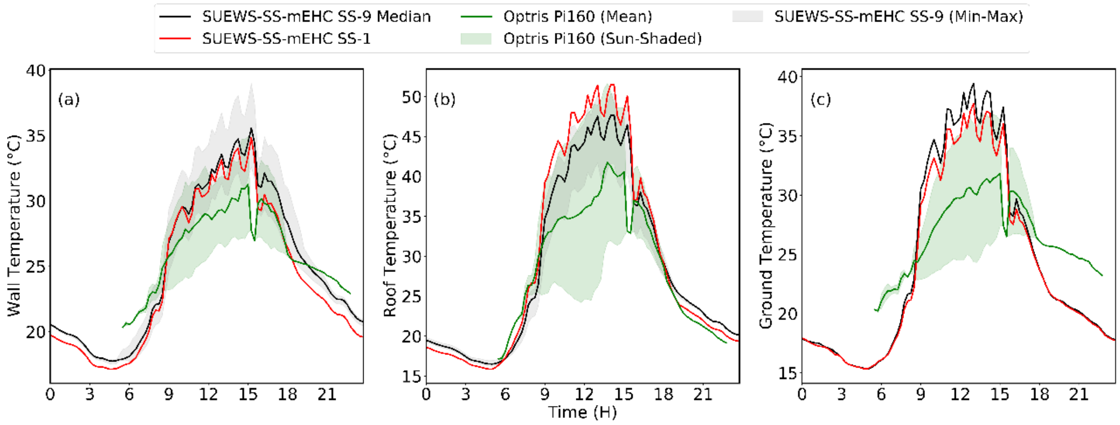

Figure 6.11: Mean (green line, sunlit and shaded weighted equally) observed surface temperature, with a sunlit-shaded range (green shading) (Morrison et al. 2021) and SUEWS-SS single- (red) and multi-layer (black, shaded) simulated for 27th August 2017 for a 2 km × 2 km area of central London (F_{Lon}, Table 6.3) for three facets: (a) wall, (b) roof, (c) paved/ground. Note y-scale differs

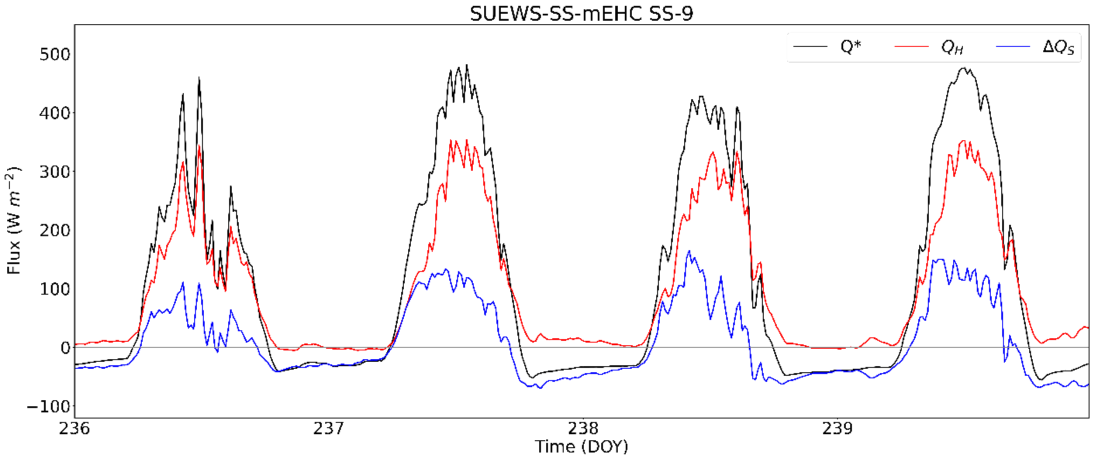

Figure 6.12: Timeseries of Q^*, $Q_{H,}$ and ΔQ_S (15-min) for four days in August 2017, for a 2 km × 2 km area in central London (F_{Lon}, Table 6.3) simulated with SUEWS-SS-mEHC multi-layer (SS-9)

6.3.4 Implication of morphology variation

To assess the role of morphology variations, the SUEWS-SS-mEHC SS-9 configuration is used to simulate a wide range of morphologies found in and across cities globally (F_{C1-9}, Section 6.2.5, Table 6.3, Figure 6.6), spanning low (< 0.1) to high (< 0.55) $\lambda_p(z = 0)$ (blue – red, e.g., $F_{C1} \rightarrow F_{C4} \rightarrow F_{C7}$), and low (< 7.5 m) to high $\overline{H}$ (< 35 m) (light – dark, e.g., $F_{C1} \rightarrow F_{C2} \rightarrow F_{C3}$). All are forced with the same meteorological data (section 6.2.2) and prescribed the same material parameters (M_{LDN1}, Table 6.4). The surface energy balance fluxes and the vertical variation of surface temperatures are analysed separately.

6.3.4.1 Surface Energy Balance

Generally, more $SW_{\uparrow}$ is reflected in areas with more open canopies (i.e., smaller $\lambda_p(z = 0)$) (Figure 6.13), with the denser morphologies F_{C7} – F_{C9} ($\lambda_p(z = 0) > 0.25$) reflecting ~ 60% less SW radiation than less dense grids (F_{C1-3}, Fig 6.13a). This results in a smaller top-of-canopy albedo, as the building density increases (blue to red, Figure 6.14), from 0.19 for F_{C1} to 0.09 for F_{C8}.

The diurnal albedo pattern varies with morphology, with F_{C1}, F_{C2}, F_{C4} and F_{C5} having an increase in albedo immediately after sunrise. Whereas in F_{C6-7} (both with mid-density high building heights, and high-density low building heights) areas, the albedo decreases (increases) almost immediately after sunrise (sunset) then increases to a middle of the day (~ 12:00) maxima, with a 'W' shape as observed in hardware models (e.g., Aida (1982)). Whilst, the F_{C8} ($\lambda_p(z = 0) = 0.34$, $\overline{H} = 10.2$ m) albedo decreases from a sunrise, giving a 'U' shape as observed in some dense urban areas (e.g., CBD of Marseilles

Grimmond et al. (2004)). Given the albedo impacts, all morphologies have similar SW* with peak values < 650 W m^{-2}, with the largest differences on the clearer days and for the areas with smallest $\lambda_p(z = 0)$.

For LW fluxes (LW*, $LW_{\uparrow}$), results are similar across all morphologies, except for high λ_p, low $\overline{H}$ domains (F_{C7}, F_{C8}). Magnitudes of daytime LW* are larger in open canopies (e.g., F_{C1}, -200 W m^{-2} on DOY 239), cf. denser ones, with differences up to ~140 W m^{-2} with increasing $\lambda_p(z = 0)$ and $\overline{H}$ (e.g., with F_{C8}), due to reduced sky view factor (fraction of the visible sky, ψ_{Sky} (Lindberg and Grimmond 2010)). This leads to a large range in Q^* between the domains (> 100 W m^{-2} on the clearest sky DOY 239), with areas with the largest $\lambda_p(z = 0)$ having the highest daytime Q^* on all days, followed by those with the highest $\overline{H}$ (Figure 6.15a). This can be attributed to areas with smaller LW*, and a highest SW* (Figure 6.13b, d), with less $LW_{\uparrow}$ emission due to the low ψ_{Sky}.

All areas have the expected nocturnal release of storage heat flux (ΔQ_S, Figure 6.15c). Across all morphology grids, the daytime maximum turbulent sensible heat flux (Q_H) > daytime maximum ΔQ_S (Figure 6.15c), consistent with results in Section 6.3.1. The largest ΔQ_S is in areas with highest $\lambda_p(z = 0)$, both for daytime (F_{C7}, F_{C8}, daytime peak ~ 150 W m^{-2}) and nocturnal emissions, consistent with lowest (highest) magnitude in daytime (nighttime) LW*. These denser morphologies have large surface area for absorption and heat loss (Sailor and Fan 2002; Lindberg et al. 2020). These impacts are also evident when there are tall buildings, as F_{C9} and F_{C6} also have high daytime ΔQ_S (Figure 6.15, ~ 100 W m^{-2}, DOY 239).

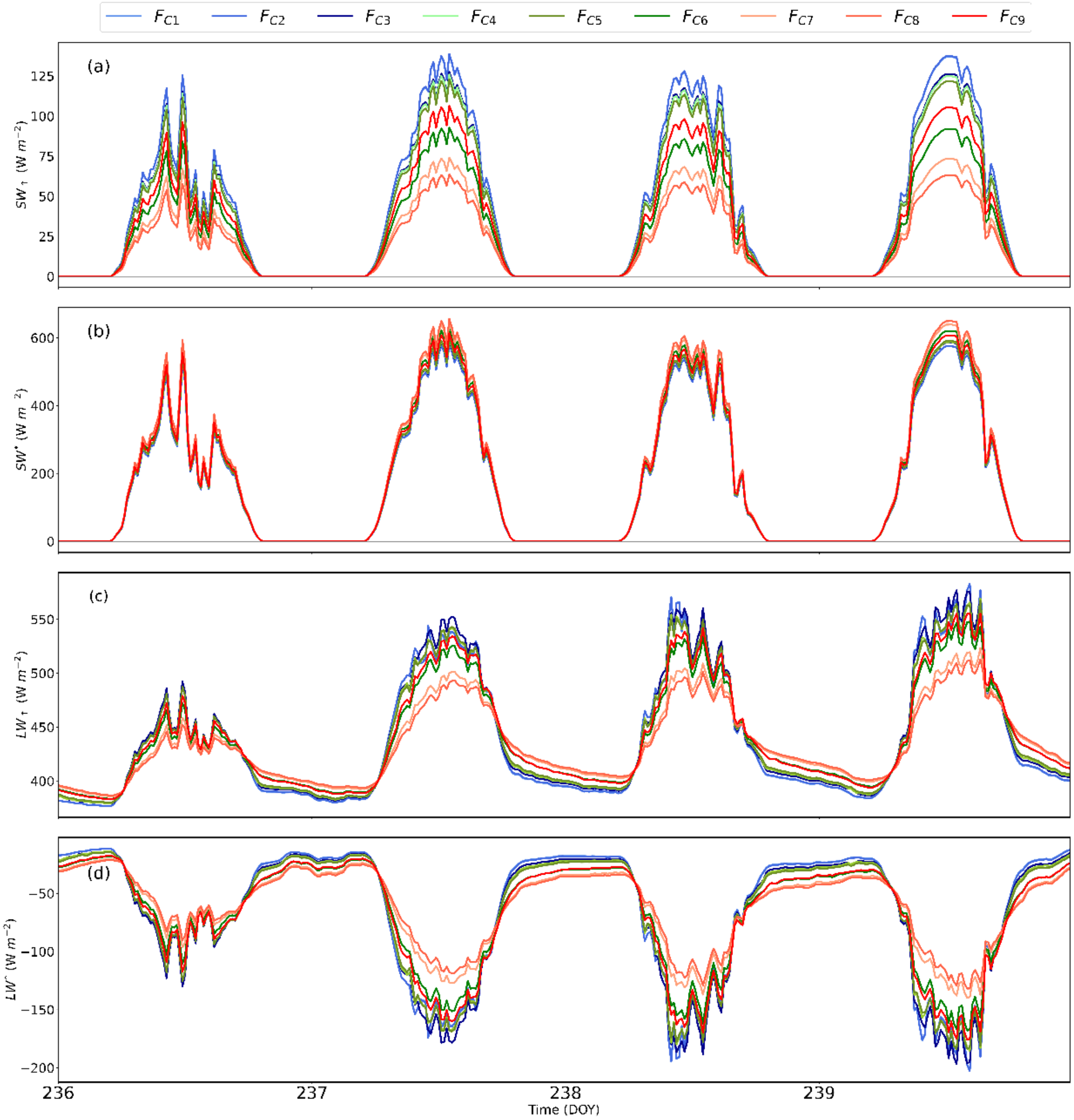

Figure 6.13: Upwelling (↑) and net (*) short (SW) and longwave (LW) radiation fluxes (15-min) for four days in August 2017, for nine (see Figure 6.6 for colour bar) 2 km × 2 km areas with common urban forms (F_{C1-9}), (Table 6.3) simulated with SUEWS-SS-mEHC multi-layer. Diurnal timeseries of (a) $SW_\uparrow$, (b) SW*, (c) $LW_\uparrow$, and (d) LW*. Morphology properties given in Table 6.3

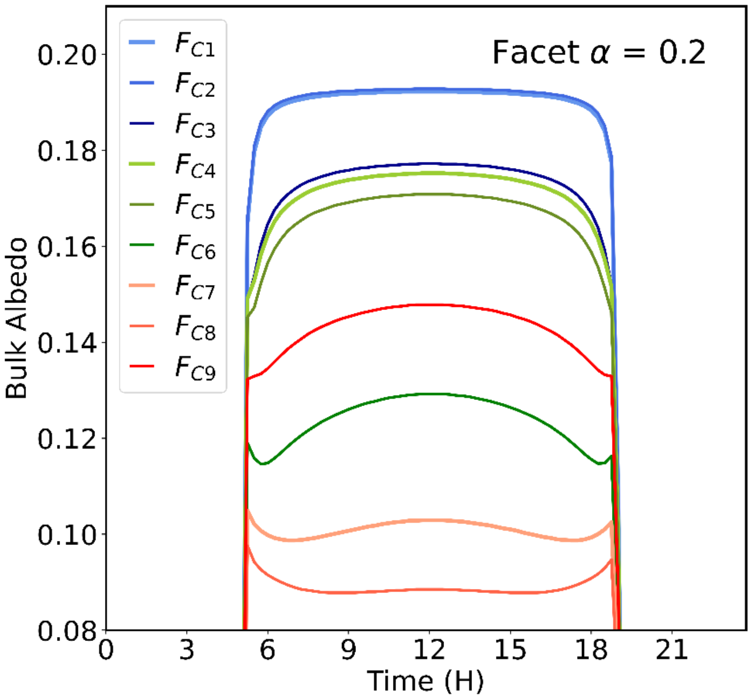

Figure 6.14: Top-of-canopy bulk albedo for nine urban forms ($F_{C1\text{-}9}$, parameters in Table 6.3 derived for 2 km × 2 km areas) simulated with SUEWS-SS-mEHC multi-layer (5-7 layers) assuming all facets (wall. Roof. Ground) material albedo is 0.2. Date: 27th August 2017, latitude: 51.5261 °N, longitude: 0.1061 °W

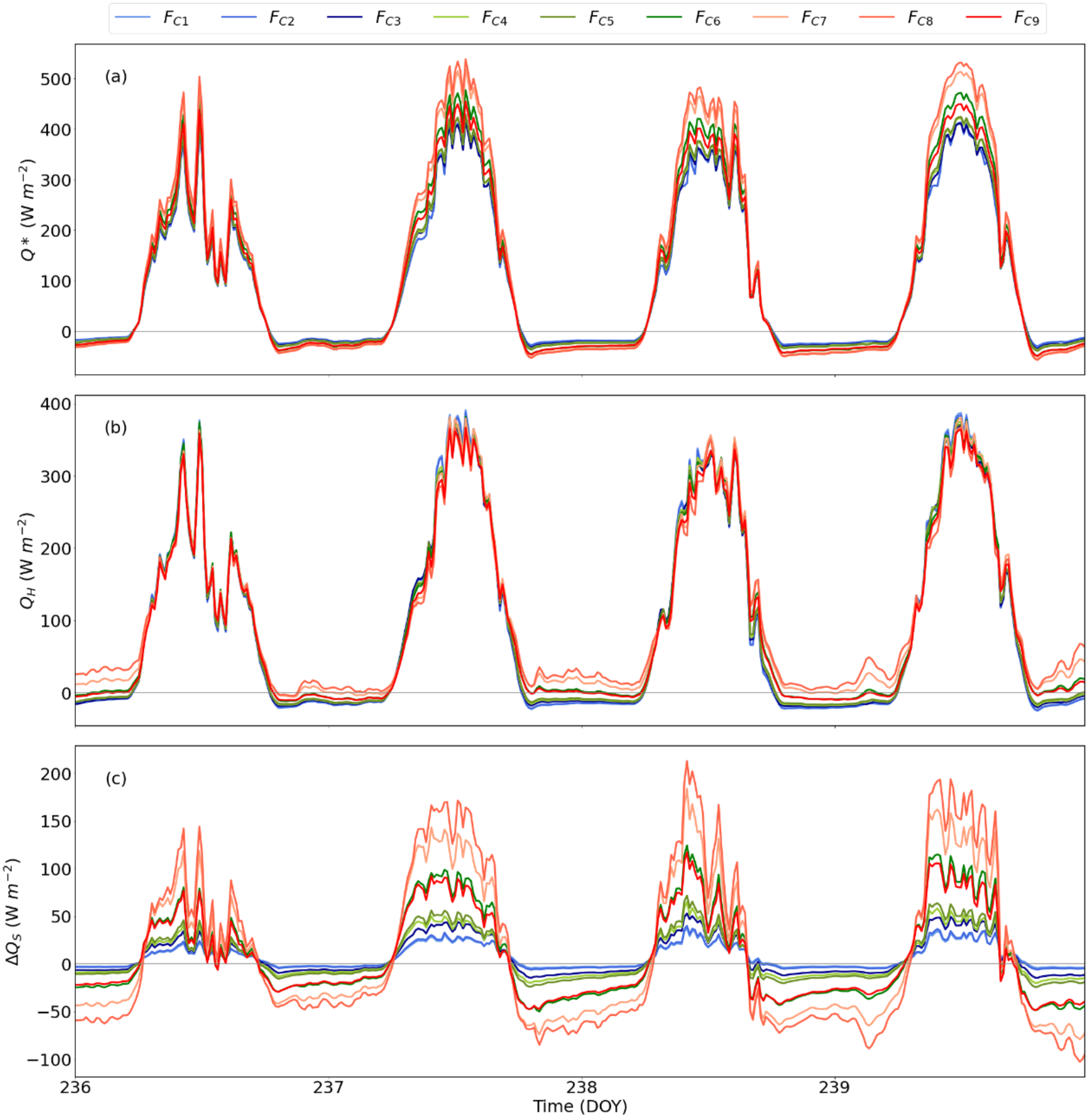

Figure 6.15: Surface energy balance fluxes (15-min) for four days in August 2017, for nine (see Figure 6.6 for colour bar) 2 km × 2 km areas with common urban forms ($F_{C1\text{-}9}$, Table 6.3) simulated with SUEWS-SS-mEHC multi-layer. Diurnal timeseries of (a) $Q*$, (b) Q_H, and (c) ΔQ_S

6.3.4.2 Vertically distributed surface temperatures

One benefit of multi-layer surface energy balance models is their ability to resolve surface temperatures vertically. Averaged surface temperature profiles derived from thermal camera observations in central London (F_{Lon}, Figure 6.6, Table 6.3) on a summer day (Chapter 4), have little vertical variation in T_{Wall} (1 – 3 ºC at all times), with higher T_{Roof} vertical variation (< 15 °C) given the range in building materials, surface orientation, and the sunlit/shaded status. As temperature gradients (with height) (T_{Roof}, T_{Wall}) may change with morphology and climate, here vertical facet T simulated with SUEWS-SS-mEHC are examined across $F_{C1\text{-}9}$.

As $\lambda_p(z = 0)$ increases, the range of T_{Roof} simulated with height increases (blue ($F_{C1\text{-}3}$) to red ($F_{C7\text{-}9}$), Figure 6.3, Figure 6.16). Most grids have a small T_{Roof} range between the height classes (line types, Figure 6.16), with the maxima being < 7°C for F_{C1} – F_{C6}, with F_{C7} having a slightly higher range (< 9 °C). The largest T_{Roof} difference across the morphologies occurs for F_{C8} during the afternoon (12:00 - 15:00), with a range ~15 °C, despite this morphology not having the largest range of building heights (Figure 6.7). In areas with the highest $\lambda_p(z = 0)$, but low $\overline{H}$ (F_{C7}, F_{C8}), the lowest roof class (0 – 2.5 m) has the coolest T_{Roof}, and the highest roof class ($1.5\overline{H} – 2\overline{H}$) the warmest T_{Roof}. Across all morphologies, the maximum T_{Roof} is similar (~ 50 °C).

For areas with both low $\lambda_p(z = 0)$ and $\overline{H}$ ($F_{C1\text{-}4}$), there is little vertical variation (< 1 °C) in T_{Wall} (Figure 6.17). For the remaining grids, the T_{Wall} increases with height (i.e., lowest layer has coolest T_{Wall}). For the tallest $\overline{H}$ categories (F_{C3}, F_{C6}, F_{C9}), the vertical gradient in T_{Wall} is higher, but still < 3 °C. Similar to T_{Roof}, the largest spread in T_{Wall} is seen in the F_{C7} and F_{C8} grids, with a range of up to 8 °C in the afternoon.

The T_{Ground} is warmest in grids with smallest $\lambda_p(z = 0)$ (Figure 6.18), corresponding to the highest bulk albedos (Figure 6.14) and therefore with more SW absorption by the ground than the walls. With more open ground, the area warms much more rapidly in the morning than those with larger $\lambda_p(z = 0)$ (Figure 6.18, blue cf. red). Between most morphology types considered, the variation in T_{Ground} is small during the daytime (~5 °C). Between 16:00 and 23:00 there is ~5 °C cooling for low building cover grids cf. higher cover grids (e.g., $F_{C7\text{-}8}$). Hence, the model is able to simulate the key controls of the urban heat island.

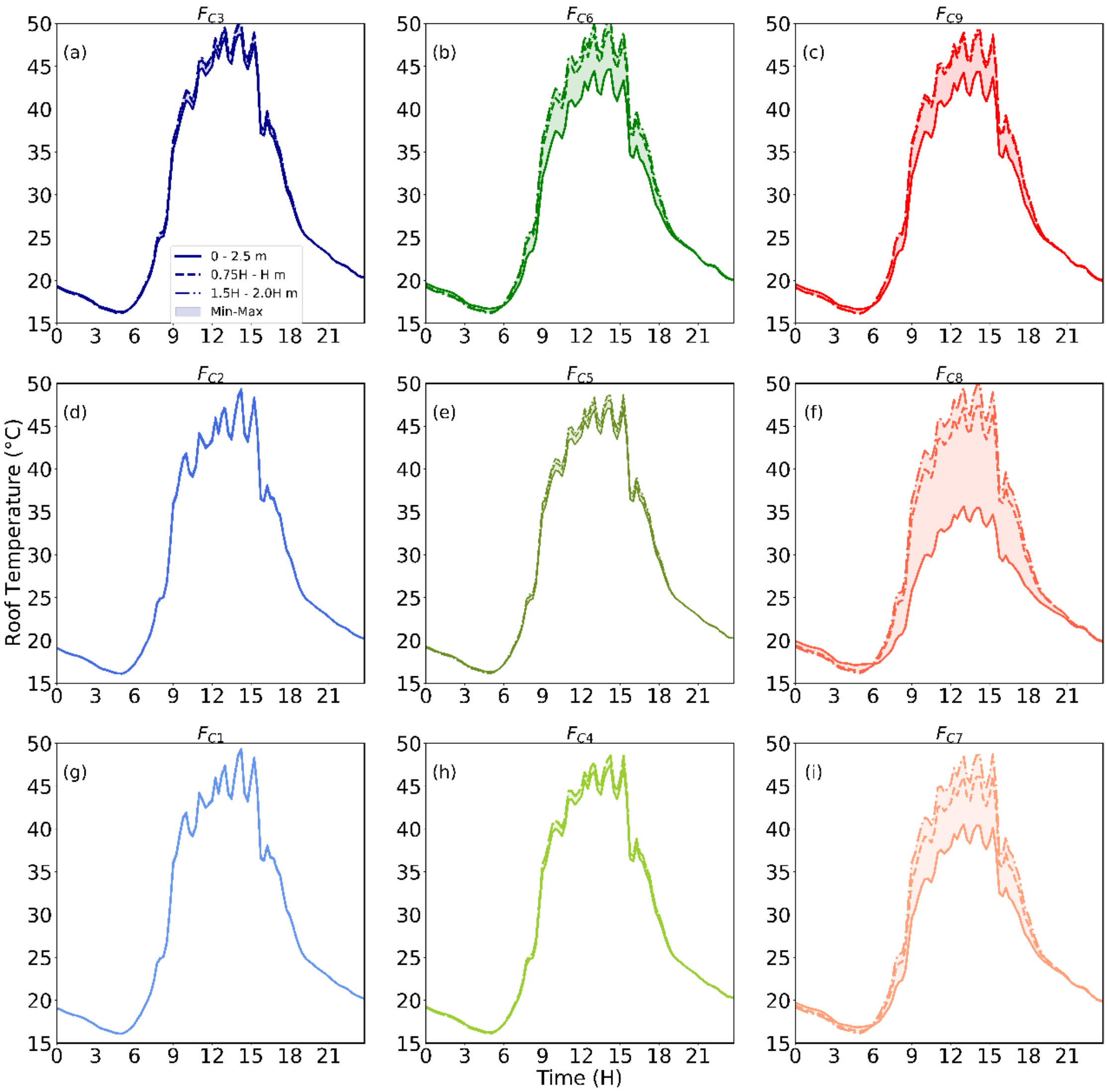

Figure 6.16: Variation of roof temperature (T_{Roof}) by morphology ($F_{C1\text{-}9}$, Figure 6.3, Figure 6.6, Table 6.3) between three roof height classes specified as a ratio of mean building height ($\overline{H}$) (linetype, key) simulated for 27th August 2017 with SUEWS-SS-mEHC (5-7 layers) for nine 2 km × 2 km areas

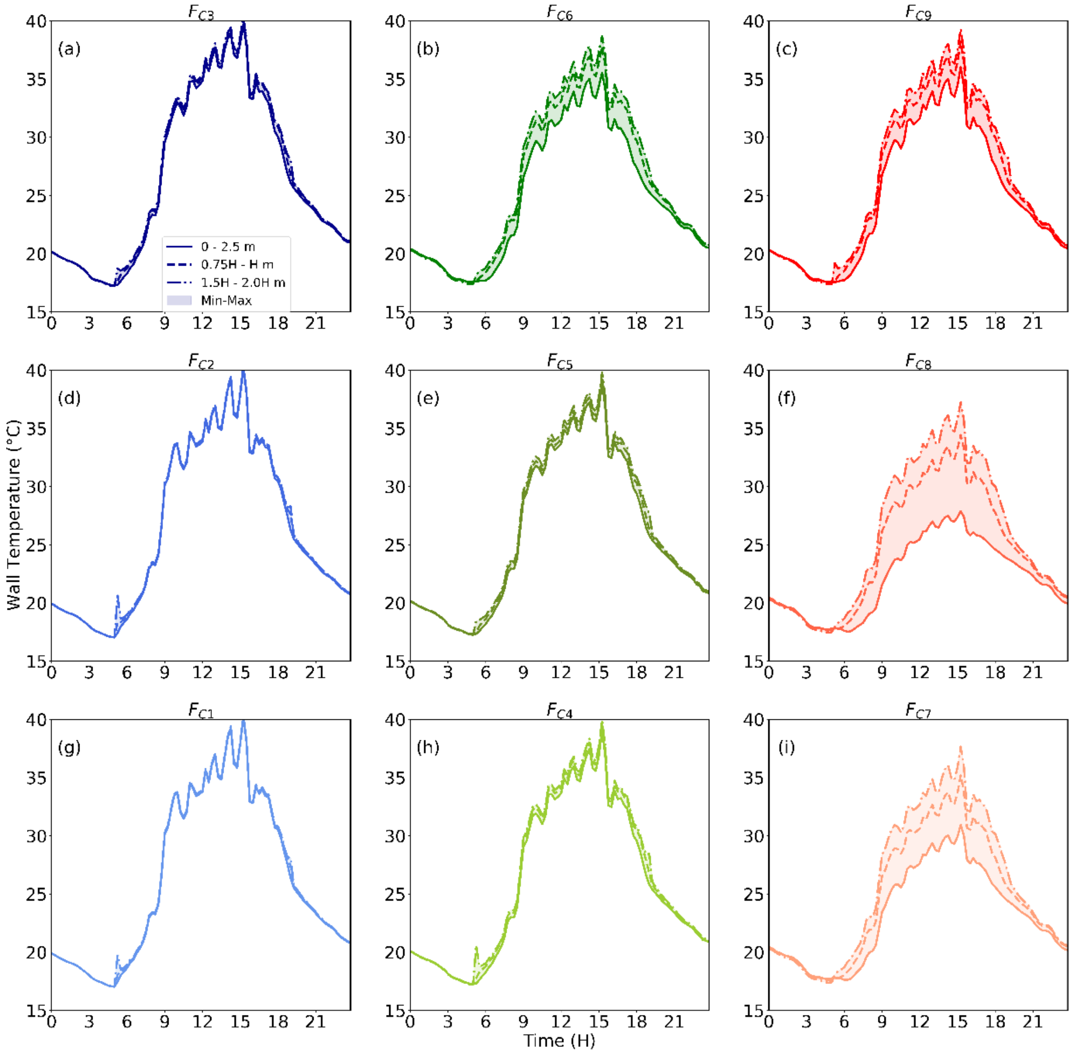

Figure 6.17: Variation of wall temperature (T_{Wall}) by morphology ($F_{C1\text{-}9}$, Figure 6.3, Figure 6.6, Table 6.3) between three roof height classes specified as a ratio of mean building height ($\overline{H}$) (linetype, key) simulated for 27th August 2017 with SUEWS-SS-mEHC (5-7 layers) for nine 2 km × 2 km areas

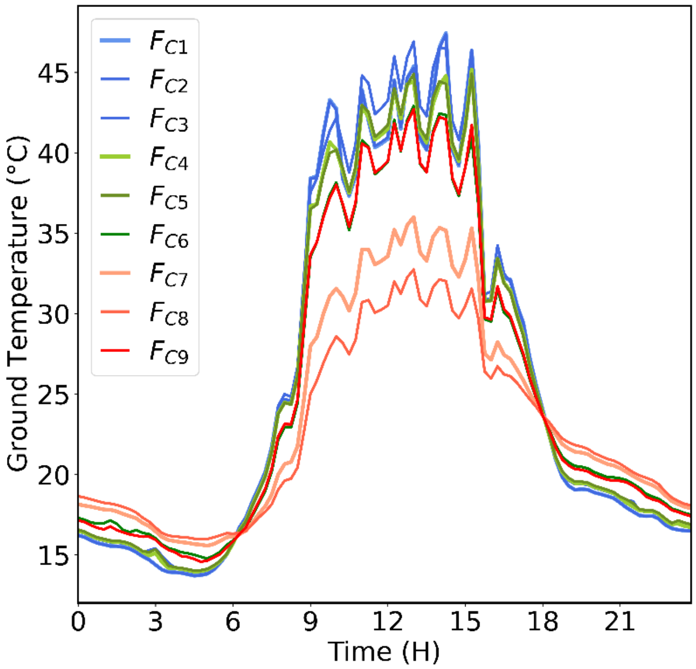

Figure 6.18: Variation of ground temperature (T_{Ground}) by morphology ($F_{C1\text{-}9}$, Figure 6.3, Figure 6.6, Table 6.3) simulated for 27th August 2017 with SUEWS-SS-mEHC (5-7 layers) for nine 2 km × 2 km areas

6.4 Conclusions

Enhancing urban energy balance models to be multi-layer allows vertical variations of heat fluxes and surface temperatures to be simulated and analysed. Notably, including vertical variations in the radiative fluxes allows realistic distribution of sunlit and shaded surfaces. Here the SUEWS model (Järvi et al. 2011, 2014; Ward et al. 2016), is coupled to the SPARTACUS-Surface radiation scheme (Hogan 2019a), and a new multi-layer storage heat module (mEHC). This new system (SUEWS-SS-mEHC) is used to examine the impact and benefits of using a multi-layer radiation scheme across different geometry found in real cities. The model is applied to multiple different 2 km × 2 km areas.

Previously, SPARTACUS-Surface has been evaluated against an explicit radiative transfer model (Chapter 3, Chapter 4). Here, SUEWS-SS-mEHC skill at simulating facet (wall, roof, and ground) surface temperatures is assessed using high resolution ground based thermal remote sensing for central London (Morrison et al. 2020, 2021). In both the single- and multi-layer SUEWS-SS-mEHC simulations, the diurnal temperature pattern is accurately captured, with daytime values always with the observed sunlit-shaded range for roofs and walls.

SUEWS-SS-mEHC simulations in central London (with buildings up to 100 m tall) are used to assess differences between the single- and multi-layer configurations. Consideration is given to material thermal properties and number of layers, both impacting results. The simulated shortwave radiative fluxes (SW) are similar across the study period. Slightly higher top-of-canopy upwelling shortwave ($SW_{\uparrow}$) are obtained for single-layer configuration, as the facet albedos and emissivities are assigned the same as the multi-layer case.

The multi-layer SUEWS-SS-mEHC has warmer wall temperatures (cf. single-layer, due to the representation of vertical sunlit fraction), and cooler daytime roof temperatures (due to shading of roofs by taller buildings) up to 5 °C (independent of vertical temperature variation). However, overnight-temperatures are slightly too high for both the walls and roofs, and lower for the ground temperatures cf. observations. Improvements between the model and observations could come with finer-tuned material characteristics, as here all facets are assumed to have a constant albedo, and emissivity, and prescribed internal materials. The materials tested and used here are unlikely to be representative of the source area of the thermal cameras themselves due to the nature of the urban heterogeneity.

Analysis of multi-layer SUEWS-SS-mEHC simulated diurnal timeseries of vertically distributed surface temperatures for multiple geometry types, shows that for most geometry types the vertical variation of roof (< 7 °C) and wall (1 – 5 °C) temperatures are low. This contrasts with the temperature profiles derived from thermal camera measurements (Chapter 4), as these showed the same low wall temperature variation (< 3 °C), but high vertical variation in roof temperatures (< 15 °C). In the current results, the expected behaviour in surface temperatures are seen. For example: (1) cooler maximum temperatures as building cover fraction increases, due to more radiative trapping; (2) grid-cells with low building cover, have large overnight radiative cooling, ~ 5 °C but largest for grid-cells with low building cover (< 0.15) between 16:00 and 23:00.

Roof temperature patterns are complex across morphology types. For all grids the highest roof temperature are in their top layer, with little vertical temperature variation in grids with low mean building heights and small surface building fraction. The largest vertical surface temperature range occurs in an area with high surface building fraction, but not the highest mean building height simulated. These analyses demonstrate the benefit and importance of simulating the real-world geometry, in order to understand the complex radiative and other interactions. The SUEWS-SS-mEHC temperature outputs are allowing more rapid inter-and intra-city street-level thermal comfort indices to be obtained.

Analysis of real cases with both single- and multi-layer configurations of the same model, shows clear benefits from vertically resolving the urban form. Evaluations of such schemes using longer observational datasets, will help identify how such models behave in different meteorological and land-cover configurations. This first investigation into SUEWS-SS-mEHC capabilities suggests the material properties of the area need careful consideration. Future model developments should use the available vertical profiles of temperature, humidity, and wind speed as model forcing (Tang et al. 2020), rather than the current inertial sub-layer values.

The SUEWS-SS-mEHC (or other such scheme) should be coupled to a NWP model to evaluate the modified (hopefully improved) top-of-canopy fluxes impacts on the atmosphere. This could improve prediction of street-level conditions (e.g., temperatures, heat stress) of interest to prepare for, and mitigate the impacts from extreme weather events on the public.

Appendix 6.A Supplementary material for Chapter 6

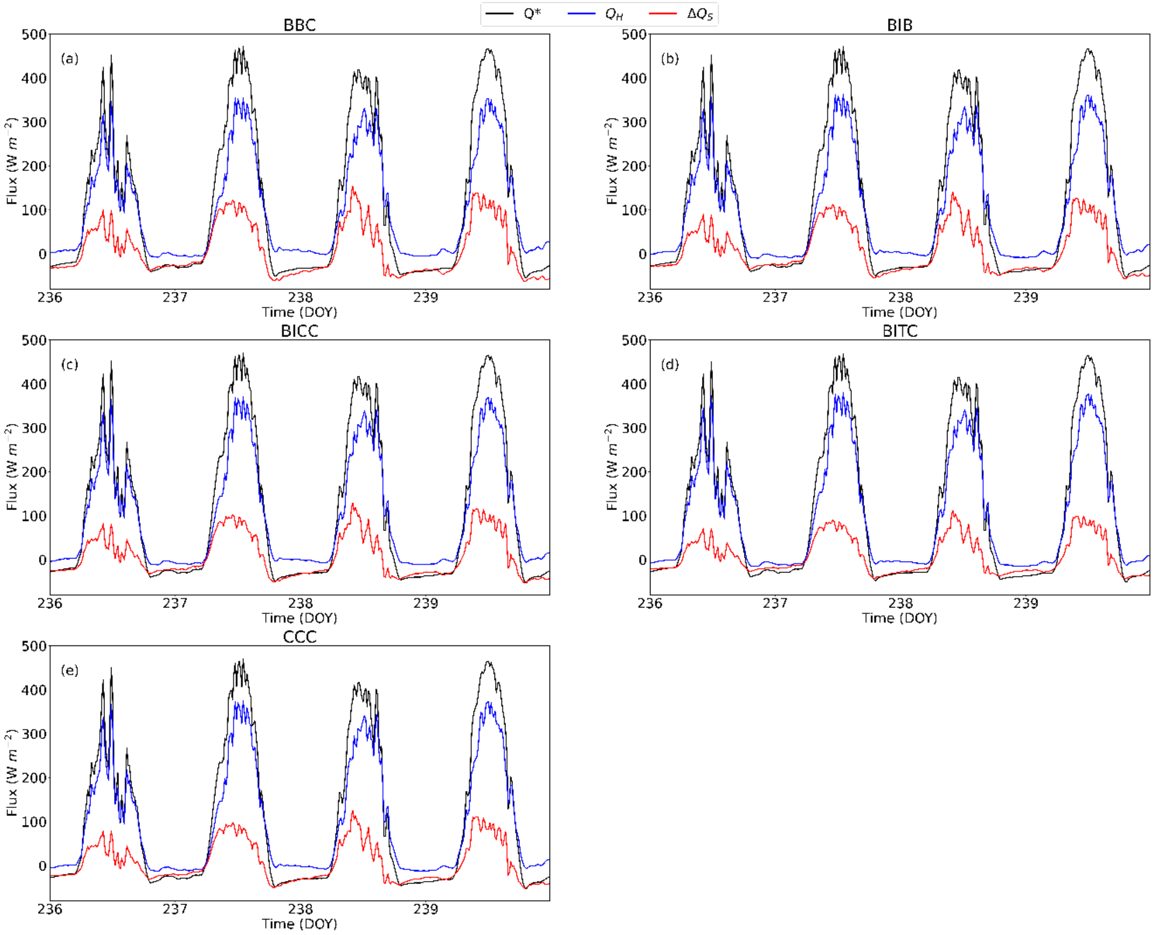

Figure 6.A.1: Impact of changing thermal parameters (colour, code in Table 6.4) in SUEWS-SS-mEHC, for thermal material parameters (M_X) in Table 6.4a (CIBSE 2015), using M_{LDN1} materials for roofs. SS-1 simulated surface energy balance fluxes (15-min) for four days in August 2017: Q^* (black), Q_H (blue), and ΔQ_S (red)

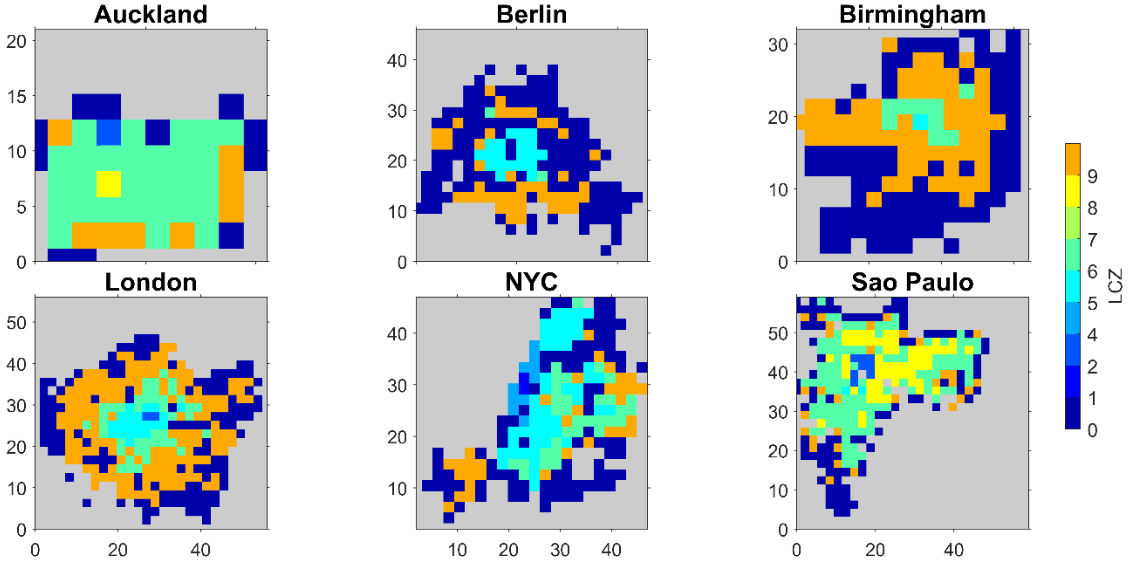

Figure 6.A.2: Local climate zones (LCZ 1-9, colour bar) (Table 6.2, Stewart and Oke (2012a)) mapped to 2 km × 2 km domains in six cities (Table 6.2) based on $\lambda_p(z = 0)$ and $\overline{H}$. Unclassified grid-cells are assigned LCZ 0. As LCZ categories overlap when using this simple basis (Figure 6.2) they are assigned the same colour (LCZ 3+8, and LCZ 5+10)

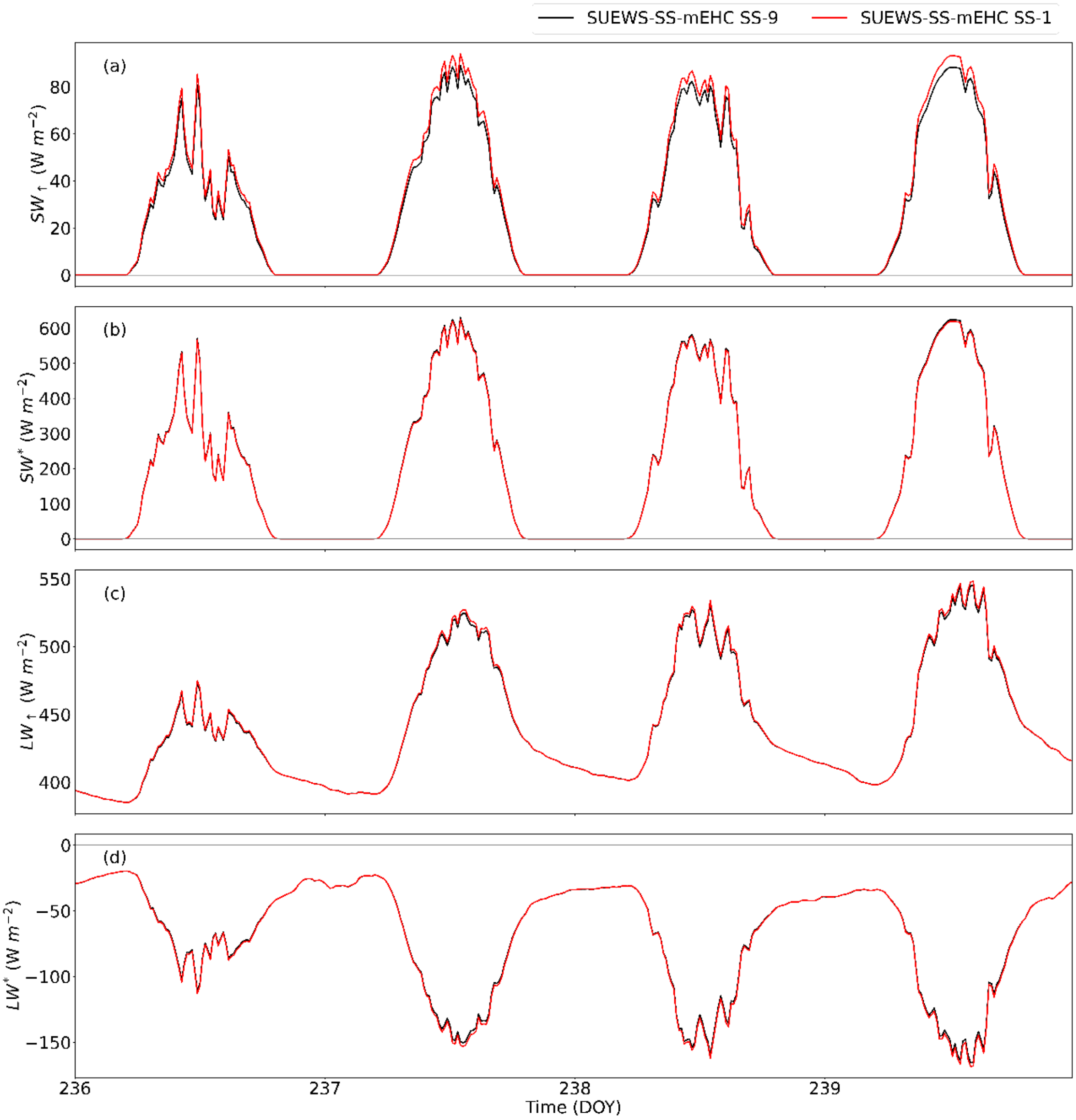

Figure 6.A.3: Upwelling (↑) and net (*) short (SW) and longwave (LW) radiation fluxes (15-min) at top of the canopy for four days in August 2017, for a 2 km × 2 km area in central London (FLon, Table 6.3) simulated with SUEWS-SS-mEHC (single layer (red) and nine layers (black)) timeseries of (a) $SW_\uparrow$, (b) SW*, (c) $LW_\uparrow$, and (d) LW*. See Figure 6.A.4 for net all-wave radiation (*Q**)

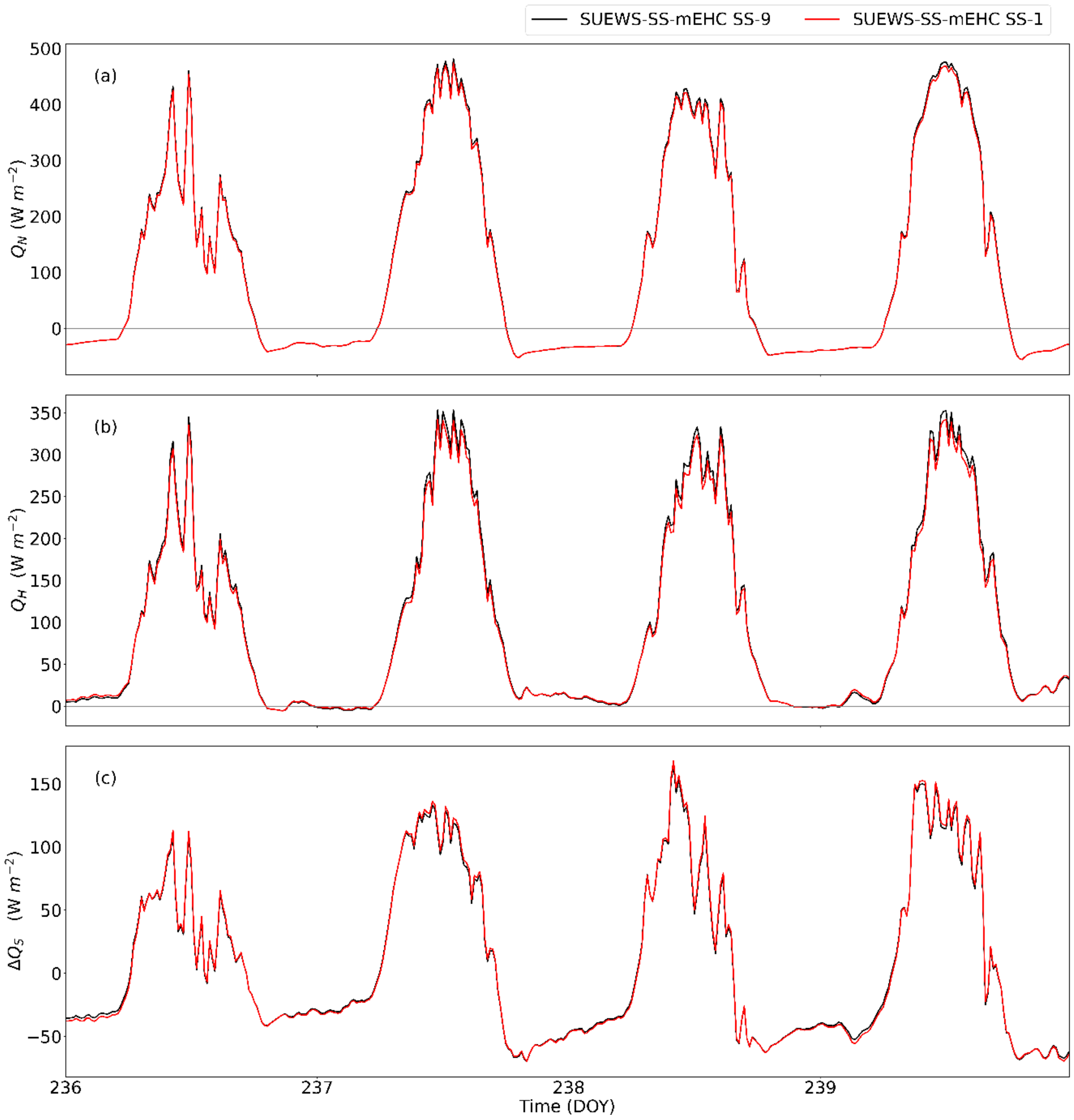

Figure 6.A.4: Surface energy balance fluxes (15-min) at top of the canopy for four days in August 2017, for a 2 km × 2 km area in central London (F_{Lon}, Table 6.3) simulated with SUEWS-SS-mEHC (single layer (red) and nine layers (black)) diurnal profiles of (a) Q^*, (b) Q_H, and (c) ΔQ_S

Chapter 7 Conclusions

7.1 Research Summary

Given predicted increases in both the frequency and intensity of extreme weather events, such as heatwaves (IPCC 2014b), it is critical that services (e.g., transport, energy, water, and planning) are provided with appropriate information to ensure preparedness, and to mitigate the effects on both human health and infrastructure. This is particularly important in cities, where extreme events may be exacerbated (Ao et al. 2019) given the diversity of materials, urban structure, and vegetation (often limited) across a city (Lindberg and Grimmond 2011b), which influence radiative exchanges and temperatures (Oke 1982b). A combination of high-resolution databases on urban morphology, materials and meteorological observations, alongside high-resolution forecasts and early-warning systems can support this process (Baklanov et al. 2018).

However, numerical weather prediction (NWP) is limited by both computer resources, and availability of datasets that provide urban form details, impacting how the urban influence on the surface energy balance can be parameterised. Currently, one common approach simplifies the urban form to a single-layer infinitely long street-canyon, with vegetation treated separately. But with NWP models increasing horizontal resolution, such as kilometre-scale (i.e., resolving neighbourhoods) for operational NWP, and 100 m scale for ‘turbulence-permitting’ (i.e., resolving large buildings), urban areas will cover multiple grid-boxes (Ronda et al. 2017; Lean et al. 2019). This is going to require multi-layer models for airflow, radiation, and surface energy balance (SEB), whilst remaining computationally cheap.

This thesis demonstrates the benefits that applying multi-layer urban models could bring to NWP, particularly with a focus on radiative fluxes. The work undertaken is:

- *A first evaluation of a multi-layer radiative transfer model for shortwave radiation, for a variety of urban forms (Chapter 3).*
- *A first evaluation of a multi-layer radiative transfer model for longwave radiation, for a summer day in a European city (London, UK), utilising surface temperature observations (Chapter 4).*

- *The development of parameterisations to provide vertical profiles of building geometry for cities globally (Chapter 5).*
- *An investigation into how multi-layer modelling approaches influence the surface energy balance, including a focus on vertical profiles of surface temperature, tested across a wide range of real morphology configurations (Chapter 6).*

7.2 Main conclusions and contributions

7.2.1 Capabilities of the SPARTACUS-Urban multi-layer radiative transfer model

Objective 1: evaluate the performance of SPARTACUS-Urban against a 3D ORM.

Here, SPARTACUS-Urban (Hogan 2019a) is evaluated for shortwave and longwave radiation, using an object resolving model (ORM) for radiative transfer, DART (Gastellu-Etchegorry et al. 2015) in a selection of 2 km × 2 km grids with varying geometry.

The SPARTACUS approach assumes the buildings and vegetation are arranged randomly in the horizontal plane. Hogan's (2019a) exponential distribution used to characterize real-world horizontal wall-to-wall separation distances performs well in shortwave simulations for both London and Indianapolis, supporting findings in Hogan (2019b). However, it underpredicts the occurrence of large building-separations, and hence the penetration of solar radiation to ground-level when the sun is low in the sky. Applying a modification to the building edge length when simulating shortwave fluxes that varies with solar zenith angle, reduces bias errors in fluxes by up to half.

Beyond demonstrating that SPARTACUS-Urban performs well relative to the ORM, it is crucial to assess the benefits of this new approach compared to a current one used operationally in NWP (e.g., Met Office, (Porson et al. 2010b), and Météo-France (Masson 2000) that utilises the single-layer infinite-street canyon approach to represent the urban form (i.e., Harman et al. (2004)). The Harman et al. (2004) method performs well compared to an ORM. Errors for fluxes at the canopy-top, critical if considering urban surface-atmosphere interactions, via the bulk albedo have normalised bias errors < 6%. However, the longwave and shortwave fluxes into walls and roofs are improved when using the multi-layer approach, with normalised mean absolute errors < 15%, compared with normalised errors for the Harman et al. (2004) approach with values of up to 31%. This is due to the wall and roof areas varying with height, allowing more realistic shadowing and radiative trapping. This is particularly the case for roof absorptions, as multi-layer modelling approaches decrease their shortwave interception, as they can be shaded by taller buildings. This has been shown in other modelling studies when building height distributions within grid-boxes are utilised (Schubert et al. 2012).

SPARTACUS-Urban longwave flux simulations show particularly good agreement to DART, with normalised bias errors in top-of-canopy upwelling and bottom-of-canopy downwelling clear-air fluxes < 2.5%. Normalised bias errors for the net facet fluxes are slightly larger at < 4%. Offline, SPARTACUS-Urban requires roof and wall temperatures as inputs. Here, vertical profiles of surface temperatures were derived for a London summer day using SPARTACUS-Urban sunlit and shaded fractions, and thermal camera observations (Morrison et al. 2020, 2021). The computed vertical gradient of wall temperatures are small at all times of the day (< 3 °C), compared to computed roof temperatures that have a vertical range up to ~15 °C (11:45; 13:45 UTC). Despite this, top-of-canopy fluxes were the same when using a vertical temperature profile, and a single average temperature. Between these simulations, the largest normalised errors were found in the net ground flux and the outgoing roof flux, but magnitudes were below 5%. These results may differ depending on geometry or climate.

Chapter 3 and Chapter 4 help to justify the need to incorporate vertical variability of the urban form, to better represent radiative fluxes. Overall, the SPARTACUS-Urban approach to urban radiation performs well in both the longwave and shortwave, when comparing against the complex and computationally demanding ORM, DART. This indicates that it is suitable for implementing into a multi-layer urban energy balance model, and when evaluated, may benefit weather and climate modelling.

7.2.2 Characterising the vertical urban form

Objective 2: to develop parameterizations to simplify urban form requirements

Despite these multi-layer modelling benefits, the implementation is limited by the grid data requirements. With a focus on SPARTACUS-Urban, vertical profiles of building fraction and wall area are parameterized, using the mean building height and surface building fraction at a 2 km × 2 km resolution for six cities. The introduced horizontal building size, the effective building diameter, varies weakly between cities ‘worldwide’, with a mean of ~21 m. Morphology is shown to be highly variable across and between cities at this resolution, both horizontally and vertically. This suggests that any parameterisations used for NWP should cover a variety of building fractions and allow for vertical variations.

Applying these parameterisations within SPARTACUS-Urban, and assessing the resultant fluxes, show that the vertical profile of the urban form is predicted well using these three parameters. Particularly, this work finds that the exact description of urban morphology has less impact on the top-of-canopy net flux (normalised bias errors < 10%) but larger impact on within-canopy interactions (< 50%), particularly when the sun is low in the sky. Further, it is concluded that neglecting the true wall area when describing the urban canopy decreases the skill in predicting within-canopy fluxes. When including this information, normalised bias error magnitudes are reduced to < 10%. However, having more building cover detail has very little impact on normalised bias errors for both albedo and absorptions.

Potentially, both the relations developed here, alongside datasets that are currently available, could be used to incorporate vertical descriptions of the urban canopy with multi-layer radiation and energy balance schemes into NWP models.

7.2.3 Coupling SPARTACUS-Surface to an urban energy balance model

Objective 3: examine the impact of using the SPARTACUS approach to urban radiation within an urban canopy model

Given SPARTACUS-Urban is shown to perform well, it is coupled to the SUEWS (Surface Urban Energy and Water balance Scheme, Järvi et al. (2011, 2014); Ward et al. (2016)) with a new multi-layer heat storage model, to allow simulation of vertical profiles of fluxes and surface temperatures (SUEWS-SS-mEHC).

SUEWS-SS-mEHC is assessed for an area in central London with surface temperature thermal camera observations (Morrison et al. 2020, 2021), but run assuming no vegetation, for a single- and multi-layer configuration. Both the prescription of the materials, and the layer number simulated lead to variable results between the model configurations. Increasing the number of layers in the SUEWS-SS-mEHC simulations results in the vertically distributed morphology reducing the top-of-canopy upwelling shortwave radiation. This is most evident on the clearest-sky days at the end of the four-day study period.

The simulated sensible heat flux is larger than the storage heat flux for the whole day. Although, the magnitude of the difference between the two fluxes changes based on the thermal materials prescribed. As there is no vegetation, water surfaces, or rainfall in the study-period/scene, the sensible heat flux would be the dominant turbulent heat flux. Comparisons with Offerle et al. (2005a)'s observed sensible heat fluxes and modelled storage heat flux for a site in Łódź (Poland) suggest that if vegetation for that site was neglected, fluxes would be consistent with those simulated using SUEWS-SS-mEHC.

Despite being unable to simulate the exact material characteristics seen within the field of view of the thermal cameras, the multi-layer SUEWS-SS-mEHC capture the diurnal pattern of all three urban facet temperatures. SUEWS-SS-mEHC simulations always encompass the range of the mean sunlit and shaded observed temperatures. The two SUEWS-SS-mEHC configurations both respond to having a vertically distributed canopy, with increasing radiative trapping and the impacts to the roof SEB. The multi-layer roof temperatures are up to 5 °C cooler than in the single-layer.

The coupled SUEWS-SS-mEHC model allows new investigation into how facet-level fluxes, and modifying surface properties, can influence the SEB. In this thesis, the SUEWS-SS-mEHC is used to systematically examine the influence of urban morphology on surface fluxes, across nine common urban morphology categories expanded from Stewart and Oke (2012) local climate zones to include residential areas the LCZ framework misses. The expected behaviour, such as an increased albedo in open canopies, is simulated by SUEWS-SS.

The novelty of this coupling comes from the ability to simulate the vertically distributed surface temperatures within the urban canopy. Across the range of morphology tested, wall temperatures generally have a small variation (1 – 3 °C) across model levels, similar to temperature profiles derived in Chapter 4 from Morrison et al.'s (2021) observations. The roof temperatures have a higher maximum magnitude (< 50 °C) than wall temperatures (< 40 °C), as expected, given their greater daytime solar insolation. With more shadowing and trapping of radiation, the denser urban areas have lower maximum temperatures simulated, but a larger temperature range – of up to 15 °C in the daytime, compared with less dense areas. These are still not as large as the temperature range in the profiles derived in Chapter 4.

7.3 Recommendations for future work

Based on the work undertaken, suggestions for future research include:

Radiative transfer modelling and evaluations of SPARTACUS-Urban

- Observations from a wider range of real-world sites, that span different morphology characteristics (e.g., mean building height, surface building fraction) for both short and longwave radiation with a wider range of wavelengths, could be used to assess SPARTACUS-Urban performance. Examples of campaigns with long-running and high spatial distribution of measurements include Nunez et al. (2000) for longwave radiation, or long-running flux measurements across various sites in London, including Kotthaus and Grimmond (2014).
- The building shadowing in the SPARTACUS-Urban model be could be improved. Real-world roofs occur at multiple height levels, with tall buildings self-shading lower levels. SPARTACUS-Urban assumes that building shadows randomly overlap any roofs they are cast on, and therefore that low roofs are attached to taller buildings. In reality, this may happen more frequently than in randomly distributed canopies, but more analysis would be needed to test if this is true, and if so, if a modification is needed.
- The SPARTACUS-Urban within-canopy vegetation skill is not evaluated despite trees playing a key role in the urban energy balance, such as being able to mitigate extreme heat events (Andersson-Sköld et al. 2015) and also play an important role in carbon fluxes. As SUEWS already has a carbon scheme, this new representation of vegetation could help address questions linked to both thermal comfort and urban carbon fluxes.
- Urban material properties have not been explored, with all facets having equal emissivity and albedo values, so evaluations could also be made more realistic. Both urban morphology and urban spectral material properties are large uncertainties, so a wider assessment would benefit NWP. Such work could perturb the realistic urban morphology (e.g., mean building height, building fraction) and materials (e.g., albedo, emissivity), utilising existing databases (e.g. Kotthaus et al. (2014)) to include more realism. This in turn will impact radiative and other fluxes, so these or temperatures could be assessed.

- Both evaluations in this thesis assume a vacuum, however SPARTACUS-Urban has the capability to include an absorbing atmosphere, so this should be tested. This is primarily important for longwave radiation and has been found to impact in-situ observations of surface temperatures by up to 2.97 K (Morrison et al. 2020), as a third of longwave energy is associated with parts of the spectrum where the mean free path is less than 50 m (Hogan 2019b), which is a typical building-building distance in many low-density areas.

Urban form parameterisations

- The urban form parameterisations developed use data for only six cities**.** Despite being from across the globe, more cities (e.g., African and Asian megacities) should be addressed if vertical data can be obtained.
- Evaluation of current approaches used in NWP, such as those based on building cover (e.g., Bohnenstengel et al. (2011)), could inform assessments of the urban variability currently seen by NWP or climate models. Further, they could be investigated to see whether they provide good inputs for the parameterisations developed here.
- A large uncertainty in radiation modelling, is the exact value of urban parameters for a given grid-box, due to the uncertainties in observing urban characteristics (e.g., in-situ sensor or satellite field of view) and processing the resulting data (e.g., methodologies). The wide range of existing urban form products, as well as high-resolution data at country or continent scale, should be compared to gain an understanding of this uncertainty.

Energy balance modelling and use in numerical weather prediction

- The SUEWS-SS-mEHC evaluation and testing is very limited, more evaluations using observations for a wider range of area should be undertaken.
- As many NWP urban schemes are single-layer, or lack urban schemes, the good and computationally cheap performance of SUEWS-SS-mEHC could be further coupled into larger NWP or climate models. Once completed, performance would need to be further evaluated with observations. This could involve surface temperatures campaigns (similar to Morrison et al. (2021)). This could also involve incorporating SUEWS-SS within wider model evaluations to examine its performance compared to a wider range of existing models with similar complexity level.

- If coupled to an NWP land surface scheme, online experiments could be completed with SUEWS-SS-mEHC to assess the effects of urban areas on downstream weather, and the impact of extreme weather events on urban areas. The latter should include an assessment of the impact on heat stress metrics, such as mean radiant temperature (Aminipouri et al. 2019).
- Climate mitigation studies could be undertaken with a verified model, similar to those in Ward and Grimmond (2017). As SUEWS-SS-mEHC is a multi-layer scheme, the effects of realistically increasing the height of buildings (using the relations developed in Chapter 5) could be investigated. The effect of climate mitigation techniques on pedestrians, such as increasing the albedo of urban surfaces (Akbari et al. 2008; Georgakis et al. 2014; Broadbent et al. 2020), and increasing both green (Zhang et al. 2019; Li et al. 2014) and blue space (Broadbent et al. 2018), could be assessed. Again, the SPARTACUS approach will enable these materials to be distributed across both walls and roofs vertically, bringing a new angle to the wide range of heat-mitigation studies.

References

Adderley, C., A. Christen, and J. A. Voogt, 2015: The effect of radiometer placement and view on inferred directional and hemispheric radiometric temperatures of an urban canopy. *Atmos. Meas. Tech.*, **8**, https://doi.org/10.5194/amt-8-2699-2015.

Aida, M., 1982: Urban albedo as a function of the urban structure - A model experiment - Part I. *Boundary-Layer Meteorol.*, **23**, 405–413, https://doi.org/10.1007/BF00116269.

——, and K. Gotoh, 1982: Urban albedo as a function of the urban structure - A two-dimensional numerical simulation - Part II. *Boundary-Layer Meteorol.*, **23**, 415–424, https://doi.org/10.1007/BF00116270.

Akbari, H., S. Menon, and A. Rosenfeld, 2008: Global cooling: increasing world-wide urban albedos to offset CO2. *Clim. Chang. 2008 943*, **94**, 275–286, https://doi.org/10.1007/S10584-008-9515-9.

Alexander, P. J., G. Mills, and R. Fealy, 2015: Using LCZ data to run an urban energy balance model. *Urban Clim.*, **13**, 14–37, https://doi.org/10.1016/J.UCLIM.2015.05.001.

Ali-Toudert, F., and H. Mayer, 2006: Numerical study on the effects of aspect ratio and orientation of an urban street canyon on outdoor thermal comfort in hot and dry climate. *Build. Environ.*, **41**, 94–108, https://doi.org/10.1016/J.BUILDENV.2005.01.013.

Aminipouri, M., D. Rayner, F. Lindberg, S. Thorsson, A. J. Knudby, K. Zickfeld, A. Middel, and E. S. Krayenhoff, 2019: Urban tree planting to maintain outdoor thermal comfort under climate change: The case of Vancouver's local climate zones. *Build. Environ.*, **158**, 226–236, https://doi.org/10.1016/j.buildenv.2019.05.022.

Andersson-Sköld, Y., and Coauthors, 2015: An integrated method for assessing climate-related risks and adaptation alternatives in urban areas. *Clim. Risk Manag.*, **7**, 31–50, https://doi.org/10.1016/J.CRM.2015.01.003.

Antoniou, N., H. Montazeri, M. Neophytou, and B. Blocken, 2019: CFD simulation of urban microclimate: Validation using high-resolution field measurements. *Sci. Total Environ.*, **695**, 133743, https://doi.org/10.1016/J.SCITOTENV.2019.133743.

Ao, X., C. S. B. Grimmond, D. Liu, Z. Han, P. Hu, Y. Wang, X. Zhen, and J. Tan, 2016: Radiation fluxes in a business district of Shanghai, China. *J. Appl. Meteorol. Climatol.*, **55**, 2451–2468, https://doi.org/10.1175/JAMC-D-16-0082.1.

——, and Coauthors, 2018: Evaluation of the Surface Urban Energy and Water Balance Scheme (SUEWS) at a dense urban site in Shanghai: Sensitivity to anthropogenic heat and irrigation. *J. Hydrometeorol.*, **19**, 1983–2005, https://doi.org/10.1175/JHM-D-18-0057.1.

——, L. Wang, X. Zhi, W. Gu, H. Yang, and D. Li, 2019: Observed synergies between urban heat islands and heat waves and their controlling factors in Shanghai, China. *J. Appl. Meteorol. Climatol.*, **58**, 1955–1972, https://doi.org/10.1175/JAMC-D-19-0073.1.

Aoyagi, T., and S. Takahashi, 2012: Development of an Urban Multilayer Radiation Scheme and Its Application to the Urban Surface Warming Potential. *Boundary-Layer Meteorol.*, https://doi.org/10.1007/s10546-011-9679-0.

Arnfield, A. J., 1982a: An approach to the estimation of the surface radiative properties and radiation budgets of cities. *Phys. Geogr.*, **3**, 97–122, https://doi.org/10.1080/02723646.1982.10642221.

——, 1982b: An approach to the estimation of the surface radiative properties and radiation budgets of cities. *Phys. Geogr.*, **3**, 97–122, https://doi.org/10.1080/02723646.1982.10642221.

——, 1988: Validation of an estimation model for urban surface albedo. *Phys. Geogr.*, https://doi.org/10.1080/02723646.1988.10642360.

Arnfield, A. J., 1990: Street design and urban canyon solar access. *Energy Build.*, https://doi.org/10.1016/0378-7788(90)90031-D.

Arnfield, A. J., and C. S. B. Grimmond, 1998: An urban canyon energy budget model and its application to urban storage heat flux modeling. *Energy Build.*, **27**, 61–68, https://doi.org/10.1016/S0378-7788(97)00026-1.

Asaeda, T., V. T. Ca, and A. Wake, 1996: Heat storage of pavement and its effect on the lower atmosphere. *Atmos. Environ.*, **30**, 413–427, https://doi.org/10.1016/1352-2310(94)00140-5.

Ashrae, 2001: ASHRAE Handbook 2001 Fundamentals. *Ashrae Stand.*, **53**.

Assimakopoulos, V. D., H. M. ApSimon, and N. Moussiopoulos, 2003: A numerical study of atmospheric pollutant dispersion in different two-dimensional street canyon configurations. *Atmos. Environ.*, **37**, 4037–4049, https://doi.org/10.1016/S1352-2310(03)00533-8.

Baklanov, A., and Coauthors, 2018: From urban meteorology, climate and environment research to integrated city services. *Urban Clim.*, **23**, 330–341, https://doi.org/10.1016/j.uclim.2017.05.004.

Baldauf, M., A. Seifert, J. Förstner, D. Majewski, M. Raschendorfer, and T. Reinhardt, 2011: Operational Convective-Scale Numerical Weather Prediction with the COSMO Model: Description and Sensitivities. *Mon. Weather Rev.*, **139**, 3887–3905, https://doi.org/10.1175/MWR-D-10-05013.1.

Balogun, A. A., J. O. Adegoke, S. Vezhapparambu, M. Mauder, J. P. McFadden, and K. Gallo, 2009: Surface energy balance measurements above an exurban residential neighbourhood of Kansas City, Missouri. *Boundary-Layer Meteorol.*, https://doi.org/10.1007/s10546-009-9421-3.

Barlow, J., and Coauthors, 2017: Developing a research strategy to better understand, observe, and simulate urban atmospheric processes at Kilometer to Subkilometer Scales. *Bulletin of the American Meteorological Society*, Vol. 98 of.

Barlow, J. F., 2014: Progress in observing and modelling the urban boundary layer. *Urban Clim.*, **10**, 216–240, https://doi.org/10.1016/j.uclim.2014.03.011.

Bathiany, S., V. Dakos, M. Scheffer, and T. M. Lenton, 2018: Climate models predict increasing temperature variability in poor countries. *Sci. Adv.*, **4**, https://doi.org/10.1126/SCIADV.AAR5809.

Bechtel, B., and C. Daneke, 2012: Classification of local climate zones based on multiple earth observation data. *IEEE J. Sel. Top. Appl. Earth Obs. Remote Sens.*, **5**, https://doi.org/10.1109/JSTARS.2012.2189873.

——, and Coauthors, 2015: Mapping local climate zones for a worldwide database of the form and function of cities. *ISPRS Int. J. Geo-Information*, **4**, 199–219, https://doi.org/10.3390/ijgi4010199.

Bergeron, O., and I. B. Strachan, 2011: CO2sources and sinks in urban and suburban areas of a northern mid-latitude city. *Atmos. Environ.*, https://doi.org/10.1016/j.atmosenv.2010.12.043.

——, and ——, 2012: Wintertime radiation and energy budget along an urbanization gradient in Montreal, Canada. *Int. J. Climatol.*, https://doi.org/10.1002/joc.2246.

Bernard, J., E. Bocher, E. Le, S. Wiederhold, F. Leconte, and V. Masson, 2022: Estimation of missing building height in OpenStreetMap data: a French case study using GeoClimate 0.0.1. *Geosci. Model Dev*, **15**, 7505–7532, https://doi.org/10.5194/gmd-15-7505-2022.

Blankenstein, S., and W. Kuttler, 2004: Impact of street geometry on downward longwave radiation and air temperature in an urban environment. *Meteorol. Zeitschrift*, **13**, 373–379, https://doi.org/10.1127/0941-2948/2004/0013-0373.

Błazejczyk, K., G. Jendritzky, P. Bröde, D. Fiala, G. Havenith, Y. Epstein, A. Psikuta, and B. Kampmann, 2013: An introduction to the Universal thermal climate index (UTCI). *Geogr. Pol.*, **86**, https://doi.org/10.7163/GPol.2013.1.

Blunn, L. P., O. Coceal, N. Nazarian, J. F. Barlow, R. S. Plant, S. I. Bohnenstengel, and H. W. Lean, 2022: Turbulence Characteristics Across a Range of Idealized Urban Canopy Geometries. *Boundary-Layer Meteorol.*, **182**, https://doi.org/10.1007/s10546-021-00658-6.

Bohnenstengel, S. I., S. Evans, P. A. Clark, and S. E. Belcher, 2011: Simulations of the London urban heat island. *Q. J. R. Meteorol. Soc.*, **137**, 1625–1640, https://doi.org/10.1002/QJ.855.

Boussetta, S., and Coauthors, 2021: Ecland: The ecmwf land surface modelling system. *Atmosphere (Basel).*, **12**, 723, https://doi.org/10.3390/ATMOS12060723/S1.

Branford, S., O. Coceal, T. G. Thomas, and S. E. Belcher, 2011: Dispersion of a Point-Source Release of a Passive Scalar Through an Urban-Like Array for Different Wind Directions. *Boundary-Layer Meteorol.*, **139**, https://doi.org/10.1007/s10546-011-9589-1.

Britter, R. E., and S. R. Hanna, 2003: Flow and Dispersion in Urban Areas. *Annu. Rev. Fluid Mech.*,.

Broadbent, A. M., A. M. Coutts, N. J. Tapper, M. Demuzere, and J. Beringer, 2018: The microscale cooling effects of water sensitive urban design and irrigation in a suburban environment. *Theor. Appl. Climatol.*, **134**, 1–23, https://doi.org/10.1007/S00704-017-2241-3/FIGURES/12.

——, E. S. Krayenhoff, and M. Georgescu, 2020: Efficacy of cool roofs at reducing pedestrian-level air temperature during projected 21st century heatwaves in Atlanta, Detroit, and Phoenix (USA). *Environ. Res. Lett.*, **15**, 084007, https://doi.org/10.1088/1748-9326/AB6A23.

Brooke Anderson, G., and M. L. Bell, 2011: Heat waves in the United States: Mortality risk during heat waves and effect modification by heat wave characteristics in 43 U.S. communities. *Environ. Health Perspect.*, **119**, 210–218, https://doi.org/10.1289/ehp.1002313.

Brousse, O., A. Martilli, M. Foley, G. Mills, and B. Bechtel, 2016: WUDAPT, an efficient land use producing data tool for mesoscale models? Integration of urban LCZ in WRF over Madrid. *Urban Clim.*, **17**, 116–134, https://doi.org/10.1016/J.UCLIM.2016.04.001.

Bruse, M., and H. Fleer, 1998: Simulating surface-plant-air interactions inside urban environments with a three dimensional numerical model. *Environ. Model. Softw.*, **13**, 373–384, https://doi.org/10.1016/S1364-8152(98)00042-5.

Burdet, E., M. Colombert, D. Morand, and Y. Diab, 2014: Integrated canopy, building energy and radiosity model for 3D urban design.

Cai, X. M., J. F. Barlow, and S. E. Belcher, 2008: Dispersion and transfer of passive scalars in and above street canyons—Large-eddy simulations. *Atmos. Environ.*, **42**, 5885–5895, https://doi.org/10.1016/J.ATMOSENV.2008.03.040.

Capel-Timms, I., S. T. Smith, T. Sun, and S. Grimmond, 2020: Dynamic Anthropogenic activitieS impacting Heat emissions (DASH v1.0): Development and evaluation. *Geosci. Model Dev.*, **13**, 4891–4924.

Castro, I. P., Z. T. Xie, V. Fuka, A. G. Robins, M. Carpentieri, P. Hayden, D. Hertwig, and O. Coceal, 2017: Measurements and Computations of Flow in an Urban Street System. *Boundary-Layer Meteorol.*, **162**, 207–230, https://doi.org/10.1007/S10546-016-0200-7/FIGURES/16.

Champeaux, J. L., V. Masson, and F. Chauvin, 2005: ECOCLIMAP: A global database of land surface parameters at 1 km resolution. *Meteorol. Appl.*, **12**, 29–32, https://doi.org/10.1017/S1350482705001519/FORMAT/PDF.

Chen, D., X. Wang, M. Thatcher, G. Barnett, A. Kachenko, and R. Prince, 2014: Urban vegetation for reducing heat related mortality. *Environ. Pollut.*, **192**, 275–284, https://doi.org/10.1016/J.ENVPOL.2014.05.002.

Chen, F., and Coauthors, 2011: The integrated WRF/urban modelling system: Development, evaluation, and applications to urban environmental problems. *Int. J. Climatol.*, **31**, 273–288, https://doi.org/10.1002/joc.2158.

Chen, K., A. J. Newman, M. Huang, C. Coon, L. A. Darrow, M. J. Strickland, and H. A. Holmes, 2022: Estimating Heat-Related Exposures and Urban Heat Island Impacts: A Case Study for the 2012 Chicago Heatwave. *GeoHealth*, **6**, https://doi.org/10.1029/2021GH000535.

Ching, J., and Coauthors, 2019: Pathway using WUDAPT's Digital Synthetic City tool towards generating urban canopy parameters for multi-scale urban atmospheric modeling. *Urban Clim.*, **28**, 100459, https://doi.org/10.1016/J.UCLIM.2019.100459.

Christen, A., and R. Vogt, 2004: Energy and radiation balance of a central European City. *Int. J. Climatol.*, **24**, 1395–1421, https://doi.org/10.1002/joc.1074.

Chrysoulakis, N., and Coauthors, 2018: Urban energy exchanges monitoring from space. *Sci. Rep.*, https://doi.org/10.1038/s41598-018-29873-x.

CIBSE, 2015: Environmental Design - CIBSE Guide A (8th Edition). *Environ. Des. CIBSE Guid. A*, **552**.

Cleugh, H. A., and T. R. Oke, 1986: Suburban-rural energy balance comparisons in summer for Vancouver, B.C. *Boundary-Layer Meteorol.*, **36**, https://doi.org/10.1007/BF00118337.

Coceal, O., A. Dobre, and T. G. Thomas, 2007: Unsteady dynamics and organized structures from DNS over an idealized building canopy. *Int. J. Climatol. Int. J. Clim.*, **27**, 1943–1953, https://doi.org/10.1002/joc.1549.

Collier, C. G., 2006: The impact of urban areas on weather. *Q. J. R. Meteorol. Soc.*, https://doi.org/10.1256/qj.05.199.

Costanzo, V., G. Evola, and L. Marletta, 2016: Energy savings in buildings or UHI mitigation? Comparison between green roofs and cool roofs. *Energy Build.*, **114**, 247–255, https://doi.org/10.1016/J.ENBUILD.2015.04.053.

Coutts, A. M., J. Beringer, and N. J. Tapper, 2007a: Impact of increasing urban density on local climate: Spatial and temporal variations in the surface energy balance in Melbourne, Australia. *J. Appl. Meteorol. Climatol.*, **46**, 477–493, https://doi.org/10.1175/JAM2462.1.

——, ——, and ——, 2007b: Characteristics influencing the variability of urban CO2 fluxes in Melbourne, Australia. *Atmos. Environ.*, **41**, https://doi.org/10.1016/j.atmosenv.2006.08.030.

——, E. C. White, N. J. Tapper, J. Beringer, and S. J. Livesley, 2016a: Erratum to: Temperature and human thermal comfort effects of street trees across three contrasting street canyon environments (Theor Appl Climatol, 10.1007/s00704-015-1409-y). *Theor. Appl. Climatol.*, **126**, 815, https://doi.org/10.1007/s00704-016-1832-8.

——, ——, ——, ——, and ——, 2016b: Temperature and human thermal comfort effects of street trees across three contrasting street canyon environments. *Theor. Appl. Climatol.*, **124**, 55–68, https://doi.org/10.1007/S00704-015-1409-Y/FIGURES/10.

Crum, S. M., and G. Darrel Jenerette, 2017: Microclimate variation among urban land covers: The importance of vertical and horizontal structure in air and land surface temperature relationships. *J. Appl. Meteorol. Climatol.*, **56**, 2531–2543, https://doi.org/10.1175/JAMC-D-17-0054.1.

Davidson, M. J., W. H. Snyder, R. E. Lawson, and J. C. R. Hunt, 1996: Wind tunnel simulations of plume dispersion through groups of obstacles. *Atmos. Environ.*, **30**, 3715–3731, https://doi.org/10.1016/1352-2310(96)00103-3.

Deardorff, J. W., 1970: A numerical study of three-dimensional turbulent channel flow at large Reynolds numbers. *J. Fluid Mech.*, **41**, 453–480, https://doi.org/10.1017/S0022112070000691.

Demographia World Urban Areas, 2020: Demographia World Urban Areas, 16th Annual Edition 2020.06. *Demographia*,.

Demuzere, M., and Coauthors, 2014: Mitigating and adapting to climate change: Multi-functional and multi-scale assessment of green urban infrastructure. *J. Environ. Manage.*, **146**, 107–115, https://doi.org/10.1016/j.jenvman.2014.07.025.

——, and Coauthors, 2017: Impact of urban canopy models and external parameters on the modelled urban energy balance in a tropical city. *Q. J. R. Meteorol. Soc.*, **143**, 1581–1596.

Demuzere, M., S. Hankey, G. Mills, W. Zhang, T. Lu, and B. Bechtel, 2020: Combining expert and crowd-sourced training data to map urban form and functions for the continental US. *Sci. Data 2020 71*, **7**, 1–13, https://doi.org/10.1038/s41597-020-00605-z.

——, J. Kittner, A. Martilli, G. Mills, C. Moede, I. D. Stewart, J. van Vliet, and B. Bechtel, 2022a: A global map of local climate zones to support earth system modelling and urban-scale environmental science. *Earth Syst. Sci. Data*, **14**, 3835–3873, https://doi.org/10.5194/ESSD-14-3835-2022.

——, ——, ——, ——, ——, I. D. Stewart, J. Van Vliet, and B. Bechtel, 2022b: A global map of local climate zones to support earth system modelling and urban-scale environmental science. *Earth Syst. Sci. Data*, **14**, 3835–3873, https://doi.org/10.5194/essd-14-3835-2022.

Dirksen, M., R. J. Ronda, N. E. Theeuwes, and G. A. Pagani, 2019: Sky view factor calculations and its application in urban heat island studies. *Urban Clim.*, **30**, https://doi.org/10.1016/J.UCLIM.2019.100498.

Dissegna, M. A., T. Yin, S. Wei, D. Richards, and A. Grêt-Regamey, 2019: 3-D Reconstruction of an Urban Landscape to Assess the Influence of Vegetation in the Radiative Budget. *Forests*, https://doi.org/10.3390/f10080700.

——, ——, H. Wu, N. Lauret, S. Wei, J. P. Gastellu-Etchegorry, and A. Grêt-Regamey, 2021:

Modeling mean radiant temperature distribution in urban landscapes using dart. *Remote Sens.*, **13**, https://doi.org/10.3390/rs13081443.

Dou, J., and S. Miao, 2017: Impact of mass human migration during Chinese New Year on Beijing urban heat island. *Int. J. Climatol.*, **37**, 4199–4210, https://doi.org/10.1002/JOC.5061.

Dou, J., S. Grimmond, Z. Cheng, S. Miao, D. Feng, and M. Liao, 2019: Summertime surface energy balance fluxes at two Beijing sites. *Int. J. Climatol.*, **39**, 2793–2810.

EEA, 2021: CORINE Land Cover - User Manual. *Copernicus L. Monit. Serv.*,.

Ellena, M., M. Breil, and S. Soriani, 2020: The heat-health nexus in the urban context: A systematic literature review exploring the socio-economic vulnerabilities and built environment characteristics. *Urban Clim.*, **34**, 100676, https://doi.org/10.1016/J.UCLIM.2020.100676.

Emmanuel, R., and E. Johansson, 2006: Influence of urban morphology and sea breeze on hot humid microclimate: The case of Colombo, Sri Lanka. *Clim. Res.*, **30**, 189–200, https://doi.org/10.3354/CR030189.

EMU, 2018: Building Heights - Top 25 Urban Areas. https://buildingheights.emu-analytics.net/ (Accessed January 15, 2019).

EMU Analytics, 2018: Building heights – Top 25 urban areas.

Esch, T., and Coauthors, 2017: Breaking new ground in mapping human settlements from space – The Global Urban Footprint. *ISPRS J. Photogramm. Remote Sens.*, **134**, https://doi.org/10.1016/j.isprsjprs.2017.10.012.

Evans, S., A. Hudson-Smith, and M. Batty, 2006: 3-D GIS; Virtual London and beyond: An exploration of the 3-D GIS experience involved in the creation of Virtual London. *CyberGeo*, **2006**, 1–20, https://doi.org/10.4000/cybergeo.2871.

Fan, J., Q. Huang, D. M. Sumner, and D. Wang, 2018: A simple method for partitioning total solar radiation into diffuse/direct components in the United States. *https://doi.org/10.1080/15435075.2018.1484357*, **15**, 497–506, https://doi.org/10.1080/15435075.2018.1484357.

Feigenwinter, C., R. Vogt, and E. Parlow, 1999: Vertical structure of selected turbulence characteristics above an urban canopy. *Theor. Appl. Climatol.*, https://doi.org/10.1007/s007040050074.

Figueiredo, L., and L. Amorim, 2007: Decoding The Urban Grid: Or Why Cities Are Neither Trees Nor Perfect Grids. *6th International Space Syntax Symposium*.

Fischereit, J., 2021: The simple urban radiation model for estimating mean radiant temperature in idealised street canyons. *Urban Clim.*, **35**, 100694, https://doi.org/10.1016/J.UCLIM.2020.100694.

Fortuniak, K., 2008: Numerical estimation of the effective albedo of an urban canyon. *Theor. Appl. Climatol.*, https://doi.org/10.1007/s00704-007-0312-6.

Fortuniak, K., W. Pawlak, and M. Siedlecki, 2013: Integral Turbulence Statistics Over a Central European City Centre. *Boundary-Layer Meteorol.*, https://doi.org/10.1007/s10546-012-9762-1.

Frantz, D., F. Schug, A. Okujeni, C. Navacchi, W. Wagner, S. van der Linden, and P. Hostert, 2021: National-scale mapping of building height using Sentinel-1 and Sentinel-2 time series. *Remote Sens. Environ.*, **252**, 112128, https://doi.org/10.1016/J.RSE.2020.112128.

Frey, C. M., G. Rigo, and E. Parlow, 2007: Urban radiation balance of two coastal cities in a hot and dry environment. *Int. J. Remote Sens.*, **28**, 2695–2712, https://doi.org/10.1080/01431160600993389.

Friedl, M. A., D. Sulla-Menashe, B. Tan, A. Schneider, N. Ramankutty, A. Sibley, and X. Huang, 2010: MODIS Collection 5 global land cover: Algorithm refinements and characterization of new datasets. *Remote Sens. Environ.*, **114**, https://doi.org/10.1016/j.rse.2009.08.016.

Fröhlich, D., M. Gangwisch, and A. Matzarakis, 2019: Effect of radiation and wind on thermal comfort in urban environments - Application of the RayMan and SkyHelios model. *Urban Clim.*, **27**, 1–7, https://doi.org/10.1016/j.uclim.2018.10.006.

Fuka, V., Z.-T. Xie, I. P. Castro, P. Hayden, M. Carpentieri, and A. G. Robins, 2018: Scalar Fluxes Near a Tall Building in an Aligned Array of Rectangular Buildings. **167**, 53–76, https://doi.org/10.1007/s10546-017-0308-4.

Gage, E. A., and D. J. Cooper, 2017: Relationships between landscape pattern metrics, vertical structure and surface urban Heat Island formation in a Colorado suburb. *Urban Ecosyst.*, https://doi.org/10.1007/s11252-017-0675-0.

Gaitani, N., I. Burud, T. Thiis, and M. Santamouris, 2017: High-resolution spectral mapping of urban thermal properties with Unmanned Aerial Vehicles. *Build. Environ.*, **121**, 215–224, https://doi.org/10.1016/j.buildenv.2017.05.027.

Gamba, P., and B. Houshmand, 2002: Joint analysis of SAR, LIDAR and aerial imagery for simultaneous extraction of land cover, DTM and 3D shape of buildings. *Int. J. Remote Sens.*, https://doi.org/10.1080/01431160110114952.

Gao, Z., X. Fan, and L. Bian, 2003: An analytical solution to one-dimensional thermal conduction-convection in soil. *Soil Sci.*, **168**, 99–107.

Gastellu-Etchegorry, J.-P., and Coauthors, 2017: DART: Recent Advances in Remote Sensing Data Modeling With Atmosphere, Polarization, and Chlorophyll Fluorescence. *IEEE J. Sel. Top. Appl. EARTH Obs. Remote Sens.*, **10**, https://doi.org/10.1109/JSTARS.2017.2685528.

Gastellu-Etchegorry, J. P., 2008: 3D modeling of satellite spectral images, radiation budget and energy budget of urban landscapes. *Meteorol. Atmos. Phys.*, https://doi.org/10.1007/s00703-008-0344-1.

Gastellu-Etchegorry, J. P., E. Grau, and N. Lauret, 2012: DART: A 3D Model for Remote Sensing Images and Radiative Budget of Earth Surfaces. *Modeling and Simulation in Engineering*, InTech.

Gastellu-Etchegorry, J. P., and Coauthors, 2015: Discrete anisotropic radiative transfer (DART 5) for modeling airborne and satellite spectroradiometer and LIDAR acquisitions of natural and urban landscapes. *Remote Sens.*, **7**, 1667–1701, https://doi.org/10.3390/rs70201667.

Georgakis, C., S. Zoras, and M. Santamouris, 2014: Studying the effect of “cool” coatings in street urban canyons and its potential as a heat island mitigation technique. *Sustain. Cities Soc.*, **13**, 20–31, https://doi.org/10.1016/J.SCS.2014.04.002.

Ghandehari, M., T. Emig, and M. Aghamohamadnia, 2018: Surface temperatures in New York City: Geospatial data enables the accurate prediction of radiative heat transfer. *Sci. Rep.*, https://doi.org/10.1038/s41598-018-19846-5.

Goldbach, A., and W. Kuttler, 2013: Quantification of turbulent heat fluxes for adaptation strategies within urban planning. *Int. J. Climatol.*, https://doi.org/10.1002/joc.3437.

Goodwin, N. R., N. C. Coops, T. R. Tooke, A. Christen, and J. A. Voogt, 2009: Characterizing urban surface cover and structure with airborne lidar technology. *Can. J. Remote Sens.*, https://doi.org/10.5589/m09-015.

Google Inc., 2019: Google Earth Pro. *Geospatial Solut.*, **16**.

Gough, H., M. F. King, P. Nathan, C. S. B. Grimmond, A. Robins, C. J. Noakes, Z. Luo, and J. F. Barlow, 2019: Influence of neighbouring structures on building façade pressures: Comparison between full-scale, wind-tunnel, CFD and practitioner guidelines. *J. Wind Eng. Ind. Aerodyn.*, **189**, 22–33, https://doi.org/10.1016/J.JWEIA.2019.03.011.

Gough, H. L., and Coauthors, 2018: Field measurement of natural ventilation rate in an idealised full-scale building located in a staggered urban array: Comparison between tracer gas and pressure-based methods. *Build. Environ.*, **137**, 246–256, https://doi.org/10.1016/J.BUILDENV.2018.03.055.

Gowardhan, A. A., E. R. Pardyjak, I. Senocak, M. J. Brown, A. A. Gowardhan, · E R Pardyjak, · M J Brown, and I. Senocak, 2011: A CFD-based wind solver for an urban fast response transport and dispersion model. **11**, 439–464, https://doi.org/10.1007/s10652-011-9211-6.

Grimmond, C. S. B., and T. R. Oke, 1986: Urban Water Balance: 2. Results From a Suburb of Vancouver, British Columbia. *Water Resour. Res.*, **22**, https://doi.org/10.1029/WR022i010p01404.

——, and ——, 1991: An evapotranspiration-interception model for urban areas. *Water Resour. Res.*, **27**, https://doi.org/10.1029/91WR00557.

Grimmond, C. S. B., and T. R. Oke, 1995: Comparison of Heat Fluxes from Summertime Observations in the Suburbs of Four North American Cities. *J. Appl. Meteorol.*, https://doi.org/10.1175/1520-0450(1995)034<0873:COHFFS>2.0.CO;2.

Grimmond, C. S. B., and T. R. Oke, 1999a: Heat storage in urban areas: Local-scale observations and evaluation of a simple model. *J. Appl. Meteorol.*, **38**, https://doi.org/10.1175/1520-0450(1999)038<0922:HSIUAL>2.0.CO;2.

Grimmond, C. S. B., and T. R. Oke, 1999b: Aerodynamic Properties of Urban Areas Derived from Analysis of Surface Form. *J. Appl. Meteorol.*, https://doi.org/10.1175/1520-0450(1999)038<1262:APOUAD>2.0.CO;2.

Grimmond, C. S. B., and T. R. Oke, 1999c: Aerodynamic properties of urban areas derived from analysis of surface form. *J. Appl. Meteorol.*, https://doi.org/10.1175/1520-0450(1999)038<1262:APOUAD>2.0.CO;2.

Grimmond, C. S. B., and T. R. Oke, 2002: Turbulent Heat Fluxes in Urban Areas: Observations and a Local-Scale Urban Meteorological Parameterization Scheme (LUMPS). *J. Appl. Meteorol.*, https://doi.org/10.1175/1520-0450(2002)041<0792:THFIUA>2.0.CO;2.

Grimmond, C. S. B., H. A. Cleugh, and T. R. Oke, 1991: An objective urban heat storage model and its comparison with other schemes. *Atmos. Environ. Part B, Urban Atmos.*, **25**, 311–326, https://doi.org/10.1016/0957-1272(91)90003-W.

——, C. Souch, and M. D. Hubble, 1996: Influence of tree cover on summertime surface energy balance fluxes, San Gabriel Valley, Los Angeles. *Clim. Res.*, **6**, 45–57.

Grimmond, C. S. B., and Coauthors, 2010a: The International Urban Energy Balance Models Comparison Project: First Results from Phase 1. *J. Appl. Meteorol. Climatol.*, **49**, 1268–1292, https://doi.org/10.1175/2010JAMC2354.1.

Grimmond, C. S. B. B., J. A. Salmond, T. R. Oke, B. Offerle, and A. Lemonsu, 2004: Flux and turbulence measurements at a densely built-up site in Marseille: Heat, mass (water and carbon dioxide), and momentum. *J. Geophys. Res. D Atmos.*, **109**, 1–19, https://doi.org/10.1029/2004JD004936.

Grimmond, C. S. B. B., and Coauthors, 2010b: The International Urban Energy Balance Models Comparison Project: First Results from Phase 1. *J. Appl. Meteorol. Climatol.*, **49**, 1268–1292, https://doi.org/10.1175/2010JAMC2354.1.

Grimmond, C. S. B. B., and Coauthors, 2011: Initial results from Phase 2 of the international urban energy balance model comparison. *Int. J. Climatol.*, **31**, 244–272, https://doi.org/10.1002/joc.2227.

Grimmond, S., 2007: Urbanization and global environmental change: Local effects of urban warming. *Geographical Journal*, Vol. 173 of, 83–88.

——, and Coauthors, 2020: Integrated urban hydrometeorological, climate and environmental services: Concept, methodology and key messages. *Urban Clim.*, **33**, 100623, https://doi.org/10.1016/J.UCLIM.2020.100623.

Guo, D., P. Zhao, R. Wang, R. Yao, and J. Hu, 2020: Numerical simulations of the flow field and pollutant dispersion in an idealized urban area under different atmospheric stability conditions. *Process Saf. Environ. Prot.*, **136**, 310–323, https://doi.org/10.1016/J.PSEP.2020.01.031.

Guo, G., X. Zhou, Z. Wu, R. Xiao, and Y. Chen, 2016: Characterizing the impact of urban morphology heterogeneity on land surface temperature in Guangzhou, China. **84**, 427–439.

Hagelin, S., J. Son, R. Swinbank, A. McCabe, N. Roberts, and W. Tennant, 2017: The Met Office convective-scale ensemble, MOGREPS-UK. *Q. J. R. Meteorol. Soc.*, https://doi.org/10.1002/qj.3135.

Hamdi, R., and V. Masson, 2008: Inclusion of a drag approach in the Town Energy Balance (TEB) scheme: Offline 1D evaluation in a street canyon. *J. Appl. Meteorol. Climatol.*, **47**, https://doi.org/10.1175/2008JAMC1865.1.

Hamilton, I. G., M. Davies, P. Steadman, A. Stone, I. Ridley, and S. Evans, 2009: The significance of the anthropogenic heat emissions of London's buildings: A comparison against captured shortwave solar radiation. *Build. Environ.*, **44**, 807–817, https://doi.org/10.1016/J.BUILDENV.2008.05.024.

Han, B., D. Sun, X. Yu, W. Song, and L. Ding, 2020: Classification of urban street networks based on tree-like network features. *Sustain.*, https://doi.org/10.3390/su12020628.

Harman, I. N., and S. E. Belcher, 2006: The surface energy balance and boundary layer over urban street canyons. *Q. J. R. Meteorol. Soc.*, **132**, 2749–2768.

——, M. J. Best, and S. E. Belcher, 2004: Radiative exchange in an urban street canyon. *Boundary-Layer Meteorol.*, **110**, 301–316, https://doi.org/10.1023/A:1026029822517.

Heaviside, C., H. Macintyre, and S. Vardoulakis, 2017: The Urban Heat Island: Implications for Health in a Changing Environment. *Curr. Environ. Heal. reports*, **4**, https://doi.org/10.1007/s40572-017-0150-3.

Hénon, A., P. G. Mestayer, J. P. Lagouarde, and J. A. Voogt, 2012: An urban neighborhood temperature and energy study from the CAPITOUL experiment with the Solene model: Part 2: Influence of building surface heterogeneities. *Theor. Appl. Climatol.*, **110**, 197–208, https://doi.org/10.1007/s00704-012-0616-z.

Heris, M. P., N. L. Foks, K. J. Bagstad, A. Troy, and Z. H. Ancona, 2020: A rasterized building footprint dataset for the United States. *Sci. Data*, https://doi.org/10.1038/s41597-020-0542-3.

Herrmann, J., and A. Matzarakis, 2012: Mean radiant temperature in idealised urban canyons-examples from Freiburg, Germany. *Int. J. Biometeorol.*, **56**, 199–203, https://doi.org/10.1007/S00484-010-0394-1/FIGURES/7.

Hersbach, H., and Coauthors, 2020: The ERA5 global reanalysis. *Q. J. R. Meteorol. Soc.*, **146**, 1999–2049, https://doi.org/10.1002/QJ.3803.

Hertwig, D., and Coauthors, A tale of three cities: challenges of global land cover data and the urban surface energy balance.

Hertwig, D., H. L. Gough, S. Grimmond, J. F. Barlow, C. W. Kent, W. E. Lin, A. G. Robins, and P. Hayden, 2019: Wake Characteristics of Tall Buildings in a Realistic Urban Canopy. *Boundary-Layer Meteorol.*, **172**, 239–270, https://doi.org/10.1007/S10546-019-00450-7/TABLES/5.

——, and Coauthors, 2020: Urban signals in high-resolution weather and climate simulations: role of urban land-surface characterisation. *Theor. Appl. Climatol.*, **142**, 701–728, https://doi.org/10.1007/s00704-020-03294-1.

——, S. Grimmond, S. Kotthaus, C. Vanderwel, H. Gough, M. Haeffelin, and A. Robins, 2021: Variability of physical meteorology in urban areas at different scales: implications for air quality. *Faraday Discuss.*, **226**, 149–172, https://doi.org/10.1039/D0FD00098A.

Hilland, R. V. J., and J. A. Voogt, 2020: The effect of sub-facet scale surface structure on wall brightness temperatures at multiple scales. *Theor. Appl. Climatol.*, **140**, 767–785, https://doi.org/10.1007/s00704-020-03094-7.

Hogan, R., M. Ahlgrimm, G. Balsamo, A. Beljaars, P. Berrisford, and A. Bozzo et al, 2017: Radiation in numerical weather prediction. *ECMWF Tech. Memo.*,.

Hogan, R. J., 2019a: Flexible Treatment of Radiative Transfer in Complex Urban Canopies for Use in Weather and Climate Models. *Boundary-Layer Meteorol.*, https://doi.org/10.1007/s10546-019-00457-0.

——, 2019b: An Exponential Model of Urban Geometry for Use in Radiative Transfer Applications. *Boundary-Layer Meteorol.*, https://doi.org/10.1007/s10546-018-0409-8.

Hogan, R. J., 2021: spartacus-surface. *GitHub Repos.*,.

Hogan, R. J., and J. K. P. Shonk, 2013: Incorporating the effects of 3D radiative transfer in the presence of clouds intol two-stream multilayer radiation schemes. *J. Atmos. Sci.*, https://doi.org/10.1175/JAS-D-12-041.1.

——, S. A. K. Schäfer, C. Klinger, J. C. Chiu, and B. Mayer, 2016: Representing 3-D cloud radiation effects in two-stream schemes: 2. Matrix formulation and broadband evaluation. *J. Geophys. Res.*, **121**, 8583–8599, https://doi.org/10.1002/2016JD024875.

——, T. Quaife, and R. Braghiere, 2018a: Fast matrix treatment of 3-D radiative transfer in vegetation canopies: SPARTACUS-Vegetation 1.1. *Geosci. Model Dev.*, **11**, 339–350, https://doi.org/10.5194/gmd-11-339-2018.

——, ——, and ——, 2018b: Fast matrix treatment of 3-D radiative transfer in vegetation canopies: SPARTACUS-Vegetation 1.1. *Geosci. Model Dev.*, **11**, 339–350, https://doi.org/10.5194/gmd-11-339-2018.

Holland, D. E., J. A. Berglund, J. P. Spruce, and R. D. McKellip, 2008: Derivation of Effective Aerodynamic Surface Roughness in Urban Areas from Airborne Lidar Terrain Data. *J. Appl. Meteorol. Climatol.*, **47**, 2614–2626, https://doi.org/10.1175/2008JAMC1751.1.

Hu, L., and J. Wendel, 2019: Analysis of urban surface morphologic effects on diurnal thermal directional anisotropy. *ISPRS J. Photogramm. Remote Sens.*, **148**, 1–12.

Ichinose, T., K. Shimodozono, and K. Hanaki, 1999: Impact of anthropogenic heat on urban climate in Tokyo. *Atmospheric Environment*, Vol. 33 of.

IPCC, 2014a: *IPCC Climate Change 2014: Fifth Assessment Report*.

——, 2014b: Assessment Report 5. Climate Change 2014: Impacts, Adaptation, and Vulnerability. Chapter 8. Urban areas. *Clim. Chang. 2014 Impacts, Adapt. Vulnerability. Part A Glob. Sect. Asp. Contrib. Work. Gr. II to Fifth Assess. Rep. Intergov. Panel Clim. Chang.*,.

Iqbal, M., 1983: An introduction to solar radiation. 390.

Jackson, T. L., J. J. Feddema, K. W. Oleson, G. B. Bonan, and J. T. Bauer, 2010: Parameterization of urban characteristics for global climate modeling. *Ann. Assoc. Am. Geogr.*, **100**, 848–865, https://doi.org/10.1080/00045608.2010.497328.

Jamei, E., D. R. Ossen, and P. Rajagopalan, 2017: Investigating the effect of urban configurations on the variation of air temperature. *Int. J. Sustain. Built Environ.*, **6**, 389–399, https://doi.org/10.1016/J.IJSBE.2017.07.001.

Jandaghian, Z., and H. Akbari, 2018: The effect of increasing surface albedo on urban climate and air quality: A detailed study for Sacramento, Houston, and Chicago. *Climate*, https://doi.org/10.3390/cli6020019.

Järvi, L., C. S. B. S. B. Grimmond, and A. Christen, 2011: The Surface Urban Energy and Water Balance Scheme (SUEWS): Evaluation in Los Angeles and Vancouver. *J. Hydrol.*, **411**, 219–237, https://doi.org/10.1016/j.jhydrol.2011.10.001.

——, A. Nordbo, H. Junninen, A. Riikonen, J. Moilanen, E. Nikinmaa, and T. Vesala, 2012: Seasonal and annual variation of carbon dioxide surface fluxes in Helsinki, Finland, in 2006-2010. *Atmos. Chem. Phys.*, **12**, 8475–8489, https://doi.org/10.5194/ACP-12-8475-2012.

——, C. S. B. Grimmond, M. Taka, A. Nordbo, H. Setälä, and I. B. Strachan, 2014: Development of the Surface Urban Energy and Water Balance Scheme (SUEWS) for cold climate cities. *Geosci. Model Dev.*, **7**, 1691–1711, https://doi.org/10.5194/gmd-7-1691-2014.

Järvi, L., and Coauthors, 2019: Spatial Modeling of Local-Scale Biogenic and Anthropogenic Carbon Dioxide Emissions in Helsinki. *J. Geophys. Res. Atmos.*, **124**, 8363–8384, https://doi.org/10.1029/2018JD029576.

Jensen, M. P., A. M. Vogelmann, W. D. Collins, G. J. Zhang, and E. P. Luke, 2008: Investigation of Regional and Seasonal Variations in Marine Boundary Layer Cloud Properties from MODIS Observations. *J. Clim.*, **21**, 4955–4973, https://doi.org/10.1175/2008JCLI1974.1.

Jin, M., R. E. Dickinson, and D. L. Zhang, 2005: The footprint of urban areas on global climate as characterized by MODIS. *J. Clim.*, **18**, https://doi.org/10.1175/JCLI3334.1.

Kanda, M., 2007: *Progress in urban meteorology: A review*. Meteorological Society of Japan,.

Kanda, M., T. Kawai, M. Kanega, R. Moriwaki, K. Narita, and A. Hagishima, 2005a: A simple energy balance model for regular building arrays. *Boundary-Layer Meteorol.*, **116**, 423–443, https://doi.org/10.1007/s10546-004-7956-x.

Kanda, M., T. Kawai, and K. Nakagawa, 2005b: A simple theoretical radiation scheme for regular building arrays. *Boundary-Layer Meteorol.*, **114**, 71–90, https://doi.org/10.1007/s10546-004-8662-4.

Karsisto, P., C. Fortelius, M. Demuzere, C. S. B. Grimmond, K. W. Oleson, R. Kouznetsov, V. Masson, and L. Järvi, 2016: Seasonal surface urban energy balance and wintertime stability simulated using three land-surface models in the high-latitude city Helsinki. *Q. J. R. Meteorol. Soc.*, **142**, 401–417, https://doi.org/10.1002/QJ.2659.

Kastner-Klein, P., and M. W. Rotach, 2004: Mean Flow and Turbulence Characteristics in an Urban Roughness Sublayer. *Boundary-Layer Meteorol. 2004 1111*, **111**, 55–84, https://doi.org/10.1023/B:BOUN.0000010994.32240.B1.

Kawai, T., and M. Kanda, 2010: Urban energy balance obtained from the comprehensive outdoor scale model experiment. Part I: Basic features of the surface energy balance. *J. Appl. Meteorol. Climatol.*, **49**, https://doi.org/10.1175/2010JAMC1992.1.

Kent, C. W., S. Grimmond, D. Gatey, and K. Hirano, 2019: Urban morphology parameters from global digital elevation models: Implications for aerodynamic roughness and for wind-speed estimation. *Remote Sens. Environ.*, **221**, 316–339, https://doi.org/10.1016/j.rse.2018.09.024.

Keogh, S., G. Mills, and R. Fealy, 2012: The energy budget of the urban surface: two locations in Dublin. *http://dx.doi.org/10.1080/00750778.2012.689182*, **45**, 1–23, https://doi.org/10.1080/00750778.2012.689182.

Kershaw, S. E., and A. A. Millward, 2012: A spatio-temporal index for heat vulnerability assessment. *Environ. Monit. Assess.*, **184**, 7329–7342, https://doi.org/10.1007/S10661-011-2502-Z/FIGURES/5.

Kimura, F., and S. Takahashi, 1991: The effects of land-use and anthropogenic heating on the surface temperature in the Tokyo Metropolitan area: A numerical experiment. *Atmos. Environ. Part B, Urban Atmos.*, **25**, https://doi.org/10.1016/0957-1272(91)90050-O.

Kobayashi, T., T. Takamura, T. Kobayashi, and T. Takamura, 1994: Upward longwave radiation from a non-black urban canopy. *BoLMe*, **69**, 201–213, https://doi.org/10.1007/BF00713303.

Kokkonen, T. V., C. S. B. Grimmond, O. Räty, H. C. Ward, A. Christen, T. R. Oke, S. Kotthaus, and L. Järvi, 2018: Sensitivity of Surface Urban Energy and Water Balance Scheme (SUEWS) to downscaling of reanalysis forcing data. *Urban Clim.*, **23**, 36–52.

Konarska, J., F. Lindberg, A. Larsson, S. Thorsson, and B. Holmer, 2014: Transmissivity of solar radiation through crowns of single urban trees-application for outdoor thermal comfort modelling. *Theor. Appl. Climatol.*, **117**, https://doi.org/10.1007/s00704-013-1000-3.

——, B. Holmer, F. Lindberg, and S. Thorsson, 2016a: Influence of vegetation and building geometry on the spatial variations of air temperature and cooling rates in a high-latitude city. *Int. J. Climatol.*, **36**, 2379–2395, https://doi.org/10.1002/JOC.4502.

——, J. Uddling, B. Holmer, M. Lutz, F. Lindberg, H. Pleijel, and S. Thorsson, 2016b: Transpiration of urban trees and its cooling effect in a high latitude city. *Int. J. Biometeorol.*, **60**, 159–172, https://doi.org/10.1007/s00484-015-1014-x.

Kondo, A., M. Ueno, A. Kaga, and K. Yamaguchi, 2001: The influence of urban canopy configuration on urban albedo. *Boundary-Layer Meteorol.*, **100**, 225–242, https://doi.org/10.1023/A:1019243326464.

Kondo, H., Y. Genchi, Y. Kikegawa, Y. Ohashi, H. Yoshikado, and H. Komiyama, 2005: Development of a multi-layer urban canopy model for the analysis of energy consumption in a big city: Structure of the urban canopy model and its basic performance. *Boundary-Layer Meteorol.*, **116**, 395–421, https://doi.org/10.1007/s10546-005-0905-5.

Kotharkar, R., and A. Bagade, 2018: Local Climate Zone classification for Indian cities: A case study of Nagpur. *Urban Clim.*, **24**, 369–392, https://doi.org/10.1016/J.UCLIM.2017.03.003.

Kotthaus, S., and C. S. B. Grimmond, 2014a: Energy exchange in a dense urban environment - Part II: Impact of spatial heterogeneity of the surface. *Urban Clim.*, **10**, 281–307, https://doi.org/10.1016/j.uclim.2013.10.001.

——, and ——, 2014b: Energy exchange in a dense urban environment - Part I: Temporal variability of long-term observations in central London. *Urban Clim.*, **10**, 261–280, https://doi.org/10.1016/j.uclim.2013.10.002.

——, T. E. L. Smith, M. J. Wooster, and C. S. B. S. B. Grimmond, 2014: Derivation of an urban materials spectral library through emittance and reflectance spectroscopy. *ISPRS J. Photogramm. Remote Sens.*, **94**, 194–212.

Krayenhoff, E. S., and J. A. Voogt, 2016: Daytime Thermal Anisotropy of Urban Neighbourhoods: Morphological Causation. *Remote Sens.* , **8**, https://doi.org/10.3390/rs8020108.

Krayenhoff, E. S., A. Christen, A. Martilli, and T. R. Oke, 2014: A Multi-layer Radiation Model for Urban Neighbourhoods with Trees. *Boundary-Layer Meteorol.*, **151**, 139–178, https://doi.org/10.1007/s10546-013-9883-1.

——, J. L. Santiago, A. Martilli, A. Christen, and T. R. Oke, 2015: Parametrization of Drag and Turbulence for Urban Neighbourhoods with Trees. *Boundary-Layer Meteorol.*, https://doi.org/10.1007/s10546-015-0028-6.

Krayenhoff, E. S., and Coauthors, 2020: A multi-layer urban canopy meteorological model with trees (BEP-Tree): Street tree impacts on pedestrian-level climate. *Urban Clim.*, **32**, https://doi.org/10.1016/j.uclim.2020.100590.

Krayenhoff, S. E., and J. A. Voogt, 2007: A microscale three-dimensional urban energy balance model for studying surface temperatures. *Boundary-Layer Meteorol.*, **123**, 433–461, https://doi.org/10.1007/s10546-006-9153-6.

Kusaka, H., and F. Kimura, 2004a: Coupling a single-layer urban canopy model with a simple atmospheric model: Impact on urban heat island simulation for an idealized case. *J. Meteorol. Soc. Japan*, **82**, 67–80, https://doi.org/10.2151/jmsj.82.67.

——, and ——, 2004b: Thermal effects of urban canyon structure on the nocturnal heat island: Numerical experiment using a mesoscale model coupled with an urban canopy model. *J. Appl. Meteorol.*, **43**, https://doi.org/10.1175/JAM2169.1.

——, H. Kondo, Y. Kikegawa, and F. Kimura, 2001a: A Simple Single-Layer Urban Canopy Model For Atmospheric Models: Comparison With Multi-Layer And Slab Models. *Boundary-Layer Meteorol. 2001 1013*, **101**, 329–358, https://doi.org/10.1023/A:1019207923078.

——, ——, ——, and ——, 2001b: A simple single-layer urban canopy model for atmospheric models: Comparison with multi-layer and slab models. *Boundary-Layer Meteorol.*, **101**, 329–358, https://doi.org/10.1023/A:1019207923078.

Landier, L., J. P. Gastellu-Etchegorry, A. Al Bitar, E. Chavanon, N. Lauret, C. Feigenwinter, Z. Mitraka, and N. Chrysoulakis, 2018: Calibration of urban canopies albedo and 3D shortwave radiative budget using remote-sensing data and the DART model. *Eur. J. Remote Sens.*, https://doi.org/10.1080/22797254.2018.1462102.

Lau, K. K. L., C. Ren, J. Ho, and E. Ng, 2016: Numerical modelling of mean radiant temperature in high-density sub-tropical urban environment. *Energy Build.*, **114**, https://doi.org/10.1016/j.enbuild.2015.06.035.

Lean, H. W., J. F. Barlow, and C. H. Halios, 2019: The impact of spin-up and resolution on the representation of a clear convective boundary layer over London in order 100 m grid-length versions of the Met Office Unified Model. *Q. J. R. Meteorol. Soc.*, **145**, 1674–1689, https://doi.org/10.1002/QJ.3519.

Lee, S. H., and S. U. Park, 2008: A vegetated urban canopy model for meteorological and environmental modelling. *Boundary-Layer Meteorol.*, https://doi.org/10.1007/s10546-007-9221-6.

Lemonsu, A., and V. Masson, 2002: Simulation of a summer urban breeze over Paris. *Boundary-Layer Meteorol.*, **104**, 463–490, https://doi.org/10.1023/A:1016509614936.

Lemonsu, A., C. S. B. Grimmond, and V. Masson, 2004: Modeling the Surface Energy Balance of the Core of an Old Mediterranean City: Marseille. *J. Appl. Meteorol.*, https://doi.org/10.1175/1520-0450(2004)043<0312:MTSEBO>2.0.CO;2.

Lemonsu, A., S. Belair, and J. Mailhot, 2009: The New Canadian Urban Modelling System: Evaluation for Two Cases from the Joint Urban 2003 Oklahoma City Experiment. **133**, 47–70, https://doi.org/10.1007/s10546-009-9414-2.

Lemonsu, A., V. Masson, L. Shashua-Bar, E. Erell, and D. Pearlmutter, 2012: Inclusion of vegetation in the Town Energy Balance model for modelling urban green areas. *Geosci. Model Dev.*, https://doi.org/10.5194/gmd-5-1377-2012.

Li, D., E. Bou-Zeid, and M. Oppenheimer, 2014: The effectiveness of cool and green roofs as urban heat island mitigation strategies. *Environ. Res. Lett.*, **9**, 055002, https://doi.org/10.1088/1748-9326/9/5/055002.

——, T. Sun, M. Liu, L. Yang, L. Wang, and Z. Gao, 2015a: Contrasting responses of urban and rural surface energy budgets to heat waves explain synergies between urban heat islands and heat waves. *Environ. Res. Lett.*, **10**, 054009, https://doi.org/10.1088/1748-9326/10/5/054009.

Li, D. H. W., S. W. Lou, and J. C. Lam, 2015b: An Analysis of Global, Direct and Diffuse Solar Radiation. *Energy Procedia*, **75**, 388–393, https://doi.org/10.1016/J.EGYPRO.2015.07.399.

Li, Y., S. Schubert, J. P. Kropp, and D. Rybski, 2020: On the influence of density and morphology on the Urban Heat Island intensity. *Nat. Commun. 2020 111*, **11**, 1–9, https://doi.org/10.1038/s41467-020-16461-9.

Liang, X., and Coauthors, 2018: Surf: Understanding and predicting urban convection and haze. *Bull. Am. Meteorol. Soc.*, https://doi.org/10.1175/BAMS-D-16-0178.1.

Lim, H. D., D. Hertwig, T. Grylls, H. Gough, M. van Reeuwijk, S. Grimmond, and C. Vanderwel, 2022: Pollutant dispersion by tall buildings: laboratory experiments and Large-Eddy Simulation. *Exp. Fluids*, **63**, 1–20, https://doi.org/10.1007/S00348-022-03439-0/FIGURES/10.

Lin, B. S., and Y. J. Lin, 2010: Cooling Effect of Shade Trees with Different Characteristics in a Subtropical Urban Park. *HortScience*, **45**, 83–86, https://doi.org/10.21273/HORTSCI.45.1.83.

Lin, T. P., A. Matzarakis, and R. L. Hwang, 2010: Shading effect on long-term outdoor thermal comfort. *Build. Environ.*, **45**, 213–221, https://doi.org/10.1016/J.BUILDENV.2009.06.002.

Lindberg, F., and C. S. B. Grimmond, 2010: Continuous sky view factor maps from high resolution urban digital elevation models. *Clim. Res.*, **42**, 177–183, https://doi.org/10.3354/cr00882.

Lindberg, F., and C. S. B. Grimmond, 2011a: The influence of vegetation and building morphology on shadow patterns and mean radiant temperatures in urban areas: Model development and evaluation. *Theor. Appl. Climatol.*, **105**, 311–323, https://doi.org/10.1007/s00704-010-0382-8.

——, and C. S. B. B. Grimmond, 2011b: Nature of vegetation and building morphology characteristics across a city: Influence on shadow patterns and mean radiant temperatures in London. *Urban Ecosyst.*, **14**, 617–634, https://doi.org/10.1007/s11252-011-0184-5.

——, B. Holmer, S. Thorsson, and B. H. S. T. F Lindberg, 2008: SOLWEIG 1.0 - Modelling spatial variations of 3D radiant fluxes and mean radiant temperature in complex urban settings. *Int. J. Biometeorol.*, **52**, 697–713, https://doi.org/10.1007/s00484-008-0162-7.

——, C. S. B. Grimmond, and F. Lindberg, 2011: Nature of vegetation and building morphology characteristics across a city: Influence on shadow patterns and mean radiant temperatures in London. **14**, 617–634, https://doi.org/10.1007/s11252-011-0184-5.

Lindberg, F., C. S. B. Grimmond, N. Yogeswaran, S. Kotthaus, and L. Allen, 2013: Impact of city changes and weather on anthropogenic heat flux in Europe 1995–2015. *Urban Clim.*, **4**, 1–15, https://doi.org/10.1016/J.UCLIM.2013.03.002.

Lindberg, F., B. Holmer, S. Thorsson, and D. Rayner, 2014: Characteristics of the mean radiant temperature in high latitude cities-implications for sensitive climate planning applications. *Int. J. Biometeorol.*, **58**, https://doi.org/10.1007/s00484-013-0638-y.

——, P. Jonsson, T. Honjo, and D. Wästberg, 2015: Solar energy on building envelopes – 3D modelling in a 2D environment. *Sol. Energy*, **115**, 369–378, https://doi.org/10.1016/J.SOLENER.2015.03.001.

——, S. Onomura, and C. S. B. B. Grimmond, 2016a: Influence of ground surface characteristics on the mean radiant temperature in urban areas. *Int. J. Biometeorol.*, **60**, 1439–1452, https://doi.org/10.1007/s00484-016-1135-x.

——, S. Thorsson, D. Rayner, and K. Lau, 2016b: The impact of urban planning strategies on heat stress in a climate-change perspective. *Sustain. Cities Soc.*, **25**, https://doi.org/10.1016/j.scs.2016.04.004.

——, and Coauthors, 2018: Urban Multi-scale Environmental Predictor (UMEP): An integrated tool for city-based climate services. *Environ. Model. Softw.*, **99**, 70–87, https://doi.org/10.1016/j.envsoft.2017.09.020.

Lindberg, F., K. F. G. G. Olofson, T. Sun, C. S. B. B. Grimmond, and C. Feigenwinter, 2020: Urban storage heat flux variability explored using satellite, meteorological and geodata. *Theor. Appl. Climatol.*, **141**, 271–284, https://doi.org/10.1007/s00704-020-03189-1.

Lipson, M., and Coauthors, 2023: Evaluation of 30 urban land surface models in the Urban-PLUMBER project: Phase 1 results. *Q. J. R. Meteorol. Soc.*,.

Lipson, M. J., N. Nazarian, M. A. Hart, K. A. Nice, and B. Conroy, 2022: A Transformation in City-Descriptive Input Data for Urban Climate Models. *Front. Environ. Sci.*, **0**, 945, https://doi.org/10.3389/FENVS.2022.866398.

Liu, Y., Z. Luo, and S. Grimmond, 2022: Revising the definition of anthropogenic heat flux from buildings: role of human activities and building storage heat flux. *Atmos. Chem. Phys*, **22**, 4721–4735, https://doi.org/10.5194/acp-22-4721-2022.

Loridan, T., and C. S. B. B. Grimmond, 2012a: Multi-site evaluation of an urban land-surface model: Intra-urban heterogeneity, seasonality and parameter complexity requirements. *Q. J. R. Meteorol. Soc.*, **138**, 1094–1113, https://doi.org/10.1002/qj.963.

——, and ——, 2012b: Characterization of energy flux partitioning in urban environments: Links with surface seasonal properties. *J. Appl. Meteorol. Climatol.*, **51**, 219–241, https://doi.org/10.1175/JAMC-D-11-038.1.

——, and Coauthors, 2010: Trade-offs and responsiveness of the single-layer urban canopy parametrization in WRF: An offline evaluation using the MOSCEM optimization algorithm and field observations. *Q. J. R. Meteorol. Soc.*, **136**, 997–1019, https://doi.org/10.1002/qj.614.

——, C. S. B. Grimmond, B. D. Offerle, D. T. Young, T. E. L. Smith, L. Järvi, and F. Lindberg, 2011: Local-Scale Urban Meteorological Parameterization Scheme (LUMPS): Longwave Radiation Parameterization and Seasonality-Related Developments. *J. Appl. Meteorol. Climatol.*, **50**, 185–202, https://doi.org/10.1175/2010JAMC2474.1.

——, and Coauthors, 2013: High Resolution Simulation of the Variability of Surface Energy Balance Fluxes Across Central London with Urban Zones for Energy Partitioning. *Boundary-Layer Meteorol.*, **147**, 493–523, https://doi.org/10.1007/S10546-013-9797-Y/FIGURES/11.

Macdonald, R. W., R. F. Griffiths, and D. J. Hall, 1998: A comparison of results from scaled field and wind tunnel modelling of dispersion in arrays of obstacles. *Atmos. Environ.*, **32**, 3845–3862, https://doi.org/10.1016/S1352-2310(98)80006-X.

Martilli, A., 2009: On the Derivation of Input Parameters for Urban Canopy Models from Urban Morphological Datasets. **130**, 301–306, https://doi.org/10.1007/s10546-008-9345-3.

——, A. Clappier, and M. W. Rotach, 2002: An Urban Surface Exchange Parameterisation for Mesoscale Models. *Boundary-Layer Meteorol.*, **104**, 261–304, https://doi.org/10.1023/A:1016099921195.

——, Y.-A. Roulet, M. Junier, F. Kirchner, M. W. Rotach, and A. Clappier, 2003: On the impact of urban surface exchange parameterisations on air quality simulations: the Athens case. *Atmos. Environ.*, **37**, 4217–4231, https://doi.org/10.1016/S1352-2310(03)00564-8.

Masson, V., 2000: A Physically-Based Scheme For The Urban Energy Budget In Atmospheric Models. *Boundary-Layer Meteorol.*, **94**, 357–397, https://doi.org/10.1023/A:1002463829265.

——, 2006: Urban surface modeling and the meso-scale impact of cities. *Theor. Appl. Climatol.*, **84**, 35–45, https://doi.org/10.1007/s00704-005-0142-3.

Masson, V., and Coauthors, 2008: The Canopy and Aerosol Particles Interactions in TOulouse Urban Layer (CAPITOUL) experiment. *Meteorol. Atmos. Phys.*, **102**, 135–157, https://doi.org/10.1007/s00703-008-0289-4.

Masson, V., and Coauthors, 2020a: City-descriptive input data for urban climate models: Model requirements, data sources and challenges. *Urban Clim.*, https://doi.org/10.1016/j.uclim.2019.100536.

Masson, V., A. Lemonsu, J. Hidalgo, and J. Voogt, 2020b: Urban climates and climate change. *Annu. Rev. Environ. Resour.*, **45**, 411–444, https://doi.org/10.1146/ANNUREV-ENVIRON-012320-083623.

Matese, A., B. Gioli, F. P. Vaccari, A. Zaldei, and F. Miglietta, 2009: Carbon dioxide emissions of the city center of Firenze, Italy: Measurement, evaluation, and source partitioning. *J. Appl. Meteorol. Climatol.*, https://doi.org/10.1175/2009JAMC1945.1.

Matzarakis, A., H. Mayer, and M. G. Iziomon, 1999: Applications of a universal thermal index: Physiological equivalent temperature. *Int. J. Biometeorol.*, **43**, https://doi.org/10.1007/s004840050119.

——, F. Rutz, and H. Mayer, 2010: Modelling radiation fluxes in simple and complex environments: Basics of the RayMan model. *Int. J. Biometeorol.*, **54**, 131–139.

Mccarthy, M. P., M. J. Best, and R. A. Betts, 2010: Climate change in cities due to global warming and urban effects. *Geophys. Res. Lett.*, https://doi.org/10.1029/2010GL042845.

Meehl, G. A., and C. Tebaldi, 2004: More intense, more frequent, and longer lasting heat waves in the 21st century. *Science*, **305**, 994–997, https://doi.org/10.1126/SCIENCE.1098704.

Met Office, 2022: UK climate information - Met Office. *Met Off.*,. http://www.metoffice.gov.uk/public/weather/climate/ (Accessed May 8, 2022).

Meyn, S. K., and T. R. Oke, 2009: Heat fluxes through roofs and their relevance to estimates of urban heat storage. *Energy Build.*, **41**, 745–752, https://doi.org/10.1016/J.ENBUILD.2009.02.005.

Miao, S. G., J. X. Dou, F. Chen, J. Li, and A. G. Li, 2012: Analysis of observations on the urban surface energy balance in Beijing. *Sci. China Earth Sci.*, **55**, 1881–1890, https://doi.org/10.1007/s11430-012-4411-6.

Middel, A., A. J. Brazel, P. Gober, S. W. Myint, H. Chang, and J. Der Duh, 2012: Land cover, climate, and the summer surface energy balance in Phoenix, AZ, and Portland, OR. *Int. J. Climatol.*, **32**, 2020–2032, https://doi.org/10.1002/JOC.2408.

Miguet, F., and D. Groleau, 2007: Urban bioclimatic indicators for urban planers with the software tool SOLENE. *Portugal SB 2007 - Sustainable Construction, Materials and Practices: Challenge of the Industry for the New Millennium*.

Mills, G. M., 1993: Simulation of the energy budget of an urban canyon-I. Model structure and sensitivity test. *Atmos. Environ. Part B, Urban Atmos.*, **27**, https://doi.org/10.1016/0957-1272(93)90002-N.

Milojevic-Dupont, N., and Coauthors, 2020: Learning from urban form to predict building heights. *PLoS One*, **15**, e0242010, https://doi.org/10.1371/JOURNAL.PONE.0242010.

Molnár, G., A. Z. Gyöngyösi, and T. Gál, 2019: Integration of an LCZ-based classification into WRF to assess the intra-urban temperature pattern under a heatwave period in Szeged, Hungary. *Theor. Appl. Climatol.*, **138**, 1139–1158, https://doi.org/10.1007/S00704-019-02881-1/FIGURES/11.

Montavez, J. P., J. I. Jimenez, and A. Sarsa, 2000: A Monte Carlo model of the nocturnal surface temperatures in urban canyons. *Boundary-Layer Meteorol.*, **96**, https://doi.org/10.1023/A:1002600523841.

Morille, B., N. Lauzet, and M. Musy, 2015: SOLENE-microclimate: A tool to evaluate envelopes efficiency on energy consumption at district scale. *Energy Procedia*, **78**, 1165–1170, https://doi.org/10.1016/J.EGYPRO.2015.11.088.

Moriwaki, R., and M. KANDA, 2004: Seasonal and Diurnal Fluxes of Radiation, Heat, Water Vapor, and Carbon Dioxide over a Suburban Area. *J. Appl. Meteorol.*, **43**, 1700–1710, https://doi.org/10.1175/JAM2153.1.

Morrison, W., and K. Benjamin, 2021: daRt. *GitHub Repos.*,.

Morrison, W., S. Kotthaus, C. S. B. Grimmond, A. Inagaki, T. Yin, J. P. Gastellu-Etchegorry, M. Kanda, and C. J. Merchant, 2018: A novel method to obtain three-dimensional urban surface temperature from ground-based thermography. *Remote Sens. Environ.*, **215**, 268–283, https://doi.org/10.1016/j.rse.2018.05.004.

——, T. Yin, N. Lauret, J. Guilleux, S. Kotthaus, J. P. Gastellu-Etchegorry, L. Norford, and S. Grimmond, 2020: Atmospheric and emissivity corrections for ground-based thermography using 3D radiative transfer modelling. *Remote Sens. Environ.*, **237**, https://doi.org/10.1016/j.rse.2019.111524.

——, S. Kotthaus, and S. Grimmond, 2021: Urban surface temperature observations from ground-based thermography: intra- and inter-facet variability. *Urban Clim.*, **35**, 100748, https://doi.org/10.1016/j.uclim.2020.100748.

Myint, S. W., E. A. Wentz, A. J. Brazel, and D. A. Quattrochi, 2013: The impact of distinct anthropogenic and vegetation features on urban warming. *Landsc. Ecol.*, **28**, 959–978, https://doi.org/10.1007/S10980-013-9868-Y/TABLES/5.

Nazarian, N., and J. Kleissl, 2015: CFD simulation of an idealized urban environment: Thermal effects of geometrical characteristics and surface materials. *Urban Clim.*, **12**, 141–159, https://doi.org/10.1016/J.UCLIM.2015.03.002.

——, E. Scott Krayenhoff, and A. Martilli, 2020: A one-dimensional model of turbulent flow through “urban” canopies (MLUCM v2.0): updates based on large-eddy simulation. *Geosci.*

Model Dev, **13**, 937–953, https://doi.org/10.5194/gmd-13-937-2020.

Newton, T., T. R. Oke, C. S. B. Grimmond, and M. Roth, 2007: The suburban energy balance in Miami, Florida. *Geogr. Ann. Ser. A Phys. Geogr.*, **89 A**, 331–347, https://doi.org/10.1111/j.1468-0459.2007.00329.x.

Nie, W. S., T. Sun, and G. H. Ni, 2014: Spatiotemporal characteristics of anthropogenic heat in an urban environment: A case study of Tsinghua Campus. *Build. Environ.*, **82**, https://doi.org/10.1016/j.buildenv.2014.10.011.

Niemela, S., P. Raisanen, H. Savijarvï, and S. Savijarvï, 2001: Comparison of surface radiative flux parameterizations Part II. Shortwave radiation. *Atmos. Res.*, **58**, 141–154.

Noilhan, J., 1981: A model for the net total radiation flux at the surfaces of a building. *Build. Environ.*, https://doi.org/10.1016/0360-1323(81)90004-4.

Nordbo, A., L. Järvi, S. Haapanala, J. Moilanen, and T. Vesala, 2012: Intra-City Variation in Urban Morphology and Turbulence Structure in Helsinki, Finland. *Boundary-Layer Meteorol. 2012 1463*, **146**, 469–496, https://doi.org/10.1007/S10546-012-9773-Y.

Nunez, M., and T. R. Oke, 1977: ENERGY BALANCE OF AN URBAN CANYON. *J. Appl. Meteorol.*, https://doi.org/10.1175/1520-0450(1977)016<0011:TEBOAU>2.0.CO;2.

——, I. Eliasson, and J. Lindgren, 2000: Spatial variation of incoming longwave radiation in Göteborg, Sweden. *Theor. Appl. Climatol.*, **67**, https://doi.org/10.1007/s007040070007.

Offerle, B., C. S. B. Grimmond, and T. R. Oke, 2003: Parameterization of net all-wave radiation for urban areas. *J. Appl. Meteorol.*, **42**, https://doi.org/10.1175/1520-0450(2003)042<1157:PONARF>2.0.CO;2.

——, C. S. B. B. Grimmond, and K. Fortuniak, 2005a: Heat storage and anthropogenic heat flux in relation to the energy balance of a central European city centre. *Int. J. Climatol.*, **25**, 1405–1419, https://doi.org/10.1002/joc.1198.

Offerle, B., P. Jonsson, I. Eliasson, and C. S. B. Grimmond, 2005b: Urban modification of the surface energy balance in the West African Sahel: Ouagadougou, Burkina Faso. *J. Clim.*, https://doi.org/10.1175/JCLI3520.1.

Offerle, B., C. S. B. Grimmond, K. Fortuniak, K. Kłysik, and T. R. Oke, 2006a: Temporal variations in heat fluxes over a central European city centre. *Theor. Appl. Climatol.*, **84**, 103–115, https://doi.org/10.1007/S00704-005-0148-X.

Offerle, B., C. S. B. Grimmond, K. Fortuniak, and W. Pawlak, 2006b: Intraurban differences of surface energy fluxes in a central European City. *J. Appl. Meteorol. Climatol.*, **45**, 125–136, https://doi.org/10.1175/JAM2319.1.

Oikawa, S., and Y. Meng, 1995: Turbulence characteristics and organized motion in a suburban roughness sublayer. *Boundary-Layer Meteorol.*, https://doi.org/10.1007/BF00712122.

Oke, T. R., 1981: Canyon geometry and the nocturnal urban heat island: Comparison of scale model and field observations. *J. Climatol.*, **1**, 237–254, https://doi.org/10.1002/JOC.3370010304.

——, 1982a: The energetic basis of the urban heat island. *Q. J. R. Meteorol. Soc.*, **108**, 1–24.

——, 1982b: The energetic basis of the urban heat-Island. *Q. J. R. Meteorol. Soc.*, **108**, 1–24, https://doi.org/10.1002/qj.49710845502.

Oke, T. R., 1987: *Boundary layer climates, Second edition*.

Oke, T. R., and R. F. Fuggle, 1972: Comparison of urban/rural counter and net radiation at night. *Boundary-Layer Meteorol.*, https://doi.org/10.1007/BF02184771.

Oke, T. R., G. Mills, A. Christen, and J. A. Voogt, 2017: *Urban climates*.

Oke, T. R. R., 1988: The urban energy balance. *Prog. Phys. Geogr. Earth Environ.*, **12**, 471–508, https://doi.org/10.1177/030913338801200401.

Oleson, K. W., and Coauthors, 2008a: An urban parameterization for a global climate model. Part 1: Formulation and evaluation for two cities. *J. Appl. Meteorol. Climatol.*, **47**, 1038–1060, https://doi.org/10.1175/2007JAMC1597.1.

Oleson, K. W., and Coauthors, 2008b: An Urban Parameterization for a Global Climate Model. Part I: Formulation and Evaluation for Two Cities. *J. Appl. Meteorol. Climatol.*, **47**, 1038–1060, https://doi.org/10.1175/2007JAMC1597.1.

——, G. B. Bonan, J. Feddema, M. Vertenstein, K. W. Oleson, G. B. Bonan, J. Feddema, and M. Vertenstein, 2008c: An Urban Parameterization for a Global Climate Model. Part II:

Sensitivity to Input Parameters and the Simulated Urban Heat Island in Offline Simulations. *J. Appl. Meteorol. Climatol.*, **47**, 1061–1076, https://doi.org/10.1175/2007JAMC1598.1.

Omidvar, H., and Coauthors, 2022: Surface Urban Energy and Water Balance Scheme (v2020a) in vegetated areas: parameter derivation and performance evaluation using FLUXNET2015 dataset. *Geosci. Model Dev.*, **15**, 3041–3078, https://doi.org/10.5194/GMD-15-3041-2022.

OPDC, 2018: Tall Buildings Statement LOCAL PLAN SUPPORTING STUDY.

Padiyedath Gopalan, S., A. Kawamura, H. Amaguchi, T. Takasaki, and G. Azhikodan, 2019: A bootstrap approach for the parameter uncertainty of an urban-specific rainfall-runoff model. *J. Hydrol.*, **579**, 124195, https://doi.org/10.1016/J.JHYDROL.2019.124195.

Pascal, M., and Coauthors, 2006: France's heat health watch warning system. *Int. J. Biometeorol.*, **50**, 144–153, https://doi.org/10.1007/S00484-005-0003-X.

Patel, P., S. Karmakar, S. Ghosh, and D. Niyogi, 2020: Improved simulation of very heavy rainfall events by incorporating WUDAPT urban land use/land cover in WRF. *Urban Clim.*, **32**, 100616, https://doi.org/10.1016/J.UCLIM.2020.100616.

Pearlmutter, D., P. Berliner, and E. Shaviv, 2005: Evaluation of Urban Surface Energy Fluxes Using an Open-Air Scale Model.

Pesaresi, M., C. Corbane, A. Julea, A. J. Florczyk, V. Syrris, and P. Soille, 2016: Assessment of the added-value of sentinel-2 for detecting built-up areas. *Remote Sens.*, https://doi.org/10.3390/rs8040299.

Petty, G. W. (Grant W., 2004: A first course in atmospheric radiation. 445.

Piringer, M., and Coauthors, 2002: Investigating the Surface Energy Balance in Urban Areas – Recent Advances and Future Needs. *Water, Air Soil Pollut. Focus 2002 25*, **2**, 1–16, https://doi.org/10.1023/A:1021302824331.

Pomerantz, M., H. Akbari, P. Berdahl, S. J. Konopacki, and A. H. Rosenfeld, 1999: Reflective surfaces for cooler buildings and cities. *Philos. Mag. B Phys. Condens. Matter; Stat. Mech. Electron. Opt. Magn. Prop.*, **79**, https://doi.org/10.1080/13642819908216984.

Porson, A., I. N. Harman, S. I. Bohnenstengel, and S. E. Belcher, 2009: How many facets are needed to represent the surface energy balance of an urban area? *Boundary-Layer Meteorol.*, **132**, https://doi.org/10.1007/s10546-009-9392-4.

Porson, A., P. A. Clark, † I N Harman, † M J Best, and S. E. Belcher, 2010a: Implementation of a new urban energy budget scheme into MetUM. Part II: Validation against observations and model intercomparison. *Q. J. R. Meteorol. Soc. Q. J. R. Meteorol. Soc*, **136**, 1530–1542, https://doi.org/10.1002/qj.572.

Porson, A., P. A. Clark, I. N. Harman, M. J. Best, and S. E. Belcher, 2010b: Implementation of a new urban energy budget scheme in the MetUM. Part I: Description and idealized simulations. *Q. J. R. Meteorol. Soc.*, **136**, 1514–1529, https://doi.org/10.1002/qj.668.

Prastacos, P., A. Lagarias, and N. Chrysoulakis, 2017: Using the Urban Atlas dataset for estimating spatial metrics. Methodology and application in urban areas of Greece. *http://journals.openedition.org/cybergeo*, **2017**, https://doi.org/10.4000/CYBERGEO.28051.

Ramamurthy, P., and E. R. Pardyjak, 2011: Toward understanding the behavior of carbon dioxide and surface energy fluxes in the urbanized semi-arid Salt Lake Valley, Utah, USA. *Atmos. Environ.*, https://doi.org/10.1016/j.atmosenv.2010.09.049.

Rao, P., 1972: Remote sensing of urban "heat islands" from an environmental satellite. *Bull Am Meteorol Soc*, **53**, 647–648.

Raupach, M. R., 1992: Drag and drag partition on rough surfaces. *Boundary-Layer Meteorol.*, https://doi.org/10.1007/BF00155203.

——, and R. H. Shaw, 1982: Averaging procedures for flow within vegetation canopies. *Boundary-Layer Meteorol.*, https://doi.org/10.1007/BF00128057.

Redon, E. C., A. Lemonsu, V. Masson, B. Morille, and M. Musy, 2017: Implementation of street trees within the solar radiative exchange parameterization of TEB in SURFEX v8.0. *Geosci. Model Dev.*, **10**, 385–411, https://doi.org/10.5194/gmd-10-385-2017.

Resler, J., and Coauthors, 2017: A new urban surface model integrated in the large-eddy simulation model PALM. *Geosci. Model Dev. Discuss.*, https://doi.org/10.5194/gmd-2017-61.

Ronda, R. J., G. J. Steeneveld, B. G. Heusinkveld, J. J. Attema, and A. A. M. Holtslag, 2017: Urban finescale forecasting reveals weather conditions with unprecedented detail. *Bull. Am. Meteorol. Soc.*, **98**, https://doi.org/10.1175/BAMS-D-16-0297.1.

Rosenfeld, A. H., H. Akbari, S. Bretz, B. L. Fishman, D. M. Kurn, D. Sailor, and H. Taha, 1995: Mitigation of urban heat islands: materials, utility programs, updates. *Energy Build.*, **22**, 255–265, https://doi.org/10.1016/0378-7788(95)00927-P.

Rotach, M. W., and Coauthors, 2005: BUBBLE - An urban boundary layer meteorology project. *Theor. Appl. Climatol.*, **81**, 231–261, https://doi.org/10.1007/s00704-004-0117-9.

Ryu, Y. H., and J. J. Baik, 2012: Quantitative analysis of factors contributing to urban heat island intensity. *J. Appl. Meteorol. Climatol.*, **51**, https://doi.org/10.1175/JAMC-D-11-098.1.

——, ——, and S. H. Lee, 2011: A new single-layer urban canopy model for use in mesoscale atmospheric models. *J. Appl. Meteorol. Climatol.*, https://doi.org/10.1175/2011JAMC2665.1.

Ryu, Y. H., J. J. Baik, K. H. Kwak, S. Kim, and N. Moon, 2013: Impacts of urban land-surface forcing on ozone air quality in the Seoul metropolitan area. *Atmos. Chem. Phys.*, **13**, 2177–2194, https://doi.org/10.5194/acp-13-2177-2013.

Sailor, D. J., 2011: A review of methods for estimating anthropogenic heat and moisture emissions in the urban environment. *Int. J. Climatol.*, **31**, 189–199, https://doi.org/10.1002/JOC.2106.

——, and H. Fan, 2002: Modeling the diurnal variability of effective albedo for cities. *Atmos. Environ.*, https://doi.org/10.1016/S1352-2310(01)00452-6.

——, and C. Vasireddy, 2006: Correcting aggregate energy consumption data to account for variability in local weather. *Environ. Model. Softw.*, **21**, 733–738, https://doi.org/10.1016/J.ENVSOFT.2005.08.001.

Sakakibara, Y., 1996: A numerical study of the effect of urban geometry upon the surface energy budget. *Atmospheric Environment*, Vol. 30 of.

Salamanca, F., A. Martilli, M. Tewari, and F. Chen, 2011: A study of the urban boundary layer using different urban parameterizations and high-resolution urban canopy parameters with WRF. *J. Appl. Meteorol. Climatol.*, https://doi.org/10.1175/2010JAMC2538.1.

Salim, M. H., S. Schubert, J. Resler, P. Krč, B. Maronga, F. Kanani-Sühring, M. Sühring, and C. Schneider, 2022: Importance of radiative transfer processes in urban climate models: A study based on the PALM 6.0 model system. *Geosci. Model Dev.*, **15**, https://doi.org/10.5194/gmd-15-145-2022.

Salim, S. M., R. Buccolieri, A. Chan, and S. Di Sabatino, 2011: Numerical simulation of atmospheric pollutant dispersion in an urban street canyon: Comparison between RANS and LES. *J. Wind Eng. Ind. Aerodyn.*, **99**, 103–113, https://doi.org/10.1016/J.JWEIA.2010.12.002.

Salvati, A., M. Kolokotroni, A. Kotopouleas, R. Watkins, R. Giridharan, and M. Nikolopoulou, 2022: Impact of reflective materials on urban canyon albedo, outdoor and indoor microclimates. *Build. Environ.*, **207**, https://doi.org/10.1016/J.BUILDENV.2021.108459.

Santamouris, M., 2013: Using cool pavements as a mitigation strategy to fight urban heat island - A review of the actual developments. *Renew. Sustain. Energy Rev.*, **26**, 224–240, https://doi.org/10.1016/j.rser.2013.05.047.

——, 2014: Cooling the cities - A review of reflective and green roof mitigation technologies to fight heat island and improve comfort in urban environments. *Sol. Energy*, **103**, 682–703, https://doi.org/10.1016/j.solener.2012.07.003.

Santamouris, M., and Coauthors, 2018: On the energy impact of urban heat island in Sydney: Climate and energy potential of mitigation technologies. *Energy Build.*, **166**, 154–164, https://doi.org/10.1016/j.enbuild.2018.02.007.

Schneider, F. D., R. Leiterer, F. Morsdorf, J. P. Gastellu-Etchegorry, N. Lauret, N. Pfeifer, and M. E. Schaepman, 2014: Simulating imaging spectrometer data: 3D forest modeling based on LiDAR and in situ data. *Remote Sens. Environ.*, https://doi.org/10.1016/j.rse.2014.06.015.

Schubert, S., S. Grossman-Clarke, and A. Martilli, 2012: A Double-Canyon Radiation Scheme for Multi-Layer Urban Canopy Models. *Boundary-Layer Meteorol.*, **145**, 439–468, https://doi.org/10.1007/s10546-012-9728-3.

Segura, R., E. S. Krayenhoff, A. Martilli, A. Badia, C. Estruch, S. Ventura, and G. Villalba, 2022: How do street trees affect urban temperatures and radiation exchange? Observations and numerical evaluation in a highly compact city. *Urban Clim.*, **46**, 101288, https://doi.org/10.1016/J.UCLIM.2022.101288.

Sellers, W. D., 1969: A Global Climatic Model Based on the Energy Balance of the Earth-Atmosphere System. *J. Appl. Meteorol.*, **8**, https://doi.org/10.1175/1520-0450(1969)008<0392:agcmbo>2.0.co;2.

Shashua-Bar, L., D. Pearlmutter, and E. Erell, 2011: The influence of trees and grass on outdoor thermal comfort in a hot-arid environment. *Int. J. Climatol.*, **31**, 1498–1506, https://doi.org/10.1002/JOC.2177.

Shepherd, J. M., 2005: A review of current investigations of urban-induced rainfall and recommendations for the future. *Earth Interact.*, https://doi.org/10.1175/EI156.1.

Smith, S. T., 2009: Modelling thermal loads for a non-domestic building stock: associating a priori probability with building form and construction-using building control laws and regulations. University of Nottingham, .

Sobrino, J. A., C. Mattar, J. P. Gastellu-Etchegorry, J. C. Jiménez-Muñoz, and E. Grau, 2011: Evaluation of the DART 3D model in the thermal domain using satellite/airborne imagery and ground-based measurements. *Int. J. Remote Sens.*, https://doi.org/10.1080/01431161.2010.524672.

Song, T., and Y. Wang, 2012: Carbon dioxide fluxes from an urban area in Beijing. *Atmos. Res.*, https://doi.org/10.1016/j.atmosres.2011.12.001.

Souch, C., and S. Grimmond, 2006: Applied climatology: Urban climate. *Prog. Phys. Geogr.*, **30**, 270–279, https://doi.org/10.1191/0309133306PP484PR.

Soux, A., J. A. Voogt, and T. R. Oke, 2004: A model to calculate what a remote sensor "sees" of an urban surface. *Boundary-Layer Meteorol.*, **112**, 109–132, https://doi.org/10.1023/B:BOUN.0000010995.62115.46.

Sparrow, E. M. (Ephraim M. ., and R. D. Cess, 1978: Radiation heat transfer. 366.

Spronken-Smith, R. A., 2002: Comparison of summer- and winter-time suburban energy fluxes in Christchurch, New Zealand. *Int. J. Climatol.*, https://doi.org/10.1002/joc.767.

Spronken-Smith, R. A., and T. R. Oke, 1999: Scale modelling of nocturnal cooling in urban parks. *Boundary-Layer Meteorol.*, https://doi.org/10.1023/A:1002001408973.

Stamnes, K., S.-C. Tsay, W. Wiscombe, and K. Jayaweera, 1988: Numerically stable algorithm for discrete-ordinate-method radiative transfer in multiple scattering and emitting layered media. *Appl. Opt.*, https://doi.org/10.1364/ao.27.002502.

Steeneveld, G. J., S. Koopmans, B. G. Heusinkveld, L. W. A. Van Hove, and A. A. M. Holtslag, 2011: Quantifying urban heat island effects and human comfort for cities of variable size and urban morphology in the Netherlands. *J. Geophys. Res. Atmos.*, **116**, https://doi.org/10.1029/2011JD015988.

Stewart, I. D., and T. R. Oke, 2012: Local climate zones for urban temperature studies. *Bull. Am. Meteorol. Soc.*, **93**, 1879–1900, https://doi.org/10.1175/BAMS-D-11-00019.1.

Stretton, M. A., W. Morrison, R. J. Hogan, and S. Grimmond, 2022: Evaluation of the SPARTACUS-Urban Radiation Model for Vertically Resolved Shortwave Radiation in Urban Areas. *Boundary-Layer Meteorol.*, **184**, 301–331, https://doi.org/10.1007/s10546-022-00706-9.

Stull, R. B., 1988: An introduction to boundary layer meteorology. *An Introd. to Bound. layer Meteorol.*, https://doi.org/10.1007/978-94-009-3027-8/COVER.

Suckling, P. W., 1981: Nocturnal observations of incoming longwave radiation and the urban heat island for a small prairie city. *Arch. Meteorol. Geophys. Bioclimatol. Ser. B*, **29**, https://doi.org/10.1007/BF02278187.

Sugawara, H., K. I. Narita, and T. Mikami, 2001: Estimation of effective thermal property parameter on a heterogeneous urban surface. *J. Meteorol. Soc. Japan*, **79**, https://doi.org/10.2151/jmsj.79.1169.

Sun, Q., C. Miao, M. Hanel, A. G. L. Borthwick, Q. Duan, D. Ji, and H. Li, 2019: Global heat stress on health, wildfires, and agricultural crops under different levels of climate warming.

Environ. Int., **128**, 125–136, https://doi.org/10.1016/J.ENVINT.2019.04.025.

Sun, T., 2023: SUEWS. *GitHub Repos.*,.

Sun, T., Z. H. Wang, W. C. Oechel, and S. Grimmond, 2017: The Analytical Objective Hysteresis Model (AnOHM v1.0): Methodology to determine bulk storage heat flux coefficients. *Geosci. Model Dev.*, **10**, 2875–2890, https://doi.org/10.5194/GMD-10-2875-2017.

——, and Coauthors, 2022: UMEP-dev/SUEWS: Development Build. https://doi.org/10.5281/ZENODO.7110675.

Sun, T., and Coauthors, 2023: WRF (v4.0)-SUEWS (v2018c) Coupled System: Development, Evaluation and Application.

Sützl, B. S., G. G. Rooney, and M. van Reeuwijk, 2020: Drag Distribution in Idealized Heterogeneous Urban Environments. *Boundary-Layer Meteorol.*, https://doi.org/10.1007/s10546-020-00567-0.

——, ——, A. Finnenkoetter, S. I. Bohnenstengel, S. Grimmond, and M. van Reeuwijk, 2021: Distributed urban drag parametrization for sub-kilometre scale numerical weather prediction. *Q. J. R. Meteorol. Soc.*, https://doi.org/10.1002/QJ.4162.

Taha, H., 1997: Urban climates and heat islands: albedo, evapotranspiration, and anthropogenic heat. **25**, 99–103.

——, 1999: Modifying a mesoscale meteorological model to better incorporate urban heat storage: A bulk-parameterization approach. *J. Appl. Meteorol.*, **38**, https://doi.org/10.1175/1520-0450(1999)038<0466:MAMMMT>2.0.CO;2.

Takane, Y., Y. Ohashi, C. S. B. Grimmond, M. Hara, and Y. Kikegawa, 2020: Asian megacity heat stress under future climate scenarios: impact of air-conditioning feedback. *Environ. Res. Commun.*, **2**, 015004, https://doi.org/10.1088/2515-7620/AB6933.

Tan, C. L., N. H. Wong, and S. K. Jusuf, 2013: Outdoor mean radiant temperature estimation in the tropical urban environment. *Build. Environ.*, **64**, 118–129, https://doi.org/10.1016/J.BUILDENV.2013.03.012.

Tang, Y., H. W. Lean, and J. Bornemann, 2013: The benefits of the Met Office variable resolution NWP model for forecasting convection. *Meteorol. Appl.*, **20**, 417–426, https://doi.org/10.1002/MET.1300.

Tang, Y., and Coauthors, 2021: Urban meteorological forcing data for building energy simulations. *Build. Environ.*, **204**, 108088, https://doi.org/10.1016/j.buildenv.2021.108088.

Terjung, W. H., and S. Louie, 1973: Solar radiation and urban heat islands. *Ann. Assoc. Am. Geogr.*, **63**, https://doi.org/10.1111/j.1467-8306.1973.tb00918.x.

Theeuwes, N. E., R. J. Ronda, I. N. Harman, A. Christen, and C. B. Sue Grimmond, 2019: Parametrizing Horizontally-Averaged Wind and Temperature Profiles in the Urban Roughness Sublayer. *Boundary-Layer Meteorol.*, **173**, 321–348, https://doi.org/10.1007/s10546-019-00472-1.

Thorsson, S., F. Lindberg, I. Eliasson, and B. Holmer, 2007: *Different methods for estimating the mean radiant temperature in an outdoor urban setting*.

——, ——, J. Björklund, B. Holmer, and D. Rayner, 2011: Potential changes in outdoor thermal comfort conditions in Gothenburg, Sweden due to climate change: the influence of urban geometry. *Int. J. Climatol.*, **31**, 324–335, https://doi.org/10.1002/JOC.2231.

——, and Coauthors, 2017: Present and projected future mean radiant temperature for three European cities. *Int. J. Biometeorol.*, **61**, 1531–1543.

Toparlar, Y., B. Blocken, B. Maiheu, and G. J. F. van Heijst, 2017: A review on the CFD analysis of urban microclimate. *Renew. Sustain. Energy Rev.*, **80**, 1613–1640, https://doi.org/10.1016/j.rser.2017.05.248.

Trenberth, K. E., J. T. Fasullo, and J. Kiehl, 2009: Earth’s Global Energy Budget. *Bull. Am. Meteorol. Soc.*, **90**, 311–324, https://doi.org/10.1175/2008BAMS2634.1.

Umweltatlas Berlin, 2010: Building and vegetation heights 2009/2010.

United Nations, 2018: *World Urbanization Prospects 2018*.

——, 2019: World urbanization prospects - population division. *United Nations*,.

US Gazetteer, 2021: Urban Areas.

Velasco, E., S. Pressley, E. Allwine, H. Westberg, and B. Lamb, 2005: Measurements of CO 2 fluxes from the Mexico City urban landscape. *Atmos. Environ.*, **39**, 7433–7446, https://doi.org/10.1016/j.atmosenv.2005.08.038.

Verseghy, D. L., and D. S. Munro, 1989: Sensitivity studies on the calculation of the radiation balance of urban surfaces: II. Longwave radiation. *Boundary-Layer Meteorol.*, **48**, 1–18, https://doi.org/10.1007/BF00121780.

Vesala, T., and Coauthors, 2008: Surface-atmosphere interactions over complex urban terrain in Helsinki, Finland. *Tellus, Ser. B Chem. Phys. Meteorol.*, https://doi.org/10.1111/j.1600-0889.2007.00312.x.

Voogt, J. A., 2008: Assessment of an Urban Sensor View Model for thermal anisotropy. *Remote Sens. Environ.*, **112**, 482–495, https://doi.org/10.1016/j.rse.2007.05.013.

Voogt, J. A., and T. R. Oke, 1991: Validation of an urban canyon radiation model for nocturnal long-wave fluxes. *Boundary-Layer Meteorol.*, https://doi.org/10.1007/BF00118866.

——, ——, and T. O. JA Voogt, 1997: Complete urban surface temperatures. *J. Appl. Meteorol.*, **36**, 1117–1132, https://doi.org/10.1175/1520-0450(1997)036<1117:CUST>2.0.CO;2.

Wang, L., G. Zhiqiu, M. Shiguang, G. Xiaofeng, S. Ting, M. Liu, and D. Li, 2015: Contrasting Characteristics of the Surface Energy Balance between the Urban and Rural Areas of Beijing. *Adv. Atmos. Sci.*, **32**, 505–514, https://doi.org/10.1007/s00376.

Wang, Y., N. Lauret, and J. P. Gastellu-Etchegorry, 2020: DART radiative transfer modelling for sloping landscapes. *Remote Sens. Environ.*, **247**, 111902, https://doi.org/10.1016/j.rse.2020.111902.

Ward, H. C., and C. S. B. Grimmond, 2017: Assessing the impact of changes in surface cover, human behaviour and climate on energy partitioning across Greater London. *Landsc. Urban Plan.*, **165**, 142–161, https://doi.org/10.1016/j.landurbplan.2017.04.001.

——, S. Kotthaus, L. Järvi, and C. S. B. Grimmond, 2016: Surface Urban Energy and Water Balance Scheme (SUEWS): Development and evaluation at two UK sites. *Urban Clim.*, **18**, 1–32, https://doi.org/10.1016/j.uclim.2016.05.001.

Weber, S., and K. Kordowski, 2010: Comparison of atmospheric turbulence characteristics and turbulent fluxes from two urban sites in Essen, Germany. *Theor. Appl. Climatol.*, https://doi.org/10.1007/s00704-009-0240-8.

Wentz, E. A., and Coauthors, 2018: Six fundamental aspects for conceptualizing multidimensional urban form: A spatial mapping perspective. *Landsc. Urban Plan.*, **179**, 55–62, https://doi.org/10.1016/j.landurbplan.2018.07.007.

Widlowski, J. L., and Coauthors, 2007: Third Radiation Transfer Model Intercomparison (RAMI) exercise: Documenting progress in canopy reflectance models. *J. Geophys. Res. Atmos.*, https://doi.org/10.1029/2006JD007821.

——, and Coauthors, 2015: The fourth phase of the radiative transfer model intercomparison (RAMI) exercise: Actual canopy scenarios and conformity testing. *Remote Sens. Environ.*, https://doi.org/10.1016/j.rse.2015.08.016.

WMO, 2019: *Guidance on Integrated Urban Hydro-Meteorological, Climate and Environmental Services*. WMO, 52 pp.

Wu, J., Y. Zhou, Y. Gao, J. S. Fu, B. A. Johnson, C. Huang, Y. M. Kim, and Y. Liu, 2014: Estimation and uncertainty analysis of impacts of future heat waves on mortality in the Eastern United States. *Environ. Heal. Persp.*, **122**, 10–16, https://doi.org/10.1289/ehp.1308042r.

Xie, X., Z. Luo, S. Grimmond, T. Sun, and W. Morrison, 2022: Impact of inter-building longwave radiative exchanges on building energy performance and indoor overheating. *Build. Environ.*, **209**, https://doi.org/10.1016/J.BUILDENV.2021.108628.

Xie, Z. T., and I. P. Castro, 2009: Large-eddy simulation for flow and dispersion in urban streets. *Atmos. Environ.*, **43**, https://doi.org/10.1016/j.atmosenv.2009.01.016.

Xu, Y., C. Ren, P. Ma, J. Ho, W. Wang, K. K. L. Lau, H. Lin, and E. Ng, 2017: Urban morphology detection and computation for urban climate research. *Landsc. Urban Plan.*, https://doi.org/10.1016/j.landurbplan.2017.06.018.

Yaghoobian, N., and J. Kleissl, 2012: An indoor-outdoor building energy simulator to study urban modification effects on building energy use - Model description and validation. *Energy Build.*, **54**, 407–417, https://doi.org/10.1016/J.ENBUILD.2012.07.019.

Yang, X., and Y. Li, 2015: The impact of building density and building height heterogeneity on average urban albedo and street surface temperature. *Build. Environ.*, **90**, 146–156.

Yao, Y., S. Miao, and G. Lv, 2021: An efficient iterative method for radiation heat conduction problems. *Int. J. Numer. Methods Fluids*, **93**, 2362–2379, https://doi.org/10.1002/FLD.4977.

Young, D. T., P. Clark, M. Hendry, and J. Barlow, 2015: Modelling Radiative Exchange in a Vegetated Urban Street Canyon Model. *ICUC9 - 9th International Conference on Urban Climate jointly with 12th Symposium on the Urban Environment Modelling*, 1–5.

Van Der Zee, J., A. Lau, and A. Shenkin, 2021: Understanding crown shyness from a 3-D perspective. *Ann. Bot.*, **128**, 725–736, https://doi.org/10.1093/AOB/MCAB035.

Zhang, G., B. J. He, Z. Zhu, and B. J. Dewancker, 2019: Impact of morphological characteristics of green roofs on pedestrian cooling in subtropical climates. *Int. J. Environ. Res. Public Health*, **16**, https://doi.org/10.3390/ijerph16020179.

Zhang, J., C. K. Heng, L. C. Malone-Lee, D. J. C. Hii, P. Janssen, K. S. Leung, and B. K. Tan, 2012: Evaluating environmental implications of density: A comparative case study on the relationship between density, urban block typology and sky exposure. *Automation in Construction*.

Zhu, Z., Y. Zhou, K. C. Seto, E. C. Stokes, C. Deng, S. T. A. Pickett, and H. Taubenböck, 2019: Understanding an urbanizing planet: Strategic directions for remote sensing. *Remote Sens. Environ.*, **228**, 164–182, https://doi.org/10.1016/j.rse.2019.04.020.